Physics, chemistry and biology of functional nanostructures

Edited by Paul Ziemann and Thomas Schimmel

Imprint

Physics, chemistry and biology of functional nanostructures

Paul Ziemann[*1] and Thomas Schimmel[*2]

Editorial

Address:
[1]Institute of Solid State Physics, Ulm University, D-89069 Ulm, Germany and [2]Institute of Nanotechnology (INT), Karlsruhe Institute of Technology (KIT), 76021 Karlsruhe, Germany

Email:
Paul Ziemann[*] - paul.ziemann@uni-ulm.de; Thomas Schimmel[*] - thomas.schimmel@kit.edu

* Corresponding author

Nanoscience emerged as a field addressing phenomena that are strongly related to and influenced by their length scale being in the nanometer range. From the very beginning its interdisciplinary character became obvious. Meanwhile, after nanoscience had left its infancy, this characteristic feature developed even further by extension of the contributing disciplines: Initially it was supported and pushed forward by physics, materials science and chemistry, with a strong interrelation with semiconductor/information technology with their road maps for the downscaling of switching and storage devices. Today, biology and thus, in a natural way, medicine are included, opening new research areas within nanoscience. As a consequence of this development towards a real transdisciplinary field of science, worldwide collaborative research networks have been installed encompassing physics, materials science, chemistry and biology as well as various areas of engineering.

One such network with focus on "Functional Nanostructures" has been successfully active for almost ten years in Baden-Württemberg (Germany) [1]. Recent results from this network form the nucleus of the present Thematic Series *"Physics,*
chemistry and biology of functional nanostructures" in the *Beilstein Journal of Nanotechnology*, complemented by contributions from international groups outside this network.

Besides the interdisciplinary approaches of nanoscience, its ongoing success can be attributed to at least three more necessary conditions:

- *Significant progress in fabricating and controlling nanometer-sized objects and functional systems.* Examples are synthesis and controlled positioning of various nanoparticles and macromolecules providing, finally, specific functions if arranged on suitable platforms in an optimized way. In the context of arranging nanoobjects, the exploitation of self-organization often in combination with suitable templates plays a major role. This aspect of the "bottom-up" methods opens routes towards novel nanolithographies, and due to the practical importance of the issue, the topic will be addressed in a number of contributions to the present Thematic Series.

- ***Continuous progress related to analytical tools and facilities*** allowing as complete as possible characterization of nanoobjects and devices. It is of special importance to gain information on the structure as well as the chemical composition and state of nanosytems in order to relate these to the various sought-after properties. With respect to tools, immediate examples are the continuous improvements of scanning-probe measurements such as scanning tunneling or scanning force microscopy (STM, AFM) [2] and their numerous variants often combined with scanning electron microscopy (SEM) or scanning helium ion microscopy (SHIM). Remarkable also are the breakthroughs in structural insight due to the advent of Cs-corrected high-resolution transmission electron microscopy (HRTEM) [3,4] or spectroscopic imaging in scanning TEM (STEM) [5]. Related to facilities, certainly the worldwide impressive progress of synchrotron facilities has made an important contribution, now providing beams with spot sizes even below 10 nm, thus promising the application of spectroscopies such as photoelectron emission microscopy (PEEM) or X-ray magnetic circular dichroism (XMCD) on a single nanoobject [6,7].
- ***Progress in the theoretical understanding of nanoscaled phenomena.*** We deem progress in theory necessary in order to gain feedback for testing new predicted phenomena or optimizing already existing nanosystems and devices.

All three of these conditions together with the given examples play a major role in the present Thematic Series, which, in turn, stands alongside previous series. Of special interest appear those reports dealing with self-assembly on solid surfaces, micro- and mesoporous solids, electrical transport through nanostructures, nanooptical aspects, organic–inorganic hybrids and properties of magnetic nanoparticles. A much broader view on biomimetic approaches can be found in [8]. The choice of these recommendations becomes obvious on summarizing the main topics of the present Thematic Series:

- Nanolithography approaches based on self-organized colloidal systems
- Experimental and theoretical description of electrical transport through nanostructures. Here, focus is put on the electrochemically controlled preparation of metallic point contacts [9,10]
- Magnetic behavior of nanoparticles and -wires
- Nanophotonics
- Effect of nanoporosity on the catalytic properties of Au oxidizing CO

- Theoretical description of organic building blocks such as polythiophenes. These molecules are especially interesting for organic solar cells [11] and have been analyzed also by STS [12].

Of course, the contributions to this Thematic Series form just a snapshot of the current activities focused on functional nanostructures. We hope, however, that our choice, which was guided by the idea to present interesting examples for the three general conditions given above, will be found inspiring by the readers as well. We give thanks to all colleagues for the valuable reports on their research and the Beilstein team for the engaged editorial work.

Paul Ziemann and Thomas Schimmel

Ulm, Karlsruhe, November 2012

References

1. Schimmel, T.; Löhneysen, H.; Barczewski, M., Eds. *Nanotechnology – Fundamentals and Applications of Functional Nanostructures;* Research Series No. 6, ISBN 978-3-00-030810-9; Baden-Württemberg Stiftung, 2011.
2. Gross, L.; Mohn, F.; Liljeroth, P.; Repp, J.; Giessibl, F. J.; Meyer, G. *Science* **2009,** *324,* 1428. doi:10.1126/science.1172273
3. Wang, Z. L. *Adv. Mater.* **2003,** *15,* 1497. doi:10.1002/adma.200300384
4. Li, Z. Y.; Young, N. P.; Di Vece, M.; Palomba, S.; Palmer, R. E.; Bleloch, A. L.; Curley, B. C.; Johnston, R. L.; Jiang, J.; Yuan, J. *Nature* **2008,** *451,* 46. doi:10.1038/nature06470
5. Pennycook, S. J.; Colliex, C. *MRS Bull.* **2012,** *37,* 13. doi:10.1557/mrs.2011.332
6. Fischer, P. *Mater. Today* **2010,** *13,* 14. doi:10.1016/S1369-7021(10)70161-9
7. Ice, G. E.; Budai, J. D.; Pang, J. W. L. *Science* **2011,** *334,* 1234. doi:10.1126/science.1202366
8. Bhushan, B. *Beilstein J. Nanotechnol.* **2011,** *2,* 66. doi:10.3762/bjnano.2.9
9. Xie, F.-Q.; Maul, R.; Augenstein, A.; Obermair, C.; Starikov, E. B.; Schön, G.; Schimmel, T.; Wenzel, W. *Nano Lett.* **2008,** *8,* 4493. doi:10.1021/nl802438c
10. Obermair, C.; Kuhn, H.; Schimmel, T. *Beilstein J. Nanotechnol.* **2011,** *2,* 740. doi:10.3762/bjnano.2.81
11. Mishra, A.; Bäuerle, P. *Angew. Chem., Int. Ed.* **2012,** *51,* 2020. doi:10.1002/anie.201102326
12. Koslowski, B.; Tschetschetkin, A.; Maurer, N.; Mena-Osteritz, A.; Bäuerle, P.; Ziemann, P. *Beilstein J. Nanotechnol.* **2011,** *2,* 561. doi:10.3762/bjnano.2.60

Revealing thermal effects in the electronic transport through irradiated atomic metal point contacts

Bastian Kopp[1], Zhiwei Yi[1], Daniel Benner[1], Fang-Qing Xie[2],
Christian Obermair[2], Thomas Schimmel[2,3], Johannes Boneberg[1],
Paul Leiderer[1] and Elke Scheer[*1]

Abstract

We report on the electronic transport through nanoscopic metallic contacts under the influence of external light fields. Various processes can be of relevance here, whose underlying mechanisms can be studied by comparing different kinds of atomic contacts. For this purpose two kinds of contacts, which were established by electrochemical deposition, forming a gate-controlled quantum switch (GCQS), have been studied. We demonstrate that in these kinds of contacts thermal effects resulting from local heating due to the incident light, namely thermovoltage and the temperature dependences of the electrical resistivity and the electrochemical (Helmholtz) double layer are the most prominent effects.

Introduction

Electronic transport on the nanoscale is one of the central topics in nanoscience. As the size of a contact between two leads is reduced to atomic dimensions, quantum phenomena become relevant in metallic point contacts [1-4], and it has even become possible to determine the conductance of individual molecules attached between two metallic tips both theoretically [4-7] and experimentally [4,8-11]. Furthermore the influence of the environment on the conductance of single-molecule junctions [12] has been revealed. In a next step towards molecular electronics, one would like to see such molecules exhibiting certain func-

tions, e.g., the electrical current through the molecules being controllable by means of external electrodes or by light [13]. Hence studying the effect of light on nanoscopic contacts is of interest both for its own sake and for future applications.

Several theoretical investigations exist, in which the influence of light on the conductance behaviour of nanocontacts has been studied, and various mechanisms for such an influence have been suggested [14,15]. In complementary experimental studies it was shown that the conductance of electrical point contacts in a range of one to several G_0 (where G_0 is the conductance quantum, $2e^2/h \approx 77.6\ \mu S = (12.9\ k\Omega)^{-1}$) can indeed be influenced by irradiation with light [16-18]. The observed modification in the conductivity has in this case been assigned to photo-assisted transport (PAT), partly mediated by plasmons, as the dominating mechanism. Yet, in general several additional effects are conceivable in experiments with illuminated electrical contacts, which may affect the characteristics of the contact. Although partly trivial, they can mask the intrinsic mechanisms of charge transport through the contact. For an unequivocal analysis and interpretation of the charge transport it is therefore essential to take these phenomena into account. As an obvious example, incident photons can give rise to a local increase in temperature, resulting in thermal expansion, thermovoltage, and resistance change in the leads. The effect of thermal expansion on a laser-irradiated metallic nanocontact has been demonstrated already some time ago in scanning tunnelling microscopy (STM) experiments [19,20]. Upon irradiating the STM tip with a short laser pulse, the junction resistance was observed to be drastically reduced due to the expansion of the tip, and the contact could even be switched for a short time from the tunnelling to the point-contact regime. In the following we will describe phenomena that will turn out to be related to thermal effects.

Results and Discussion
Electrochemically closed contacts (immersed in electrolyte) [GCQS]

The first type of sample consisted of two Au electrodes, which were immersed in an $AgNO_3/HNO_3$ electrolyte and were separated by a 50 nm wide gap. This gap was fabricated by sputtering using a carbon fibre as mask. This is the basis for the atom transistor described by Obermair and co-workers [21-23] in more detail. The contact can be repeatedly opened and closed, and well-defined conductance values can be achieved with this "gate-controlled quantum switch" (GCQS).

By applying proper potentials, Ag crystallites were deposited and the contact was established. The area of the working electrodes that was exposed to the electrolyte had a triangular shape with a size of about $200 \times 150\ \mu m^2$; the remaining part of the

electrodes was covered by an insulating layer of varnish. For the measurements in electrolyte, a mixture of $AgNO_3$ (2 mM) and HNO_3 (0.1 M) in bidistilled water is used. Between the two working electrodes a small potential difference of typically −12.9 mV was applied in order to determine the conductance of the contact between them. Figure 1 presents a scanning electron microscope (SEM) image after the deposition of Ag. Obviously one of the electrodes (on the right) is covered by distinctly more Ag crystallites than the other one, due to the slightly different potentials applied to the two electrodes.
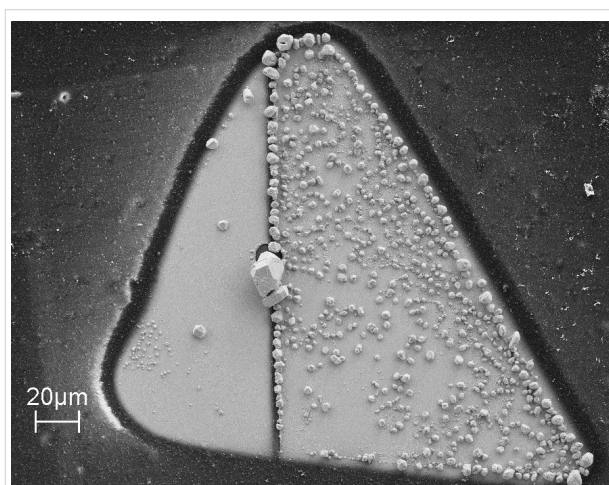
Figure 1: SEM image of the Au electrodes; the gap between the two segments, distinguishable by the border of the region covered by Ag crystallites, is somewhat left from the middle (size of the image $200 \times 150\ \mu m^2$).

The illumination experiments of these electrodes were carried out with a pulsed Nd:YAG laser (second harmonic, wavelength $\lambda = 532$ nm). The laser focus had a diameter of 10 μm, much smaller than the active electrode areas, making spatially resolved measurements feasible. A typical light-induced signal is shown in Figure 2a. Since the voltage across the contact was kept constant at −12.9 mV by the electronic circuit, this signal represents the additional current between the two electrodes induced by the light pulses. For comparison, a signal obtained in earlier measurements on a mechanically controlled break-junction (MCBJ) is shown in Figure 2b [16]. In the latter case, the signal is caused by a change in the ohmic conductance of the junction. The signal in Figure 2a, however, contains a dominating capacitive contribution.

A possible interpretation is that the signal for the electrolytic cell in Figure 2a does not originate from the nanoscopic ohmic contact between the two working electrodes (formed by a deposited Ag crystallite), but is rather caused by a light-induced change of the capacitance of the electrochemical (Helmholtz) double layer between the Au electrodes and the surrounding
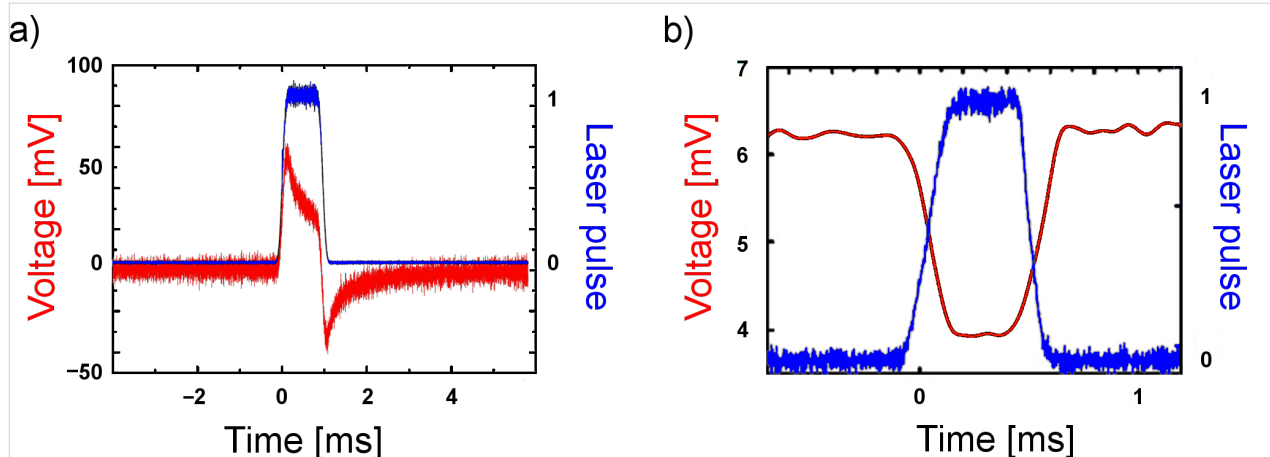
Figure 2: (a) Red: Light-induced signal of a gold electrode under illumination (see Figure 1) in an electrochemical environment. Blue: laser pulse (duration 1 ms). (b) Red: Light-induced signal under illumination of a mechanically controlled break-junction. Blue: laser pulse (duration 0.5 ms) [16].

electrolyte [24]. This is corroborated by the fact that signals like in Figure 2a can also be obtained when there is no direct ohmic contact between the two electrodes, meaning that any charge transport between the working electrodes has to take place through the electrolyte. Furthermore, the signal depends on the surface conditions of the electrodes, as shown in Figure 3. Here

we present a "map" of the signal for an area of 30×40 μm^2 on both sides of the gap of the electrodes. The left and the right parts refer to the relatively smooth and the rough segments, respectively, as shown in the SEM image (Figure 1). Apparently, the signals are nearly constant within each segment, irrespective of the detailed position of the laser focus, but a prom-
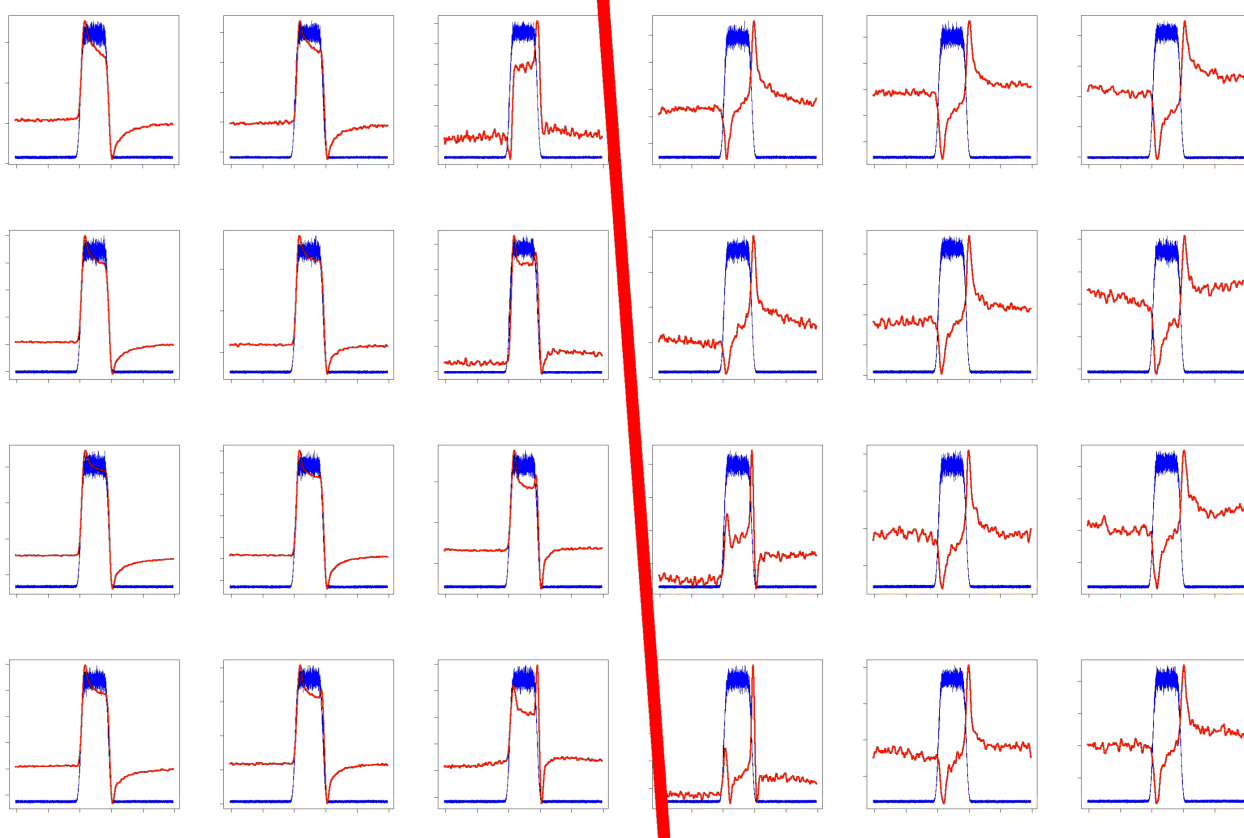
Figure 3: Spatial dependence of the light-induced signal (see Figure 2a) for the two working electrodes. The probed area (90 × 60 μm^2) is split by the gap between the electrodes as the red line indicates.

inent difference between the smooth and the rough electrode is observed. This supports the interpretation that the Helmholtz layer, which depends on the details of the surface of an electrode, is responsible for the signals in Figure 2a and Figure 3.

Why should the Helmholtz layer be influenced by incident light pulses? It is known that the electrical properties of the layer depend on temperature [25]. Therefore, if an incident light pulse leads to a temperature change at the metal–electrolyte interface, an electrical signal will be generated. For the laser pulses used in our experiment we estimate temperature changes at the interface in the range of a few kelvin. The corresponding signals are consistent with those reported by Gründler et al. [24] when we take into account that in our experiment only a small fraction of the metal–electrolyte interface is heated by the focused laser beam.

To be sure that what is observed here is primarily a temperature effect and not a photon-induced phenomenon, such as a photochemical reaction at the interface, we carried out a control experiment in which the Au layer was first irradiated from the

electrolyte and then from the glass substrate side. If the effect is purely thermal, the light-induced signals for the two directions should essentially be the same, whereas for a photon-dominated mechanism an illumination of the Au electrode from the glass side should result in a strongly reduced signal, since the light intensity at the metal–electrolyte interface in this case is negligible. As it turned out, the signals for both illumination directions were similar, confirming the idea of a thermal effect.

All the signals reported so far were obtained for fixed potentials between the respective electrodes (reference, counter and working electrodes). By varying the potentials in a controlled way one should be able to obtain additional information about the temperature-induced changes of the Helmholtz layer. We therefore carried out voltammetric studies in order to determine the regions of the voltammogram in which the laser-induced signals are most prominent.

Light-induced signals in the cyclic voltammogram of $AgNO_3$ were observed as shown in Figure 4. The inset figures illustrate that the illumination triggered changes in the current: when the
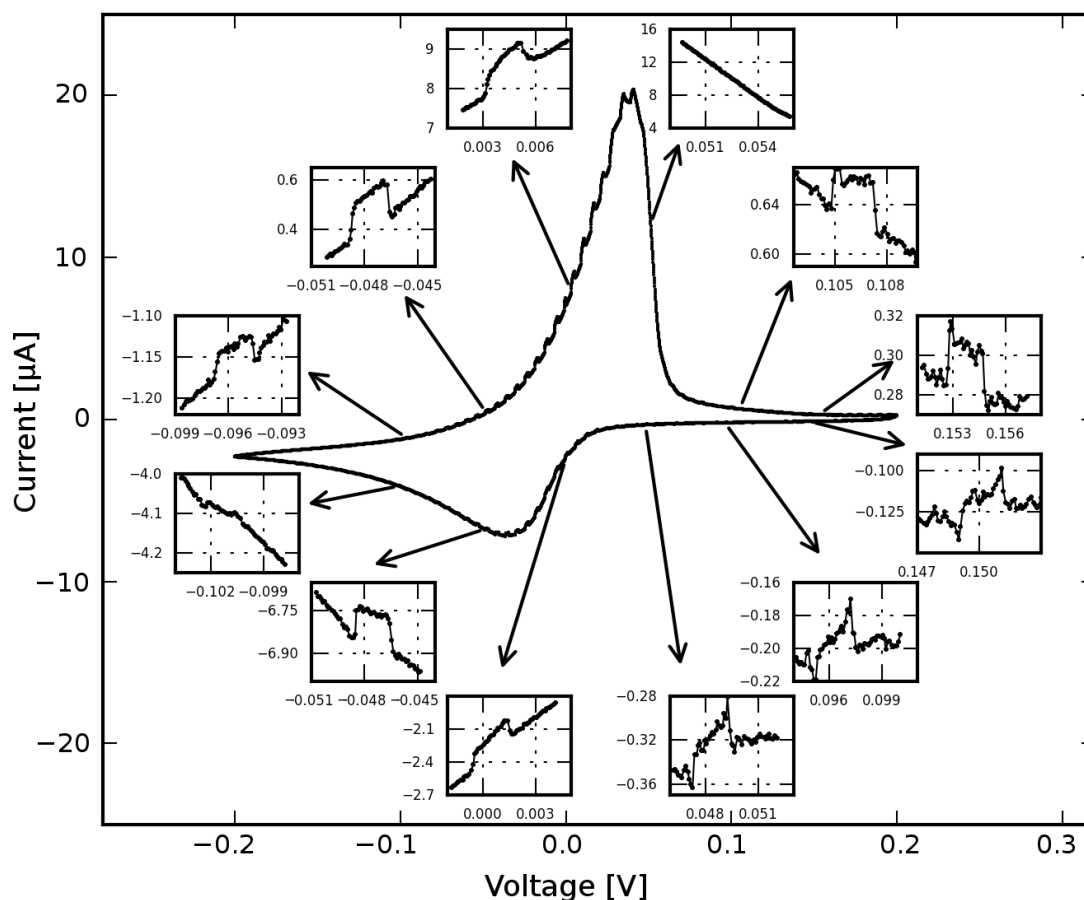

Figure 4: Cyclic voltammogram of $AgNO_3$ under illumination. Twelve insets of zoomed areas at different potentials are presented here (scan rate is 20 mV/s).
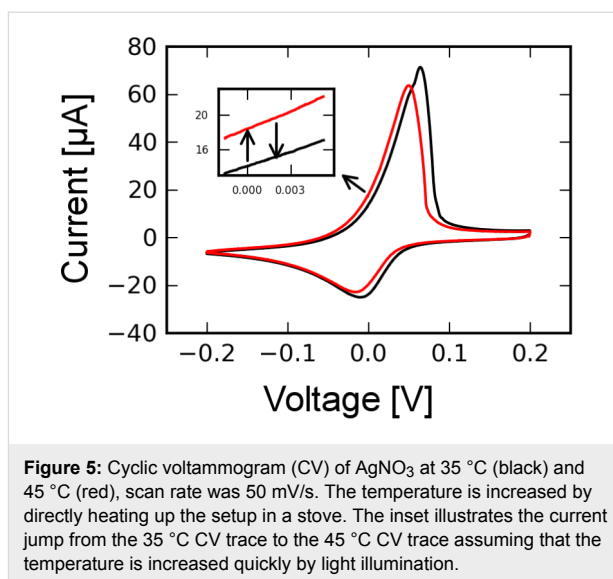
laser was switched on, the current jumped to a new level, and when the laser was switched off, the current went back to the original trace. The magnitude of the current increase depended on the potential and the redox states of the sample. In the forward scan, the signals were most pronounced at 0 V, with a current increase of 0.25 µA and were less pronounced at 0.1 V, where the current increase is about 0.04 µA. No light-induced signals were observed at 0.05 V. In the backward scan, the largest signals were observed around −0.05 V, with a current increase of 0.25 µA. The signals were much smaller at other potentials.

Since the light illumination unavoidably goes along with heating, it is reasonable to consider thermal effects, e.g., the temperature increase at the solid–liquid interface, as a potential origin of the light-induced signals.
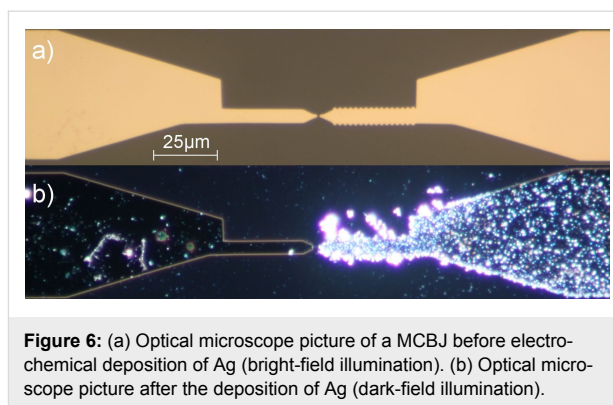
To check this hypothesis, cyclic voltammetry was performed at different temperatures by directly heating up the whole setup in a stove. Cyclic voltammograms (CVs) recorded at 45 and 35 °C are shown in Figure 5, which indicates that the redox peak shifted to negative potentials and the peak current decreased when the temperature increased. This feature qualitatively explains the light-induced signals shown in Figure 4. When the light was switched on (indicated by the upward arrow in the inset of Figure 5), the temperature of the electrode increased and the current trace jumped to the trace corresponding to a higher temperature. As long as the electrode was illuminated the current followed the trace of higher temperature. Once the light was switched off (indicated by the downward arrow), the current jumped back to its original trace, thus forming the light-induced current changes shown in Figure 4. Furthermore, the current change in Figure 5 was most prominent at a potential of around 0 V and was less pronounced at other potentials, which also agrees with the features in the experiment on the light-induced current change (Figure 4). However, in the potential range from 0.05 to 0.1 V, light-induced signals were not observed, but current changes were observed on comparison of the CV at 45 °C with the CV at 35 °C. One reason for the discrepancy may be that the heating by light is local and the heating by a stove is homogeneous. We argue that a homogeneous temperature increase involving the whole surface area may have a more pronounced influence on the diffusion process than local heating does.

Dried electrochemically closed contacts

One possible route to eliminate the unwanted contribution of the double layer is to remove the electrolyte after the contact has been fabricated electrochemically. For these experiments we used an electrode design similar to the one typical for MCBJs (Figure 6a). The electrodes were prepared by electron-

Figure 5: Cyclic voltammogram (CV) of $AgNO_3$ at 35 °C (black) and 45 °C (red), scan rate was 50 mV/s. The temperature is increased by directly heating up the setup in a stove. The inset illustrates the current jump from the 35 °C CV trace to the 45 °C CV trace assuming that the temperature is increased quickly by light illumination.

beam lithography, but in contrast to usual MCBJs we used glass substrates and a 500 nm wide gap between the two contact leads. This gap was then closed, as for the GCQS described in the previous section, by electrochemical deposition in an $AgNO_3$ electrolyte. Before the electronic measurements were performed the electrolyte was carefully removed. In spite of the mechanical perturbations it was possible to keep the contact at a conductance value of a few G_0, adjusted during deposition, even in the dry state. With these samples we were able to identify two sources of signals appearing upon illumination of the junction, namely thermovoltage and temperature dependence of the lead resistance.

Figure 6: (a) Optical microscope picture of a MCBJ before electrochemical deposition of Ag (bright-field illumination). (b) Optical microscope picture after the deposition of Ag (dark-field illumination).

Thermovoltage

As an advantage compared to the GCQS in Figure 1, the location where the contact is formed is now well-defined on a sub-micrometer length scale. This allows one to determine the spatially resolved response of the junction with high resolution. As Figure 7a shows, also for such samples a light-induced signal is observable.

Figure 7: (a) Light-induced signal (red) of a dry, electrochemically closed break junction, and the laser pulse (blue). (b) Spatially resolved measurements of the light-induced signal as in (a). The signal drops to zero, when the laser focus is exactly aligned on the centre of the junction.
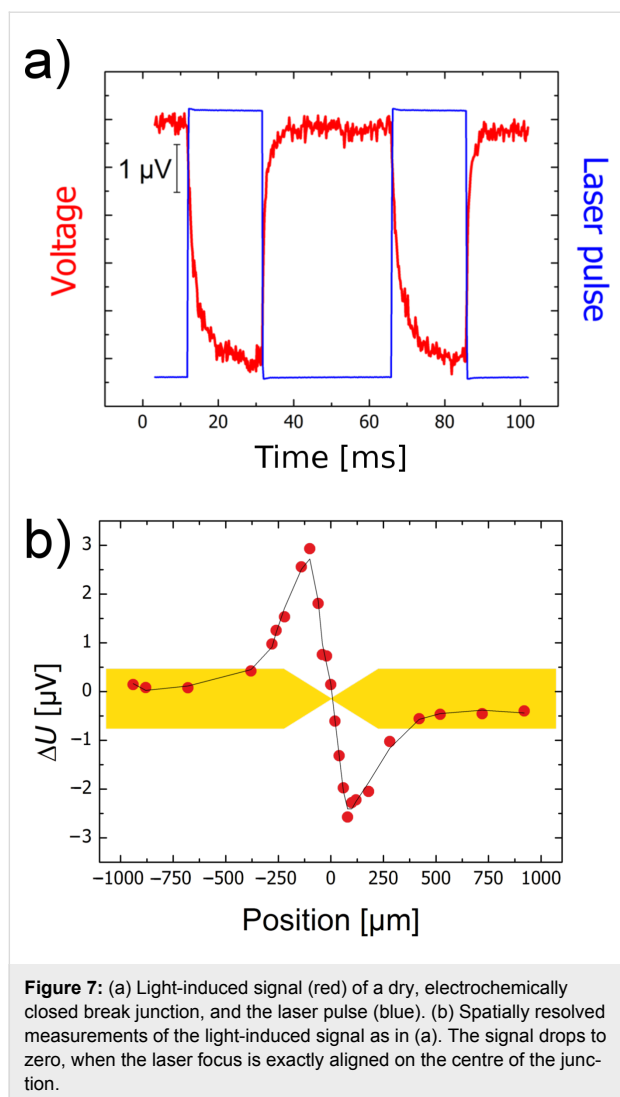
At first sight, the shape of the signal appears to be similar to the one of PAT (Figure 2b), and, as expected, a capacitive part which would result from an electrochemical double layer is not present here. Besides, the signals display a pronounced spatial dependence and are observable only in the vicinity of the point contact (Figure 7b). The signal vanishes when the laser focus is exactly at the contact position, and it changes sign when the focus is scanned from one side of the contact to the other. These observations are in contrast with the results for PAT. They can be explained when the topology of the electrochemically closed contact is taken into account, as sketched in Figure 8a.
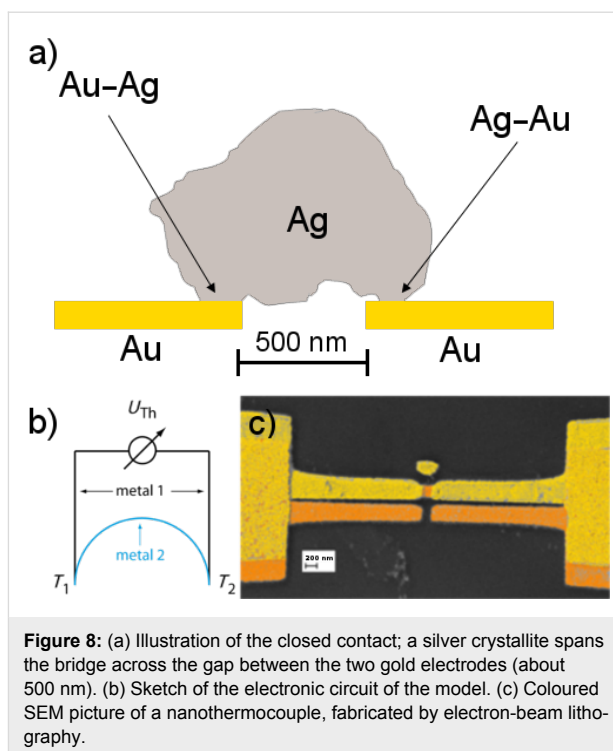
Actually, one is not dealing with a single, but rather with two point contacts, namely an Au–Ag and an Ag–Au contact in series. These act as a thermocouple in which the sensor and the reference contact are closely spaced. For asymmetric heat input (i.e., when the junction is not illuminated exactly in the centre) one of the contacts will be at a higher temperature than the other

Figure 8: (a) Illustration of the closed contact; a silver crystallite spans the bridge across the gap between the two gold electrodes (about 500 nm). (b) Sketch of the electronic circuit of the model. (c) Coloured SEM picture of a nanothermocouple, fabricated by electron-beam lithography.

one, resulting in a thermovoltage proportional to the temperature difference, as visualized in Figure 8b. This voltage will change its sign, when the position of the warmer contact is switched, in agreement with the behaviour shown in Figure 7b. For the combination Au–Ag, as was used here, the Seebeck coefficient is rather small, i.e., 0.3 µV/K. Nevertheless the effect is readily observable. The maximum signal in Figure 7a corresponds to a temperature difference of about 17 K between the two contacts of the junction. For other material combinations, such as Au–Pt or Au–Ni, the effect can be one to two orders of magnitude higher, and this expectation was confirmed in control experiments. Finally, we confirmed that similar effects were observed in lithographically defined junctions that were never exposed to electrolytes, Figure 8c. These control experiments demonstrate that no electrochemical process is at the origin of the observations.

Temperature dependence of the lead resistance

The leads towards the nanocontact, as seen in Figure 6, consist of an evaporated Au film with a thickness of 100 nm and width of 4 µm. The electrical resistance of these leads is several tens of ohms. Since the material is a pure metal, the resistance at 300 K varies roughly linearly with temperature. For a light-induced temperature change of the leads of around 10 K, as suggested on the basis of the measured thermovoltage, one will therefore expect a change in the resistance of the whole sample on the order of 1 Ω. This can also give rise to a signal upon illu-

mination, which, however, can easily be distinguished from the thermovoltage, because it is proportional not only to the temperature change, but also to the bias current through the sample. In Figure 9 we have plotted the voltage changes across the contact upon illumination for a sequence of bias currents. As the data show, the contributions of the thermovoltage and the lead resistance to the observed signal can be separated by using the relation $\Delta U = A\, I_{bias} + B$, where the first term is due to the temperature-induced change in the lead resistance and the second one to the thermovoltage. The experimental values for both contributions are consistent with the estimated temperature increase during the illumination.
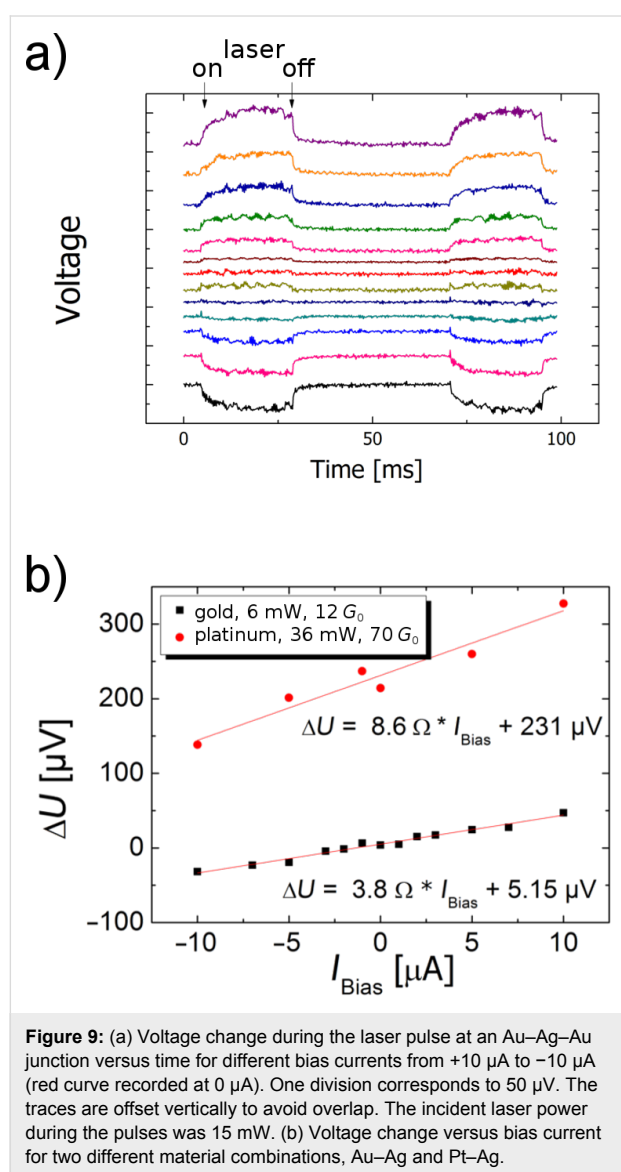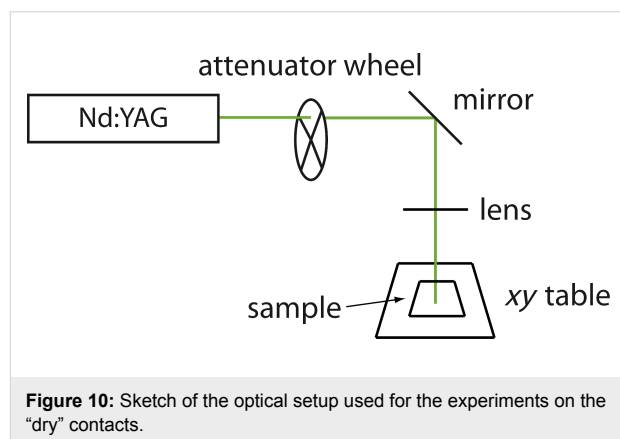
signal of a GCQS under laser illumination. In contrast, for the electrochemically closed, but dried contacts the thermovoltage due to a two-material system is the dominating effect. The two contacts between the two metals act as a micron-size thermocouple, which produces a thermovoltage under asymmetric laser illumination. Furthermore it was shown that a conductance change of the leads can make a noticeable contribution when small contacts are illuminated.

Experimental
Optical setups
For the individual experiments several optical setups with different laser sources have been used as described in the individual sections above. In all experiments we used cw-lasers, the radiation of which was chopped into pulses with a mechanical attenuation wheel. In all setups the laser beams were focussed with combinations of lenses onto the sample surface. The spot diameters are also indicated in the respective sections. In the spatially resolved experiments the samples were mounted on *xy* tables that were manually moved by using micrometer screws. As an example, we show in Figure 10 the one used for recording the data shown in Figure 7 and Figure 9.

Figure 10: Sketch of the optical setup used for the experiments on the "dry" contacts.

Figure 9: (a) Voltage change during the laser pulse at an Au–Ag–Au junction versus time for different bias currents from +10 µA to −10 µA (red curve recorded at 0 µA). One division corresponds to 50 µV. The traces are offset vertically to avoid overlap. The incident laser power during the pulses was 15 mW. (b) Voltage change versus bias current for two different material combinations, Au–Ag and Pt–Ag.

Conclusion
The results show that the temperature dependence of the Helmholtz double layer is the main reason for the light-induced

Electrical measurements at constant potential
All electrical measurements are performed at room temperature (20–25 °C) if not stated differently. Figure 11 shows the electronic circuit for controlling the electrochemical deposition, with the two Au electrodes as working electrodes 1 and 2, and in addition a reference and a counter electrode. A voltage of −12.9 mV is applied across the two working electrodes for the conductance measurement of the metallic atomic-scale point contact. The potential at one working electrode is controlled by the virtual ground technique implemented by the operational amplifier (OP2) in this current–voltage converter. The size of the atomic contact is controlled by applying the control potential U_{ec} through amplifier OP1. The whole measurement is controlled by a home-written software code described in [23].
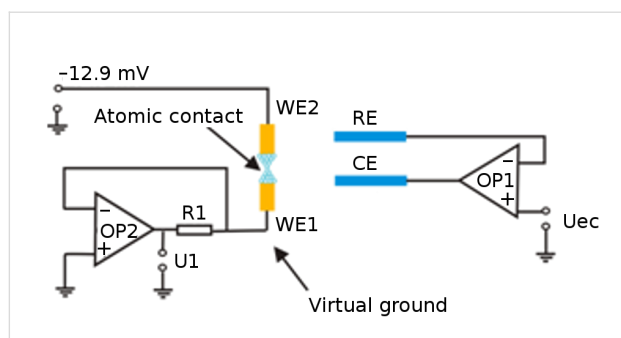
Figure 11: Sketch of the electronic circuit used for the measurements on the electrochemically controlled contacts. The two working electrodes (WE1, WE2) are prepared by shadow sputtering on a glass substrate. They are about 100 nm thick, and ca. 50 nm apart. The reference (RE) and counter (CE) electrodes are made of highly pure silver wires.

The measurements on the dry contacts were performed in current bias mode by using a voltage source (Yokogawa model 7651) providing the voltage across the series circuit of the sample and a large series resistance of 100 kΩ (see Figure 12). The current is measured by the voltage drop across the series resistance. This signal, as well as the voltage drop U_{sample} across the sample are measured with fast voltage amplifiers (Femto DLPVA-100-F-D). All signals are fed to a digital storage oscilloscope (LeCroy Waverunner 6050A).
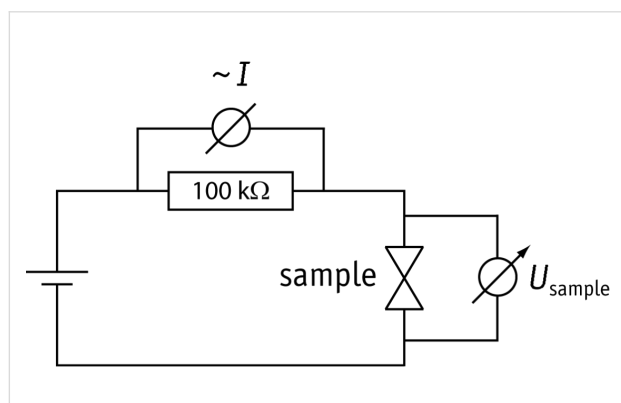

Figure 12: Sketch of the electrical circuit used for the measurements on the "dry" contacts.

Cyclic voltammetry

The cyclic voltammograms were recorded by using a potentiostat SP-300 (BioLogic Science Instrument), which was used to control the voltage and monitor the current. The sweep-rates are indicated in the figure captions. For recording the CVs at elevated temperature, the electrochemical cell with all the electrodes and connection cables was heated in a stove for five minutes at a preset temperature, monitored by a thermocouple to a precision of ± 2 °C. Then the cyclic voltammetry was performed in situ.

A home-made electrochemical setup (as shown in Figure 13) was used to investigate the light-induced transport changes in the liquid environment. Two silver wires with a diameter of 0.5 mm were used as reference electrode (RE) and counter electrode (CE). A 10 nm film of titanium and 50 nm of gold was evaporated on a glass slide and used as the working electrode. Silver nitride (1 mM) in nitride acid (10 mM) was used as the supporting electrolyte. An Ar/Kr laser with output power of 5 mW and 532 nm wavelength was used as the light source. Laser pulses of 0.1 s length and 0.2 s dark time were produced by a mechanical chopper wheel, and the laser was focused to a spot with diameter of 100 μm by an optical lens.
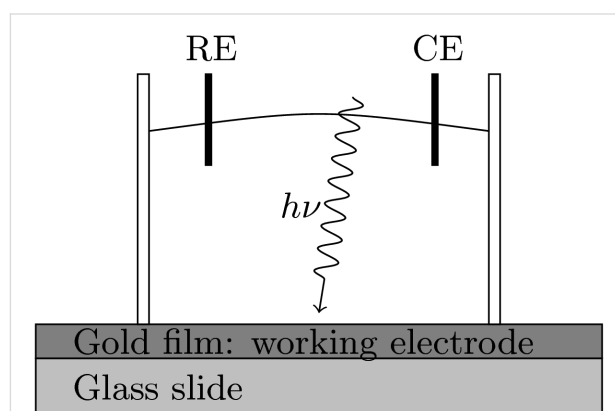

Figure 13: Diagram of an electrochemical cell used for studying the influence of laser illumination on the charge transport at solid–liquid interfaces.

Electron-beam lithography

Prior to the electron-beam lithography process, a thin polyimide layer and a double layer of electron-beam resists, MMA-MAA/PMMA, were deposited by spincoating on the wafer and soft-baked in an oven at 170 °C. The polyimide layer served for both planarization of the commercial glass substrate and for enhancing the adhesion of the metal layers. To avoid deterioration of the electron-beam-defined pattern caused by charge accumulation on the insulating glass substrate, a 5 nm thin Al layer was evaporated. The electron-beam writing was performed in a scanning electron microscope equipped with a pattern generator. After being developed in a mixture of MIBK:IPA (1:3), the patterned samples were mounted in an electron-beam evaporator under high vacuum (10^{-6} mbar) and metal (Au or Pt) was deposited at a rate of 1 Å/s. The metal thickness for the electrodes to be closed by electrochemistry was in the range of 80 to 100 nm. When shadow evaporation is applied for defining the nano-thermocouple, the metal thicknesses amount to 40 nm for the first layer and 30 nm for the second layer. The lift-off is performed at room temperature in acetone for several tens of seconds. The samples are then rinsed in IPA and blown dry under a gentle flow of nitrogen.

Acknowledgements

References

1. Agraït, N.; Levy Yeyati, A.; van Ruitenbeek, J. M. *Phys. Rep.* **2003,** *377,* 81–279. doi:10.1016/S0370-1573(02)00633-6
2. Obermair, C.; Kuhn, H.; Schimmel, T. *Beilstein J. Nanotechnol.* **2011,** *2,* 740–745. doi:10.3762/bjnano.2.81
3. Scheer, E.; Agraït, N.; Cuevas, J. C.; Levy Yeyati, A.; Ludoph, B.; Martín-Rodero, A.; Bollinger, G. R.; van Ruitenbeek, J. M.; Urbina, C. *Nature* **1998,** *394,* 154–157. doi:10.1038/28112
4. Cuevas, J. C.; Scheer, E. *Molecular Electronics: An Introduction to Theory and Experiment;* World Scientific Publishing, 2010. doi:10.1142/7434
5. Bergfield, J. P.; Barr, J. D.; Stafford, C. A. *Beilstein J. Nanotechnol.* **2012,** *3,* 40–51. doi:10.3762/bjnano.3.5
6. Solomon, G. C.; Bergfield, J. P.; Stafford, C. A.; Ratner, M. A. *Beilstein J. Nanotechnol.* **2011,** *2,* 862–871. doi:10.3762/bjnano.2.95
7. Strange, M.; Thygesen, K. S. *Beilstein J. Nanotechnol.* **2011,** *2,* 746–754. doi:10.3762/bjnano.2.82
8. Quek, S. Y.; Kamenetska, M.; Steigerwald, M. L.; Choi, H. J.; Louie, S. G.; Hybertsen, M. S.; Neaton, J. B.; Venkataraman, L. *Nat. Nanotechnol.* **2009,** *4,* 230–234. doi:10.1038/nnano.2009.10
9. Kamenetska, M.; Koentopp, M.; Whalley, A. C.; Park, Y. S.; Steigerwald, M. L.; Nuckolls, C.; Hybertsen, M. S.; Venkataraman, L. *Phys. Rev. Lett.* **2009,** *102,* 126803. doi:10.1103/PhysRevLett.102.126803
10. Song, H.; Kim, Y.; Ku, J.; Jang, Y. H.; Jeong, H.; Lee, T. *Appl. Phys. Lett.* **2009,** *94,* 103110. doi:10.1063/1.3097217
11. Hong, W.; Valkenier, H.; Mészáros, G.; Zsolt Manrique, D.; Mishchenko, A.; Putz, A.; Moreno García, P.; Lambert, C. J.; Hummelen, J. C.; Wandlowski, T. *Beilstein J. Nanotechnol.* **2011,** *2,* 699–713. doi:10.3762/bjnano.2.76
12. Nakashima, S.; Takahashi, Y.; Kiguchi, M. *Beilstein J. Nanotechnol.* **2011,** *2,* 755–759. doi:10.3762/bjnano.2.83
13. Kim, Y.; Hellmuth, T. J.; Sysoiev, D.; Pauly, F.; Pietsch, T.; Wolf, J.; Erbe, A.; Huhn, T.; Groth, U.; Steiner, U. E.; Scheer, E. *Nano Lett.* **2012,** *12,* 3736–3742. doi:10.1021/nl3015523
14. Viljas, J. K.; Cuevas, J. C. *Phys. Rev. B* **2007,** *75,* 075406. doi:10.1103/PhysRevB.75.075406
15. Galperin, M.; Nitzan, A.; Ratner, M. *Phys. Rev. Lett.* **2006,** *96,* 166803. doi:10.1103/PhysRevLett.96.166803
16. Guhr, D. C.; Rettinger, D.; Boneberg, J.; Erbe, A.; Leiderer, P.; Scheer, E. *Phys. Rev. Lett.* **2007,** *99,* 086801. doi:10.1103/PhysRevLett.99.086801
17. Ittah, N.; Noy, G.; Yutsis, I.; Selzer, Y. *Nano Lett.* **2009,** *9,* 1615–1620. doi:10.1021/nl803888q
18. Ittah, N.; Selzer, Y. *Nano Lett.* **2011,** *11,* 529–534. doi:10.1021/nl103398z
19. Huber, R.; Koch, M.; Feldmann, J. *Appl. Phys. Lett.* **1998,** *73,* 2521–2523. doi:10.1063/1.122502
20. Boneberg, J.; Münzer, H.-J.; Tresp, M.; Ochmann, M.; Leiderer, P. *Appl. Phys. A* **1998,** *67,* 381–384. doi:10.1007/s003390050789
21. Obermair, C.; Xie, F.-Q.; Schimmel, T. *Europhys. News* **2010,** *41,* 25–28. doi:10.1051/epn/2010403
22. Xie, F.; Maul, R.; Obermair, C.; Wenzel, W.; Schön, G.; Schimmel, T. *Adv. Mater.* **2010,** *22,* 2033–2036. doi:10.1002/adma.200902953
23. Obermair, C. Ph.D. Thesis, Univeristy of Karlsruhe, Cuvillier Verlag, Göttingen, Germany, 2005.
24. Gründler, P.; Kirbs, A.; Dunsch, L. *ChemPhysChem* **2009,** *10,* 1722–1746. doi:10.1002/cphc.200900254
25. Gründler, P.; Flechsig, G.-U. *Microchim. Acta* **2006,** *154,* 175–189. doi:10.1007/s00604-006-0512-2

License and Terms

Controlled positioning of nanoparticles on a micrometer scale

Fabian Enderle[*], Oliver Dubbers, Alfred Plettl and Paul Ziemann

Abstract

For many applications it is desirable to have nanoparticles positioned on top of a given substrate well separated from each other and arranged in arrays of a certain geometry. For this purpose, a method is introduced combining the bottom-up self-organization of precursor-loaded micelles providing Au nanoparticles (NPs), with top-down electron-beam lithography. As an example, 13 nm Au NPs are arranged in a square array with interparticle distances >1 μm on top of Si substrates. By using these NPs as masks for a subsequent reactive ion etching, the square pattern is transferred into Si as a corresponding array of nanopillars.

Introduction

Nanoparticles (NPs) still play a major role in nanoscience from both an application and a fundamental point of view. Common to both aspects is the interest in possible new properties when reducing the sample size of a material down to the nanoscale. Quite generally, all material properties display in practice such size effects, while not all of them are advantageous for applications. An example for the latter case is provided by magnetic NPs, which for smaller and smaller particle volumes start exhibiting strong directional fluctuations in their magnetization and, thus, render their use for magnetic storage impossible at ambient temperature. On the other hand, this superparamagnetism poses experimental challenges to try and test new materials and alternative arrangements or novel concepts on the

nanoscale to satisfy high-density magnetic data storage [1-4]. In this context, percolating magnetic media may be mentioned or "race track" arrangements, both relying on well-defined and positioned pinning sites for magnetic domain walls [5,6]. In a magnetic thin film, such pinning could be realized by local holes ("antidots") leading immediately to quite a different application of NPs: using them as masks for subsequent etching procedures to transfer the NP pattern into their supporting substrate. In this respect, the notion of a nanoparticle should include as well colloids and micelles since their use for patterning is more widely spread [7-12]. Of course, in addition to their magnetic behavior, NPs offer attractive optical [13,14] or electrical [15,16] properties. In these cases, NPs fabricated

from the complete spectrum of materials, i.e., insulators, semiconductors and metals are required. As a consequence, preparational progress in that field is still of utmost importance [17,18]. Assuming that a fabrication recipe has been developed for NPs of a desired material, there is, however, for many applications still another demanding requirement: positioning the NPs at predesigned locations, either with respect to geometry, such as forming squares or triangles, or, at least, with respect to interparticle distances, or even both. Restricting these distances to the nanoscale as well, some self-organization approaches exist that exploit hierarchical structure formation, allowing at least partial fulfillment of the above requirements [19-22]. For interparticle distances of some tens of nanometers creative ideas have been realized based on even three-dimensional DNA spacers linked to Au NPs [23]. Somewhat more flexible with respect to the type of NPs is their positioning, exploiting wettability contrast of a substrate previously prepared by, e.g., microcontact printing [24,25] or improved direct nanoscale embossing [26]. Though, in this case, the interparticle distances can be largely enhanced, the difficulty here is to avoid obtaining more than one particle at a given location. For interparticle distances of some hundred nanometers colloidal approaches have been successfully demonstrated. Though related to two-dimensional non-close-packed colloidal crystals [11] and, thus, primarily leading to the formation of hexagonal arrays of NPs, the method is novel in that it applies colloids carrying metal precursors. Once the colloidal carriers form a self-assembled ordered array, plasma processes are exploited to remove the organic matrix and to reduce the precursors into metallic NPs [10,12]. Though this technique appears quite versatile with respect to the type of NPs, it still has restrictions related to geometries other than hexagonal symmetry and distances well above 1 μm. It is exactly this problem of combining the nano- with the micro-scale that is the focus of the present contribution. In the following approach, NPs prepared by exploiting the self-organization of precursor loaded micelles formed from diblock-copolymers play a major role as a starting point. Thus, the genuine symmetry of their original arrangement again will be hexagonal. However, as will be demonstrated below, combining the micellar method with conventional electron-beam lithography not only extends interparticle distances from typically 100 nm into the micrometer range, but additionally allows a broad variation of geometries for the finally arranged NPs.

Results and Discussion
Preparation of Au nanoparticles (NPs)

The starting point of the present approach is the fabrication of hexagonally arranged Au NPs applying a previously reported recipe based on the self-organization of precursor-loaded micelles [7,8,21]. In short, commercially available *diblock*-copolymers [polystyrene-block-poly-2-vinylpyridine (PS-b-

P2VP) from Polymer Source Inc, Canada] forming spherical reverse micelles in an apolar solvent, such as toluene, are loaded with $HAuCl_4$ salt as precursor. After optimized dip coating of the substrate (presently n-doped (001)-oriented Si wafers; in general, however, any reasonably flat substrate material is suitable), one single layer of hexagonally ordered micelles is obtained. By exposing such micellar layers to a hydrogen plasma the organic species can be completely removed and the precursor can be reduced to metallic Au NPs. The most attractive features of this approach are the control over the size of the NPs (determined by the amount of added precursor) as well as over the interparticle distance (determined by the total length of the *diblock*-copolymer and the substrate velocity during dip coating [8]). Furthermore, and most important for the present work, the final position of the Au NPs mirrors the self-assembled hexagonal array of the micellar carriers. This is demonstrated by the SEM image given in Figure 1 showing a typical array of Au NPs on top of a Si substrate.
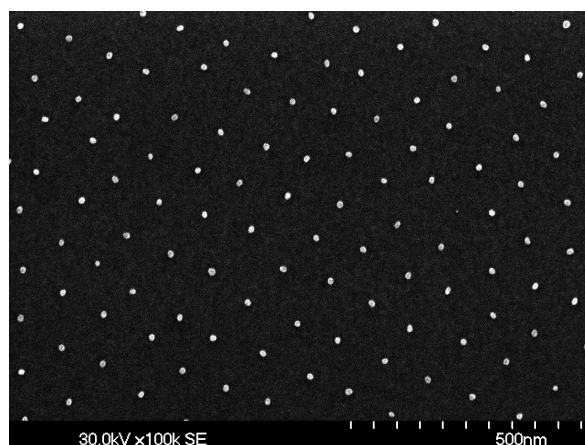
Figure 1: SEM image of Au nanoparticles (average diameter 13 nm, interparticle distance 102 nm) deposited on top of a Si substrate by applying an approach based on self-organization of precursor-loaded reverse micelles.

The high degree of hexagonal order is clearly visible, although deviations from perfect order are obvious as well. In the present work, exclusively Au NPs with average diameters of 13 ± 1.6 nm were used. Smaller Au NPs, however, with diameters down to 2 nm would be easily available. Also, the interparticle distance was fixed at an average value of 102 ± 3 nm, for reasons to be discussed further below.

Selecting Au nanoparticles on the micrometer scale

The basic idea behind selecting individual Au NPs on the micrometer scale is outlined by the schematics presented in Figure 2.
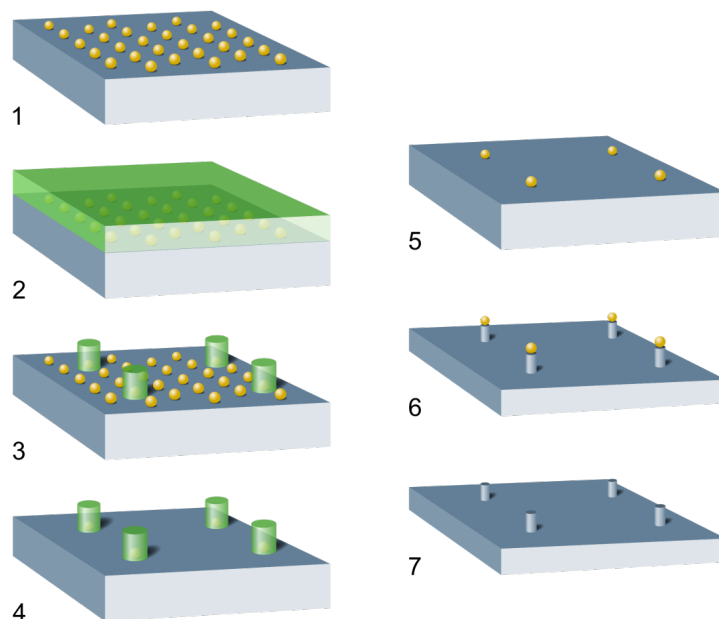
Figure 2: Schematics of the process leading to positioning nanoparticles on the micrometer scale: (1) Start; nanoparticles (NP) prepared by applying a method based on the self-organization of precursor loaded micelles on top of a flat substrate; here Au NP on Si; (2) Spin-coated negative resist for electron-beam lithography (EBL); (3) Resist disks arranged in a square lattice as obtained after EBL; (4) Removal of the residual Au NP between the disks by I/KI solution; (5) Stripping of the resist delivers the final NP arrangement; (6) Optional; using the NP as masks for a subsequent RIE etching step resulting in correspondingly arranged nanopillars; (7) Optional; removing the residual NP masks.

A negative resist (AR-N7500-18, Allresist, 6000 rpm, thickness approximately 300 nm) is spin coated above the primarily deposited Au NPs. Prior to this step, it is important to give the Si substrate with the NPs a short HF dip (2% HF, 10 s), which significantly enhances the adhesion of the resist. After a standard prebake of the resist (60 s at 85 °C on a hot plate), a square arrangement of circles is written into the resist by an electron beam (20 kV, 15 pA). The diameter of these circles has to be adjusted with respect to the interparticle distance of the Au NPs since each written resist disk should cover just one single NP. For the presently used mutual particle distance of 100 nm, a diameter of the resist disks of also 100 nm was chosen. This choice is the appropriate compromise to avoid having either no Au NPs covered by the circular resist island or more than one. By writing various square arrays of disks the optimum electron dose is determined, and the resist is thus developed (developer: 140–160 s, AR300-47 with water as stopper) followed by a postbake (80 s at 120 °C on a hot plate) of the exposed disks. The situation after this resist-removal step is illustrated by the SEM image shown in Figure 3. The four resist disks arranged in a square are clearly visible by their darker contrast while the bright dots image the residual Au NPs. Obviously, due to the development process the original hexagonal order of the NPs (Figure 1) is almost completely destroyed and some of the original Au NPs are even removed together with the unexposed resist.
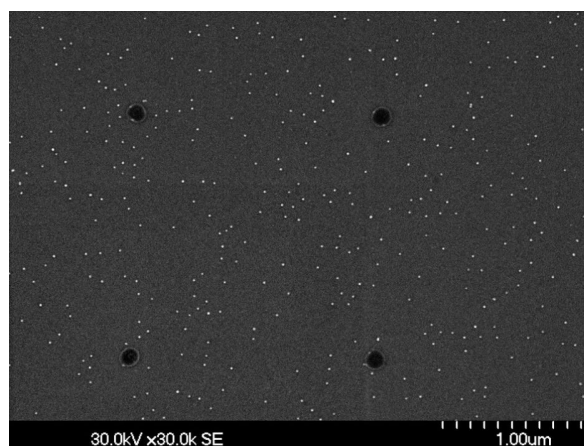
Figure 3: SEM image of resist disks arranged in a square (dark contrasts) as obtained after development (step 3 in Figure 2). The bright dots image the still present residual Au NPs, which have completely lost their hexagonal order during removal of the unexposed resist.

Next, the residual uncovered Au NPs are removed by dipping the substrate into an I/KI solution for 30 s followed by the final stripping of the resist (1–2 min acetone, 20 s IPA). In principle, this last step finalizes the process delivering 13 nm Au NPs arranged in a square lattice with mutual distances in the micrometer range. However, to enhance visibility of these NPs in an

overview SEM image, the particles are used as a mask during a subsequent reactive ion etching (RIE) of the Si substrate transforming the NPs into nanopillars. The result is demonstrated in Figure 4.
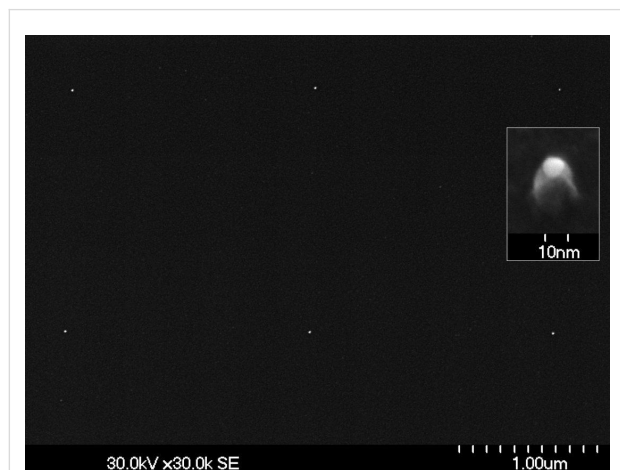
Figure 4: SEM image of two squares of nanopillars as obtained after RIE with single Au NPs, arranged in a square, as etching masks (step 5 in Figure 2). Distance between pillars: 1.8 μm. Inset: magnified SEM image (tilted by 30°) of one nanopillar with residual Au mask as cap.

Further squares of correspondingly prepared nanopillars can be visualized by reducing the interparticle distance from 1.7 μm in Figure 4 to 1.3 μm in Figure 5.
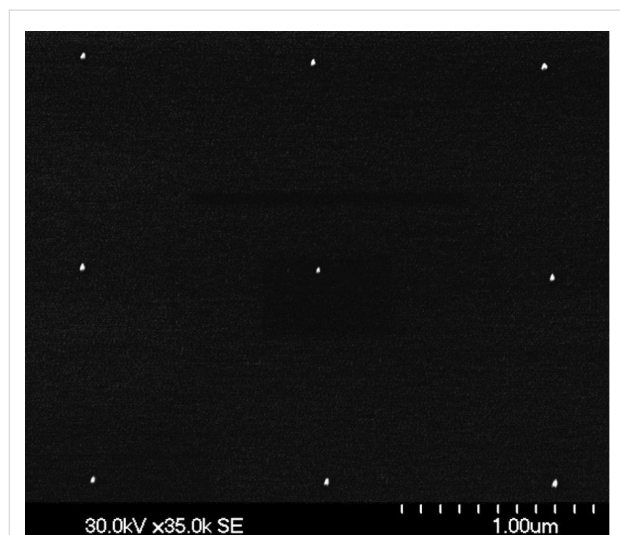
Figure 5: SEM image of four squares of nanopillars as obtained after RIE with single Au NPs, arranged in a square, as etching masks (step 5 in Figure 2). Distance between pillars: 1.2 μm.

Problems and compromises

Though the SEM images presented in Figure 4 and Figure 5 successfully deliver a proof of principle for the presently suggested positioning procedure, some problems should be addressed as well. The first point is related to the absolute precision of positioning the Au NPs. Writing any pattern such as the square array of disks by the electron beam is performed relative to a predetermined rectangular coordinate system fixed within the sample surface. When restricting the patterning to a 100 μm × 100 μm area, no mechanical movement of the sample holder is necessary, rather all programmed positions are approached by steering the electron beam. During the writing process, however, one observes a time-dependent drift, which in the present case of 100 nm disks arranged in squares added up to approximately 50 nm. Added to this error is the uncertainty of the exact position of the Au NP within any disk. Due to the finite hexagonal order, over larger areas this position can be assumed as random within the disk area. Thus, a very conservative estimate of the deviation of the NP location from an ideal square position is <150 nm, i.e., on the order of 10% in the present examples.

For many applications, however, positional precision of the NPs is not the primary goal. Rather, the NPs should be well separated from each other and individually identifiable against the background. Two classes of applications may illustrate these requirements. The first example is spectroscopy applied either directly to nanoparticles or, indirectly, on, e.g., molecules specifically ligated to the NPs, such as bonding to Au NPs through a thiol-group. To suppress interactions between nanoparticles or the molecules bound to them, usually interparticle distances of 50 nm are sufficient (for a recent study on near-field effects around a single dot see [27]). To guarantee single particle/molecule spectroscopy significantly larger distances are necessary as provided by the present method, depending in detail on the wavelength of the exciting radiation or the achievable focus size. In a second class of experiments, metallic NPs may be used as electrical contacts connected to the backside of the substrate by vias (vertical interconnect access), which, in turn, are further connected to pads on the micrometer scale. An example would be contacting a biological cell with typical lateral extensions of more than 10 μm at well-defined positions, e.g., 1 μm apart.

Though the presently obtained lateral precision of the particle positioning is sufficient for the just mentioned applications, further improvements appear possible. A necessary prerequisite for this would be a better long-range order of the starting NPs. For this, changing to self-assembled precursor-loaded colloids rather than micelles is promising [10-12]. In the ideal case, positioning of the resist disks would no longer be purely statistical but instead conform to multiples of the lattice parameter of the underlying hexagonal colloid lattice. To exploit the high long-range colloidal order, however, a sample holder with laser-

interference-controlled translations becomes a must. In this way, positioning with a precision of better than 50 nm appears possible.

Conclusion

A general procedure is introduced to position nanoparticles on the micrometer scale on top of a given substrate. The method is demonstrated for Au NPs (diameters 13 nm) on Si wafers in a square lattice with interparticle distances above 1 µm. The underlying idea is to combine the self-organization of precursor loaded micelles formed from *diblock*-copolymers in toluene, which is a bottom-up process providing nanoparticles, with top-down electron-beam lithography. As a first simple application, the resulting array of Au NPs is used as a mask for a subsequent reactive-etching process delivering correspondingly arranged Si nanopillars.

Acknowledgement

References

1. Wiedwald, U.; Ziemann, P. *Beilstein J. Nanotechnol.* **2010,** *1,* 21–23. doi:10.3762/bjnano.1.4
2. Eisenmenger, J.; Schuller, I. K. *Nat. Mater.* **2003,** *2,* 437–438. doi:10.1038/nmat934
3. Wiedwald, U.; Han, L.; Biskupek, J.; Kaiser, U.; Ziemann, P. *Beilstein J. Nanotechnol.* **2010,** *1,* 24–47. doi:10.3762/bjnano.1.5
4. Weller, D.; Moser, A.; Folks, L.; Best, M. E.; Wen, L.; Toney, M. F.; Schwickert, M.; Thiele, J.-U.; Doerner, M. F. *IEEE Trans. Magn.* **2000,** *36,* 10–15. doi:10.1109/20.824418
5. Brombacher, C.; Saitner, M.; Pfahler, C.; Plettl, A.; Ziemann, P.; Makarov, D.; Assmann, D.; Siekman, M. H.; Abelmann, L.; Albrecht, M. *Nanotechnology* **2009,** *20,* 105304. doi:10.1088/0957-4484/20/10/105304
6. Parkin, S. S. P.; Hayashi, M.; Thomas, L. *Science* **2008,** *320,* 190–194. doi:10.1126/science.1145799
7. Spatz, J. P.; Mössmer, S.; Hartmann, C.; Möller, M.; Herzog, T.; Krieger, M.; Boyen, H.-G.; Ziemann, P.; Kabius, B. *Langmuir* **2000,** *16,* 407–415. doi:10.1021/la990070n
8. Bansmann, J.; Kielbassa, S.; Hoster, H.; Weigl, F.; Boyen, H. G.; Wiedwald, U.; Ziemann, P.; Behm, R. J. *Langmuir* **2007,** *23,* 10150–10155. doi:10.1021/la7012304
9. Bita, I.; Yang, J. K. W.; Jung, Y. S.; Ross, C. A.; Thomas, E. L.; Berggren, K. K. *Science* **2008,** *321,* 939–943. doi:10.1126/science.1159352
10. Manzke, A.; Pfahler, C.; Dubbers, O.; Plettl, A.; Ziemann, P.; Crespy, D.; Schreiber, E.; Ziener, U.; Landfester, K. *Adv. Mater.* **2007,** *19,* 1337–1341. doi:10.1002/adma.200601945
11. Zhang, J.; Li, Y.; Zhang, X.; Yang, B. *Adv. Mater.* **2010,** *22,* 4249–4269. doi:10.1002/adma.201000755
12. Vogel, N.; Ziener, U.; Manzke, A.; Plettl, A.; Ziemann, P.; Biskupek, J.; Weiss, C. K.; Landfester, K. *Beilstein J. Nanotechnol.* **2011,** *2,* 459–472. doi:10.3762/bjnano.2.50
13. Meixner, A. J. *Beilstein J. Nanotechnol.* **2011,** *2,* 499–500. doi:10.3762/bjnano.2.53
14. Gonçalves, M. R.; Makaryan, T.; Enderle, F.; Wiedemann, S.; Plettl, A.; Marti, O.; Ziemann, P. *Beilstein J. Nanotechnol.* **2011,** *2,* 448–458. doi:10.3762/bjnano.2.49
15. Waser, R., Ed. *Nanoelectronics and Information Technology;* Wiley-VCH : Weinheim, Germany, 2003.
16. Boyen, H.-G.; Kästle, G.; Weigl, F.; Koslowski, B.; Dietrich, C.; Ziemann, P.; Spatz, J. P.; Riethmüller, S.; Hartmann, C.; Möller, M.; Schmid, G.; Garnier, M. G.; Oelhafen, P. *Science* **2002,** *297,* 1533–1536. doi:10.1126/science.1076248
17. Kinge, S.; Crego-Calama, M.; Reinhoudt, D. N. *ChemPhysChem* **2008,** *9,* 20–42. doi:10.1002/cphc.200700475
18. Goesmann, H.; Feldmann, C. *Angew. Chem., Int. Ed.* **2010,** *49,* 1362–1395. doi:10.1002/anie.200903053
19. Ziemann, P. *Beilstein J. Nanotechnol.* **2011,** *2,* 363–364. doi:10.3762/bjnano.2.41
20. Popov, K. I.; Palyulin, V. V.; Möller, M.; Khokhlov, A. R.; Potemkin, I. I. *Beilstein J. Nanotechnol.* **2011,** *2,* 569–584. doi:10.3762/bjnano.2.61
21. Kästle, G.; Boyen, H.-G.; Weigl, F.; Lengl, G.; Herzog, T.; Ziemann, P.; Riethmüller, S.; Mayer, O.; Hartmann, C.; Spatz, J. P.; Möller, M.; Ozawa, M.; Banhart, F.; Garnier, M. G.; Oelhafen, P. *Adv. Funct. Mater.* **2003,** *13,* 853–861. doi:10.1002/adfm.200304332
22. Mena-Osteritz, E.; Urdanpilleta, M.; El-Hosseiny, E.; Koslowski, B.; Ziemann, P.; Bäuerle, P. *Beilstein J. Nanotechnol.* **2011,** *2,* 802–808. doi:10.3762/bjnano.2.88
23. Auyeung, E.; Cutler, J. I.; Macfarlane, R. J.; Jones, M. R.; Wu, J.; Liu, G.; Zhang, K.; Osberg, K. D.; Mirkin, C. A. *Nat. Nanotechnol.* **2012,** *7,* 24–28. doi:10.1038/nnano.2011.222
24. Yao, X.; Song, Y.; Jiang, L. *Adv. Mater.* **2011,** *23,* 719–734. doi:10.1002/adma.201002689
25. Aizenberg, J.; Black, A. J.; Whitesides, G. M. *Nature* **1999,** *398,* 495–498. doi:10.1038/19047
26. Lee, M. H.; Huntington, M. D.; Zhou, W.; Yang, J.-C.; Odom, T. W. *Nano Lett.* **2011,** *11,* 311–315. doi:10.1021/nl102206x
27. Walhorn, V.; Paskarbeit, J.; Frey, H. G.; Harder, A.; Anselmetti, D. *Beilstein J. Nanotechnol.* **2011,** *2,* 645–652. doi:10.3762/bjnano.2.68

Towards atomic resolution in sodium titanate nanotubes using near-edge X-ray-absorption fine-structure spectromicroscopy combined with multichannel multiple-scattering calculations

Carla Bittencourt[*1], Peter Krüger[2], Maureen J. Lagos[3], Xiaoxing Ke[3], Gustaaf Van Tendeloo[3], Chris Ewels[4], Polona Umek[5,6] and Peter Guttmann[7]

Address:
[1]ChIPS, University of Mons, B-7000, Mons, Belgium, [2]ICB, UMR 6303 CNRS-Université de Bourgogne, F-21078 Dijon, France, [3]EMAT, University of Antwerp, B-2020, Antwerp, Belgium, [4]Institut des Matériaux de Nantes (IMN), Université de Nantes, CNRS, Nantes, France, [5]Jožef Stefan Institute, Jamova cesta 39, 1000 Ljubljana, Slovenia, [6]Center of Excellence NAMASTE, Jamova cesta 39, 10000 Ljubljana, Slovenia and [7]Helmholtz-Zentrum Berlin für Materialien und Energie GmbH, Institute for Soft Matter and Functional Materials, Albert-Einstein-Str. 15, 12489 Berlin, Germany

Email:
Carla Bittencourt[*] - carla.bittencourt@umons.ac.be

* Corresponding author

Keywords:
multichannel multiple scattering; nanotubes; NEXAFS; sodium titanates

Abstract

Recent advances in near-edge X-ray-absorption fine-structure spectroscopy coupled with transmission X-ray microscopy (NEXAFS–TXM) allow large-area mapping investigations of individual nano-objects with spectral resolution up to $E/\Delta E = 10^4$ and spatial resolution approaching 10 nm. While the state-of-the-art spatial resolution of X-ray microscopy is limited by nanostructuring process constrains of the objective zone plate, we show here that it is possible to overcome this through close coupling with high-level theoretical modelling. Taking the example of isolated bundles of hydrothermally prepared sodium titanate nanotubes ((Na,H)TiNTs) we are able to unravel the complex nanoscale structure from the NEXAFS–TXM data using multichannel multiple-scattering calculations, to the extent of being able to associate specific spectral features in the O K-edge and Ti L-edge with oxygen atoms in distinct sites within the lattice. These can even be distinguished from the contribution of different hydroxyl groups to the electronic structure of the (Na,H)TiNTs.

Introduction

Transmission X-ray microscopy (TXM) is a popular microscopy technique used in biology [1-3]. Recently, we have extended the range of its applications to the spectroscopic characterization of nanoscale materials by combining it with near-edge X-ray-absorption fine-structure spectroscopy (NEXAFS–TXM) [4]. The nanoscale spatial resolution of the NEXAFS–TXM allows the exclusion of impurity regions and thus the presence of signals related to impurities in the absorption spectrum of the nanostructures. State of the art TXMs allow a spatial resolution of 11 nm [5-7]. However, we show in the current study that the combination of NEXAFS–TXM with high-level theoretical modelling allows us to move beyond this spatial-resolution limit and extract more spatially refined information [8]. Indeed this combination of theory and spectroscopy paves the way towards atomic-scale resolution in similar techniques with lower spectral resolution [9,10].

We investigate here the electronic structure of sodium titanate nanotubes ((Na,H)TiNTs) by means of near-edge X-ray-absorption fine-structure spectroscopy (NEXAFS) coupled with first-principles NEXAFS calculations (density functional for the O K-edge and multichannel multiple scattering (MCMS) method for the Ti $L_{2,3}$-edge spectra) [8,11,12]. The susceptibility of both O K-edge and Ti L-edge features to the local bonding environment in TiO_2-based materials makes NEXAFS ideal for providing diagnostic information about the crystal structures and oxidation states. Here, the electronic structure of the nanotubes is discussed in terms of the ligand field splitting of the Ti ions and the connectivity of the TiO_6 octahedral

network. Among the different structures proposed for these nanotubes [13-17], it is currently accepted that the structure of the layered titanate $H_2Ti_nO_{2n+1}$ better describes the (Na,H)TiNTs [17,18].

Potential applications in lithium-ion batteries, catalyst supports, photocatalysts, and dye-synthesized solar cells have effectively resulted in an increasing interest in titanate nanostuctures [19-29]. All these applications require a deep understanding of the electronic structure of the material. In addition to spatial resolution, the NEXAFS–TXM offers higher-energy resolution and lower-damage yield when compared to other advanced spectromicroscopy techniques, such as electron energy loss spectroscopy (EELS) performed in aberration-corrected transmission electron microscopes operated at low electron acceleration voltages [30]. Alkali titanate nanostructures are very sensitive to electron-beam irradiation, which has prevented detailed studies at high energetic resolution by electron spectroscopy. Using NEXAFS–TXM has allowed us to probe our samples at 0.1 eV energy resolution while in recent reports [18,31] based on EELS the energy resolution for analysing similar samples was limited to 0.5 eV.

Results and Discussion

Figure 1a shows a typical TEM image of the sodium titanate nanostructures. Figure 1b shows a high-resolution TEM image of several long structures, showing parallel dark contrast, typical for tubular morphology (see Supporting Information File 1). The nanotube edges consist of several layers spaced by
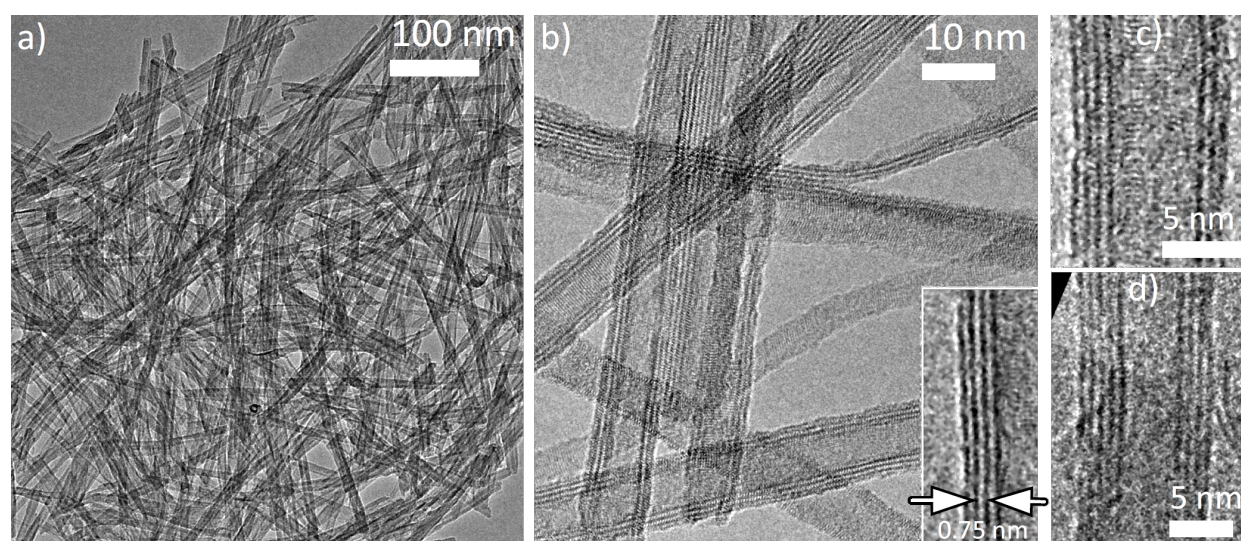
Figure 1: TEM image of sodium titanate nanotubes (a) typical region used to record the NEXAFS–TXM data. (b) HRTEM image revealing the hollow core of these nanostructures (inset shows the interlayer spacing). (c–d) HRTEM images showing typical image contrast pattern associated with the scroll-like morphology. Note the number of layers in opposing tube walls is different in each case.

0.75 nm (see Figure 1 insert). Typical high-resolution TEM images (Figure 1c and Figure 1d) show that the tubes have a different number of layers in each edge (for instance Figure 1c has four layers on the left, three on the right), suggesting that these are very likely hollow nanoscrolls, consistent with previous observations [11,32]. Characteristic nanoscrolls have walls consisting of 2–6 layers, the outer diameters of the synthesized nanotubes are between 8 and 12 nm, while the inner diameters are found in the range between 4 and 7 nm. They display high aspect ratio with lengths of a few hundred nanometers.

The NEXAFS spectra were recorded in the transmission mode with a zone plate objective with an outermost zone width of 40 nm. This allows the study of selected areas of the samples and reduces the uncertainties due to the presence of impurities.

Figure 2 shows a few X-ray images of the image stack used to record the NEXAFS spectra. For absorption spectroscopy it is necessary to measure two spectra: one spectrum $I(E)$ of transmission through the specimen and another of the incident flux $I_0(E)$. The spectrum is obtained as an optical density $OD(E) = -\log [I(E)/I_0(E)]$ [33]. A region containing a bundle with a few (Na,H)TiNTs was used to record the $I(E)$ spectrum, and the $I_0(E)$ was recorded in a bare region of the sample support close to the sample region (Figure 2). During the measurements the system was kept in focus, and the alignment of the images was performed by using a cross-correlation method from the IMOD tomography package [34].

The titanium L-edge NEXAFS spectrum of the (Na,H)TiNTs shares common general features with the spectra recorded on anatase and $SrTiO_3$ (Figure 3): they are composed of distin-
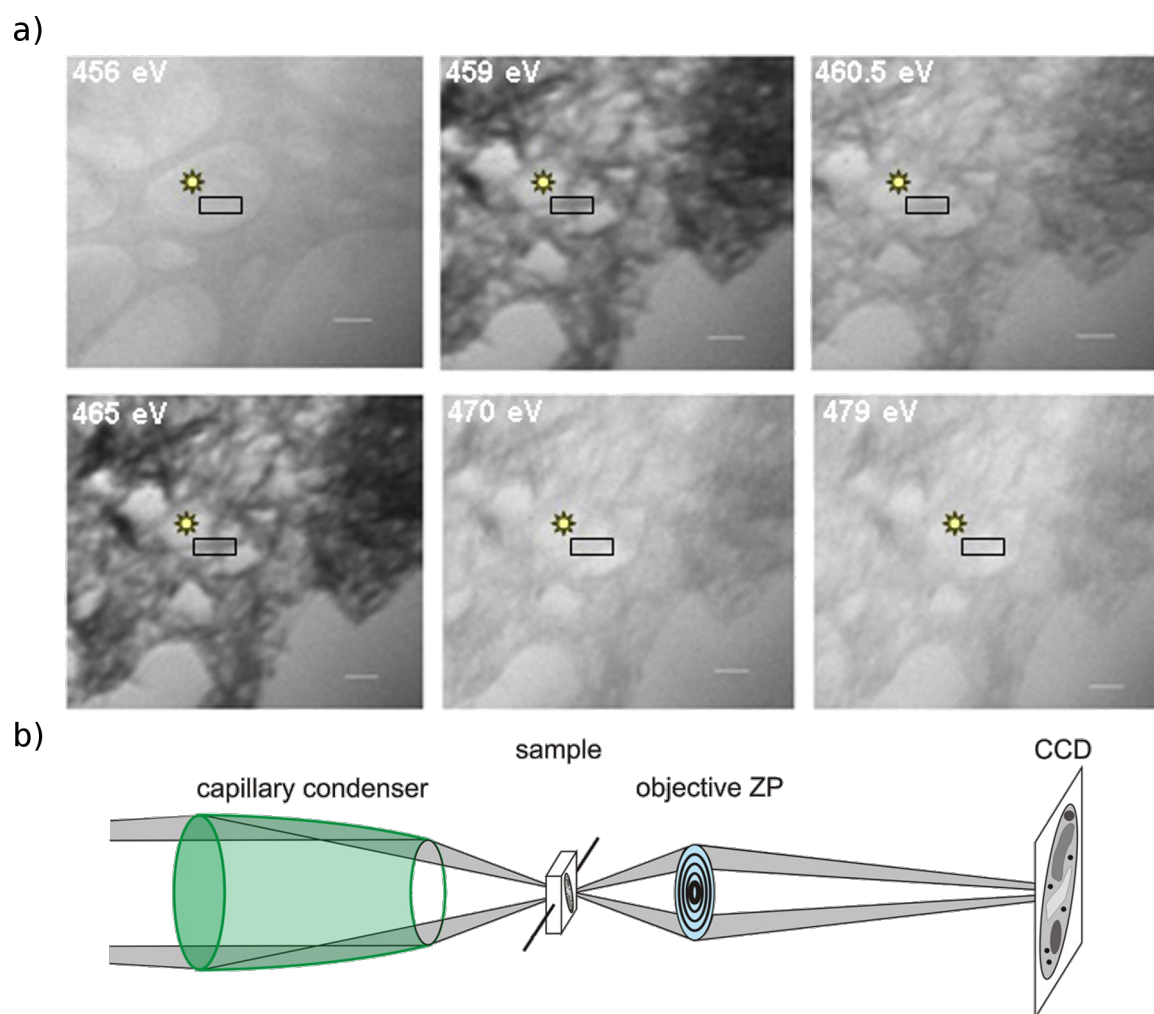
Figure 2: (a) X-ray images at different photon energies *E* from an image stack recorded on the (Na,H)TiNTs at the U41 beamline by using the TXM. The NEXAFS–TXM (Ti L-edge (see Figure 3a) and O K-edge (see Figure 5)) spectra were recorded in the area delimited by the rectangle. The spot indicates the point at which the I_0 was recorded. (b) Setup of the NEXAFS–TXM measurements.
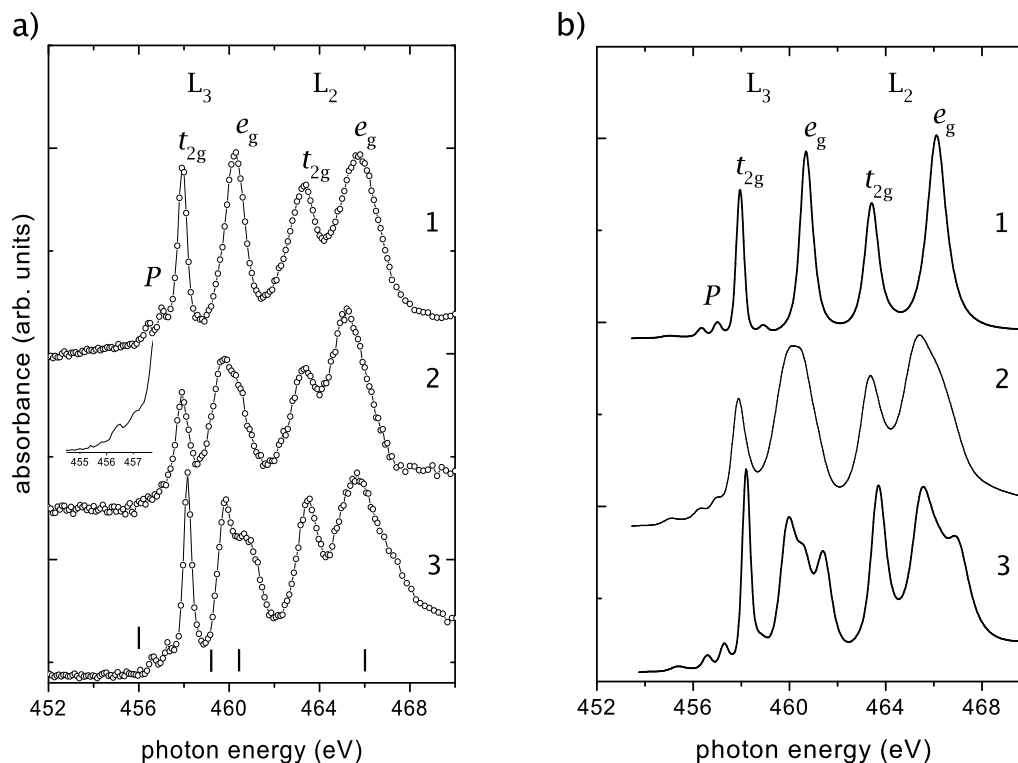
Figure 3: NEXAFS spectra at the Ti L-edge recorded on (1) $SrTiO_3$, (2) (Na,H)TiNTs and (3) anatase. The vertical lines indicate the photon energy of the first four X-ray images in Figure 2. The inset shows the pre-edge structures in the nanotube spectrum. (b) Ti L-edge spectra of (1) $SrTiO_3$, (2) (Na,H)TiNTs and (3) anatase calculated with the MCMS method.

guishable peaks in the range between 455 and 470 eV corresponding to excitations of the Ti 2p states into the empty Ti 3d states [35]. Due to the hydrothermal process used to synthesize the tubes, the binding energy of Ti 2p photoemission lines are shifted slightly to lower binding energy, showing that the local environment around the Ti ions in the (Na,H)TiNTs is different from that in the anatase-type TiO_2 (see also Supporting Information File 1, Figure S1). The absence of extra peaks or broadening of the Ti 2p photoemission lines suggest that the chemical environment of the Ti ions does not change during the hydrothermal treatment of TiO_2.

The Ti L-edge shows two groups of peaks arising from the spin-orbit splitting of the Ti 2p core level into $2p_{1/2}$ (L_2-edge) and $2p_{3/2}$ levels (L_3-edge), corresponding to Ti(IV) in a tetragonal structure [36]. These levels are then further split by the strong ligand field arising from the surrounding oxygen atoms. For TiO_6 octahedra, even if distorted, the cubic component dominates the ligand field [37]. The cubic field splits the Ti 3d band into two sublevels with t_{2g} and e_g symmetry [38]. In the following we shall label the Ti 3d states with these approximate characters for simplicity, even when the exact point symmetry of the Ti site is much lower than O_h, and so the degeneracy within the t_{2g} and e_g groups is lifted, as in the case

of the nanotubes. The sharp L_3–t_{2g} feature reflects the weak interaction between the O 2p orbitals forming directional "π-type" bonds and the t_{2g} orbitals (d_{xy}, d_{xz} and d_{yz}) pointing between the oxygen neighbors. Conversely, the O 2p orbitals form strong directional bonds with the e_g orbitals ($d_{x^2-y^2}$ and d_{z^2}) that point directly towards the oxygen ligands and, therefore, the line-shape of the e_g band is highly sensitive to the local symmetry around the metal cations [39]. In Figure 3a, the structure of the L_3–e_g transition seems to be characteristic of a tetragonal system [36,40,41]. At energies below the L_3-edge, the low-intensity peaks observed in all samples were reported to arise from the spin-forbidden $p_{3/2} \rightarrow d_{3/2}$ transition [38] and are related to particle–hole Coulomb coupling [8].

The most prominent difference between the spectra of the studied oxides is the value of the energy splitting of the fine structure in the L_3–e_g band. From Figure 3a, we can see that this value is 0, 0.44 and 0.82 eV, respectively, for $SrTiO_3$, (Na,H)TiNTs and anatase. Krüger showed that the L_3–e_g peak splitting in TiO_2 is a band-structure effect, which mainly reflects the connectivity of the TiO_6 octahedra rather than local distortions of the individual octahedra [8]. In the $SrTiO_3$ structure all octahedra are connected by their corners such that the

oxygen atoms have coordination 2. In anatase the oxygen atoms have coordination 3 and connect one corner- and two edge-sharing octahedra. Considering the value of the energy split of the L_3–e_g band evaluated from the NEXAFS spectra, half way between $SrTiO_3$ and anatase, we can postulate a structure having oxygen atoms with an average coordination number of 2.5 for our scrolls. The generally accepted model for the structure of the (Na,H)TiNTs can be described as weakly bent sheets made of two layers of Ti–O_6 octahedra, not stacked in perfect registry [17]. In this model, the different O sites have one to four O–Ti bonds with bond lengths ranging between 1.7 and 2.4 Å. The average coordination of the O sites is 2.57, in good agreement with our value. The unit cell has a Ti_6O_{14} basis with three nonequivalent Ti sites (see Figure 4).

In order to move beyond the resolution limits imposed by the experiment, we next perform a series of MCMS calculations [8] using the structural model "H(1,3)" for $H_2Ti_3O_7$ given in [17]. The finite-cluster multiple-scattering calculations were done for a disk of 148 atoms in a single titanate sheet. The atomic data (phase shifts and radial matrix elements) were calculated from self-consistent potentials of bulk TiO_2 anatase [8]. We also tested potentials of bulk $SrTiO_3$ and obtained only negligible differences in spectral line shape. The calculated Ti $L_{2,3}$ spectra of the (Na,H)TiNTs is shown in Figure 3b along with those of

anatase and $SrTiO_3$. The latter were, for direct comparison, recalculated here by using the same cluster size (~150 atoms) and the same atomic potentials as the (Na,H)TiNTs. All calculated spectra were rigidly shifted by −14.5 eV to match the experimental energy scale, other computational details are the same as in [8].

The agreement between experimental and calculated spectra in Figure 3 is remarkable. All major differences between the (Na,H)TiNTs spectra and the reference spectra are well reproduced in the calculation. In the (Na,H)TiNTs, the L_3–t_{2g} lines and L_2–t_{2g} lines are broader and considerably less intense than those in the bulk phases. For both L_3 and L_2, the t_{2g}–e_g splitting is reduced, especially as compared to $SrTiO_3$. The weak pre-edge peaks are much more broadened than in $SrTiO_3$ and TiO_2. As for the L_3–e_g peak, the calculation gives a more rounded shape than the data, but the characteristic width (or splitting) of the peak lies between $SrTiO_3$ and anatase in excellent agreement with experiment.

Further information on the electronic state can be obtained by the analysis of the O K-edge. Figure 5 shows the O K-edge NEXAFS spectra of (Na,H)TiNTs and TiO_2 anatase, the latter compares well with the literature [38,42]. The peaks A and B just above threshold correspond to Ti-3d–O-2p antibonding

Figure 4: (a) Calculated NEXAFS spectra. Ti atoms at different sites of the (Na,H)TiNTs structure (Figure 4b). (b) Ball-and-stick model of one Ti_3O_7 sheet of the generally accepted structure of (Na,H)TiNTs [16]. Ti atoms in blue with labels 1–3 for the three nonequivalent sites, and O atoms in red. Three unit cells are shown in side view (along −b).

Figure 5: Comparison of NEXAFS spectra calculated by using density functional theory (red) and O K-edge spectra recorded on anatase and (Na,H)TiNTs (black).

states. They are mainly of Ti-3d character and split into t_{2g} (A) and e_g (B) by the octahedral ligand field. The higher energy peaks (C, D and E) are due to more delocalized states that have been attributed to the hybridization of O p with Ti sp. In the (Na,H)TiNT spectrum, peaks A and B have nearly the same energy positions as in anatase, reflecting the octahedral coordination of Ti sites in both structures. The only obvious difference is that the peaks A, B are somewhat broader in the (Na,H)TiNTs. Much more pronounced changes are observed for higher energy peaks. In the (Na,H)TiNT spectrum peak C is strongly suppressed and D is shifted to lower energy such that these two peaks have merged into a single asymmetric peak. Peak E is slightly weaker than in anatase. Since the peaks C–E correspond to hybridization of O p with delocalized states, they are sensitive to the structural changes around the O sites, rather than around the Ti sites, as in the case of peaks A and B. The pronounced difference between the (Na,H)TiTNs and anatase observed in this spectral region thus indicates a very different connectivity of the TiO_6 octahedra. However, the resolution limits of the NEXAFS–TXM approach do not allow further discrimination with the spectra based on local structure, and for this we now turn to the simulations.

In Figure 5 the O K-edge spectra are compared with density functional calculations performed in the local density approximation with the Vienna ab initio package [43,44]. As for the Ti L_{23}-edge, the structural model "H(1,3)" for H_2TiO_3 of [23] is used for the (Na,H)TiNTs. As the core hole was found to have a negligible effect on the O K-edge NEXAFS spectra of TiO_2, the absorption spectra can be modeled by using the O p projected ground-state density of states (DOS) [42]. The DOS was broadened with a Lorentzian of energy-dependent width, to account for finite core hole lifetime and photoelectron mean free path (see the Supporting Information File 1 for details).

The calculated spectra agree very well with the experimental data. In anatase, all peaks A–E are reproduced both in position and relative intensity. Importantly, all differences observed in the (Na,H)TiNT spectrum are also reproduced in the calculation.

While all oxygen atoms are structurally equivalent in TiO_2 anatase, there are seven different oxygen sites in the $H_2Ti_3O_7$ structure and the measured O K-edge spectrum is an average over these seven sites. The individual spectra (Figure 6) are strongly different from each other, reflecting the different local environment of the O sites. All spectra except O5 and O7 show essentially the four main peaks A–D of anatase, albeit with extra fine structure in A and B, shifting of C and D, and considerable intensity variations. The spectra of the hydroxyl atoms O5 and O7 have a distinctly different shape where peaks A, B are strongly decreased and the dip between B and C is gone. This shows that the O K-edge spectra are highly sensitive to the number of H and Ti bonds, and thereby to the connectivity of the octahedra. In particular, for the non-hydroxyl O atoms, the A/B intensity ratio is found to be simply correlated with the O–Ti coordination: A > B for the 2-fold sites O4, O6; A ≈ B for the 3-fold site O8; and A < B for the 4-fold sites O9, O10. Thus, the A/B intensity ratio at the O K-edge XAS provides a direct local measure of the connectivity of the octahedra. This finding can be understood as follows: The O–Ti coordination of a given O atom equals its number of O-p–Ti-d sigma bonds. These bonds involve the Ti–e_g orbitals and, thus, correspond to peak B of the O K-edge spectrum. Therefore, the B-peak intensity increases (i.e., the A/B intensity ratio decreases) with increasing O–Ti coordination number, as seen in Figure 6.

Finally, the experimental observation that the (Na,H)TiNTs spectrum appears broader than that of anatase is easily understood as an averaging effect over several oxygen sites with markedly different bonding properties. Remaining small differences between the theoretical and experimental (Na,H)TiNT O K-edge spectrum may be attributed to the fact that the $H_2Ti_3O_7$ model cannot fully account for the three-dimensional
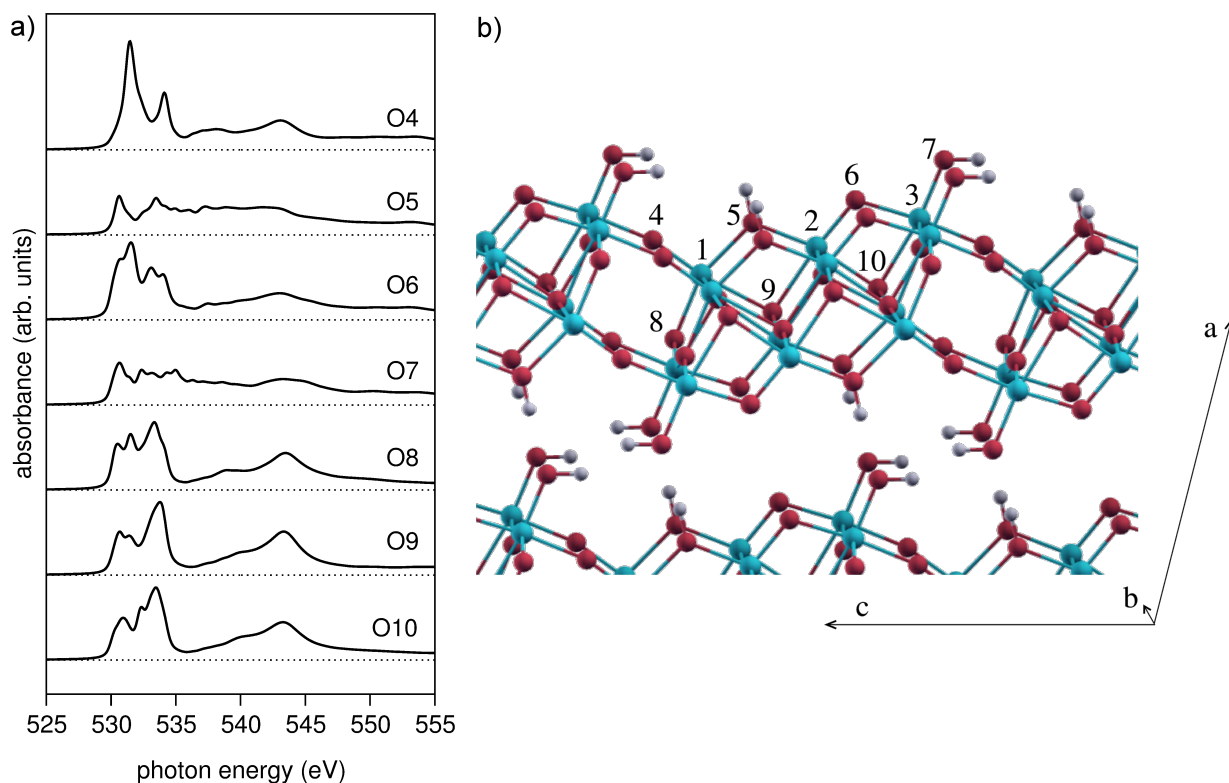
Figure 6: (a) Contribution to the O K-edge spectrum of oxygen atoms at different sites of the (Na,H)TiNTs structure (Figure 6b). (b) Ball-and-stick model of $H_2Ti_3O_7$ [17], the generally accepted structure of (Na,H)TiNTs. Oxygen atoms in red with labels 4–10 for the seven nonequivalent sites, Ti atoms in blue are labeled 1–3 for the three Ti nonequivalent sites. Hydrogen atoms are in grey.

structure of the nanoscrolls. In the latter, the titanate sheets are bent and the stacking may slightly differ from the $H_2Ti_3O_7$ crystal, which can be expected to influence the position of the hydroxyl groups [17].

Comparison of precise peak energy allows us to attribute specific peaks in the experimental O 1s spectrum to different oxygen locations within the crystal structure. The broader peak centred at 543 eV is primarily due to oxygen atoms O8, O9 and O10, i.e., oxygen in the layer centre. This is consistent with its similarity to peak D in anatase. The sharp peak at 531.5 eV, at the higher energy edge of peak A, is almost uniquely due to O4 and O6, i.e., oxygen atoms at the layer surfaces. Finally, the weak shoulder visible at 535 eV is seen only in the calculated spectra for O5 and O7, i.e., the surface hydroxyl groups. Thus the powerful combination of theoretical simulation with the high energy and spatial resolution of NEXAFS–TXM allows unambiguous identification of the presence of different oxygen bonding within individual layers of the (Na,H)TiNT.

In summary, we have shown that near-edge X-ray-absorption fine-structure spectroscopy combined with transmission X-ray microscopy (NEXAFS–TXM) is a powerful technique to

investigate the electronic structure of titanate nanostructures when supported by multichannel multiple scattering and density functional theory. Already in one experimental data set several nanostructures are accessible to gain statistical results. By analysing the O K-edge and Ti L-edge of titanium-based materials (TiO$_2$, SrTiO$_3$, (Na,H)TiNTs) we show the effect of the connectivity of the TiO$_6$ octahedra in the electronic states. (Na,H)TiNTs have an average connectivity between that of SrTiO$_3$ and anatase, with differences in the splitting of the Ti L$_3$–e$_g$ line and O K-edge peaks ≈10 eV above threshold. These peaks correspond to the hybridization of O p with delocalized states and are thus particularly sensitive to structural changes around the O sites. This sensitivity allows direct comparison between experiment and simulations and subsequent assignment of specific peaks and shoulders in the O K-edge to oxygen in different bonding environments within individual titanate layers of the nanostructure. The excellent agreement between the experimental data and the theoretical modelling confirms the assignment of the (Na,H)TiNT structure to a layered titanate of the $H_2Ti_nO_{2n+1}$ family. High-level spectroscopic modelling appears to be an important way to extend further the resolution of NEXAFS–TXM towards the atomic limit.

Experimental
Materials
Sodium titanate nanotubes ((Na,H)TiNTs) were synthesized from anatase TiO_2 (Aldrich, –325 mesh), and 10 M NaOH(aq) under hydrothermal conditions at 135 °C. The anatase (Aldrich, –325 mesh), and $SrTiO3$ (Alfa Aesar) were used as standard

Characterization
The morphology of the synthesized material was investigated with a TEM (Jeol 2100, 200 keV).

The NEXAFS spectra were recorded with the TXM installed at the undulator beamline U41-XM at BESSY II, Berlin.

XPS (X-ray photoelectron spectroscopy) measurements were also performed in a VERSAPROBE PHI 5000, equipped with a monochromatic Al Kα X-ray source. The relative amount of sodium was evaluated to be 12% in accordance with EDS (11%) [FE-SEM (Carl Zeiss, Supra 35 LV)].

Supporting Information

Supporting Information File 1
Broadening of the O K-edge spectra, comparison of the XPS Ti spectra recorded on the anatase and on the (Na,H)TiNTs, and experimental details.
[http://www.beilstein-journals.org/bjnano/content/supplementary/2190-4286-3-88-S1.pdf]

Acknowledgments

References

1. Schneider, G.; Guttmann, P.; Heim, S.; Rehbein, S.; Mueller, F.; Nagashima, K.; Heymann, J. B.; Müller, W. G.; McNally, J. G. *Nat. Methods* **2010,** *7,* 985–987. doi:10.1038/nmeth.1533

2. Schneider, G.; Guttmann, P.; Rehbein, S.; Werner, S.; Follath, R. *J. Struct. Biol.* **2012,** *177,* 212–223. doi:10.1016/j.jsb.2011.12.023

3. Sakdinawat, A.; Attwood, D. *Nat Photon* **2010,** *4,* 840–848. doi:10.1038/nphoton.2010.267

4. Guttmann, P.; Bittencourt, C.; Rehbein, S.; Umek, P.; Ke, X.; Van Tendeloo, G.; Ewels, C. P.; Schneider, G. *Nat Photon* **2012,** *6,* 25–29. doi:10.1038/nphoton.2011.268

5. Rehbein, S.; Heim, S.; Guttmann, P.; Werner, S.; Schneider, G. *Phys. Rev. Lett.* **2009,** *103,* 110801–110804. doi:10.1103/PhysRevLett.103.110801

6. Chao, W.; Fischer, P.; Tyliszczak, T.; Rekawa, S.; Anderson, E.; Naulleau, P. *Opt. Express* **2012,** *20,* 9777–9783. doi:10.1364/OE.20.009777

7. Rehbein, S.; Guttmann, P.; Werner, S.; Schneider, G. *Opt. Express* **2012,** *20,* 5830–5839. doi:10.1364/OE.20.005830

8. Krüger, P. *Phys. Rev. B* **2010,** *81,* 125121–125126. doi:10.1103/PhysRevB.81.125121

9. Suenaga, K.; Koshino, M. *Nature* **2010,** *468,* 1088–1090. doi:10.1038/nature09664

10. Suenaga, K.; Sato, Y.; Liu, Z.; Kataura, H.; Okazaki, T.; Kimoto, K.; Sawada, H.; Sasaki, T.; Omoto, K.; Tomita, T.; Kaneyama, T.; Kondo, Y. *Nat. Chem.* **2009,** *1,* 415–418. doi:10.1038/nchem.282

11. Umek, P.; Korošec, R. C.; Jančar, B.; Dominko, R.; Arčon, D. *J. Nanosci. Nanotechnol.* **2007,** *7,* 3502–3508. doi:10.1166/jnn.2007.838

12. Kasuga, T.; Hiramatsu, M.; Hoson, A.; Sekino, T.; Niihara, K. *Adv. Mater.* **1999,** *11,* 1307–1311. doi:10.1002/(SICI)1521-4095(199910)11:15<1307::AID-ADMA1307>3.0.CO;2-H

13. Wang, W.; Varghese, O. K.; Paulose, M.; Grimes, C. A.; Wang, Q.; Dickey, E. C. *J. Mater. Res.* **2004,** *19,* 417–422. doi:10.1557/jmr.2004.19.2.417

14. Chen, Q.; Du, G. H.; Zhang, S.; Peng, L. *Acta Crystallogr., Sect. B: Struct. Sci.* **2002,** *58,* 587–593. doi:10.1107/S0108768102009084

15. Yang, J. J.; Jin, Z.; Wang, X.; Li, W.; Zhang, J.; Zhang, S.; Guo, X.; Zhang, Z. *Dalton Trans.* **2003,** 3898–3901. doi:10.1039/b305585j

16. Ma, R. Z.; Bando, Y.; Sasaki, T. *Chem. Phys. Lett.* **2003,** *380,* 577–582. doi:10.1016/j.cplett.2003.09.069

17. Zhang, S.; Chen, Q.; Peng, L. M. *Phys. Rev. B* **2005,** *71,* 014104–014115. doi:10.1103/PhysRevB.71.014104

18. Gloter, A.; Ewels, C.; Umek, P.; Arcon, D.; Colliex, C. *Phys. Rev. B* **2009,** *80,* 035413. doi:10.1103/PhysRevB.80.035413

19. Jamnik, J.; Dominko, R.; Erjavec, B.; Remskar, M.; Pintar, A.; Gaberscek, M. *Adv. Mater.* **2009,** *21,* 2715–2719. doi:10.1002/adma.200803032

20. Han, C.-H.; Hong, D.-W.; Kim, I.-J.; Gwak, J.; Han, S.-D.; Singh, K. C. *Sens. Actuators, B* **2007,** *128,* 320–325. doi:10.1016/j.snb.2007.06.025

21. Baiju, K. V.; Zachariah, A.; Shukla, S.; Biju, S.; Reddy, M. L. P.; Warrier, K. G. K. *Catal. Lett.* **2009,** *130,* 130–136. doi:10.1007/s10562-008-9798-5

22. Qu, J.; Gao, X. P.; Li, G. R.; Jiang, Q. W.; Yan, T. Y. *J. Phys. Chem. C* **2009,** *113,* 3359–3363. doi:10.1021/jp810692t

23. Huusko, J.; Lantto, V.; Torvela, H. *Sens. Actuators, B* **1993,** *16,* 245–248. doi:10.1016/0925-4005(93)85188-G

24. Linsebigler, A. L.; Lu, G. Q.; Yates, J. T. *Chem. Rev.* **1995,** *95,* 735–758. doi:10.1021/cr00035a013

25. Huang, S. Y.; Kavan, L.; Exnar, I.; Grätzel, M. *J. Electrochem. Soc.* **1995,** *142,* L142–L144. doi:10.1149/1.2048726

26. Wang, R.; Hashimoto, K.; Fujishima, A.; Chikuni, M.; Kojima, E.; Kitamura, A.; Shimohigoshi, M.; Watanabe, T. *Nature* **1997,** *388,* 431–432. doi:10.1038/41233

27. Wagemaker, M.; van Well, A. A.; Kearley, G. J.; Mulder, F. M. *Solid State Ionics* **2004,** *175,* 191–193. doi:10.1016/j.ssi.2003.11.030

28. Armstrong, A. R.; Armstrong, G.; Canales, J.; García, R.; Bruce, P. G. *Adv. Mater.* **2005,** *17,* 862–865. doi:10.1002/adma.200400795

29. Roy, P.; Berger, S.; Schmuki, P. *Angew. Chem., Int. Ed.* **2011,** *50,* 2904–2939. doi:10.1002/anie.201001374

30. Hitchcock, A. P.; Dynes, J. J.; Johansson, G.; Wang, J.; Botton, G. *Micron* **2008,** *39,* 311–319. doi:10.1016/j.micron.2007.09.008

31. Ohwada, M.; Kimoto, K.; Suenaga, K.; Sato, Y.; Ebina, Y.; Sasaki, T. *J. Phys. Chem. Lett.* **2011,** *2,* 1820–1823. doi:10.1021/jz200781u

32. Umek, P.; Cevc, P.; Jesih, A.; Gloter, A.; Ewels, C. P.; Arčon, D. *Chem. Mater.* **2005,** *17,* 5945–5950. doi:10.1021/cm050928w

33. Jacobsen, C.; Wirick, S.; Flynn, G.; Zimba, C. J. *J. Microsc. (Oxford, U. K.)* **2000,** *197,* 173–184. doi:10.1046/j.1365-2818.2000.00640.x

34. Kremer, J. R.; Mastronarde, D. N.; McIntosh, J. R. *J. Struct. Biol.* **1996,** *116,* 71–76. doi:10.1006/jsbi.1996.0013

35. Diebold, U. *Surf. Sci. Rep.* **2003,** *48,* 53–229. doi:10.1016/S0167-5729(02)00100-0

36. Casu, M. B.; Braun, W.; Bauchspieß, K. R.; Kera, S.; Megner, B.; Heske, C.; Thull, R.; Umbach, E. *Surf. Sci.* **2008,** *602,* 1599–1606. doi:10.1016/j.susc.2008.02.030

37. Groot, F. M. F.; Figueiredo, M. O.; Basto, M. J.; Abbate, M.; Petersen, H.; Fuggle, J. C. *Phys. Chem. Miner.* **1992,** *19,* 140–147. doi:10.1007/BF00202101

38. Brydson, R.; Williams, B. G.; Engel, W.; Sauer, H.; Zeitler, E.; Thomas, J. M. *Solid State Commun.* **1987,** *64,* 609–612. doi:10.1016/0038-1098(87)90792-7

39. Biener, J.; Bäumer, M.; Wang, J.; Madix, R. J. *Surf. Sci.* **2000,** *450,* 12–26. doi:10.1016/S0039-6028(99)01216-9

40. Lusvardi, V. S.; Barteau, M. A.; Chen, J. G.; Eng, J., Jr..; Frühberger, B.; Teplyakov, A. *Surf. Sci.* **1998,** *397,* 237–250. doi:10.1016/S0039-6028(97)00740-1

41. Soriano, L.; Abbate, M.; Vogel, J.; Fuggle, J. C.; Fernández, A.; González-Elipe, A. R.; Sacchi, M.; Sanz, J. M. *Surf. Sci.* **1993,** *290,* 427–435. doi:10.1016/0039-6028(93)90725-Y

42. Wu, Z. Y.; Ouvrard, G.; Gressier, P.; Natoli, C. R. *Phys. Rev. B* **1997,** *55,* 10382–10391. doi:10.1103/PhysRevB.55.10382

43. Kresse, G.; Furthmüller, J. *Phys. Rev. B* **1996,** *54,* 11169–11186. doi:10.1103/PhysRevB.54.11169

44. Kresse, G.; Joubert, D. *Phys. Rev. B* **1999,** *59,* 1758–1775. doi:10.1103/PhysRevB.59.1758

Tuning the properties of magnetic thin films by interaction with periodic nanostructures

Ulf Wiedwald[*1], Felix Haering[1], Stefan Nau[1,2], Carsten Schulze[3], Herbert Schletter[3], Denys Makarov[3,4], Alfred Plettl[1], Karsten Kuepper[1,5], Manfred Albrecht[3], Johannes Boneberg[6] and Paul Ziemann[1]

Abstract

The most important limitation for a significant increase of the areal storage density in magnetic recording is the superparamagnetic effect. Below a critical grain size of the used CoCrPt exchange-decoupled granular films the information cannot be stored for a reasonable time (typically ten years) due to thermal fluctuations arbitrary flipping of the magnetization direction. An alternative approach that may provide higher storage densities is the use of so-called percolated media, in which defect structures are imprinted in an exchange-coupled magnetic film. Such percolated magnetic films are investigated in the present work. We employ preparation routes that are based on (i) self-assembly of Au nanoparticles and (ii) homogeneous size-reduction of self-assembled polystyrene particles. On such non-close-packed nanostructures thin Fe films or Co/Pt multilayers are grown with in-plane and out-of-plane easy axis of magnetization. The impact of the particles on the magnetic switching behavior is measured by both integral magnetometry and magnetic microscopy techniques. We observe enhanced coercive fields while the switching field distribution is broadened compared to thin-film reference samples. It appears possible to tailor the magnetic domain sizes down to the width of an unperturbed domain wall in a continuous film, and moreover, we observe pinning and nucleation at or close to the imprinted defect structures.

Introduction

Perpendicular recording media currently in use consist of magnetic CoCrPt grains that are exchange-decoupled from each other by a thin layer of Si oxide or Ti oxide at the grain bounda-ries. A single magnetic bit is stored on the hard disk by magne-tizing a small region consisting of several tens of magnetic grains with parallel magnetization either pointing up- or down-

wards. Increasing areal densities of recording bits, while maintaining the signal-to-noise ratio, demands a reduction of the grain size [1]. As a result of the miniaturization, however, the grain size approaches the superparamagnetic limit, below which stored information is lost due to thermal fluctuations of the magnetization. To some extent this problem can be circumvented by increasing magnetic anisotropy energy densities [2-8], but alternative approaches such as tilted magnetic recording [9], exchange-coupled composite media [10,11], exchange-spring media [12], or percolated perpendicular media [13,14] promise storage layers with significantly reduced transition noise at increased areal densities. In this contribution we focus on the latter approach: percolated magnetic films.

Such percolated media consist of exchange-coupled magnetic films with densely distributed pinning centers. In this case the magnetic stability is determined by the energy needed to dislodge a domain wall from its pinning site. The principle is illustrated in Figure 1. Domain walls are pinned at artificial defects imprinted by nanostructuring techniques. Defects may consist of an array of voids [15] or, even simpler, of nonmagnetic nanoobjects, such as particles, optimized with respect to both mutual distance and rather low filling factor. In that case, the information-storing layer is subsequently deposited onto the

nanoobjects. In this way, in addition to the exchange-coupled film in between the objects, magnetic caps are formed on top of them. As a result, the achievable storage density is determined by the defect density.

Different preparation techniques have been tested for high defect densities, i.e., serial e-beam or ion-beam lithography, nanoperforated templates, polymer structures, or colloids, to name a few [15-18]. In the present contribution we have chosen a platform that allows the variation of the relevant parameters such as nanostructure size and their mutual distance, which are not easily accessible by the approaches mentioned above. The technique is based on self-assembly and homogeneous size reduction of polystyrene (PS) colloids [19] ending up with a non-close-packed monolayer of colloidal particles, which, in turn, serves as a template for subsequent deposition of magnetic films.

In the following we first discuss the achievements and limitations of the technique. Then the tailoring of the magnetic switching process is presented for in-plane- and out-of-plane-magnetized films. Finally, an alternative approach towards smaller defect structures is introduced. We studied the magnetic reversal of Co/Pt multilayers with out-of-plane anisotropy deposited on a more densely packed array of Au nanoparticles.

Results and Discussion
Preparation of percolated magnetic thin films
Percolated magnetic thin films have been prepared by various techniques [15,16]. One necessary requirement is a homogeneous coverage of a given substrate on centimeter length scales. Such structures can be achieved by self-assembly of PS spheres [20] and subsequent plasma-assisted etching of these particles down to the targeted diameter [19]. This approach allows variations of the distance and the size of the nanostructure by choice of (commercially available) colloids and the adjustment of the remaining diameter by total etching time, respectively. Figure 2 presents a scheme illustrating the method for one initial diameter and three final sizes of PS spheres at constant distance achieved after different plasma etching times, as indicated by the arrow in Figure 2. Deposition parameters (thickness and material) of the magnetic film can then be chosen in such a way that intrinsic properties of the magnetic film result in a domain-wall width matching the distance of the nanostructure underneath. This interplay of nanostructuring and magnetism will be discussed in the following subsections. First, we present achievements and limitations of the approach.

Monolayers of PS spheres have been prepared by drop-drying [21], spin-coating [22], Langmuir–Blodgett deposition or dip-coating techniques [23]. For PS sizes of 200 nm and below it
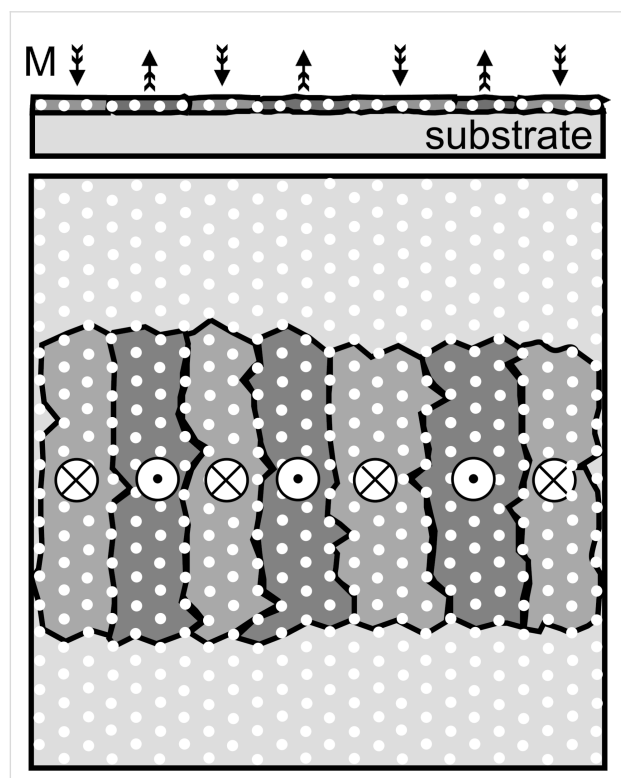

Figure 1: Principle of percolated perpendicular media. The exchange-coupled film is interspersed by nonmagnetic nanostructures (white dots) allowing domain-wall (black lines) pinning.
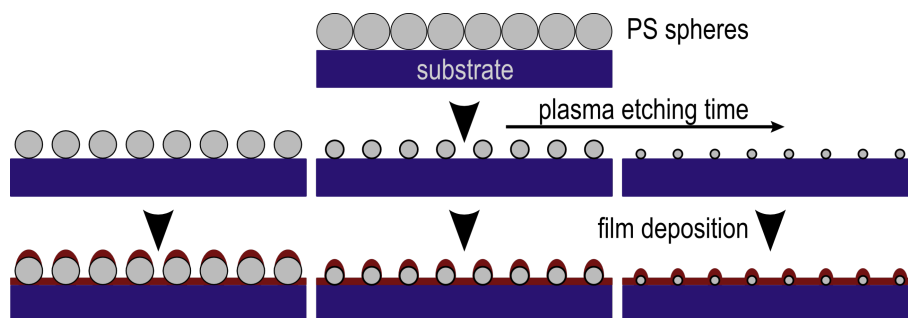
Figure 2: Schematics of the sample preparation. Self-assembled, close-packed monolayers of PS spheres are deposited on a substrate. Isotropic oxygen-plasma etching results in the homogeneous size reduction of PS particles. Finally, a magnetic film is deposited onto the substrates and capped by a thin Pt layer for oxidation protection.

turned out experimentally that a homogeneous monolayer free of large spare, double or multilayer subregions (a prerequisite for integral magnetic characterization) can be achieved best by dip coating. For this purpose, Si substrates were used after hydrophilization in oxygen plasma, resulting in SiO_2 layer thicknesses of about 5 nm. Commercial PS spheres [24] of average initial diameter of 190 or 95 nm were diluted to 1% w/v in purified water followed by dip-coating at a retraction velocity of typically 1 mm/min. Note that all parameters are slightly adjusted for each PS suspension. One general limitation is that the degree of hexagonal order of PS spheres becomes worse for smaller particle sizes due to the broadening of the relative size distributions of the colloids. This effect, however, plays a minor role in the context of the present work, since domain wall pinning, nucleation, and propagation are related to the nanostructure size and distance and in the simplest approximation not to the degree of hexagonal order.

The homogeneous size reduction of close-packed monolayers was performed by isotropic oxygen plasma etching at a constant pressure of about 7 Pa and ambient temperature. Details can be found elsewhere [19,25]. The applied conditions resulted in typical etching rates of 6–8 nm/min maintaining both the spherical shape and the initial position of the PS particles. Figure 3 presents results of the etching process for 190 and 95 nm particles as a function of etching time in panels (a) and (b), respectively. The diameter of particles constantly shrinks during the etching process as indicated by the linear fits. It is worth noting that the homogeneity of the etching process can be improved by an annealing step at 75 °C for 2 h at an intermediate diameter for surface smoothing, as shown by the circles in Figure 3b. This, however, enhances the etching rate by a factor of three. The etching technique is by no means restricted to 200 nm PS particles or below and can easily be adapted to larger initial sphere diameters, which are, however, not the focus of the present work.

After the preparation of the non-close-packed PS nanostructure, subsequent growth of magnetic films can be carried out in standard deposition chambers under ultrahigh-vacuum conditions. The percolated magnetic films discussed below were deposited either by pulsed laser ablation (Fe films) or e-beam evaporation (Co/Pt multilayers). For preparation details see, e.g., [25,26]. Panels (c) and (d) in Figure 3 show top-view scanning electron microscopy (SEM) images of Fe films (thickness $t = 11$ nm) deposited on top of $d = 35 \pm 8$ nm and $d = 50 \pm 8$ nm particles at a distance of $a = 95 \pm 7$ nm, respectively. Note that 1–3 nm Pt capping layers were used for oxidation protection. PS particles can be clearly seen while the Fe film exhibits contrast preferentially in cross-section SEM images. The cross-section SEM image Figure 3e, however, unambiguously reveals the morphology of the percolated Fe film. While between the 35 nm particles a smooth film grows on Si/SiO_2 substrates, Fe caps can be easily identified. Remarkably, Fe caps are in contact with the film between the colloidal spheres, although the deposited film thickness (11 nm) is small compared to the average particle diameter of $d = 35$ nm. Note that PS spheres including the magnetic caps on top may also be removed by chemo-mechanical polishing leading to a void structure, which may potentially be used as 2-D artificial spin-ice systems [27]. In the following, however, we focus on percolated films with magnetic caps present. In summary, the described fabrication delivers a percolated magnetic film, from which strongly modified magnetic properties can be expected as compared to an unstructured reference film. Magnetic studies following the above approach are presented for in-plane- and out-of-plane-magnetized films in the next two subsections, respectively.

Alternatively to film deposition on size-reduced PS particles for percolated magnetic films, one may use self-assembly of inorganic spheres, such as Au nanoparticles, for nanostructuring. Commercially available Au colloid solutions with particle sizes of 60 and 40 nm have been used to prepare monolayers of self-
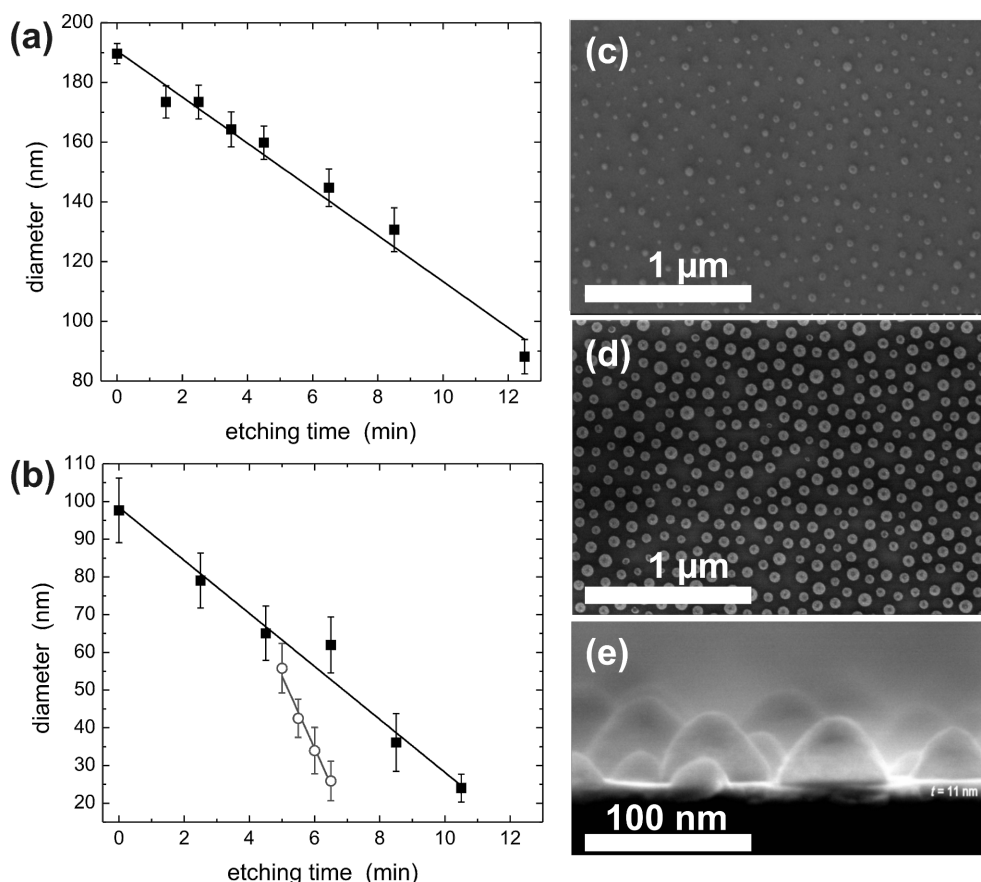
Figure 3: Size reduction of PS spheres as a function of etching time in isotropic oxygen plasma at ambient temperature for an initial particle diameter of (a) 190 ± 3 nm and (b) 95 ± 8 nm. Details are given in the text. Panels (c) and (d) show top-view SEM images of percolated Fe films deposited on size-reduced PS spheres of d = 35 ± 8 nm and d = 50 ± 8 nm at distance a = 95 ± 7 nm, respectively. The cross-section SEM image in (e) clearly reveals the magnetic-cap structure on PS spheres at film thickness t = 11 ± 1 nm on Si/SiO$_2$ substrates. Panels (a) and (b) are reproduced with permission from reference [19] – Copyright 2009 Wiley.

assembled Au particles on thermally oxidized Si(100) substrates [28]. The Au colloid solution was diluted with pure ethanol in the volume ratio of 2:1. A volume of 60 µL of such solution was dispersed onto the substrates and dried under ambient conditions in a covered box to prevent air flow (see [29] for details). The arrangement of the nanoparticles in the islands was investigated by SEM. Due to the low particle concentration in the colloid solution they form a number of irregularly shaped islands, which extend over several tens of microns. Figure 4 presents two SEM micrographs of such samples with Au nanoparticle arrangements with particle diameters of 60 and 40 nm, respectively. The 60 nm sized particles arrange in a hexagonal close-packed order, only disturbed by particles of slightly different size. The 40 nm particles do not order as well as those with 60 nm diameter. Voids with sizes of about 10 to 20 nm are formed in between Au particles. On the one hand, this approach allows significant reduction of the average distance of nanostructures as compared to the PS colloids; on the

other hand the homogeneity of coverage is strongly reduced. The impact of these differences on the magnetic behavior of the percolated film is discussed in the following sections.
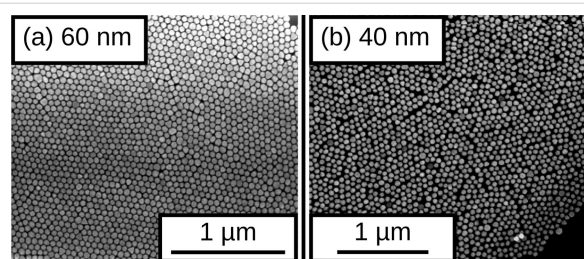
Figure 4: SEM images of monolayer assemblies of commercial Au nanoparticles with (a) 60 nm diameter and (b) 40 nm diameter on Si/SiO$_2$ substrates.

After preparation, the Au particle assemblies were introduced in a molecular beam epitaxy (MBE) chamber equipped with an

e-beam evaporator loaded with Co and Pt (purity greater than 99.99%). The multilayer stack [Co(0.3 nm)/Pt(0.8 nm)]$_8$ was deposited on a 5 nm thick Pt buffer layer. An additional 3 nm thick Pt cover layer was deposited to protect the samples from oxidation. The deposition of the metal films was performed simultaneously on particle assemblies as well as on planar substrates for reference.

Magnetic switching in percolated Fe films

The impact of such percolated structures as a function of thickness t, the remaining diameter of particles d and the average center-to-center distance a on the magnetic reversal was investigated by integral superconducting quantum interference device (SQUID) magnetometry. Figure 5a compares in-plane hysteresis loops of a percolated film (a = 95 nm, d = 66 nm, t = 17 nm) and a simultaneously prepared thin-film (t = 17 nm) reference sample on Si/SiO$_2$ substrate at ambient temperature. While the thin Fe film has a narrow and steep hysteresis with high remanent magnetization with respect to the saturation

magnetization, and small coercive field, the percolated Fe film of identical thickness exhibits a strongly enhanced coercive field of H_C = 250 Oe. Moreover, the hysteresis is more S-shaped with slightly reduced remanent magnetization and large saturation field of about 3000 Oe as compared to the reference. Such behavior can be attributed to domain wall pinning, presumably at the locations of the particles. For deeper insights into the switching process, however, it is necessary to apply magnetic microscopy techniques, as discussed below.

Using integral characterization techniques, such as SQUID magnetometry, it is convenient to determine the coercive field H_C as a function of the geometric parameters t, d, and a of the samples, as shown in Figure 5b–d, respectively. In panel (b) H_C is displayed as a function of the film thickness t for different remaining particle diameters. All samples were prepared from PS spheres with an initial diameter of a = 95 nm. The coercive field is found to be larger in all samples compared to the reference films having H_C < 10 Oe. It is apparent that H_C has a grad-
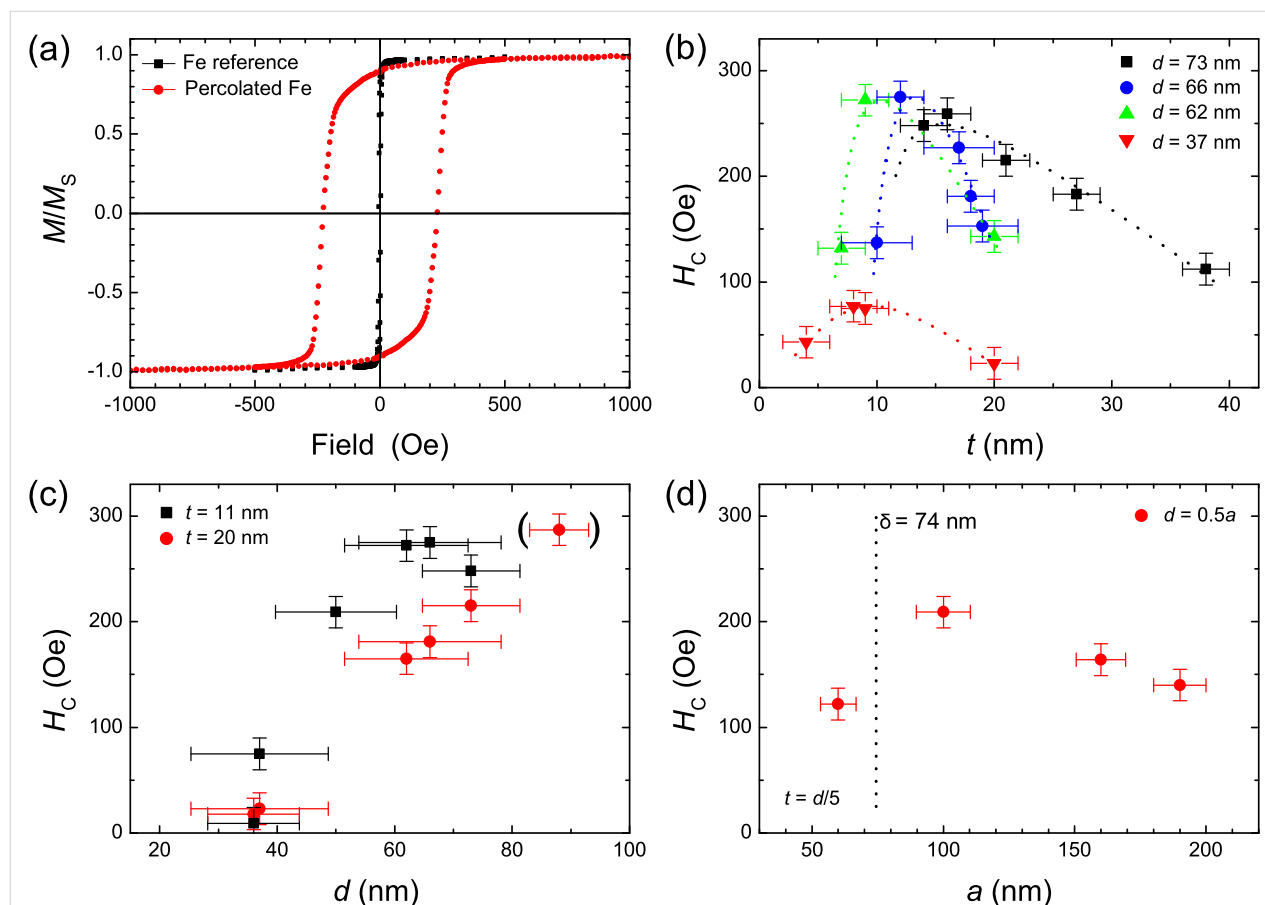
Figure 5: (a) Magnetic hysteresis loops of a percolated Fe film (a = 95 nm, d = 66 nm, t = 17 nm) and a thin-film reference sample taken in the in-plane geometry at ambient temperature. Panel (b) shows the experimental coercive field as a function of Fe layer thickness t for different diameters d of PS spheres at a distance a = 95 nm. Dotted lines are guides to the eye. In (c) H_C is presented as a function of d at a = 95 nm for two layer thicknesses t. In panel (d) the coercive field is displayed as a function of the sample periodicity a for PS sphere diameter d = 0.5a and optimized Fe film thickness t = d/5. Additionally, the experimentally determined domain wall width δ = 74 nm of continuous Fe films is marked.

ually shifting maximum moving from about $t = 10$ nm for $d = 37$ nm towards $t = 16$ nm for $d = 73$ nm. This indicates that the optimum pinning effect has to be adjusted for each individual set of parameters t, d, and a. The appearance of a maximum H_C can be explained as follows: For small thicknesses t the samples consist of films with non-magnetic holes inside and exchange-decoupled Fe caps on top of the PS particles. In this limit the cap structures have a minor influence on the integral magnetic reversal behavior of the film. Consequently, the switching is dominated by the film reversal, where the small holes, which eventually pin domain walls, will lead to an enhancement of the coercive field to $H_C = 45$ Oe as compared to the reference. Above a certain thickness, film and caps form an exchanged-coupled magnetic structure as shown in the cross-section SEM image in Figure 3e. In this case, domain-wall pinning is expected to be reduced. For larger particle diameters a larger film thickness t is necessary to grow an exchanged-coupled percolated sample. In this way the rise and the shift of H_C can be explained qualitatively. For thicker films, however, the sample morphology appreciably changes towards a rippled, but rather continuous film leading to decreased coercive fields. The pinning effect is further investigated as a function of particle diameter d for two thicknesses $t = 11$ nm and $t = 20$ nm as shown in Figure 5c. We observe a gradual increase of H_C up to 280 Oe for $t = 11$ nm, while H_C of the thicker film lags behind probably due to the minor impact of thicker films on the magnetic switching, as discussed above.

The strongest influence of the imprinted nanostructures on the magnetic switching behavior may be expected when the diameter and/or distance matches a magnetic length scale such as the domain wall width of unperturbed films. In such a case, growing domains would experience the largest resistance while for even smaller periods a strongly distorted domain pattern can be expected. To elucidate such correlations we vary the inter-particle distance a while etching their diameter to $d = a/2$ and adjust the film thickness to $t = d/5$. Parameters were chosen in such a way as to guarantee a pinning effect close to its maximum as expected from Figure 5b. The results are shown in Figure 5d for periods between 60 and 180 nm. Although only a limited number of experimental points are available due to the complicated sample processing in this case, we expect the highest coercive field for this set of parameters in the interval between 60 and 100 nm. This finding can be compared to the experimentally determined, unperturbed Fe domain wall width as measured by scanning transmission X-ray microscopy (STXM).

For a deeper understanding of the micromagnetism, selected samples were investigated by STXM at the PolLux beamline at the Swiss Light Source, Paul-Scherrer-Institute in Villigen,

Switzerland. The setup has been presented in detail elsewhere [30]. Percolated Fe films were prepared on commercial Si_3N_4 membranes (thickness 100 nm) in-line with the description for Si/SiO_2 substrates above. Two $Fe-L_3$ images were measured by scanning the sample with left and right circularly polarized light. The ratio of the two images reveals the magnetic domain structures at a resolution of better than 25 nm at the PolLux beamline. Sensitivity to in-plane magnetization of Fe films in the remanent state was achieved by tilting the sample normal by 30° with respect to the propagation direction of X-rays. Before imaging at ambient temperature, the samples were demagnetized by decreasing alternating fields in the horizontal in-plane direction.

A small fraction (a few percent) of the surface that is free of particles is typically found on samples prepared by dip-coating. In these areas the domain pattern of unperturbed films can be directly measured on one and the same sample. While typical domain sizes are in the range of 5–10 μm^2, we determined the domain wall width δ of a continuous Fe film as $\delta = 74 \pm 21$ nm by a number of line scans across a domain wall of maximum contrast (not shown). This value is in good agreement with the thickness of the Bloch domain wall in Fe, which is about 80 nm. Furthermore, the thickness of the domain wall corresponds to the estimated period $a = 60$–100 nm in percolated Fe films (with $5t = d$ and $2d = a$) giving a strong hint to the correlation of the distance between the nanostructures with the intrinsic domain wall width δ for the largest coercive fields due to magnetic pinning.

The magnetic domain pattern was measured in more detail for a percolated Fe film with nominally $a = 95$ nm, $d = 35$ nm, $t = 18$ nm. The parameters were chosen in such a way that the maximum field available in the setup (300 Oe) was sufficient to switch the magnetization of the sample. Figure 6a presents a single STXM image taken with right circularly polarized light. Some particles are clearly visible in the upper part of the sample while magnetic contrast of domains is directly observable. Enhancement of the magnetic signal can be achieved by division of STXM images taken with opposite helicities of X-rays at the price of losing the particle contrast almost completely. This is demonstrated in Figure 6b. The magnification in Figure 6c reveals the actual sample morphology. Starting on the lower left of the image the faint contrast visible in single domains is produced by 35 nm particles at $a = 95$ nm while on the upper right some hundred larger particles have self-assembled with a period of 150–170 nm. In our experiments, such demixing effects of a small contamination of larger particles are often observed during self-assembly. The fraction of larger particles was estimated by large-scale SEM imaging and was found to be well below 0.1%. Taking equal etching rates for the
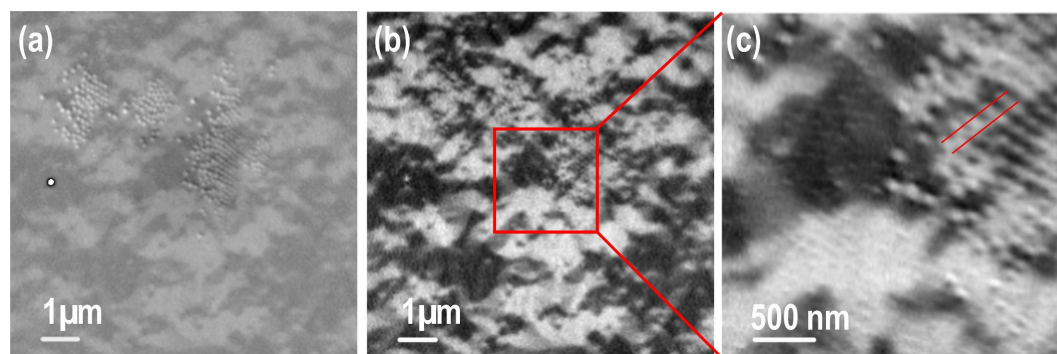
Figure 6: (a) Scanning transmission X-ray microscopy images of Fe films taken with right circularly polarized light at the Fe-L_3 edge show PS particles as well as magnetic contrast in the film after sample demagnetization. Panel (b) presents the XMCD image of the identical sample spot. In (c) an XMCD image at higher resolution is shown revealing two regions (lower left and top right) of different PS particle diameters. The underlying domain sizes appear strongly varied in these regions.

95 nm and approximately 160 nm particles, as suggested by the data presented in Figure 3, the upper right area reveals the ratio $d/a = 100$ nm$/160$ nm $= 0.63$ while in the lower left area we set $d/a = 0.37$. Based on the drastic difference in the diameter-to-period ratio and the results shown in Figure 5 we expect a much stronger pinning effect of the percolated film at larger d/a ratio. In the extreme, this may result in domain patterns with a minimum size as small as the distance between two particles. This feature is observed in Figure 6 indicated by the parallel red lines.

Magnetic switching in percolated perpendicular media

The concept of percolated perpendicular media is tested by film deposition onto size-reduced PS particles with $a = 180$ nm and $d = 40$ nm and a planar reference sample. Note that for such small nanostructures prepared from particles initially spaced at 180 nm the spherical shape is not maintained and rather semispheres are formed on the Si/SiO$_2$ substrate [25]. A [Co(0.3 nm)/Pt(0.8 nm)]$_{12}$ multilayer stack with an effective perpendicular magnetic anisotropy of 0.3 MJ/m^3 [31] has been deposited by alternating evaporation from pure Co and Pt sources by e-beam evaporation under ultrahigh vacuum conditions at ambient temperature. For integral characterization polar magneto-optical Kerr effect (MOKE) magnetometry with a spot size of about 100 µm was used to investigate magnetic switching (details are given in reference [25]). For this sample, with structure sizes of 40 nm at a distance of 180 nm, the contribution of magnetic caps to the MOKE signal is small due to the reduced filling factor and the stronger scattering of the reflected laser beam off the particle caps. The planar reference film shows a sharp switching at a coercive field of $\mu_0 \cdot H_C = 290$ mT and full remanent magnetization, indicating a reversal process dominated by the nucleation and subsequent propagation of domain walls [32].

The domain pattern of the sample has been recorded by atomic and magnetic force microscopy (AFM and MFM) after demagnetization in a perpendicular field. While in AFM mode the 40 nm dots were clearly resolved, the magnetic structure of the Co/Pt multilayer showed domain sizes of about 200 nm. Moreover, every single cap structure is in a single-domain state and decoupled from the film in between the particles. It turned out that magnetic domain walls correspond to the positions of the particles, this being the energetically favored configuration. For deeper understanding of the magnetic reversal process, in-field MFM in a custom-built setup using the constant-height mode was employed [33]. Figure 7 presents the switching process after saturating the sample in positive field perpendicular to the sample plane. The particle positions are displayed by circles as provided by an AFM prescan. The color code shows whether the particle cap has switched (orange) or not (purple). It is obvious that the nucleation of domains starts at about −210 mT close to the particle positions as displayed in Figure 7a and Figure 7b. Interestingly, the first magnetic caps already switch at this low field. The reversal mode of the film, however, is still dominated by domain-wall propagation. This can be easily identified when tracking the reversed areas in Figure 7b–g, and the domain walls preferentially stop at or close to the particle positions, i.e., domain walls are pinned at the defect sites. We do not observe strong exchange coupling between film and caps, since the majority of caps still remains in the initial state while the film is completely reversed (cf. Figure 7i). Thus, it is likely that magnetostatic interactions are important here leading to a strongly broadened switching field distribution (SFD) and a significantly enhanced coercive field. The most important contribution to the SFD is the nucleation field of individual magnetic caps, which is defined by its local magnetic anisotropy, size and shape. Thus, any size distribution of particles directly leads to the broadening of the SFD. From additional MFM investigations as a function of the external field,
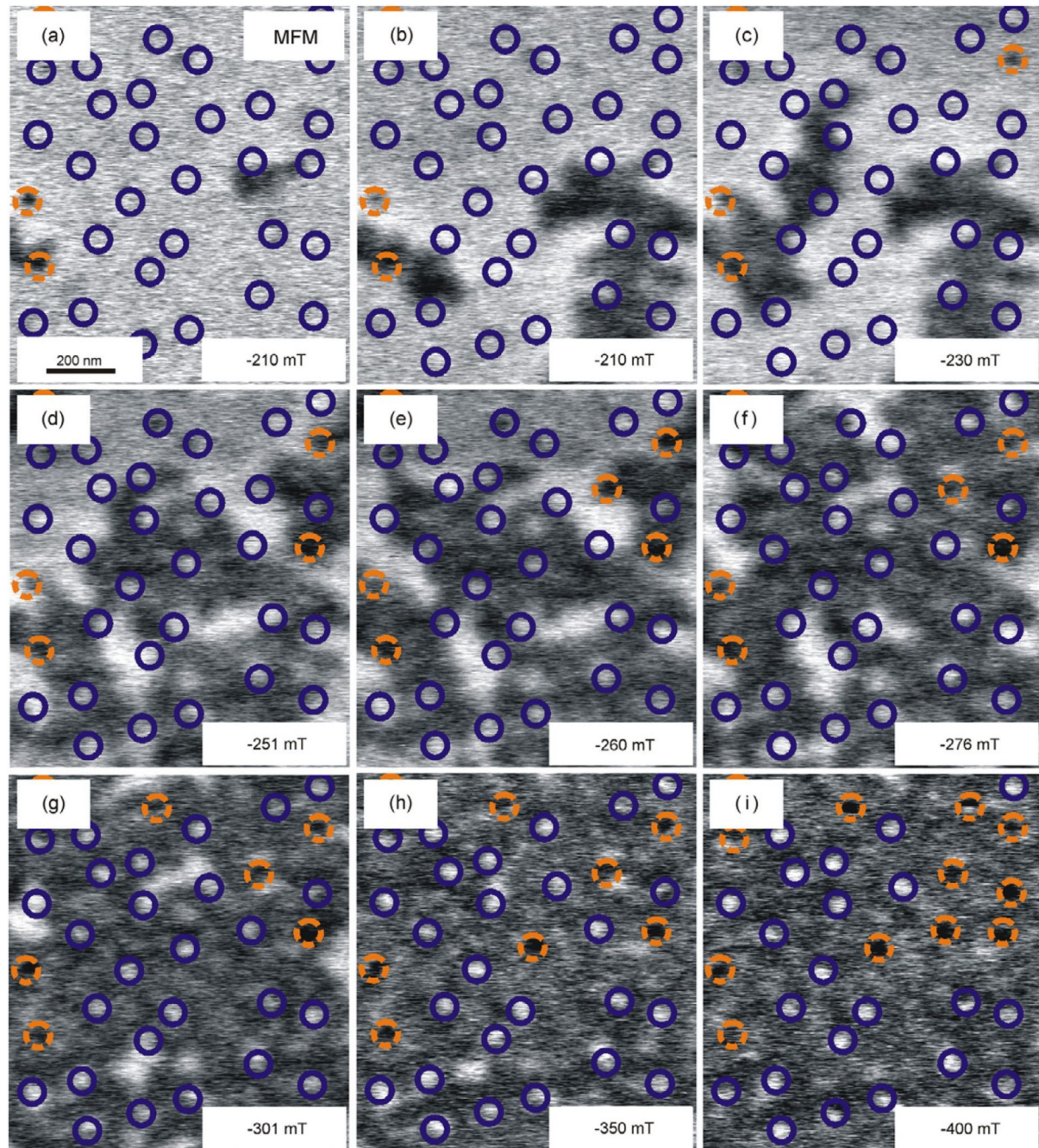
Figure 7: (a–i) MFM images of the same spot taken in different perpendicular fields after driving the sample to the positive saturated state at +1.6 T. Switched magnetic caps are indicated by dashed orange circles, while purple circles mark the unaffected caps. Panels (a) and (b) are two scans at identical field showing the growth of nucleated domains in the direction of the external field. This process is either thermally activated or induced by the tip. The figure has been reproduced with permission from [25] – Copyright 2009 Institute of Physics.

the hysteresis loops of the magnetic caps and the film can be separated by counting the number of switched caps and calculating the ratio of bright and dark contrast in the film region (see reference [25] for details). For the magnetic caps, this approach yields $\mu_0 \cdot H_C = 450$ mT and a broad SFD around 500 mT for the

sample shown in Figure 7. Moreover, due to the low filling factor of defects, one expects that the MFM-extracted film hysteresis loop is similar to the hysteresis measured by integral techniques such as MOKE. Indeed, this has been demonstrated in reference [25].

Magnetization reversal in arrays of spherical gold particles capped with Co/Pt multilayers

An alternative approach towards realizing percolated perpendicular media is the deposition of magnetic films with out-of-plane anisotropy on a densely packed array of hard spheres. This method was tested by growing a $[Co(0.3\ nm)/Pt(0.8\ nm)]_8$ multilayer stack (sandwiched between 5 nm Pt buffer layer and a 3 nm Pt capping layer) on commercially available Au nanoparticles as described above.

The structure of the magnetic multilayer on the nanoparticles strongly influences its magnetic properties. By means of SEM and cross-sectional scanning transmission electron microscopy (STEM) investigations, it was found that, independent of the particle size, the multilayer (with a nominal thickness of 16.8 nm) follows the curvature of the particle array (Figure 8a). By electron energy loss spectroscopy (EELS) along the line displayed in Figure 8a, the Co content was probed by using intensity profiling of the Co-$L_{3,2}$ edges. Figure 8b shows the Co signal, as well as the dark field (DF) intensity along the line scan. From the EELS line scan, Co is found to be present in the film material filling the contact region between the neighboring particle caps, suggesting that those caps are magnetically connected across the contact region, and form a continuous magnetic layer on top of the particle array [29]. Although no quantitative analysis of the amount of Co at the interconnection region was possible, exchange coupling between the particle caps is expected even if the multilayer structure of the Co/Pt film were disturbed, since Co–Pt alloys are ferromagnetic at room temperature down to a Co concentration of about 15 atom % [34].

MOKE remanence curves were measured by saturating the sample, subsequently applying a reverse field and recording the remanent magnetization (Figure 9). The angle θ of the external magnetic field with respect to the sample normal was varied between 0 (perpendicular to the substrate plane) and 90° (in the substrate plane) without changing the polar detection geometry, thus allowing an angular-dependent study of the integral magnetic signal. The remanence curves taken on the samples at a field angle θ = 0° show that the switching field of the reference sample is as large as 2.4 kOe with rather narrow SFD. The switching field is substantially increased for the multilayers grown on nanoparticle arrays, and the SFD is significantly broadened compared to the reference sample. Considering the morphology of the magnetic film on the nearly densely-packed Au particles, one can understand this finding qualitatively: the rims around the 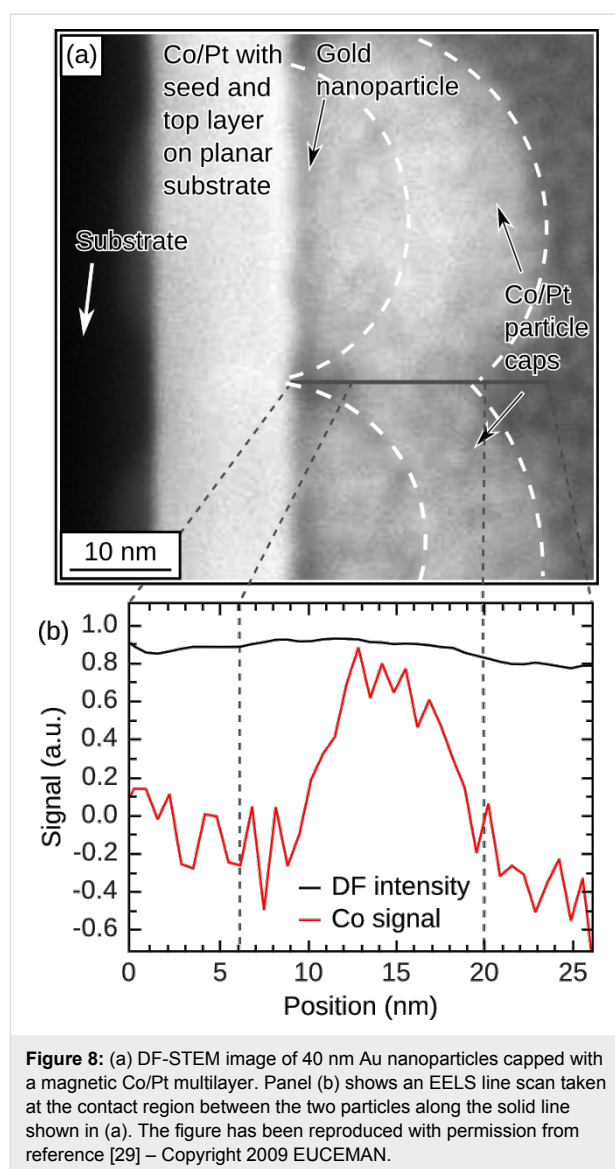particles act as sites for preferential domain-wall nucleation, while the pinning effect rather occurs in between particles, acting as defects here. The interplay of both effects may lead to the local stabilization of a magnetic domain

Figure 8: (a) DF-STEM image of 40 nm Au nanoparticles capped with a magnetic Co/Pt multilayer. Panel (b) shows an EELS line scan taken at the contact region between the two particles along the solid line shown in (a). The figure has been reproduced with permission from reference [29] – Copyright 2009 EUCEMAN.

in an individual particle cap. The broadening of the SFD is mainly attributed to the particle size distribution as well as to the magneto-static coupling between the neighboring caps in the array [35,36].

Increasing the angle θ results in a gradual increase of the switching field of the reference sample (Figure 9b) as expected for a strongly exchange-coupled magnetic film according to Kondorsky's model of depinning 180° domain walls (dashed line) [37]. The magnetic caps on arrays of 40 and 60 nm particles are found to be single-domain [29]. For a small, homogeneously magnetized nanostructure in a single-domain state, a coherent rotation process with a Stoner–Wohlfarth angular dependence [38] is expected (dotted line in Figure 9b). The magnetic caps, however, show only a weak angular dependence of the switching field with a small increase at high angles.

Figure 9: (a) MOKE remanence curves for Co/Pt multilayers grown on a planar substrate as well as on arrays of Au nanoparticles of 40 and 60 nm diameter. (b) Angular dependence of the switching field for the samples. The values beyond 60° for 60 nm particles and beyond 70° for 40 nm particles are not plotted, since the samples were not saturated in the available field. The figure has been reproduced with permission from reference [29] – Copyright 2009 EUCEMAN.

This deviation can be understood, in part, by taking into account the distribution of easy axes within the nanocaps following the surface curvature. This necessarily leads to a rather incoherent magnetization reversal process in an individual cap [39], which has also been demonstrated by micromagnetic simulations [32].

Conclusion

On the way towards alternative magnetic storage media, we have tested possible realizations of percolated media, consisting of magnetic films on top of periodic nanostructures. Such structures, realized by particle self-assembly techniques are able to effectively pin magnetic domains at the imprinted particle-induced defect structures. We generally observe enhanced coercive fields while the switching-field distribution is broadened compared to their continuous film counterparts.

In the first part of this contribution we presented results on nanostructuring techniques such as the self-assembly of PS

particles and subsequent plasma etching ending up with well-separated nanostructures with adjustable sizes and distances. A linear dependence of the particle size with etching time has been observed down to particle sizes of 25 nm starting from initially 95 and 190 nm PS particles, respectively. Alternatively, the Au nanoparticles deposited on planar substrates may act as a nanostructuring material, which generally allows smaller distances of nanostructures, albeit with strongly reduced variability of diameter and interparticle distance.

On these nanostructures we deposited magnetic thin films with in-plane (Fe) and out-of-plane (Co/Pt multilayers) orientation of the magnetization under UHV conditions, respectively. Thereby, the film thicknesses have been adjusted to the height of the nanoparticles or below leading to an exchange-coupled film with magnetic cap structures grown on the particles in contact with the film. For thin Fe films, studies of the integral magnetic hysteresis as a function of film thickness, distance and size of the particles have demonstrated that strong magnetic pinning can be established at ambient temperature. In the extreme, we find a strongly enhanced coercive field H_C up to 280 Oe compared to Fe thin-film reference samples of identical thickness ($H_C < 10$ Oe). Further studies of the domain configuration by scanning transmission X-ray microscopy have provided first evidence that the particles (with magnetic caps) effectively decrease the domain size, if the distance, diameter, film thickness and magnetization are properly chosen. In this way it is possible to corral an individual magnetic domain in between a number of neighboring dots. Note that the optimum parameters are not completely independent and the strongest magnetic pinning cannot be unequivocally predicted on the basis of the presented experiments, since exchange-coupling to the magnetic caps is critical and difficult to control.

In a second study, we investigated the impact of such size-reduced colloidal nanostructures on film/particle systems with out-of-plane anisotropy. The magnetic reversal mode was strongly altered compared to the thin film reference. By detailed MFM investigations we have shown that magnetic domains first nucleate at particle positions and propagate further until pinning eventually occurs at the next particle position, i.e., a defect in the film morphology. Thus, this feature can be exploited to limit the domain size in between a lateral arrangement of defects on the nanoscale, which is the essential requirement for realizing percolated perpendicular media. However, the density of particles still has to increase towards periodic structures with interparticle distances below 20 nm. In turn, hard magnetic alloys such as FePt or CoPt have to be used for smaller defect periods.

Such a further reduction of size has been tested by self-assembly of 40 nm Au nanoparticles and subsequent deposition

of Co/Pt multilayer films on top. Although magnetic exchange coupling between the caps in the array is expected, the magnetic caps are found to be in a single-domain state. In this respect, it is very likely that the differences in activation volume for nucleation and depinning of domain walls at defect sites induced by the underlying particle template alter the magnetic reversal mechanism.

In summary, the applied nanostructuring methods have proven very effective in limiting domain sizes by pinning domain walls at defect structures for both in-plane- and out-of-plane-magnetized thin films, as demonstrated by integral magnetometry and magnetic microscopies. The individual, local switching field can be tuned by adjusting the dimensions of the nanostructures and the film parameters. However, it turned out that nearly perfect homogeneity is necessary to achieve a narrow and predictable switching-field distribution. Further reduction of the nanostructure dimensions and the use of highly anisotropic materials are necessary to be competitive with storage media employing percolated perpendicular media.

Acknowledgements

References

1. Ishio, S.; Wasiya, T.; Saito, H.; Bai, J.; Pei, W. *J. Appl. Phys.* **2006,** *99,* 093907. doi:10.1063/1.2195427

2. Granz, S. D.; Barmak, K.; Kryder, M. H. *J. Appl. Phys.* **2012,** *111,* 07B709. doi:10.1063/1.3677766

3. Sun, S.; Murray, C. B.; Weller, D.; Folks, L.; Moser, A. *Science* **2000,** *287,* 1989–1992. doi:10.1126/science.287.5460.1989

4. Wiedwald, U.; Han, L.; Biskupek, J.; Kaiser, U.; Ziemann, P. *Beilstein J. Nanotechnol.* **2010,** *1,* 24–47. doi:10.3762/bjnano.1.5

5. Alloyeau, D.; Ricolleau, C.; Langlois, C.; Le Bouar, Y.; Loiseau, A. *Beilstein J. Nanotechnol.* **2010,** *1,* 55–59. doi:10.3762/bjnano.1.7

6. Dmitrieva, O.; Spasova, M.; Antoniak, C.; Acet, M.; Dumpich, G.; Kästner, J.; Farle, M.; Fauth, K.; Wiedwald, U.; Boyen, H.-G.; Ziemann, P. *Phys. Rev. B* **2007,** *76,* 064414. doi:10.1103/PhysRevB.76.064414

7. Müller, M.; Albe, K. *Beilstein J. Nanotechnol.* **2011,** *2,* 40–46. doi:10.3762/bjnano.2.5

8. Gruner, M. E.; Entel, P. *Beilstein J. Nanotechnol.* **2011,** *2,* 162–172. doi:10.3762/bjnano.2.20

9. Wang, J.-P. *Nat. Mater.* **2005,** *4,* 191–192. doi:10.1038/nmat1344

10. Wang, J.-P.; Shen, W.; Bai, J. *IEEE Trans. Magn.* **2005,** *41,* 3181–3186. doi:10.1109/TMAG.2005.855278

11. McCallum, A. T.; Krone, P.; Springer, F.; Brombacher, C.; Albrecht, M.; Dobisz, E.; Grobis, M.; Weller, D.; Hellwig, O. *Appl. Phys. Lett.* **2011,** *98,* 242503. doi:10.1063/1.3599573

12. Suess, D.; Schrefl, T.; Fähler, S.; Kirschner, M.; Hrkac, G.; Dorfbauer, F.; Fidler, J. *Appl. Phys. Lett.* **2005,** *87,* 012504. doi:10.1063/1.1951053

13. Tang, Y.; Zhu, J.-G. *IEEE Trans. Magn.* **2006,** *42,* 2360–2362. doi:10.1109/TMAG.2006.878688

14. Suess, D.; Fidler, J.; Porath, K.; Schrefl, T.; Weller, D. *J. Appl. Phys.* **2006,** *99,* 08G905. doi:10.1063/1.2164437

15. Rahman, T. M.; Lai, C.-H.; Vokoun, D.; Shams, N. N. *IEEE Trans. Magn.* **2007,** *43,* 2133–2135. doi:10.1109/TMAG.2007.893142 And references therein.

16. Schulze, C.; Faustini, M.; Lee, J.; Schletter, H.; Lutz, M. U.; Krone, P.; Gass, M.; Sader, K.; Bleloch, A. L.; Hietschold, M.; Fuger, M.; Suess, D.; Fidler, J.; Wolff, U.; Neu, V.; Grosso, D.; Makarov, D.; Albrecht, M. *Nanotechnology* **2010,** *21,* 495701. doi:10.1088/0957-4484/21/49/495701 And references therein.

17. Grobis, M.; Schulze, C.; Faustini, M.; Grosso, D.; Hellwig, O.; Makarov, D.; Albrecht, M. *Appl. Phys. Lett.* **2011,** *98,* 192504. doi:10.1063/1.3587635

18. Makarov, D.; Krone, P.; Lantiat, D.; Schulze, C.; Liebig, A.; Brombacher, C.; Hietschold, M.; Hermann, S.; Laberty, C.; Grosso, D.; Albrecht, M. *IEEE Trans. Magn.* **2009,** *45,* 3515–3518. doi:10.1109/TMAG.2009.2025181

19. Plettl, A.; Enderle, F.; Saitner, M.; Manzke, A.; Pfahler, C.; Wiedemann, S.; Ziemann, P. *Adv. Funct. Mater.* **2009,** *19,* 3279–3284. doi:10.1002/adfm.200900907

20. Gonçalves, M. R.; Makaryan, T.; Enderle, F.; Wiedemann, S.; Plettl, A.; Marti, O.; Ziemann, P. *Beilstein J. Nanotechnol.* **2011,** *2,* 448–458. doi:10.3762/bjnano.2.49

21. Micheletto, R.; Fukuda, H.; Ohtsu, M. *Langmuir* **1995,** *11,* 3333–3336. doi:10.1021/la00009a012

22. Jiang, P.; McFarland, M. J. *J. Am. Chem. Soc.* **2004,** *126,* 13778–13786. doi:10.1021/ja0470923

23. Dimitrov, A. S.; Nagayama, K. *Langmuir* **1996,** *12,* 1303–1311. doi:10.1021/la9502251

24. Polystyrene particles were purchased from Life Technologies.

25. Brombacher, C.; Saitner, M.; Pfahler, C.; Plettl, A.; Ziemann, P.; Makarov, D.; Assmann, D.; Siekman, M. H.; Abelmann, L.; Albrecht, M. *Nanotechnology* **2009,** *20,* 105304. doi:10.1088/0957-4484/20/10/105304

26. Trautvetter, M.; Wiedwald, U.; Paul, H.; Minkow, A.; Ziemann, P. *Appl. Phys. A* **2011,** *102,* 725–730. doi:10.1007/s00339-010-5972-x

27. Haering, F.; Wiedwald, U.; Häberle, T.; Han, L.; Plettl, A.; Koslowski, B.; Ziemann, P. *Nanotechnology.* Submitted for publication.

28. Denkov, N.; Velev, O.; Kralchevsky, P.; Ivanov, I.; Yoshimura, H.;
Nagayama, K. *Langmuir* **1992,** *8,* 3183–3190.
doi:10.1021/la00048a054

29. Schulze, C.; Schletter, H.; Makarov, D.; McFadzean, S.; Craven, A. J.;
Hietschold, M.; Wolff, U.; Neu, V.; Albrecht, M.
Micromaterials and Nanomaterials **2010,** *12,* 74–78.

30. Raabe, J.; Tzvetkov, G.; Flechsig, U.; Böge, M.; Jaggi, A.;
Sarafimov, B.; Vernooij, M. G. C.; Huthwelker, T.; Ade, H.; Kilcoyne, D.;
Tyliszczak, T.; Fink, R. H.; Quitmann, C. *Rev. Sci. Instrum.* **2008,** *79,*
113704. doi:10.1063/1.3021472

31. Ulbrich, T. C.; Assmann, D.; Albrecht, M. *J. Appl. Phys.* **2008,** *104,*
084311. doi:10.1063/1.3003064

32. Ulbrich, T. C.; Makarov, D.; Hu, G.; Guhr, I. L.; Suess, D.; Schrefl, T.;
Albrecht, M. *Phys. Rev. Lett.* **2006,** *96,* 077202.
doi:10.1103/PhysRevLett.96.077202

33. Murillo, R.; Siekman, M. H.; Bolhuis, T.; Abelmann, L.; Lodder, J. C.
Microsyst. Technol. **2007,** *13,* 177–180.
doi:10.1007/s00542-006-0143-x

34. Maret, M.; Cadeville, M. C.; Herr, A.; Poinsot, R.; Beaurepaire, E.;
Lefebvre, S.; Bessière, M. *J. Magn. Magn. Mater.* **1999,** *191,* 61–71.
doi:10.1016/S0304-8853(98)00373-4

35. Krone, P.; Makarov, D.; Schrefl, T.; Albrecht, M. *J. Appl. Phys.* **2009,**
106, 103913. doi:10.1063/1.3260240

36. Hellwig, O.; Berger, A.; Thomson, T.; Dobisz, E.; Bandic, Z. Z.;
Yang, H.; Kercher, D. S.; Fullerton, E. E. *Appl. Phys. Lett.* **2007,** *90,*
162516. doi:10.1063/1.2730744

37. Kondorsky, E. *J. Phys. (Moscow)* **1940,** 161–181.

38. Stoner, E. C.; Wohlfarth, E. P. *Philos. Trans. R. Soc. London, Ser. A*
1948, *240,* 599–642. doi:10.1098/rsta.1948.0007

39. Ulbrich, T. C.; Bran, C.; Makarov, D.; Hellwig, O.;
Risner-Jamtgaard, J. D.; Yaney, D.; Rohrmann, H.; Neu, V.;
Albrecht, M. *Phys. Rev. B* **2010,** *81,* 054421.
doi:10.1103/PhysRevB.81.054421

Highly ordered ultralong magnetic nanowires wrapped in stacked graphene layers

Abdel-Aziz El Mel[1], Jean-Luc Duvail[1], Eric Gautron[1], Wei Xu[2], Chang-Hwan Choi[2], Benoit Angleraud[1], Agnès Granier[1] and Pierre-Yves Tessier[*1]

Abstract

We report on the synthesis and magnetic characterization of ultralong (1 cm) arrays of highly ordered coaxial nanowires with nickel cores and graphene stacking shells (also known as metal-filled carbon nanotubes). Carbon-containing nickel nanowires are first grown on a nanograted surface by magnetron sputtering. Then, a post-annealing treatment favors the metal-catalyzed crystallization of carbon into stacked graphene layers rolled around the nickel cores. The observed uniaxial magnetic anisotropy field oriented along the nanowire axis is an indication that the shape anisotropy dominates the dipolar coupling between the wires. We further show that the thermal treatment induces a decrease in the coercivity of the nanowire arrays. This reflects an enhancement of the quality of the nickel nanowires after annealing attributed to a decrease of the roughness of the nickel surface and to a reduction of the defect density. This new type of graphene–ferromagnetic-metal nanowire appears to be an interesting building block for spintronic applications.

Introduction

Magnetic nanowires have been widely investigated during the last two decades for fundamental physics [1-7], and nano-engineering [7-10]. The various properties of these nanostructures make them very interesting as building block materials for applications in spintronics [8,11], nanobiotechnology [9,10],

and for the development of magnetic storage media [12]. Despite a long history of study devoted to the development of different fabrication strategies with a predilection for template methods [1-12], ferromagnetic nanowires still suffer from their relatively short length, which cannot reach up to the macro-

scopic scale. In addition, the manipulation of such one-dimensional (1D) nanostructures is often considered as a complicated process and a barrier for a simple integration of nanowires into electrical devices.

The past few years have witnessed the rise of graphene as an extraordinary functional material with unique properties [13-16]. This material is one of the best candidates that can be used for the development of electronics, sensors, and energy-related devices [17-19]. The combination between the electrical properties of graphene and the magnetic properties of 1D ferromagnetic nanostructures would offer wide prospects for spintronic applications. Fabricating coaxial nanowires with ferromagnetic cores and graphene stacking shells is an elegant way to combine the unique properties of these two materials [20-23]. In addition, similar to a polymeric layer covering a magnetic nanowire [7], and considering the efficient protection of a single graphene layer [24], the stacked graphene layers (i.e., the shell) wrapping the nanowires could be considered as an outstanding shield protecting the metal cores against oxidation. Core–shell nanowires consisting of metal cores and graphene stacking shells, also known as metal-filled carbon nanotubes, are in general produced by chemical vapor deposition (CVD) [20-23]. Such a technique allows accurate controlling over the characteristics (i.e., density, length, tube diameter, etc.) of the vertically grown metal-filled nanotubes. Despite this accurate growth control, CVD does not allow the growth of metal-filled nanotubes with a length up to the macroscale while retaining an excellent alignment. Additionally, in some cases the metal is found to be discontinuous inside the tubes [20].

In a previous study, we demonstrated the possibility to synthesize an array of aligned Ni nanowires on a patterned silicon surface [25]. In this letter we present a simple and efficient method to prepare an array of highly ordered coaxial nickel/graphene-stacks core–shell nanowires with a length up to 1 cm.

The process involves the deposition of nickel nanowires containing a low amount of carbon (3 atom %) by a hybrid sputtering technique [26] on a patterned silicon substrate consisting of periodic nanograting structures (Figure 1, left) prepared by laser interference lithography coupled to deep reactive-ion etching [27]. After the deposition, in order to form stacked graphene layers rolled around the nickel nanowires (Figure 1, right), the carbon-containing nickel (C–Ni) nanowires were thermally annealed at 400 °C for 60 min (details concerning the selection of the annealing conditions are presented in Supporting Information File 1).

Results and Discussion

The SEM micrographs of the post-annealed carbon-containing nickel nanowires (Figure 2) show the organization and alignment of these nanostructures on the top surface of the silicon nanogrates. The nanowires have a homogenous morphology with a mean diameter of ≈145 nm (corresponding to the width of the grates) and a length up to 1 cm (corresponding to the size of the substrate). The preferential growth of nickel on the top surface of the grating structures can be mainly attributed to the
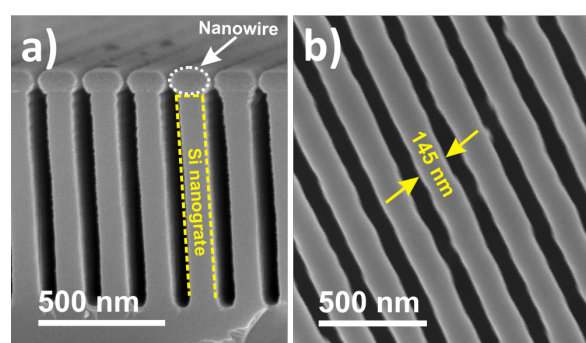
Figure 2: SEM micrographs of the post-annealed carbon-containing nickel nanowires on silicon nanograted structures. Cross section (a) and plan (b) view.
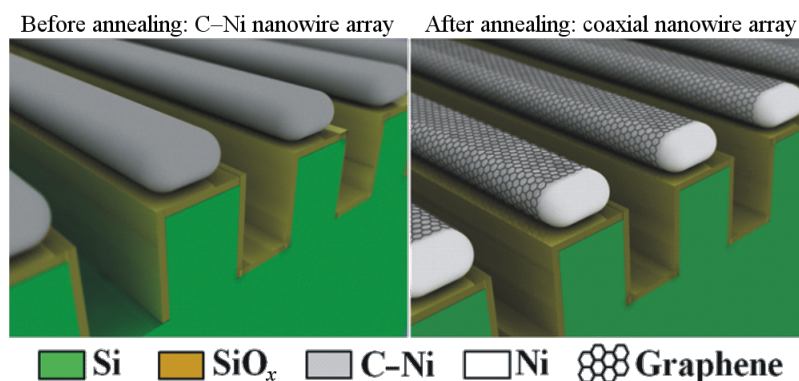
Figure 1: Schematics of the carbon-containing nickel nanowire array before (left) and after (right) post-annealing for 1 h at 400 °C.

following mechanisms: (i) the low directionality of the deposition process; (ii) the low width of the nanotrench separating two subsequent nanogrates; and (iii) the high depth-to-width ratio of the trenches (here, typically 12) [25,28].

In order to prove that these nanowires have a core–shell structure with a nickel core and graphene stacking shell, they were placed on a carbon-coated copper grid and their surfaces were examined by TEM (Figure 3a). A typical high-resolution TEM micrograph of the surface of a nanowire is presented in Figure 3b. The TEM analysis reveals the presence of a few graphene stacked layers (ca. 12) with a low nanotextural order neighboring the nickel nanowire surface. The interlayer distance of two adjacent graphene layers, evaluated from the high-resolution TEM micrograph, was about 0.347 nm. This value is very close to the interlayer distance of two graphene mono-layers in graphite (0.335 nm). The presence of the graphene stacks was further demonstrated by electron diffraction (Figure 3c). The obtained diffraction pattern was very similar to the one recorded on Ni-filled carbon nanotubes that we synthesized in a previous study by thermal annealing of Ni nanowires organized in an amorphous carbon film [29]. Thus, although the synthesis method developed in this work is completely different to the one used in our previous study [29], the nanostructures obtained with both methods exhibit a similar crystalline structure.

Indeed, in both cases only the 002 reflections corresponding to crystalline hexagonal graphite were present [29,30]. They appear as arcs instead of rings due to the anisotropic nanotexture in the analyzed area [30]. The 004 reflections and *hk* bands (i.e., 10 and 11 bands of turbostratic carbon) are probably absent due to the low number of analyzed stacked graphene layers. The other rings observed on the diffraction pattern are attributed to face-centered cubic (fcc) nickel. The formation of the stacked graphene layers results from the phase separation and the nickel-catalyzed crystallization of carbon by thermal annealing. During the post-annealing stage of the carbon-containing nickel nanowires, the carbon atoms diffuse and homogenously dissolve in the nickel phase [31,32]. As the limit of the solid solubility of carbon in the nickel phase is reached during the cool-down step, the carbon atoms precipitate into graphene stacked layers on the free surface of the nanowires. This mechanism has been recently used for the synthesis of a few layered graphene sheets [31,33,34].

The magnetic behavior of the nanowire arrays after post-annealing has been investigated at 300 K by using a Quantum Design SQUID magnetometer. The in-plane magnetization hysteresis loops were measured for an applied field parallel (black curve) and perpendicular (red curve) to the wire axis
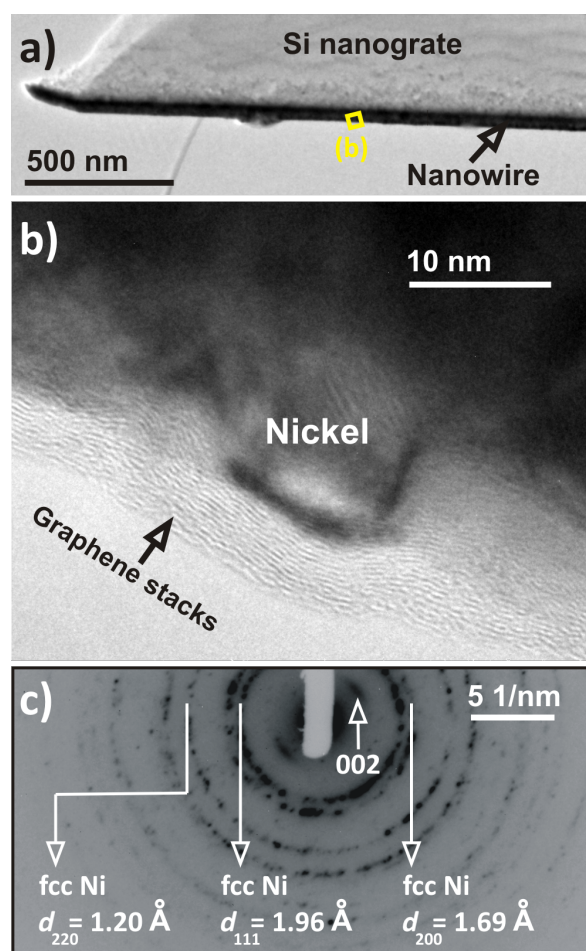
Figure 3: (a) TEM micrograph of a coaxial nanowire as prepared on a silicon nanograted structure. (b) High-resolution TEM micrograph showing the presence of several stacked graphene layers wrapping the nickel nanowire. (c) Selected-area electron diffraction pattern recorded on a single wire. The 002 reflection indicated in (c) is attributed to graphitic carbon.

(Figure 4). The saturation fields, measured in both configurations, were found to be almost equal to the ones obtained for the as-grown C–Ni nanowires before annealing (Table 1 and Supporting Information File 1, Figure S3). The smaller saturation field ($H_S^{\parallel} = 1500$ Oe) and the larger squareness ($M_r/M_s = 0.4$) when the external magnetic field is applied parallel to the nanowire axis, compared to the perpendicular configuration (roughly $H_S^{\perp} = 3100$ Oe and $M_r/M_s = 0.14$), indicate that the nanowire array exhibits a preferential magnetic orientation along the wire axis (i.e., easy axis parallel to the nanowires).

In the case of polycrystalline ferromagnetic nanowires, such uniaxial magnetic anisotropy originates from the shape anisotropy resulting from the very high aspect ratio of these nanostructures [7,35-43]. Concerning the coercive field, it is slightly higher ($H_C^{\parallel} = 32$ Oe) when the external magnetic field

Figure 4: (a) Normalized hysteresis loops of the coaxial nanowire array measured at 300 K with an applied magnetic field parallel (black curve) and perpendicular (red curve) to the wire axis. Panel (b) is a magnified region of (a).

between two subsequent nanowires can promote dipolar coupling between the wires. Indeed, the magnetic interactions between separated lines are due to magnetostatic effects that become relevant when the line separation is typically less than the line width [38,42]. For a field applied parallel to the lines, the coercive field and the squareness are reduced when the line separation decreases [36,38,41]. As a consequence, no square hysteresis loop, as measured for single-domain and isolated nanowires [3], is expected here, and complex magnetic configurations can take place. Moreover, by comparing the coercive fields measured before and after the post-annealing procedure we can conclude that they are reduced after thermal annealing (Table 1). The decrease in the coercive fields suggests that the surface of the nickel wire, i.e., the interface with the graphene shell, becomes very smooth after annealing since morphological defects favor pinning of the domain walls and, thus, result in higher coercivity [34].

The presence of carbon impurities within the as-grown C–Ni nanowires may also be another factor resulting in higher coercive fields before annealing, since these impurities may generate some defects in the crystalline structure of the nickel phase. In addition, the small coercive fields recorded after annealing suggest that there is no oxide layer surrounding the nickel core, which would produce a bias exchange between the magnetizations of nickel and nickel oxide. This non-oxidized nickel nanowire is expected due to the presence of the stacked graphene layers as a barrier.

Conclusion

In summary, an efficient method for the synthesis of an array of ultralong and organized coaxial nanowires, with nickel cores and graphene stacking shells, has been demonstrated. The TEM analysis revealed that the stacked graphene layers forming the shell have a turbostratic structure and a nanotextural order. We have further demonstrated the presence of a preferential magnetic orientation along the wire axis, which has been attributed to the shape anisotropy. The low coercive fields reflect the low roughness and low structural defects as well as dipolar coupling between the nanowires. This new type of graphene ferromagnetic metal nanowire appears to be an interesting building block for spintronics, for example, for the injection of a spin-polarized current from the metal to the high-carrier-

is applied parallel to the nanowire array, than the one measured for the perpendicular configuration ($H_C^{\perp} = 21$ Oe). It can be seen that the measured values are very low compared to the ones reported in literature for nickel nanowires with the same diameter (roughly 350 Oe) [3].

Here, for nickel nanowires with a 150 nm diameter, a multidomain configuration is expected. Indeed, this diameter is significantly larger than the exchange length λ_{ex} and the domain wall width λ_w whose values for nickel are about 20 and 90 nm, respectively [44]. Moreover, the small gap of about 100 nm

Table 1: Summary of the magnetic characteristics recorded at 300 K for C–Ni nanowire arrays before and after thermal annealing at 400 °C.

Sample	$H_S^{\parallel}$ (Oe)	$H_S^{\perp}$ (Oe)	$H_C^{\parallel}$ (Oe)	$H_C^{\perp}$ (Oe)
As-grown C–Ni nanowires	1550	3100	127	34
Postannealed C–Ni nanowires	1500	3100	32	21

mobility graphene structure. Its integration in a planar configuration opens the way to further device characterization. Moreover, the metal-catalyzed crystallization of carbon by thermal annealing, which is the mechanism employed in this work, allows the synthesis of graphene sheets of a few layers with low defects [31-33]. Therefore, after an optimization of the materials and the processing conditions of the technique developed in this work (e.g., the amount of carbon incorporated in the nickel phase, the post-annealing temperature, the metal used as catalyst, the dimensions of the nanograting structures, etc.) this strategy can be adopted for the growth of graphene nanoribbons a few layers thick and of macroscopic length.

Experimental

As described elsewhere [27], the nanograted substrate, which served as a template to prepare the nanowires, was fabricated by laser interference lithography followed by deep reactive ion etching. The size of the substrate was 1×1 cm^2, and the periodicity of the nanograting patterns was 240 nm. The width of each nanograte was about 140 nm. The details of the plasma process employed for the synthesis of the (C–Ni) nanowires are presented elsewhere [26]. Briefly, it consists of simultaneous depositions of metal and carbon by using a hybrid sputtering technique. For the deposition of nickel, a radio-frequency (RF) generator, operating at 13.56 MHz, was connected to a magnetron source in order to sputter a nickel target of 50 mm in diameter and 99.99 % in purity. For the simultaneous deposition of carbon, a carbon-coated one-turn stainless coil was placed at equal distance between the nickel target and the substrate. When applying RF power of 150 W to this coil, an additional plasma of pure argon was generated leading to the sputtering of the carbon layer coated on the coil, and hence, a small amount of carbon (3 atom %) was deposited. The base pressure before deposition was 10^{-4} Pa, whereas the deposition argon pressure was fixed to 0.67 Pa. The deposition was performed for 2 min at a floating potential and at a low temperature ($T < 150$ °C). After the growth, the postannealing treatment of the C–Ni nanowires at 400 °C for 60 min was performed in an oven at atmospheric pressure and under argon flow. After annealing, the samples were cooled down at a rate of 12 °C/min. Scanning electron microscopy (SEM) imaging was performed at 5 kV on a JEOL JSM 7600 F microscope. Transmission electron microscopy (TEM) imaging and selected-area electron diffraction (SAED) were performed on a Hitachi H-9000 NAR microscope (LaB$_6$ filament, 300 kV, Scherzer resolution: 0.18 nm). After the postannealing procedure of the carbon-containing Ni nanowires, the TEM specimens were prepared by a simple scratching of the sample surface with a pair of tweezers over a carbon-coated copper grid. Then, a drop of ethanol was placed on to the copper grid for the purpose of dispersion of the collected nanostructures.

Supporting Information

The optimization of the thermal-annealing procedure and the magnetic characterization of the as-grown nanowires are available in the Supporting Information.

Supporting Information File 1

Annealing procedure and hysteresis loops of the as-grown C–Ni nanowires.
[http://www.beilstein-journals.org/bjnano/content/supplementary/2190-4286-3-95-S1.pdf]

Acknowledgements

References

1. Piraux, L.; George, J. M.; Despres, J. F.; Leroy, C.; Ferain, E.; Legras, R.; Ounadjela, K.; Fert, A. *Appl. Phys. Lett.* **1994**, *65*, 2484. doi:10.1063/1.112672
2. Dubois, S.; Marchal, C.; Beuken, J. M.; Piraux, L.; Duvail, J. L.; Fert, A.; George, J. M.; Maurice, J. L. *Appl. Phys. Lett.* **1997**, *70*, 396. doi:10.1063/1.118385
3. Piraux, L.; Dubois, S.; Duvail, J. L.; Ounadjela, K.; Fert, A. *J. Magn. Magn. Mater.* **1997**, *175*, 127. doi:10.1016/S0304-8853(97)00157-1
4. Ferré, R.; Ounadjela, K.; George, J. M.; Piraux, L.; Dubois, S. *Phys. Rev. B* **1997**, *56*, 14066. doi:10.1103/PhysRevB.56.14066
5. Zheng, M.; Menon, L.; Zeng, H.; Liu, Y.; Bandyopadhyay, S.; Kirby, R. D.; Sellmyer, D. J. *Phys. Rev. B* **2000**, *62*, 12282. doi:10.1103/PhysRevB.62.12282
6. Whitney, T. M.; Searson, P. C.; Jiang, J. S.; Chien, C. L. *Science* **1993**, *261*, 1316. doi:10.1126/science.261.5126.1316
7. Lorcy, J. M.; Massuyeau, F.; Moreau, P.; Chauvet, O.; Faulques, E.; Wéry, J.; Duvail, J. L. *Nanotechnology* **2009**, *20*, 405601. doi:10.1088/0957-4484/20/40/405601
8. Darques, M.; De la Torre Medina, J.; Piraux, L.; Cagnon, L.; Huynen, I. *Nanotechnology* **2010**, *21*, 145208. doi:10.1088/0957-4484/21/14/145208
9. Fung, A. O.; Kapadia, V.; Pierstorff, E.; Ho, D.; Chen, Y. *J. Phys. Chem. C* **2008**, *112*, 15085. doi:10.1021/jp806187r
10. Gao, N.; Wang, H.; Yang, E.-H. *Nanotechnology* **2010**, *21*, 105107. doi:10.1088/0957-4484/21/10/105107
11. Nautiyal, T.; Rho, T. H.; Kim, K. S. *Phys. Rev. B* **2004**, *69*, 193404. doi:10.1103/PhysRevB.69.193404
12. Thurn-Albrecht, T.; Schotter, J.; Kästle, G. A.; Emley, N.; Shibauchi, T.; Krusin-Elbaum, L.; Guarini, K.; Black, C. T.; Tuominen, M. T.; Russell, T. P. *Science* **2000**, *290*, 2126. doi:10.1126/science.290.5499.2126
13. Geim, A. K.; Novoselov, K. S. *Nat. Mater.* **2007**, *6*, 183. doi:10.1038/nmat1849
14. Geim, A. K. *Science* **2009**, *324*, 1530. doi:10.1126/science.1158877

15. Guttmann, P.; Bittencourt, C.; Rehbein, S.; Umek, P.; Ke, X.; Van Tandeloo, G.; Ewels, C. P.; Schneider, G. *Nat. Photonics* **2012,** *6,* 25. doi:10.1038/nphoton.2011.268

16. Wagner, P.; Ewels, C. P.; Ivanovskaya, V. V.; Briddon, P. R.; Pateau, A.; Humbert, B. *Phys. Rev. B* **2011,** *84,* 134110. doi:10.1103/PhysRevB.84.134110

17. Wang, X.; Zhi, L.; Mullen, K. *Nano Lett.* **2008,** *8,* 323. doi:10.1021/nl072838r

18. Stoller, M. D.; Park, S.; Zhu, Y.; An, J.; Ruoff, R. S. *Nano Lett.* **2008,** *8,* 3498. doi:10.1021/nl802558y

19. Lin, Y.-M.; Jenkins, K. A.; Valdes-Garcia, A.; Small, J. P.; Farmer, D. B.; Avouris, P. *Nano Lett.* **2009,** *9,* 422. doi:10.1021/nl803316h

20. Camilli, L.; Scarselli, M.; Del Gobbo, S.; Castrucci, P.; Lamastra, F. R.; Nanni, F.; Gautron, E.; Lefrant, S.; D'Orazio, F.; Lucari, F.; De Crescenzi, M. *Carbon* **2012,** *50,* 718. doi:10.1016/j.carbon.2011.09.034

21. Zeeshan, M. A.; Shou, K.; Pané, S.; Pellicer, E.; Sort, J.; Sivaraman, K. M.; Baró, M. D.; Nelson, B. J. *Nanotechnology* **2011,** *22,* 275713. doi:10.1088/0957-4484/22/27/275713

22. Wang, R.; Hao, Y.; Wang, Z.; Gong, H.; Thong, J. T. L. *Nano Lett.* **2010,** *10,* 4844. doi:10.1021/nl102445x

23. Gao, X. P.; Zhang, Y.; Chen, X.; Pan, G. L.; Yan, J.; Wu, F.; Yuan, H. T.; Song, D. Y. *Carbon* **2004,** *42,* 47. doi:10.1016/j.carbon.2003.09.015

24. Topsakal, M.; Şahin, H.; Ciraci, S. *Phys. Rev. B* **2012,** *85,* 155445. doi:10.1103/PhysRevB.85.155445

25. El Mel, A. A.; Gautron, E.; Angleraud, B.; Granier, A.; Xu, W.; Choi, C. H.; Briston, B. J.; Inkson, B. J.; Tessier, P. Y. *Nanotechnology* **2012,** *23,* 275603. doi:10.1088/0957-4484/23/27/275603

26. El Mel, A. A.; Bouts, N.; Grigore, E.; Gautron, E.; Granier, A.; Angleraud, B.; Tessier, P. Y. *J. Appl. Phys.* **2012,** *111,* 114309. doi:10.1063/1.4728164

27. Choi, C.-H.; Kim, C.-J. *Nanotechnology* **2006,** *17,* 5326. doi:10.1088/0957-4484/17/21/007

28. Hamaguchi, S.; Rossnagel, S. M. *J. Vac. Sci. Technol., B* **1995,** *13,* 183. doi:10.1116/1.587995

29. El Mel, A. A.; Gautron, E.; Angleraud, B.; Granier, A.; Tessier, P. Y. *Carbon* **2011,** *49,* 4595. doi:10.1016/j.carbon.2011.06.001

30. Allouche, H.; Monthioux, M. *Carbon* **2005,** *43,* 1265. doi:10.1016/j.carbon.2004.12.023

31. Baraton, L.; He, Z.; Lee, C. S.; Maurice, J.-L.; Cojocaru, C. S.; Gourgues-Lorenzon, A.-F.; Lee, Y. H.; Pribat, D. *Nanotechnology* **2011,** *22,* 085601. doi:10.1088/0957-4484/22/8/085601

32. Lander, J. J.; Kern, H. E.; Beach, A. L. *J. Appl. Phys.* **1952,** *23,* 1305. doi:10.1063/1.1702064

33. Zheng, M.; Takei, K.; Hsia, B.; Fang, H.; Zhang, X.; Ferralis, N.; Ko, H.; Chueh, Y.-L.; Zhang, Y.; Maboudian, R.; Javey, A. *Appl. Phys. Lett.* **2010,** *96,* 063110. doi:10.1063/1.3318263

34. Garaj, S.; Hubbard, W.; Golovchenko, J. A. *Appl. Phys. Lett.* **2010,** *97,* 183103. doi:10.1063/1.3507287

35. Encinas-Oropesa, A.; Demand, M.; Piraux, L.; Huynen, I.; Ebels, U. *Phys. Rev. B* **2001,** *63,* 104415. doi:10.1103/PhysRevB.63.104415

36. Encinas-Oropesa, A.; Demand, M.; Piraux, L.; Ebels, U.; Huynen, I. *J. Appl. Phys.* **2001,** *89,* 6704. doi:10.1063/1.1362638

37. Demand, M.; Encinas-Oropesa, A.; Kenane, S.; Ebels, U.; Huynen, I.; Piraux, L. *J. Magn. Magn. Mater.* **2002,** *249,* 228. doi:10.1016/S0304-8853(02)00535-8

38. Martín, J. I.; Nogués, J.; Liu, K.; Vincent, J. L.; Schuller, I. K. *J. Magn. Magn. Mater.* **2003,** *256,* 449. doi:10.1016/S0304-8853(02)00898-3

39. Adeyeye, A. O.; Bland, J. A. C.; Daboo, C.; Lee, J.; Ebels, U.; Ahmed, H. *J. Appl. Phys.* **1996,** *79,* 6120. doi:10.1063/1.361893

40. Blundell, S. J.; Shearwood, C.; Gester, M.; Baird, M. J.; Bland, J. A. C.; Ahmed, H. *J. Magn. Magn. Mater.* **1994,** *135,* L17. doi:10.1016/0304-8853(94)90168-6

41. Adeyeye, A. O.; Bland, J. A. C.; Daboo, C.; Hasko, D. G.; Ahmed, H. *J. Appl. Phys.* **1997,** *82,* 469. doi:10.1063/1.365840

42. Adeyeye, A. O.; Bland, J. A. C.; Daboo, C.; Hasko, D. G. *Phys. Rev. B* **1997,** *56,* 3265. doi:10.1103/PhysRevB.56.3265

43. Adeyeye, A. O.; Bland, J. A. C.; Daboo, C. *J. Magn. Magn. Mater.* **1998,** *188,* L1. doi:10.1016/S0304-8853(98)00178-4

44. Schabes, M. E. *J. Magn. Magn. Mater.* **1991,** *95,* 249. doi:10.1016/0304-8853(91)90225-Y

License and Terms

Beilstein Journal
of Nanotechnology

Sub-10 nm colloidal lithography for circuit-integrated spin-photo-electronic devices

Adrian Iovan, Marco Fischer, Roberto Lo Conte and Vladislav Korenivski[*]

Full Research Paper

Open Access

Address:
Nanostructure Physics, Royal Institute of Technology, 10691 Stockholm, Sweden

Email:
Vladislav Korenivski[*] - vk@kth.se

* Corresponding author

Abstract

Patterning of materials at sub-10 nm dimensions is at the forefront of nanotechnology and employs techniques of various complexity, efficiency, areal scale, and cost. Colloid-based patterning is known to be capable of producing individual sub-10 nm objects. However, ordered, large-area nano-arrays, fully integrated into photonic or electronic devices have remained a challenging task. In this work, we extend the practice of colloidal lithography to producing large-area sub-10 nm point-contact arrays and demonstrate their circuit integration into spin-photo-electronic devices. The reported nanofabrication method should have broad application areas in nanotechnology as it allows ballistic-injection devices, even for metallic materials with relatively short characteristic relaxation lengths.

Introduction

Colloidal lithography [1] is a method to reproduce patterns in a variety of natural systems and is used more and more as an efficient fabrication tool in bio-, opto-, and nanotechnology. Nanoparticles in the colloid are made to form a mask on a given material surface, which can then be transferred by etching into nanostructures of various sizes, shapes, and patterns [2,3]. Such nanostructures can be used in biology for detecting proteins [4] and DNA [5,6], and for producing artificial crystals in photonics [7,8] and gigahertz oscillators in spin-electronics [9-14]. Scaling of colloidal patterning down to 10 nm and below, dimensions comparable or smaller than the main relaxation lengths in the relevant materials, including metals, is expected to enable a variety of new ballistic transport and photonic devices, such as spin-flip terahertz lasers [15]. In this work we extend the practice of colloidal lithography to produce large-area, near-ballistic-injection, sub-10 nm point-contact arrays and demonstrate their integration into spin-photo-electronic devices.

Electron-beam and focused-ion-beam techniques are typically limited to feature sizes of tens of nanometres, if the features are to be well defined, and are rather inefficient for large-area nanopatterning since both methods employ series point-by-point pattern transfer. The two promising techniques of nano-imprint lithography [16,17] and extreme-ultraviolet interference lithography [18] do indeed open sub-10 nm nanostructures for exploration. The instrumentation required, however, can in many cases be of great complexity and cost. Recently, membranes of nano-porous anodic aluminium oxide [19] were shown to scale to sub-10 nm dimensions and potentially compete with the above advanced lithographic techniques at this scale. Another potential alternative for sub-10 nm patterning is colloidal lithography, which is very attractive at larger dimensions due to its ease of use and low cost. Colloid-based patterning is known to be capable of producing individual sub-10 nm objects. However, ordered large-area nano-arrays fully integrated into photonic or electronic devices have not been demonstrated by using colloidal lithography. In this work we use a self-assembled monolayer of polystyrene nanoparticles, reduced in size by an isotropic etching process [20], which we scale to sub-10 nm feature sizes with large-area coverage in a well-defined hexagonal lattice and full integration for electrical circuit biasing and read out. We demonstrate the fabrication technique using spin-torque and spin-flip photoemission material combinations, considered promising for gigahertz oscillators and terahertz lasers.

Results and Discussion
Self-assembled monolayer of nanoparticles

The most widely used colloidal lithography medium is polystyrene nanoparticles in aqueous solution. Such colloidal solutions are commercially available with a variety of concentrations and particle sizes [21]. We used a range of diameters (down to 40 nm) and found the most consistent results in terms of self-assembly for 200 nm diameter and 2% particle concentration. Different methods of forming a monolayer of colloidal particles on a surface exist [22]. We found the spinning of the polystyrene colloidal water solution to yield good results. In calibrating the speed and duration of the spinning we aimed at forming the largest-area continuous monolayer possible. Thus, spinning in three stages, 500 rpm for 10 s, 1000 rpm for 30 s, and 2000 rpm for 10 s, facilitated self-assembly and yielded continuous nanoparticle monolayers of hundreds of micrometres in area (see Experimental for details). This was sufficient for our purposes to demonstrate a wide range of integrated device sizes.

Figure 1a and b show the tapping-mode atomic force microscopy (AFM) images of a typical monolayer, with the particle diameter (and the interparticle distance) of 200 nm. The
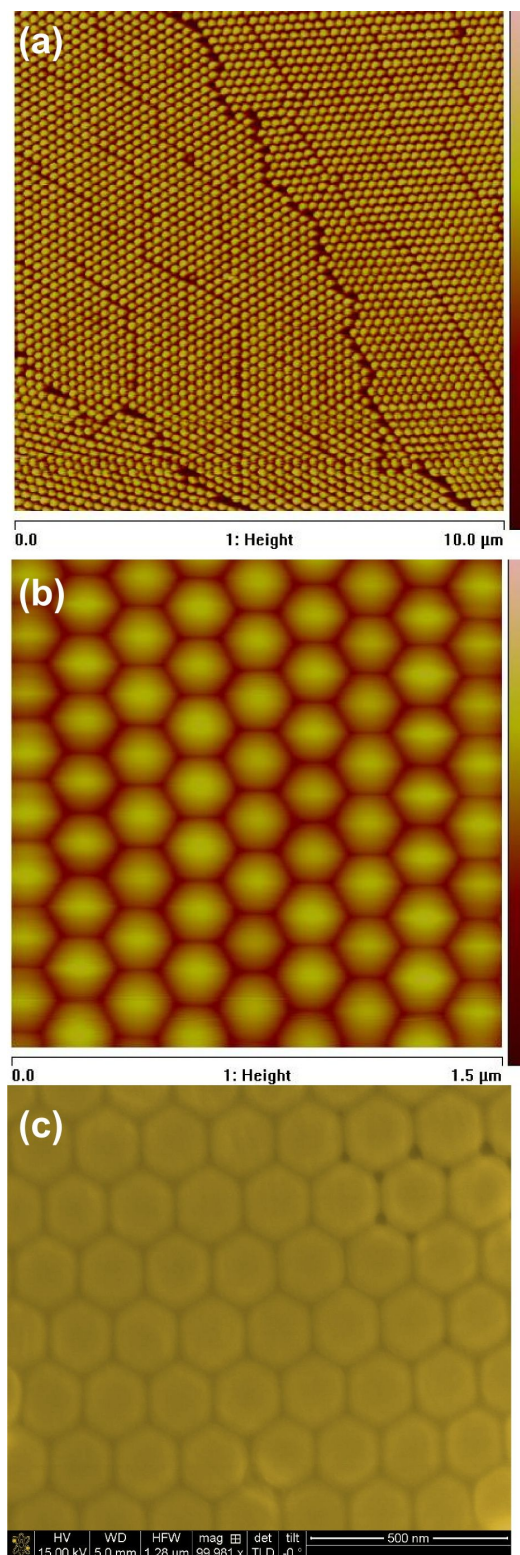
Figure 1: Tapping-mode atomic force microscopy images of a typical monolayer, with the particle diameter (and the inter-particle distance) of 200 nm on (a) a large scale and (b) a small scale. Scanning electron microscopy image of the sample (c) shows that the nanoparticle array has a nearly perfect close-packed hexagonal lattice.

monolayer film is of good quality, with only minor defects on the large scale (Figure 1a). On the small scale (Figure 1b) the lattice is clearly hexagonal. The scanning electron microscopy (SEM) image of the sample in Figure 1c shows that the nanoparticle array has a nearly perfect close-packed hexagonal lattice. The dispersion in the particle size at 200 nm diameter is small (approximately 1%), which favours the translation of the hexagonal pattern over large areas, i.e., hundreds of microns in the case of our optimized self-assembly process.

Downscaling to sub-10 nm

Our process of down scaling the particles of the polystyrene monolayer to the 10-nm range consists of four main steps, illustrated in Figure 2. Once the monolayer is formed (Figure 2a), reactive oxygen plasma is used to reduce the size of the particles (Figure 2b). When the desired particle diameter is reached, a reinforcing layer of aluminium is deposited, as shown in Figure 2c, which in the later process stages acts as a hard mask. A lift-off of the particles by etching completes the fabrication of the nanomask, as illustrated in Figure 2d. The very sensitive process step of the downscaling of the particles is achieved by reactive plasma etching, which must be done in a very clean chamber [23] in order to have a uniform reduction in the particle size across the large-area array. The final particle diameter is found to be a smooth function of the etching time, so the feature size of the nanomask can be controlled rather precisely. The typical etching power used is relatively low (50 W) to avoid potential disruptive etching at higher power. The key process detail, that we found to be critical for achieving sub-10 nm resolution, is a superimposed inductively coupled plasma (ICP) of relatively high power (250 W), which increases

the ionization in the chamber, translating into a more isotropic reduction in the particle size. A previous study of isotropic etching for nanosizing of polystyrene particles has shown the high capability of colloidal lithography [20]. According to this study the sample temperature has a strong influence on the etching process and can be critical for the uniformity of the etching. In our process we keep the sample temperature constant at near room temperature (30 °C) using a liquid-nitrogen cooling line. The polystyrene particles remain nearly spherical during the process, even as their size is reduced by more than an order of magnitude. The oxygen pressure was found to be optimum at 40 mTorr.

A typical monolayer after the etching procedure is shown in Figure 3, imaged by AFM for etching quality, surface topography, and particle size. The height of the particles is measured accurately, but not the diameter, since the convolution of a small particle and the tip produces a width distortion. Keeping all the process parameters constant and varying only the ICP etching time, we reproduce the general result of the previous studies [2,20] of a gradual reduction in the particle size. In our case, the particles remain well attached to the substrate and form a well-defined hcp pattern down to the smallest dimensions of 10–15 nm, as discussed below.

Figure 3a–c, show the particle monolayer after etching for 165, 180, and 195 seconds, respectively. The key advance made in this work, compared to the results on colloidal lithography reported to date, is that our modified process scales to sub-10 nm dimensions. For example, for the etching time of 2 min 45 s (Figure 3a) the particle diameter is reduced to
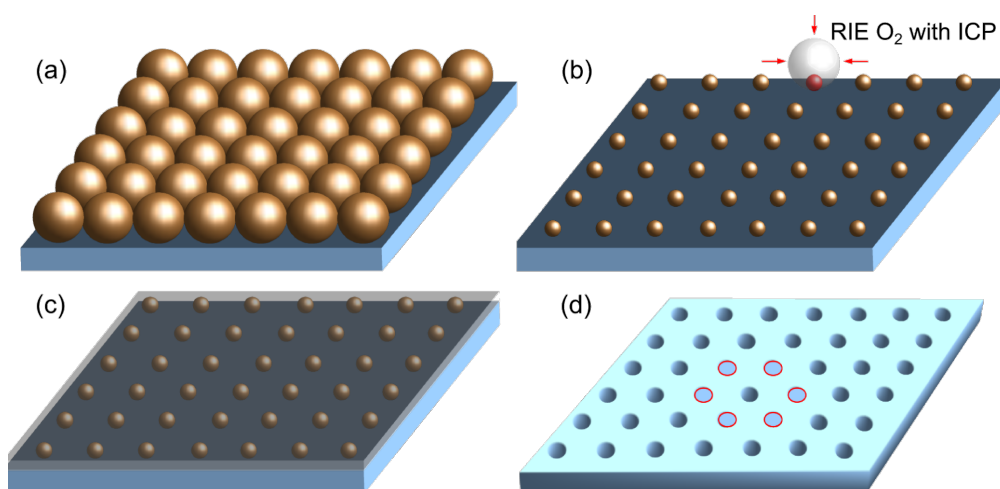
Figure 2: Illustration of the four steps in down-scaling of the particles of a polystyrene monolayer to the 10-nm range, which is to later serve as a nano-array mask. (a) Forming a self-assembled hexagonal-close-packed monolayer. (b) Reactive oxygen plasma with ICP is used to reduce the size of the particles. (c) A reinforcing layer of aluminum is deposited to serve as a hard mask. (d) A lift-off of the particles by etching completes the fabrication of the nanomask.
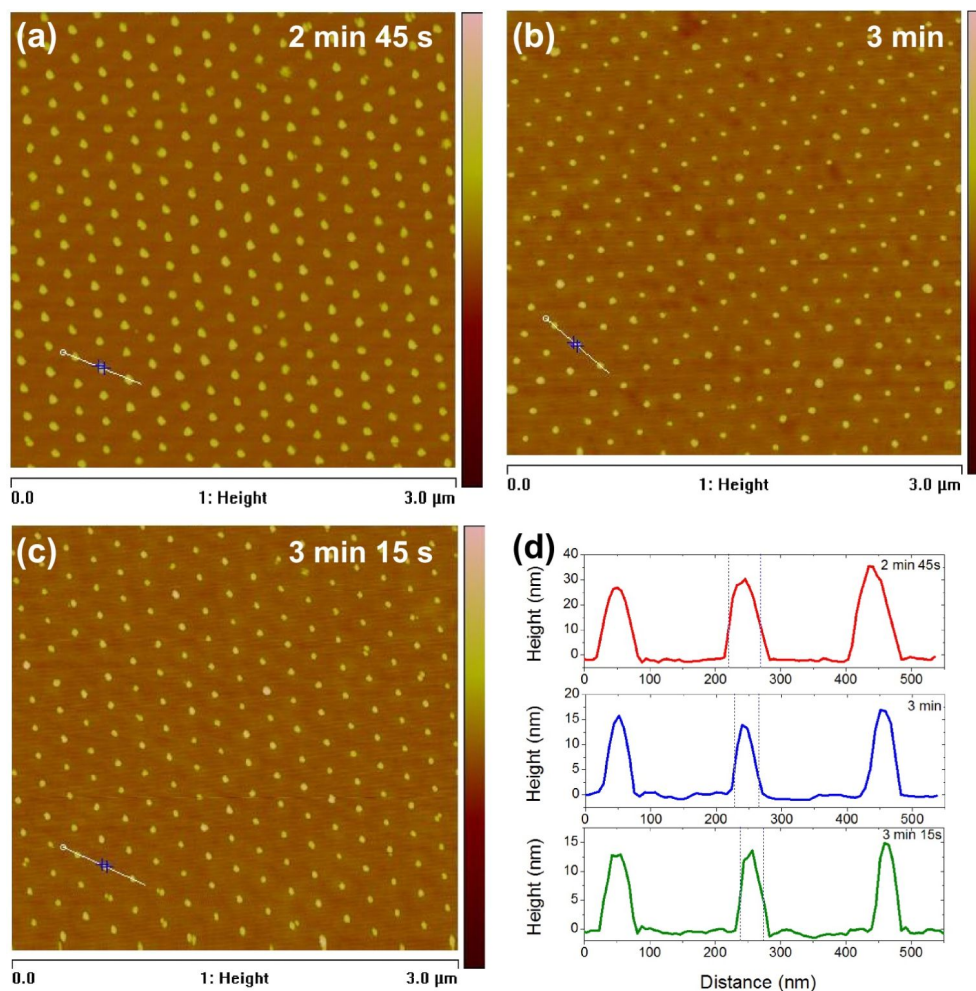
Figure 3: Polystyrene nanoparticles monolayer after plasma-ICP etching for (a) 165, (b) 180, and (c) 195 seconds. (d) AFM height profiles of the three samples shown in (a–c): raw data, without deconvolution.

10–15 nm (measured by AFM with particle–tip deconvolution). For 3 min etching time the average diameter is below 10 nm (Figure 3b). Etching for 3 min 15 s reduces the average size further but induces some perturbations. Already at 3 min 30 s etching time the monolayer is significantly over-etched and the pattern is partly removed. The true size of the particles can be estimated by using AFM traces, such as those shown in Figure 3d. The size of the particles here is smaller than the actual curvature of the AFM tip, determined from scanning calibration samples to be approximately 50 nm. Therefore, a deconvolution procedure was used to obtain the particle sizes stated above, which compare well with those obtained by SEM (see below). The AFM height is a more direct measurement and shows approximately 30 nm for 2 min 45 s and 15 nm for 3 min etching time. Figure 3 thus illustrates the fine control of the particle size at ≈10 nm by varying the plasma etching time.

The technological viability of the obtained polystyrene nanoparticle array depends on the ability to transfer it into a reliable mask to be used in subsequent nanodevice integration. The most straightforward approach, used widely in the literature for patterns of larger particle size, would be to directly etch the underlying substrate (e.g., SiO_2, Si, or Au) using the particle array as the mask. Our extensive tests showed, however, that the particle-mask itself is significantly modified during this process, which makes the pattern transfer at the desired 10 nm diameter range essentially impossible. We therefore developed an additional lift-off process step to reinforce the mask. It includes a deposition by e-beam evaporation of an Al metal layer onto the etched particle array, with a subsequent lift-off step to remove the polystyrene particles, and yields the hard mask illustrated in Figure 2d. This transferred the particle pattern into a hole mask of Al, with slightly larger particle sizes, 15–30 nm, rather than the smallest particles we could

achieve (≈10 nm). The thickness of the Al reinforcing layer (e.g., 15 nm) was selected to be less than the particle size used, such that the subsequent oxygen-RIE step could reach and remove polystyrene through the thinned Al at the sides of the particles. It was found that the Al hard mask effectively reduced the feature size, possibly due to some shadow-filling and/or particle-shape modification during Al deposition. We found this mask-transfer process to reliably yield hole-masks in the ≈10 nm range, as verified by SEM, AFM, and transport data.

A successful and stable lift-off process at these small length scales was found to be reactive ion etching (RIE) with oxygen, in which the polystyrene particles are first etched predominantly from the sides, where the Al film is much thinner due to the shadowing effect of the e-beam coating of the polystyrene spheres. During this RIE etching step the Al film surface oxidizes and forms a hard mask for subsequent ion milling.

After a 5 min Ar-plasma etch to remove surface residue, 7 min long ion milling etches through the 10 nm thick Au layer and slightly into the SiO_2 substrate, thus transferring the hexagonal pattern of sub-10 nm polystyrene particles into sub-10 nm pattern of holes in Au on SiO_2. The Al-oxide layer acts as the hard mask in this process. The Au under-layer for the polystyrene-particle monolayer was used in the process from the beginning, but was later found to be not critical for the process, and similar results were obtained without this layer (between SiO_2 and Al).

Figure 4 shows SEM images of a typical nanohole array mask. Long-range order is maintained over the micrometre range, as shown in Figure 4a and b. The process was repeated many times and showed good reproducibility. The average interdot distance is 200 nm, corresponding to the original particle diameter (Figure 4c and d) and the average hole size reaches down to the sub-10 nm range. The SEM data is well calibrated and confirms
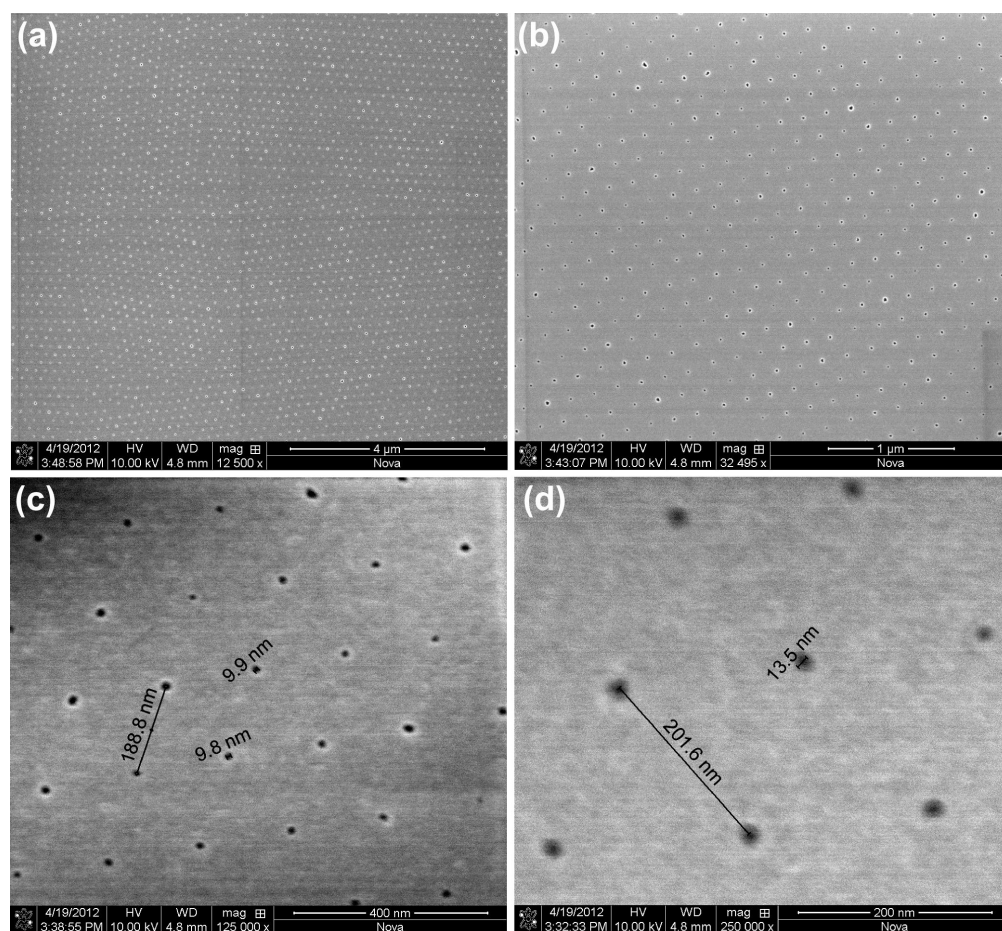
Figure 4: SEM images of a typical colloidal-monolayer mask, shown on four scales in (a–d). The average interdot distance is 200 nm (c,d), corresponding to the original polystyrene particle diameter. The average dot size is variable by adjustment of the ICP etching time, and reaches down the sub-10 nm range (c). (d) Shows a mask close-up with a nearly perfect hexagonal-close-packed pattern, with a lattice constant of 200 nm and a hole diameter of 13 nm. (a–d) correspond to different sections of the same mask.

the deconvoluted AFM data discussed above as regards the morphology of the array and the size of the particles, throughout the process.

Device integration

Having developed a reliable process for producing nano-dot array masks scalable to sub-10 nm dimensions, we next demonstrate their integration into advanced spin-photo-electronic devices, such as new types of nano-oscillators [9-14] and the newly proposed lasers [15]. The 1–10 nm scale is particularly interesting as it enables devices based on nonequilibrium injection, even for metals, due to the single-dot size being comparable or smaller than the characteristic relaxation length scales in the material. Fabricating and integrating sub-10 nm dot arrays into circuit-driven devices is a nontrivial task for any patterning technique (see Introduction) and, to our knowledge, has not been demonstrated to date.

For the spin-laser device of [15], for example, the bottom electrode must be thick to serve as an efficient electron and phonon bath under high-current injection. We take that into account in the design and start the structure with a sputter-deposited trilayer of $Al(180$ nm$)/SiO_2(15$ nm$)/Au(10$ nm$)$ onto a Si/ $SiO_2(500$ nm$)$ substrate. The bottom electrode, later to serve as one side of a 10–100 μm range optical resonator, is patterned by using standard optical lithography (see Experimental for details).

The sample is then cleaned by oxygen RIE for 2 min, which makes the surface hydrophilic, and covered with 2–3 drops of the colloid solution forming the polystyrene particle monolayer during the above spinning sequence. The particles are scaled down using the multistep process detailed above to form a nanohole array mask on the bottom electrode surface. Plasma RIE with CF_4 is used for 2 min for making the contact through the 15 nm thick SiO_2 with the 180 nm thick bottom electrode of Al. The etching time for 15 nm of SiO_2 is 1 min. Using the chemical selectivity of CF_4 to etch SiO_2, we etch two times longer (2 min) in order to form a good undercut in SiO_2, which is important for the following deposition steps.

Magnetron sputtering was used for deposition of the active point-contact region. The material combination was selected to represent the spin-injection laser device [15,24,25], and consisted of a spin-majority/minority ferromagnetic bi-layer $Fe_{0.7}Cr_{0.3}(10$ nm$)/Fe(15$ nm$)$ [25] capped with Cu(10 nm), for spin-population-inversion injection. Even though the deposition technique is not highly directional, we find that the angle of incidence through the 10 nm openings in the mask (angle between the normal to the sample surface and the normal to the sputtering target surface) is an important parameter deter-

mining the size of the resulting point contacts: the closer to normal incidence the closer the resulting contact size to the mask feature size (normal incidence), and the larger the angle of incidence the deeper below 10 nm the nanocontacts are due to the double shadowing effect illustrated in Figure 5a (direct mask shadowing and shadowing from material build up on the mask edge). We note that the SiO_2 under the openings in the Al mask is significantly undercut (approximately 30 nm diameter) and therefore is no obstacle to material deposition into the nanopores. We additionally note that the Al layer, originally ≈15 nm thick, is thinned by the Ar-etching steps to ≈10 nm. Thus, the effective nanopores are an array of ≈10 nm holes in ≈10 nm thin Al.

We used two angles of deposition, near-normal incidence and approximately 45° incidence, and estimate that the average size of the nanocontacts obtained for the angled deposition was approximately 5 nm. Finally, surface protection for subsequent processing steps was done with two layers of Cr(5 nm)/ Au(10 nm) deposited by e-beam evaporation. The key elements of the point-contact structure obtained are illustrated in the bottom panel of Figure 5a. The final integration step is photolithographic patterning of the top electrode, in the case of the demonstrator devices below in the shape of a photon resonator for IR–terahertz photons (Figure 5a, top panel; see Experimental for process details).

Device examples

The focus of this paper is the new method of integrating sub-10 nm structures into nanodevices. We briefly demonstrate the method using two physical effects found in magnetic nanocontacts, namely, spin-magnon and spin-photon relaxation. The method is not limited to photonics or spintronics, however, and should have a wide application range in various types of physical systems.

We first estimate the expected circuit characteristics of our typical integrated point-contact array. For individual 5–10 nm metallic point contacts the resistance is essentially given by the geometry (the so-called Sharvin resistance [27]) and is approximately 10–20 Ω. For an ideal 10×10 μm^2 point-contact array with a 200 nm intercontact spacing, the number of contacts is 2500. Therefore, the expected resistance of the array is on the order of 10 mΩ. A nonideal array would have fewer contacts and therefore higher resistance. Overetching the polystyrene monolayer and sharp-angle deposition of the core material, as discussed in detail above, can result in only a fraction of the array actually being connected and the individual nanocontact size being substantially smaller than the mask feature size of 10 nm, as measured by SEM and AFM. In this limit we are able to reach the array resistance range of the order of 1 Ω.
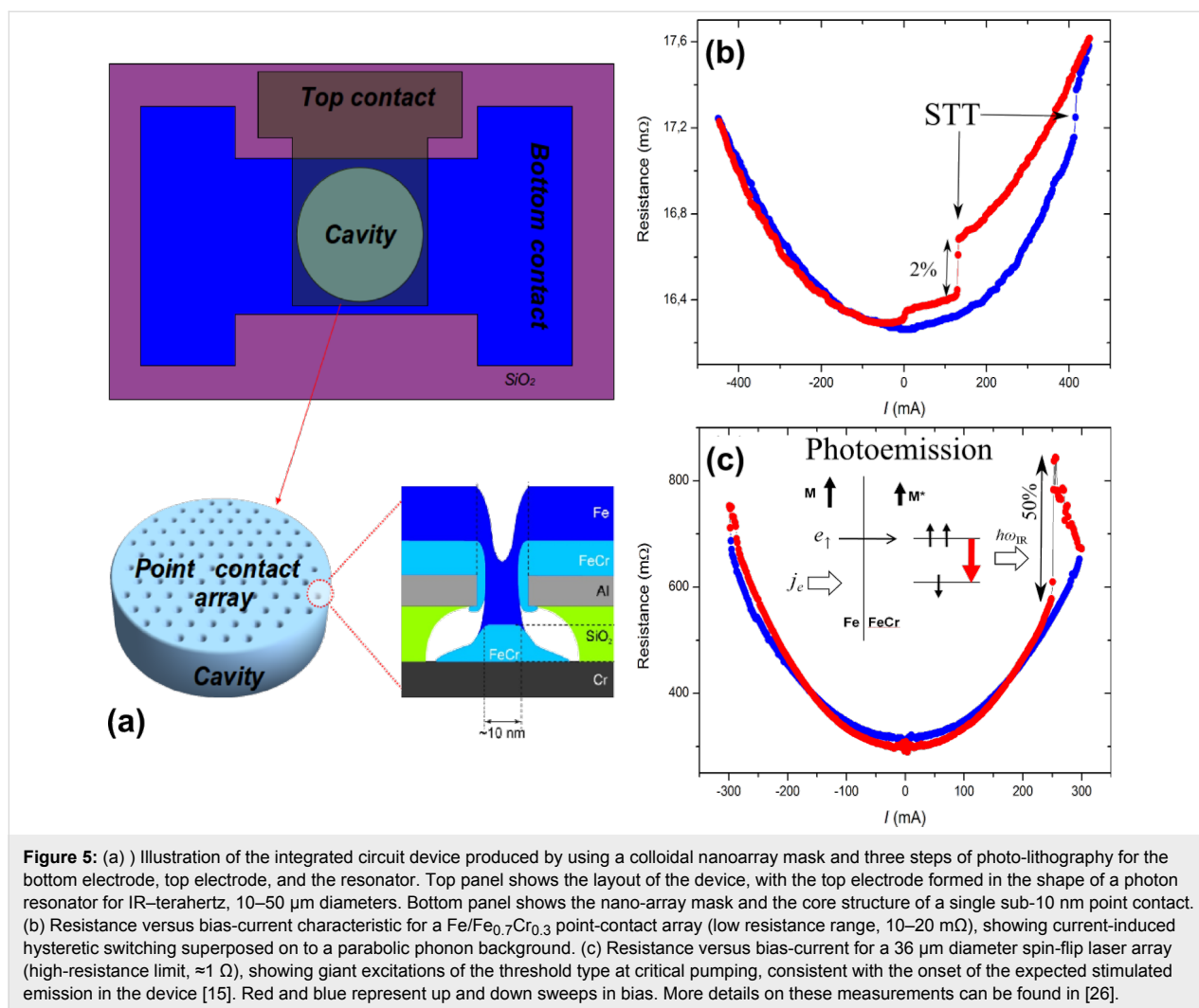
Figure 5: (a)) Illustration of the integrated circuit device produced by using a colloidal nanoarray mask and three steps of photo-lithography for the bottom electrode, top electrode, and the resonator. Top panel shows the layout of the device, with the top electrode formed in the shape of a photon resonator for IR–terahertz, 10–50 µm diameters. Bottom panel shows the nano-array mask and the core structure of a single sub-10 nm point contact. (b) Resistance versus bias-current characteristic for a Fe/Fe$_{0.7}$Cr$_{0.3}$ point-contact array (low resistance range, 10–20 mΩ), showing current-induced hysteretic switching superposed on to a parabolic phonon background. (c) Resistance versus bias-current for a 36 µm diameter spin-flip laser array (high-resistance limit, ≈1 Ω), showing giant excitations of the threshold type at critical pumping, consistent with the onset of the expected stimulated emission in the device [15]. Red and blue represent up and down sweeps in bias. More details on these measurements can be found in [26].

We have prepared test samples with the point-contact core made of a single nonmagnetic metallic element (Cu with a Cr under-layer), where no effects due to spin-flip relaxation are expected, only phonon relaxation (heat). The typical array resistance is measured to be 10–20 mΩ. The current–voltage characteristic is smooth and approximately parabolic, typical of the expected phonon background. Thus, these test data agreed with the expected behaviour and showed that the fabricated nanocontact arrays are of high quality.

We next demonstrate a point-contact array with the contacts having a magnetic core. More specifically, the core material is a majority/minority ferromagnetic bi-layer of Fe/Fe$_{0.7}$Cr$_{0.3}$ [28], where due to the opposite spin-polarizations of the two materials at the interface a strong spin accumulation is expected. Figure 5b is a resistance versus bias-current characteristic for the device and shows a clear current-induced hysteretic switching, typical of magnetic point contacts [29,30], superposed on the phonon background. The mechanism behind this is

the formation of atomic/nanoscale domain walls in the nanoconstriction under the spin-transfer torque (STT) from the spin accumulation at the Fe/FeCr interface. The switching in both directions occurs at one bias polarity, which is characteristic of the STT effect. The change in resistance is approximately 2%, typical of domain wall magnetoresistance. The array resistance is on the order of 10 mΩ, consistent with the expected range for a nearly fully connected sub-10 nm point-contact array. Thus, we demonstrate the STT effect in the fabricated nanodevices. The extremely regular array layout with the extremely small contact size, as well as the relative ease of the colloidal monolayer process, should make this structure very promising for gigahertz nano-oscillators [9-14]. Optimization would involve substituting improved spin-valve materials for the core region and, if needed, tuning the array lattice spacing to achieve better interference of spin-wave modes.

Another interesting application of the spin-majority/minority Fe/Fe$_{0.7}$Cr$_{0.3}$ contact-core material used above is the spin-flip

photon-emission effect [15,24,25], which requires spin-polarized and energetically nonequilibrium injection and, therefore, near-ballistic point-contact arrays. The energetics of the process is illustrated in the inset to Figure 5c, where the spin-majority carriers from the Fe injector create spin-population inversion in the spin-minority FeCr, relaxing through emission of terahertz or infrared (IR) photons. To achieve this we have performed fabrication at the limit of the etching and angle-deposition parameters discussed above, for deep sub-10 nm point-contact size and a smaller operating fraction of the array, so that the injection voltage per contact is greater than the exchange splitting in the ferromagnetic point contact core (10–100 mV, see [24,25] for more details). Such high-bias, high-density, spin-polarized injection produces large nonequilibrium spin accumulation in the contact core, which allows spin-flip photon-emission transitions, vertical in the momentum of the electron. A photon emitted by a spin-flip process is contained within the resonator and enhanced by the high-dielectric constant, high-transparency SiO_2 oxide matrix [15]. The lifetime of the emitted photon is long due to the high transparency of the oxide, so the photon has a high probability to stimulate another spin-flip transition. At a critical bias, a cascading avalanche of stimulated spin-flip photon-emitting transitions, i.e., a laser action, takes place, generating high-density electromagnetic modes in the resonator. This critical photon-emission threshold must manifest itself as threshold-type changes in the current–voltage characteristics of our fully enclosed optical resonator. Such threshold-type excitations, of giant magnitude, are indeed observed in the device resistance (conductance changes of a factor of 2), as shown in Figure 5c. This demonstration opens the way to explore a new type of IR–terahertz lasers based on stimulated spin-flip photon emission [26].

Conclusion

Colloidal patterning in the form of large-area hexagonal-lattice arrays is demonstrated to scale down to sub-10 nm dimensions in the feature size. This is comparable or smaller than the key relaxation lengths in various materials including metals, which enables a wide range of new applications in nanotechnology. Large-area, near-ballistic-injection point-contact arrays are used to demonstrate integration of the developed nanofabrication technique into new types of spintronic and photonic devices.

Experimental

Self-assembled monolayer process sequence: The first step of the spinning sequence allowed the particles to gently segregate onto the substrate and, to a large extent already here, form a hexagonal pattern. The second step of spinning at a higher speed (rpm) prevented formation of additional layers of vertically stacked particles. The last step was used to remove the remaining solution, predominantly in the corners of the sample.

The spinning process was developed by using SiO_2 substrates, about 2×2 cm^2, covered with a 10 nm thick Au layer. Prior to spinning, the substrate was etched in plasma oxygen for two minutes in order to make the surface hydrophilic [31]. As an alternative route, we found that a good quality monolayer, with a well-defined long-range order, can be obtained if a small amount of Triton X surfactant [32] is added into the colloidal solution. However, the subsequent extensive tests showed that the use of Triton X is problematic for later processing during the device-integration steps. Traces of Triton remaining on the surface produce residue that prevents reliable integration. We therefore selected the route of forming large-area self-assembled monolayer arrays of nanoparticles by making the substrate hydrophilic with the help of RIE plasma oxygen. The equipment specifics are Oxford Plasmalab 100, with the capability for gases O_2, Ar, CF_4, CHF_3, SF_6, Cl_2.

Colloidal mask transfer: Oxygen plasma was tested for removal of the particles, without success. Chemical removal of polystyrene particles after down-scaling by using acetone and mechanical polishing also did not work. Another technique tested with only partial success was heating of the sample just below the melting point of polystyrene, where the dilatation coefficient makes the particles expand in volume significantly and thereby break open holes in the Al film. This is a promising technique; however, we found it difficult to control the size and shape of the resulting ≈10 nm holes opened by polystyrene exploding through the Al.

Optical lithography: A double-layer resist LOR7B(500 nm)/ S1813(1.5 μm) is spun onto the Au surface, thermally treated, mask exposed, developed, ion milled for 2 h, and lifted off in 1165 remover at 60 °C to form a 100 μm wide bottom electrode.

Optical lithography of the top electrode/resonator: The process is analogous to the one used for the bottom electrode, but employs a different photomask. The top electrode mask has different diameter disks and half-disks in the range of 10–50 μm. The pattern transfer is done by ion milling for 1 h. The etching time was calibrated by using surface profilometry such as to stop the etching at the Al bottom electrode. The sample was then capped with a 40 nm thick SiO_2 layer for insulation, rotating the sample holder during deposition. Finally, the resist was lifted off, and the last step of lithography was the use of negative resist and deposition of a 200 nm thick Al top electrode.

Transport measurements: The current–voltage (*I–V*) characteristics of the integrated devices were measured by the conventional four-point technique, with the device resistance defined

as $R(I) = V(I)/I$. For more details on the spin-transfer-torque measurements see [29,30]. For more details on stimulated spin-photo-emission (spin lasing) see [15,24-26].

Acknowledgements

References

1. Deckman, H. W.; Dunsmuir, J. H. *Appl. Phys. Lett.* **1982**, *41,* 377–379. doi:10.1063/1.93501
2. Haginoya, C.; Ishibashi, M.; Koike, K. *Appl. Phys. Lett.* **1997**, *71,* 2934–2936. doi:10.1063/1.120220
3. Gullapalli, S.; Wong, M. S. *Chem. Eng. Prog.* **2011**, *107,* 28–32.
4. Shi, H.; Tsai, W.-B.; Garrison, M. D.; Ferrari, S.; Ratner, B. D. *Nature* **1999**, *398,* 593–597. doi:10.1038/19267
5. Xie, P.; Xiong, Q.; Fang, Y.; Qing, Q.; Lieber, C. M. *Nat. Nanotechnol.* **2012**, *7,* 119–125. doi:10.1038/nnano.2011.217
6. Venkatesan, B. M.; Bashir, R. *Nat. Nanotechnol.* **2011**, *6,* 615–624. doi:10.1038/nnano.2011.129
7. Yu, X.; Zhang, H.; Oliverio, J. K.; Braun, P. V. *Nano Lett.* **2009**, *9,* 4424–4427. doi:10.1021/nl9027236
8. Barnes, W. L.; Dereux, A.; Ebbesen, T. W. *Nature* **2003**, *424,* 824–830. doi:10.1038/nature01937
9. Kiselev, S. I.; Sankey, J. C.; Krivorotov, I. N.; Emley, N. C.; Schoelkopf, R. J.; Buhrman, R. A.; Ralph, D. C. *Nature* **2003**, *425,* 380–383. doi:10.1038/nature01967
10. Hoefer, M. A.; Ablowitz, M. J.; Ilan, B.; Pufall, M. R.; Silva, T. J. *Phys. Rev. Lett.* **2005**, *95,* 267206. doi:10.1103/PhysRevLett.95.267206
11. Mancoff, F. B.; Rizzo, N. D.; Engel, B. N.; Tehrani, S. *Nature* **2005**, *437,* 393–395. doi:10.1038/nature04036
12. Houssameddine, D.; Ebels, U.; Delaët, B.; Rodmacq, B.; Firastrau, I.; Ponthenier, F.; Brunet, M.; Thirion, C.; Michel, J.-P.; Prejbeanu-Buda, L.; Cyrille, M.-C.; Redon, O.; Dieny, B. *Nat. Mater.* **2007**, *6,* 447–453. doi:10.1038/nmat1905
13. Ruotolo, A.; Cros, V.; Georges, B.; Dussaux, A.; Grollier, J.; Deranlot, C.; Guillemet, R.; Bouzehouane, K.; Fusil, S.; Fert, A. *Nat. Nanotechnol.* **2009**, *4,* 528–532. doi:10.1038/nnano.2009.143
14. Madami, M.; Bonetti, S.; Consolo, G.; Tacchi, S.; Carlotti, G.; Gubbiotti, G.; Mancoff, F. B.; Yar, M. A.; Åkerman, J. *Nat. Nanotechnol.* **2011**, *6,* 635–638. doi:10.1038/nnano.2011.140
15. Shekhter, R. I.; Shekhter, A. M.; Jonson, M.; Smotrova, E. I.; Nosich, A. I.; Korenivski, V. *Opt. Lett.* **2011**, *36,* 2381–2383. doi:10.1364/OL.36.002381
16. Chou, S. Y.; Krauss, P. R.; Zhang, W.; Guo, L.; Zhuang, L. J. *J. Vac. Sci. Technol., B: Microelectron. Process. Phenom.* **1997**, *15,* 2897–2904. doi:10.1116/1.589752
17. Wu, W.; Tong, W. M.; Bartman, J.; Chen, Y.; Walmsley, R.; Yu, Z.; Xia, Q.; Park, I.; Picciotto, C.; Gao, J.; Wang, S.-Y.; Morecroft, D.; Yang, J.; Berggren, K. K.; Williams, R. S. *Nano Lett.* **2008**, *8,* 3865–3869. doi:10.1021/nl802295n
18. Päivänranta, B.; Langner, A.; Kirk, E.; David, C.; Ekinci, Y. *Nanotechnology* **2011**, *22,* 375302. doi:10.1088/0957-4484/22/37/375302
19. Moyen, E.; Santinacci, L.; Masson, L.; Wulfhekel, W.; Hanbücken, M. *Adv. Mater.* **2012**, *24,* 5094–5098. doi:10.1002/adma.201200648
20. Plettl, A.; Enderle, F.; Saitner, M.; Manzke, A.; Pfahler, C.; Wiedemann, S.; Ziemann, P. *Adv. Funct. Mater.* **2009**, *19,* 3279–3284. doi:10.1002/adfm.200900907
21. Microparticles GmbH, Research and Development Laboratory, Volmerstr.9A, UTZ, Geb.3.5.1, D-12489 Berlin, http://www.microparticles.de/micropartengl.html
22. Yang, S.-M.; Jang, S. G.; Choi, D.-G.; Kim, S.; Yu, H. K. *Small* **2006**, *2,* 458–475. doi:10.1002/smll.200500390
23. Before each step of etching, the chamber was cleaned for 90 min at high power of 250 W with Cl_2, SF_6, Ar and O_2.
24. Kadigrobov, A. M.; Shekhter, R. I.; Kulinich, S. I.; Jonson, M.; Balkashin, O. P.; Fisun, V. V.; Naidyuk, Yu. G.; Yanson, I. K.; Andersson, S.; Korenivski, V. *New J. Phys.* **2011**, *13,* 023007. doi:10.1088/1367-2630/13/2/023007
25. Naidyuk, Yu. G.; Balkashin, O. P.; Fisun, V. V.; Yanson, I. K.; Kadigrobov, A.; Shekhter, R. I.; Jonson, M.; Neu, V.; Seifert, M.; Andersson, S.; Korenivski, V. *New J. Phys.* **2012**, *14,* 093021. doi:10.1088/1367-2630/14/9/093021
26. Korenivski, V.; Iovan, A.; Kadigobov, A.; Shekhter R. I. Giant excitations in near-ballistic majority/minority ferromagnetic point-contact arrays integrated into photon resonators: toward THz metal-based spin-flip lasers. 2012, arXiv:1208.0550v1 [cond-mat.mes-hall].
27. Sharvin, Y. V. *Sov. Phys. - JETP* **1965**, *21,* 655.
28. Vouille, C.; Barthélémy, A.; Mpondo, F. E.; Fert, A.; Schroeder, P. A.; Hsu, S. Y.; Reilly, A.; Loloee, R. *Phys. Rev. B* **1999**, *60,* 6710–6722. doi:10.1103/PhysRevB.60.6710
29. Chen, T. Y.; Li, Y.; Chien, C. L.; Stiles, M. D. *Phys. Rev. Lett.* **2004**, *93,* 026601. doi:10.1103/PhysRevLett.93.026601
30. Yanson, I. K.; Naidyuk, Yu. G.; Fisun, V. V.; Konovalenko, A.; Balkashin, O. P.; Triputen, L. Yu.; Korenivski, V. *Nano Lett.* **2007**, *7,* 927–931. doi:10.1021/nl0628192
31. Smith, T. *J. Colloid Interface Sci.* **1980**, *75,* 51–55. doi:10.1016/0021-9797(80)90348-3
32. Romero-Cano, M. S.; Martín-Rodríguez, A.; de las Nieves, F. J. *J. Colloid Interface Sci.* **2000**, *227,* 322–328. doi:10.1006/jcis.2000.6862

License and Terms

Diamond nanophotonics

Katja Beha[1], Helmut Fedder[*2], Marco Wolfer[3], Merle C. Becker[2],
Petr Siyushev[2], Mohammad Jamali[2], Anton Batalov[1], Christopher Hinz[1],
Jakob Hees[3], Lutz Kirste[3], Harald Obloh[3], Etienne Gheeraert[4],
Boris Naydenov[5], Ingmar Jakobi[2], Florian Dolde[2], Sébastien Pezzagna[6],
Daniel Twittchen[7], Matthew Markham[7], Daniel Dregely[8], Harald Giessen[8],
Jan Meijer[6], Fedor Jelezko[5], Christoph E. Nebel[3], Rudolf Bratschitsch[9],
Alfred Leitenstorfer[1] and Jörg Wrachtrup[2]

Full Research Paper

Address:
[1]Department of Physics and Center for Applied Photonics, Konstanz, Germany, [2]3. Physikalisches Institut and Scope Research Centre University of Stuttgart, Stuttgart, Germany, [3]Fraunhofer-Institut für Angewandte Festkörperphysik, Freiburg i. Br., Germany, [4]Institut Neel, CNRS and Université Joseph Fourier, Grenoble, France, [5]Institut für Quantenoptik, Universität Ulm, Ulm, Germany, [6]RUBION, Ruhr-Universität Bochum, Bochum, Germany, [7]Element Six Ltd, Ascot, United Kingdom, [8]4. Physikalisches Institut and Scope Research Centre, Stuttgart, Germany and [9]Institute of Physics, Chemnitz University of Technology, Chemnitz, Germany

Email:
Helmut Fedder[*] - helmut.fedder@gmail.com

* Corresponding author

Keywords:
CVD diamond doping; diamond; nanophotonics; NV center; plasmonic resonator; solid immersion lens

Abstract

We demonstrate the coupling of single color centers in diamond to plasmonic and dielectric photonic structures to realize novel nanophotonic devices. Nanometer spatial control in the creation of single color centers in diamond is achieved by implantation of nitrogen atoms through high-aspect-ratio channels in a mica mask. Enhanced broadband single-photon emission is demonstrated by coupling nitrogen–vacancy centers to plasmonic resonators, such as metallic nanoantennas. Improved photon-collection efficiency and directed emission is demonstrated by solid immersion lenses and micropillar cavities. Thereafter, the coupling of diamond nanocrystals to the guided modes of micropillar resonators is discussed along with experimental results. Finally, we present a gas-phase-doping approach to incorporate color centers based on nickel and tungsten, in situ into diamond using microwave-plasma-enhanced chemical vapor deposition. The fabrication of silicon–vacancy centers in nanodiamonds by microwave-plasma-enhanced chemical vapor deposition is discussed in addition.

Introduction

Single quantum emitters coupled to plasmonic and dielectric microresonators hold promise for novel photonic devices, such as optical transistors [1], optical quantum memories [2,3] and controlled single-photon sources. Color centers in diamond are well suited quantum emitters with outstanding coherence properties of their electron spin and single-photon operation even at room temperature. However, several key challenges need to be addressed to fully benefit from the above-mentioned properties. First of all, color centers in diamond need to be created in a well-defined way, and new color centers with desired emission and spin properties for quantum optics need to be identified. Both ion implantations as well as doping of diamond during CVD growth are of importance here. Furthermore, future applications rely on color centers with high emission rates. Resonator structures offer an enhanced light out-coupling and an increased spontaneous emission. The remaining challenge here is the coupling of color centers to nanophotonic devices. This is for two reasons: First, most of the emitters are relatively broadband. Therefore, optical resonators must be engineered with a short length, i.e., the mode volume of the resonator should be small. Second, to achieve strong coupling, a single color center must be placed at the maximum of the optical field with high spatial precision. In the present case of broadband plasmonic structures, typically about 10 nm positioning accuracy must be achieved. Herein, the controlled positioning of single color centers in diamond is realized with nanometer spatial precision by ion-beam implantation through nanometer-sized apertures and by fabricating plasmonic structures with hot spots around diamond nanocrystals.

Results and Discussion
1 Creation of single color centers in diamond with nanometer spatial control

An approach that is well suited to create single color centers in diamond with nanometer spatial control is the implantation of nitrogen ions through a mask [4]. At low implantation energies, which generate color centers a few nanometers below the surface, polymer resists with apertures written by electron beam lithography can be used. At higher energies, which create color centers up to a micron deep inside the diamond, suitable masks are thin mica sheets (thickness few micrometers), which contain channels a few nanometers wide. Such channels can be created by bombardment with high-energy heavy ions [4]. These mica masks provide the required thickness to stop those ions that do not enter the apertures, and at the same time provide the required high aspect ratio of the apertures (the channels) to ensure a narrow width of the implantation beam. Both methods are complementary to provide the controlled creation of color centers with low and high implantation energy, respectively. In the following, the second method shall be discussed. A third

approach that is suitable in the context of plasmonic structures is to use nanometer-sized diamond crystals with embedded color centers and fabricate plasmonic structures around them. This approach will be discussed in the subsequent section.

Figure 1a shows an electron micrograph of a mica mask. The ion channels have a width of about 50 nm, which is well suited for high-energy implantation with high spatial resolution. The channels have a rhombic cross section that reflects the crystal structure of the mica. The mica mask is then placed on the surface of a diamond. Electrostatic forces ensure good sticking of the mica sheet on the diamond surface. Subsequently, the masked diamond is irradiated with a nitrogen ion (N^+) beam with an energy of 1 MeV, thereby creating implanted spots with about 100 nm spatial control [4]. Note that with the given high implantation energy, the spatial accuracy of the implantation process is determined entirely by straggle, i.e., the deviation of the ion trajectory inside the diamond crystal, caused by collisions with the lattice atoms. Such implantation processes can be studied in detail with theoretical simulations. A suitable method is scattering calculations. The "Stopping Range of Ions in Matter" (SRIM) package implements such simulations [5]. Figure 1b shows the simulated ion traces achieved with the high-aspect-ratio mica mask. The simulations confirm that the spatial accuracy of the implantation is limited by straggle to about 100 nm. Figure 2a shows a high-resolution optical microscope image of a single implanted color center obtained with nonlinear optical excitation in ground state depletion (GSD) mode [6]. In this imaging mode, the color center is illuminated with a doughnut-shaped beam of high optical intensity. The saturation behavior of the optical transition provides a nonlinear relation between illumination intensity and observed fluorescence, which enables one to overcome the Rayleigh resolution limit of classical optical imaging. The image is generated by scanning the beam in the image plane. The resulting fluorescence image is the doughnut-shaped illumination pattern multiplied by the saturation function of the color center. At low laser power (first image) the fluorescence is proportional to the illuminated light field and the resulting image is equivalent to the illuminating doughnut beam. In this case the central dark spot has a size on the order of the optical wavelength. At higher laser power, the nonlinearity of the saturation function becomes important and the central dark spot shrinks well below the optical wavelength, providing super-resolution optical imaging capability. This technique is suitable to determine the position of an implanted color center with high precision. The accuracy of this imaging method is limited only by the applicable laser power and ultimately by instrument drift of the sample scanning unit. The mica mask implantation and GSD imaging method are suitable to create and characterize one or more color
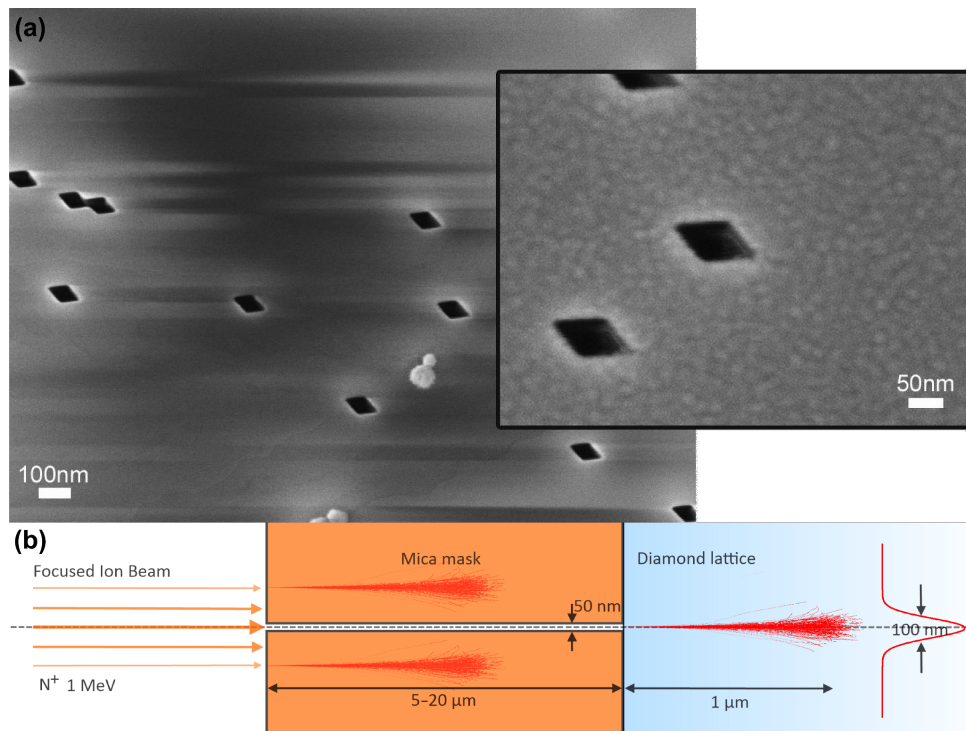
Figure 1: (a) Scanning electron micrograph of a mica mask. High aspect ratio channels were created by bombardment with 1.6 GeV samarium ions. The channels appear as dark parallelograms. The inset shows the dimensions of an individual ion channel. (b) SRIM simulation of the ion implantation process through the mica mask. The thickness of the mica mask is chosen in the range 5–20 μm, such that the nitrogen ions (N$^+$) are effectively stopped by the mask. The ions entering the channel create an implanted ion spot with a FWHM of about 100 nm, limited by straggle.

centers in diamond with sub 100 nm spatial control deep inside the diamond crystal (Figure 2b). This deep implantation is of great importance when spin and optical properties must be of the highest quality and well protected from the environment.

2 Coupling of nanodiamond quantum emitters to plasmonic resonators

At room temperature, most solid state defects have a broadband optical emission spectrum. The resonant optical line width is
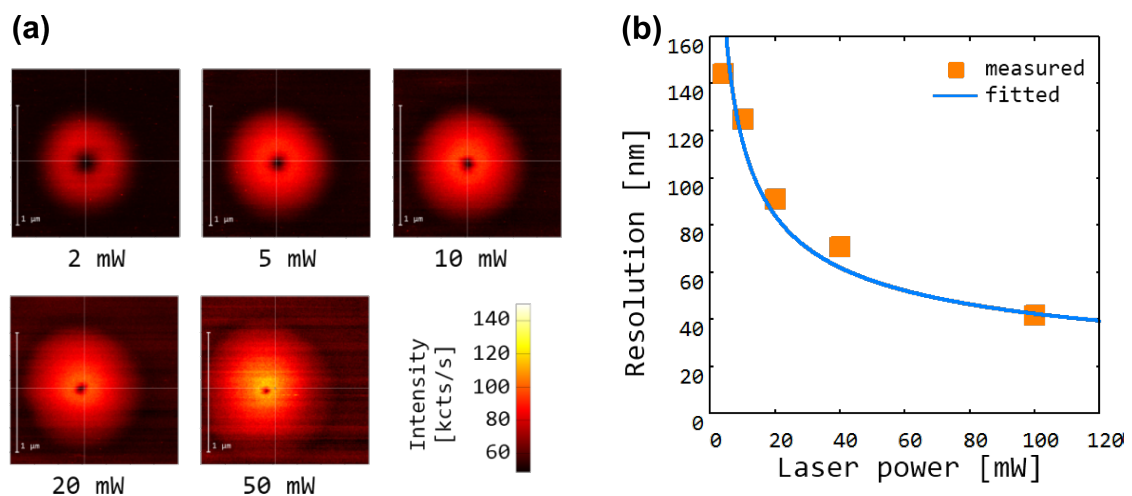
Figure 2: Nonlinear optical microscopy of implanted color centers by using ground-state-depletion microscopy mode. (a) Images of a color center obtained with increasing depletion laser power. (b) Measured optical resolution as a function of laser power. The solid line shows a theoretical fit for the achievable resolution $r = c / \sqrt{P} + r_\infty$, where c is a proportionality constant, P is the optical power and r_∞ represents the maximum achievable resolution at infinite power, which is determined by technical limitations such as imperfections of the optical mode [6].

typically several nanometers wide. Frequently, in addition to the resonant line, a broad emission band is observed that can be up to few 100 nm wide. This broad emission band corresponds to vibrational levels and its strength depends on how much the optical emission couples to lattice vibrations. Figure 3 shows a typical room-temperature optical emission spectrum of the nitrogen–vacancy (NV) color center in diamond. The resonant optical emission appears as a weak peak at a wavelength of 637 nm (zero-phonon line, ZPL), and a broad emission band ranging from about 630 up to 750 nm is observed. In order to couple such broadband quantum emitters to a resonant optical light field a suitable broadband optical resonator is required. To realize a broadband resonator that has at the same time a high finesse, the optical mode volume must be sufficiently small. Plasmonic resonators are well suited to provide such small mode volumes. In this case metals are used rather than dielectrics to confine optical light fields. The negative refractive index of the metal ensures that guided (localized) modes exist, even when the dimensions of the device are much smaller than the optical wavelength. In this way, resonators with mode volumes much smaller than a cubic wavelength can be realized. Such structures are often optical equivalents of corresponding macroscopic electromagnetic antennas. Figure 4 illustrates some of the antennas considered in this study [7-9]. The prototype of a resonant plasmonic antenna is a metallic strip (Figure 4a) with a width and thickness of few tens of nanometers and a length corresponding to half of the optical wavelength. The electric field, *I*, has a maximum in the center of the stripe. Quantum emitters should be placed as close as possible to this location. The coupling between a quantum emitter and the optical field can be enhanced by cutting the antenna in two parts and creating a small (about 10–20 nm) gap in between, analogous to the feed gap of a radio antenna. The quantum emitter is placed in the feed gap, where the optical field is maximal. The field in the gap can be increased by tapering both antenna arms and reshaping their ends at the feed gap with sharp tips. This leads to the so-called "bow tie" antenna structure shown in Figure 4b. An antenna with polarization independent far-field radiation pattern can be created by combining two bow-tie antennas to a crosslike structure as also shown in Figure 4b.

An approach that is suitable to couple solid state quantum emitters to plasmonic resonators is the use of diamond nanocrystals containing photoactive color centers. Such diamond nanocrystals can be as small as 10 nm. By using suitable fabrication steps, plasmonic structures can be fabricated around such crystals with precise spatial control. In this process, first, gold markers are fabricated on a glass substrate by using electron beam lithography. Subsequently, diamond nanocrystals are spin coated onto the substrate. By using a dual atomic force micro-
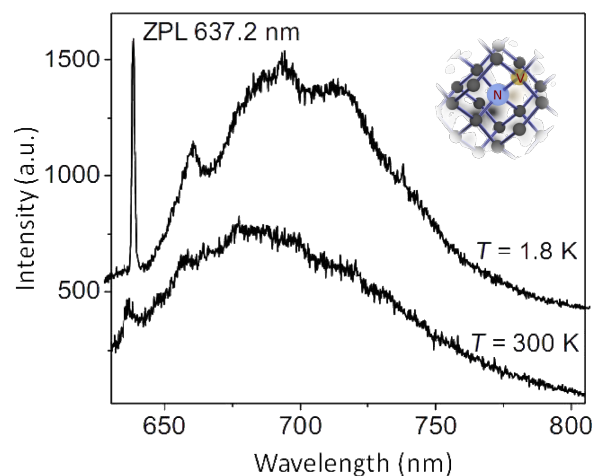
Figure 3: Fluorescence spectra of the nitrogen–vacancy defect in diamond. The upper curve shows the spectrum at liquid-helium temperature, the lower curve shows the spectrum at room temperature. The peak at a wavelength of 637.2 nm corresponds to the resonant optical transition (ZPL). The broad band at longer wavelength corresponds to phonon-broadened emission. The inset shows the molecular structure of the NV center in diamond consisting of a substitutional nitrogen atom with an adjacent vacancy.
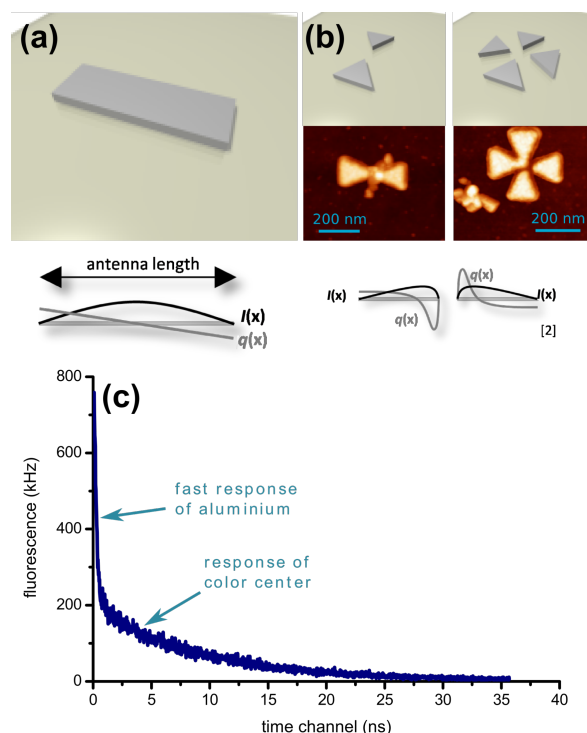
Figure 4: Plasmonic resonator geometries, field *I* and current *q* for (a) half-wave antenna, (b) bow tie and crossed bow tie structure along with AFM images of the devices with embedded nanodiamond color center. (c) Fluorescence lifetime measurement of the coupled color center. A double exponential decay is observed. The initial fast decay is due to aluminium interband transitions and background. The second, slow decay is due to the coupled color center.

scope (AFM) and confocal microscopy setup, diamond nanocrystals that contain single color centers are then identified by fluorescence microscopy and second-order photon autocorrelation, and their position relative to the gold markers is measured with nanometer precision by AFM. Finally, plasmonic structures are fabricated around the selected diamond nanocrystals.

The middle panel of Figure 4b shows AFM images of the plasmonic resonators coupled to diamond nanocrystals. A positioning accuracy of about 20 nm is achieved. This ensures that the quantum emitters are located well inside the hot spot of the plasmonic structures. A method that is suitable to verify the coupling of the color centers to the resonators is optical lifetime measurements. Lifetime measurements were performed with supercontinuum pulsed laser excitation with a pulse length of about 50 ps. Figure 4c shows a typical lifetime measurement. A double exponential decay is observed. The initial fast decay is due to fast interband transitions of the metal and background fluorescence. The second slow decay is due to the color center. Table 1 summarizes the observed decay constants. For all resonators, the decay time is reduced by about a factor of four compared to an uncoupled color center. The strongest coupling is observed with the bow-tie resonator.

Table 1: Decrease of the fluorescence lifetimes.

resonator	lifetime [ns]
uncoupled	24
wire	6.6
bow tie	3.6
cross	4.2

3 Dielectric diamond photonics

While plasmonic resonators focus on strong coupling between quantum emitters and resonators, frequently the most important aspect is to collect as much light as possible from a single solid-state quantum emitter. In case of diamond, this task is challenging due to the high refractive index ($n = 2.4$) of the host material. Total internal reflection at the sample surface prevents light from traversing the diamond/air interface, and many of the emitted photons are effectively trapped inside the diamond. Figure 5a illustrates this effect. Due to refraction, the effective numerical aperture (NA) for light collection is strongly reduced. A device that is suitable to overcome this effect is a so-called solid immersion lens (SIL), i.e., a hemispherical lens fabricated out of diamond. Due to the hemispherical shape, all light rays that emanate from the center of curvature are normal to the surface of the sphere, such that no refraction occurs (Figure 5b). With such a lens, we expect an increase of the collection effi-

ciency by 6 to 8 times [10], depending on the numerical aperture of the collection objective. Figure 5c shows the relation between the collection efficiency and the numerical aperture. The effect is particularly pronounced with large numerical apertures (NA = 0.70–0.95), which are typically used for high efficiency light collection from solid-state quantum emitters. There are two complementary ways to fabricate a hemispherical lens out of diamond. On the one hand, one can produce a macroscopic (about a millimeter) size lens. On the other hand, one can use a focused ion beam (FIB) to fabricate a micrometer-sized hemisphere around a preselected diamond color center. In the following, both approaches are discussed. We first focus on a macroscopic solid immersion lens.

Figure 5: Enhancement of the collection efficiency with a hemispherical solid immersion lens (SIL). (a) Reduction of the effective numerical aperture due to refraction at the surface of a high-index medium. (b) Elimination of refraction with a hemispherical lens. (c) Collection efficiency as a function of numerical aperture with (red line) and without (black line) the solid immersion lens. Reproduced with permission from [10]. Copyright 2010 American Institute of Physics.

Figure 6a shows a photograph of a macroscopic hemispherical lens fabricated out of high-purity single-crystalline diamond (Element Six Ltd., London, UK). In this particular lens, a single color center is located close to the origin of the hemisphere and can be optically addressed. Figure 6b shows a confocal scanning microscope image of the focal region of the lens. The bright spot in the center of the image corresponds to a single color center. The nature of the color center can be determined by its fluorescence spectrum. Figure 6c shows the fluorescence spectrum. A characteristic resonant line at a wavelength of

637 nm (ZPL of NV⁻) is observed, identifying the color center as a negatively charged nitrogen–vacancy defect. To ensure that this is indeed a single quantum emitter, we measure its second-order photon autocorrelation. Figure 6d shows the data. The dip at time delay zero drops clearly below 0.5, showing that this is a single quantum emitter. Finally, we determine the maximum possible photon count rate achievable with the solid immersion lens. Figure 6e shows saturation curves of the single quantum emitter with and without taking advantage of the hemisphere. For this purpose, we probe the same quantum emitter, first through the flat bottom surface of the hemisphere and subsequently through the curved surface. The saturation curves are well described with a rate model for a two-level system. With this macroscopic diamond hemisphere, fluorescence count rates up to about 420 kHz are observed, which is sufficient for a number of important applications targeting low-temperature quantum control, such as single-shot electron-spin readout [11] or resonant-charge-state discrimination [12].

Due to the high cost associated with a macroscopic diamond lens, it would be very interesting to fabricate instead a microscopic hemisphere (ca. 10 micrometers) into the surface of a standard diamond sample. Due to the small size, thousands of microscopic lenses could be fabricated into a single diamond sample, and moreover, each lens could be fabricated precisely around a single fluorescent color center. A suitable fabrication technique is focused ion beam milling. We therefore explore whether this can be used to produce high-quality micrometer-sized diamond SILs. In order to register a SIL precisely on top of a single color center, we first fabricate a grid of markers (circular holes) into the surface of a diamond sample using a FIB. Figure 7a shows a scanning electron microscopy (SEM) image of such FIB markers. Subsequently, we analyze the sample with a confocal fluorescence microscope and determine single color centers within the grid (Figure 7b). The position of the color centers relative to the FIB markers as well as their depth below the diamond surface is determined with about 100 nm precision. Thereafter, a solid immersion lens with a

Figure 6: Macroscopic solid immersion lens [10]. (a) Photograph of a single crystalline diamond hemisphere. (b) Confocal fluorescence image of the focus plane. The bright spot in the center corresponds to a single nitrogen–vacancy defect. (c) Fluorescence emission spectrum. The peak at a wavelength of 637 nm (ZPL) corresponds to the resonant optical emission of the NV⁻ center. (d) Photon antibunching. The dip at time delay $\tau = 0$ is well below 0.5, indicating a single quantum emitter. (e) Saturation curves with and without the solid immersion lens. Reproduced with permission from [10]. Copyright 2010 American Institute of Physics.

Figure 7: Fabrication of a microscopic diamond hemisphere by focused ion beam milling. (a) Grid of FIB markers for the precise alignment of the SIL on top of a single color center. (b) Fluorescence microscope image of one quadrant of FIB markers. The bright blue spots are single color centers. A color center a few microns below the surface (not visible in this image) is selected as the target emitter. Note that the image distortion between subsequent scan lines is caused by bi-directional motion of the imaging piezo scanner. (c) SEM image of a microscopic SIL. The complete FIB process takes approximately 30 min.

radius corresponding to the depth of the color center is fabricated by using the focused ion beam. Figure 7c shows an example of such a microfabricated SIL. Note the cone around the SIL, which is fabricated in order not to cause additional refraction for the emitted fluorescence light. The ringlike ablation material at the bottom of the SIL lies within a spatial angle that is not detected by the high NA microscope objective of 0.95. With such a microscopic diamond hemisphere, fluorescence count rates up to about 480 kHz were observed, which is even slightly better than the result obtained with the macroscopic SIL. The device is therefore a highly promising microstructure that provides a universal performance boost for diamond quantum applications.

4 Dielectric pillar microcavities with embedded diamond nanocrystals

An alternative approach for increasing the collection efficiency exploits the Purcell effect. In this case, a single quantum emitter is placed into an optical resonator and the emitted photons exit preferentially into a resonator mode, much like the stimulated-emission process of a laser. The resonant photons can be coupled out with high efficiency from the resonator. In order to enhance the emission at the zero-phonon line (ZPL) of nitrogen–vacancy centers, diamond nanocrystals containing single NV centers were embedded into high quality pillar resonators (Figure 8a). In a first step, a bottom Bragg mirror composed of TiO_2/SiO_2 layer pairs is fabricated by magnetron radio-frequency sputtering. In a second step, nanodiamonds with a diameter of less than 20 nm (Figure 8b) are spin coated onto the dielectric mirror. The area density of the nanocrystals may be chosen by the concentration of the nanodiamond solution and/or by varying the rotation speed of the spin-coater. The nanocrystals are embedded in a TiO_2 spacer layer, i.e., a region of a high index of refraction. Therefore, a so-called "λ-cavity" is manufactured. In a third step, the top Bragg mirror is sputtered to create a planar cavity structure with one-dimensional confinement of light. In order to achieve a three-dimensional light confinement, pillar microcavities are milled out of the planar structure by focused ion beam. As a consequence, the light field is concentrated vertically between the two dielectric Bragg mirrors and laterally due to the total internal reflection at the pillar sidewalls [13,14]. Due to the waveguide nature of pillar resonators, the photoluminescence emission is strongly directional, which results in the efficient collection of radiation with a microscope objective.

A broadband light transmission measurement through a single-pillar resonator is shown in Figure 8e. The transmission spectrum is dominated by the fundamental mode HE11 of the pillar microcavity. Also a faint first HE01/HE2 and third HE12 excited mode is discernible (Figure 8e). Since the incoherent light source generates an approximately planar wavefront, light

Figure 8: (a) Scanning electron microscopy (SEM) image of a micropillar resonator with embedded diamond nanocrystals in the central spacer layer. (b) Transmission electron microscopy (TEM) image of diamond nanocrystals. The average size of the nanodiamonds is 20 nm. (c–e) Mode spectrum of a pillar microcavity (2.9 µm diameter) with an ensemble of diamond nanocrystals in the spacer layer. (c) Simulated spatial cavity modes. (d) Spatio-spectrally resolved photoluminescence emission and (e) white-light transmission spectrum. Calculated spectral mode positions are indicated by vertical grey lines.

preferably couples to the symmetric fundamental mode. The entire spectrum of cavity modes is clearly visible in the photoluminescence emission with continuous-wave laser excitation of an ensemble of diamond nanocrystals at a wavelength of 532 nm (Figure 8d). The spectral positions of these resonances (Figure 8d) are calculated based on an effective-waveguide model. The theoretical results are in excellent agreement with the values obtained by the experiment. The simulations also yield the spatial mode patterns depicted in Figure 8c. The recorded CCD image of the photoluminescence emission provides us with one-dimensional spatial resolution along the entrance slit of the spectrometer. For this reason a vertical cut through the center of the calculated two-dimensional mode patterns (Figure 8c) can be compared to the CCD image in Figure 8d. In particular, the fundamental mode HE11 exhibits one intensity maximum. The first excited mode HE01/HE21 has two constituents.

To elucidate the nature of photon emission and characterize the coupling of NV centers to an optical cavity, we perform second-order autocorrelation measurements. The normalized intensity function $g^{(2)}(\tau)$ is recorded with an optical setup according to Hanbury Brown and Twiss. As seen in Figure 9a, a clear anti-bunching effect ($g^{(2)}(\tau) < 1$) can be observed at zero time delay ($\tau = 0$) from an optical cavity with 1.6 μm diameter. This is strong evidence for nonclassical light emission. The depth of the antibunching dip at zero time delay amounts to 0.21. A value below 0.5 would explicitly indicate that a single NV center coupled to the cavity is a single photon source. There are two main factors that may currently limit the depth of the anti-bunching dip. First, background photoluminescence from the dielectric materials, especially from SiO_2 layers, and second, background emission from the diamond nanocrystal itself. By optimization of the sputter parameters, we recently achieved a

reduction in photoluminescence of sputtered SiO_2 layers by a factor of nine at a wavelength of 637 nm (ZPL of NV^- centers, Figure 9b). In the future, this process optimization may be used to reduce the background photoluminescence of the cavity.

5 Fabrication of Ni-, W- and Si-based color centers in CVD diamond
5.1 Motivation
Diamond is an excellent host for fluorescent defects. Due to the large band-gap energy of 5.46 eV, it is likely that localized defect states are present in the forbidden band. Not surprisingly over 500 such "deep trap" centers are meanwhile known in diamond [15,16]. Their fluorescence emission covers a broad spectral range reaching from the UV to the far IR. Admittedly, origin and composition of many color centers in diamond are yet not well understood or even known. Above all, not every fluorescent defect center exhibits the desired characteristics for applications in quantum information processing [17], such as a small bandwidth, a low electron–phonon coupling, or a high oscillator strength. For this reason two main challenges need to be addressed by diamond researchers:

- New color centers in diamond with favorable properties for quantum-information-processing technologies need to be identified.
- A reproducible fabrication method for color centers (such as the nickel-related NE8-center) in high-quality diamond layers has to be developed.

As demonstrated and discussed in Section 1, ion implantation into bulk diamond crystals of high purity is a well-established technique [4] to produce defects such as the NV center, offering nanometer spatial resolution and a controlled defect density. A drawback, on the other hand, is the inevitable damage caused to
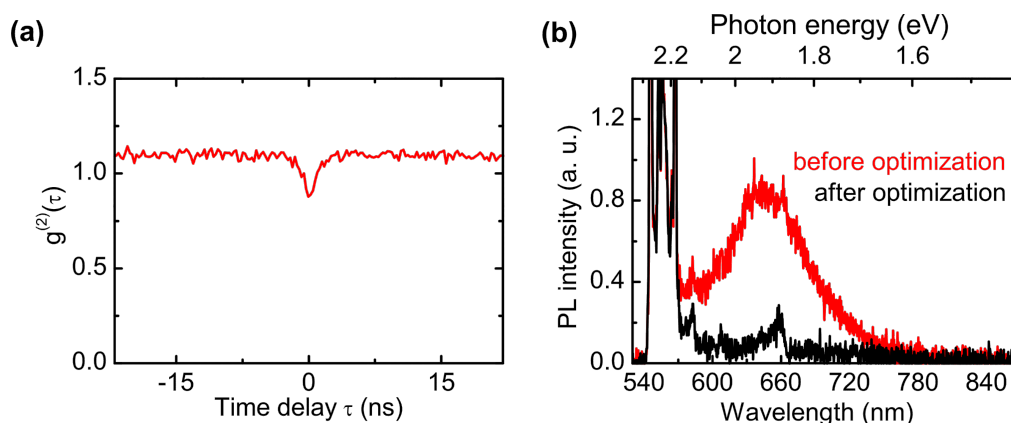

Figure 9: (a) Normalized intensity autocorrelation function $g^{(2)}(\tau)$ from a micropillar cavity of 1.6 μm diameter with embedded diamond nanocrystals. (b) Comparison between the photoluminescence emission from a standard (black) and an optimized (red) sputtered SiO_2 layer.

the diamond lattice, which leads to an additional photoluminescence (PL) background and disturbances of the photoluminescence emission [18]. Furthermore, not every color center in diamond can be produced by implantation with an adequate yield [15]. The direct synthesis of diamond crystals by microwave plasma enhanced chemical vapor deposition (MWPECVD) offers an alternative route to integrate color centers and was investigated in addition to ion implantation [19,20]. We deposited single-crystal diamond layers of high phase and structural purity by MWPECVD. Emphasis was placed on a reproducible dopant addition to the growth process aiming at a targeted in situ incorporation of color centers based on nickel and tungsten impurities.

A very promising single-photon-emitting defect for quantum-cryptographic applications is the so-called NE8-center [17]. This nickel–nitrogen based defect exhibits superior properties, such as a sharp emission line at around 800 nm, with a width of only 2 nm at room temperature, together with a short intrinsic lifetime of 2 ns, and an efficient emission concentrated in the zero-phonon line. Different attempts were already conducted to produce this center [21,22]. However, the yield of nickel–nitrogen-related centers seems to be rather low. Tungsten is known to produce a family of so-called W_5-centers with several luminescence lines near 714 nm [23]. Up to now these centers were only produced by chance in polycrystalline diamond samples grown by the hot-filament technique. Accordingly, not much is known about their luminescence properties. Our aim was to produce the W-centers in a well-defined way, in order to enable further studies on these color centers.

The goal of our work is the fabrication of stable single-photon emitters with a high emission rate in the red and infrared spectral range. However, as discussed in Section 3 the high refractive index of diamond impedes light extraction from the bulk, thereby lowering the achievable count rates. A further way to circumvent this disadvantage is to implement color centers in small nanodiamond crystals with diameters well below the wavelength, guaranteeing an efficient light extraction. Moreover, single nanodiamonds can be implemented into dielectric cavities enhancing the efficiency, as demonstrated in Section 4. We will discuss our approaches to incorporate silicon–vacancy (SiV)-centers in dispersed nanodiamond particles fabricated by MWPECVD in Section 5.5.

5.2 Nickel and tungsten doping of single-crystal diamond layers

Homoepitaxial growth of diamond - Homoepitaxial diamond growth was performed at low pressure conditions in a microwave-activated hydrogen-rich plasma atmosphere in an ellipsoidal cavity reactor [24]. The necessary carbon species for

the diamond growth were supplied by the addition of 1–2% methane to the process gas. Single-crystal diamond plates of type Ib with (001) and (111) surface orientation and dimensions of 3 × 3 mm² served as substrates. In order to provide optimal growth conditions, a high plasma-power-density regime (100–150 W/cm³) was achieved by applying a pressure of 200 mbar and a microwave power of 2–3 kW. Figure 10 shows the holder configuration we used to focus the plasma ball. The main advantage of such a small reaction volume is that neither the reactor base plate nor the quartz walls of the surrounding bell jar is touched by the plasma. Major contaminations from the reactor walls were therefore avoided.
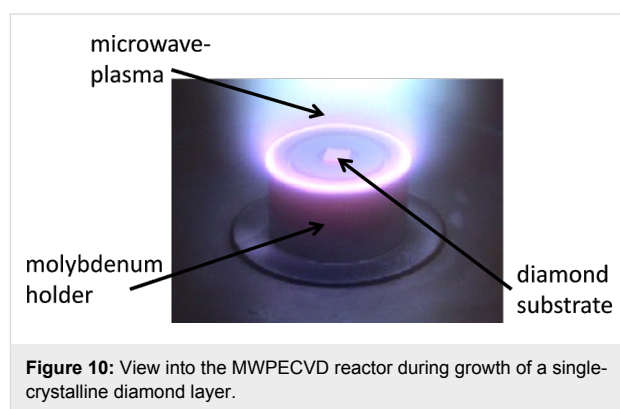
Figure 10: View into the MWPECVD reactor during growth of a single-crystalline diamond layer.

Gaseous nickel and tungsten precursors - The controlled and targeted addition of dopants during diamond growth is a crucial step for the in situ synthesis of color centers. A frequently applied method is to expose a solid state source containing the dopant material directly to the reactive plasma [15,19,21]. We also used this approach for the doping of nanodiamond crystals with silicon, which will be discussed in section 5.5. A drawback of a solid-state doping source is the limited control over the dopant concentration during growth. To ensure a reproducible doping we studied the applicability of gaseous metal precursors, namely nickelocene $Ni(C_5H_5)_2$ and tungsten hexacarbonyl $W(CO)_6$, for the doping of diamond with nickel and tungsten. Both precursors are solids at room temperature but exhibit a high vapor pressure [20]. Nickelocene and tungsten hexacarbonyl, separately, were sublimated in a temperature-controlled dopant reservoir. Argon was passed through this reservoir, saturated with the vapor of one of the precursors and afterwards introduced to the process chamber. By using an inert carrier gas, we paid attention to the fact that the two precursors are unstable in a hydrogen-rich atmosphere [20]. We thereby avoided a premature decomposition of the precursors in the gas line.

A major advantage of our gas-phase-doping approach is that it offers a targeted dopant addition. The dopant concentration in

the gas phase can be adjusted either by the temperature of the precursor material in the dopant reservoir or by the carrier gas flux. The reproducibility of our doping approach was verified by checking for nickel- or tungsten-related emission lines in the MWPECVD plasma by using optical emission spectroscopy (OES). Tungsten transitions in the MWPECVD plasma are rather weak and it was difficult to separate them from the bright plasma background. Nickel exhibits in contrast some prominent emission lines in the UV. We choose an intense transition with an emission line at a wavelength of 341.47 nm, as shown in Figure 11a, to study the addition of nickelocene. Figure 11b shows the temporal evolution of the 341.47 nm emission for different argon fluxes through the nickelocene bubbler. During the first 10 min no nickelocene was added to the carrier gas. Accordingly, no nickel signal is visible. Afterwards the carrier gas flux was altered every 10 min. The signal presented in Figure 11b follows this variation. Furthermore, a steady signal

is visible for a stable argon addition. The rapid decrease of the nickel signal after lowering the argon flux at both 40 min and 50 min indicates the absence of unwanted hysteresis effects.

5.3 Verification of nickel incorporation

The incorporation of nickel into the as-grown diamond layers was verified by secondary ion mass spectrometry (SIMS). An unambiguous assignment of nickel was achieved by measuring two different nickel isotopes (namely ^{58}Ni and ^{62}Ni) and comparing the measured count rates with the known natural abundances of these isotopes. Figure 12(a) shows a SIMS measurement performed on a 500 ± 100 nm thick diamond layer grown with constant nickelocene addition. During MWPECVD growth a mole fraction of 10^{-7} of nickelocene was added to the process gas. The SIMS measurement reveals that nickel concentrations up to 10^{18} cm^{-3} are present in this layer. However, although it was verified by OES that a constant amount of
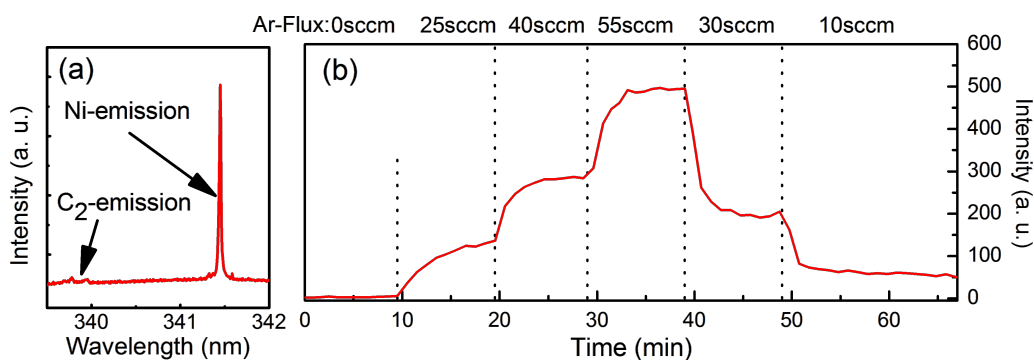
Figure 11: (a) Optical emission spectroscopy: observed nickel emission in the MWPECVD plasma during diamond growth with addition of nickelocene. **(b)** Temporal evolution of the nickel emission (341.47 nm line) during MWPECVD diamond growth altering the argon/nickelocene addition. The intensity of the nickel emission is solely determined by the carrier gas flux to the reactor. Furthermore, the nickel emission is steady for constant nickelocene additions thereby demonstrating the reproducibility of the utilized gas-phase-doping approach. Reproduced with permission of the author from [25].
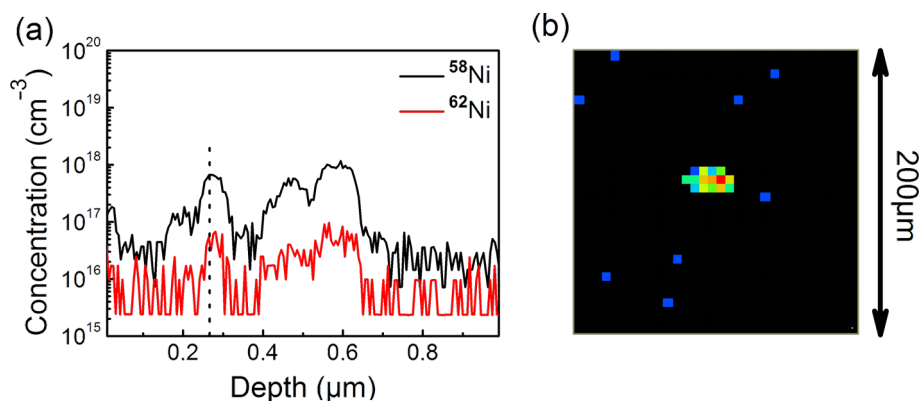
Figure 12: (a) SIMS depth profile of nickel-doped single-crystal diamond layer. The intensity of the two "marker" isotopes ^{58}Ni and ^{62}Ni is in accordance with the known natural abundance, thereby verifying nickel incorporation. **(b)** SIMS-signal from picture (a) observed at a depth of 0.25 μm. The nickel signal emanates from a spot indicating the formation of nickel clusters during diamond growth with simultaneous nickelocene addition. Reproduced with permission of the author from [25].

nickelocene was added during the deposition process, a nonuniform depth profile is visible. Furthermore, the nickel signal was not uniformly distributed in the lateral direction, as seen in Figure 12b. Both results indicate that nickel clusters were formed during growth, and nickel is rather encapsulated than incorporated into the diamond film.

Additional measurements were performed to ensure the incorporation of nickel atoms into the diamond lattice. Of avail in this context is that nickel is known to form the so-called 1.4 eV defect in diamond [16]. This fluorescent center exhibits two narrow lines at a wavelength of around 884 nm, which are readily excited by cathodoluminescence (CL). Figure 13 shows a CL-measurement performed on a nickel-doped diamond layer. Several lines at a wavelength of around 884 nm are visible in the spectra of the nickel-doped layer. The two most prominent lines are located at 883.37 nm (1.4035 eV) and 885.12 nm (1.4008 eV), which is in accordance with values known for the 1.4 eV center [16].

CL measurements on the same nickel-doped sample revealed further nickel-related lines. As shown in Figure 13b a luminescence line at a wavelength of 794 nm was detected accompanied by two phonon sidebands on the lower energy side, shifted by 16 meV and 39 meV. The origin of this luminescence line is the 1.563 eV center, also sometimes referred to as the "NE8-center". From this observation it can be concluded that nickel was not solely encapsulated during MWPECVD growth. In fact nickel-related color centers were produced by using nickelocene as a nickel precursor during diamond MWPECVD growth.

5.4 Verification of tungsten incorporation

A direct verification of tungsten incorporation into the as-grown diamond layers by SIMS was not possible, thus indicating that the tungsten concentrations were well below the detection limits of 10^{16}–10^{17} cm^{-3}. However, confocal micro-photoluminescence measurements provided confirmation of tungsten incorporation. Layers grown with the addition of $W(CO)_6$ exhibited a broad luminescence with emission in the spectral window between 680 nm and 825 nm. Additional features became visible when PL measurements were performed at a temperature of 77 K as shown in Figure 14d. The bright line at a wavelength of 714 nm is the zero-phonon line of the emission. The ZPL is accompanied on the lower energy side by several phonon sidebands, which are nearly equidistantly spaced by 25 meV. Position of the ZPL, as well as of the sidebands, are in agreement with the so-called W_5-center [16,23]. The same luminescence emission was reported in the past for diamond layers deposited by the hot-filament technique and accordingly by the DC-arcjet technique [16,23]. The W_5-center was hence ascribed to impurities originating from the filament material and accordingly from the cathode material of the reactor systems. The observation of the W_5-luminescence in diamond layers grown with the addition of $W(CO)_6$ confirms the previous assignment.

The gas-phase doping approach offered furthermore the possibility to adjust the density of W_5 centers by the addition of $W(CO)_6$ during diamond deposition. The μ-PL mappings on samples doped with different additions of $W(CO)_6$ in Figure 14a–c confirm this statement. The tungsten concentration during growth was raised by a factor of ten going from
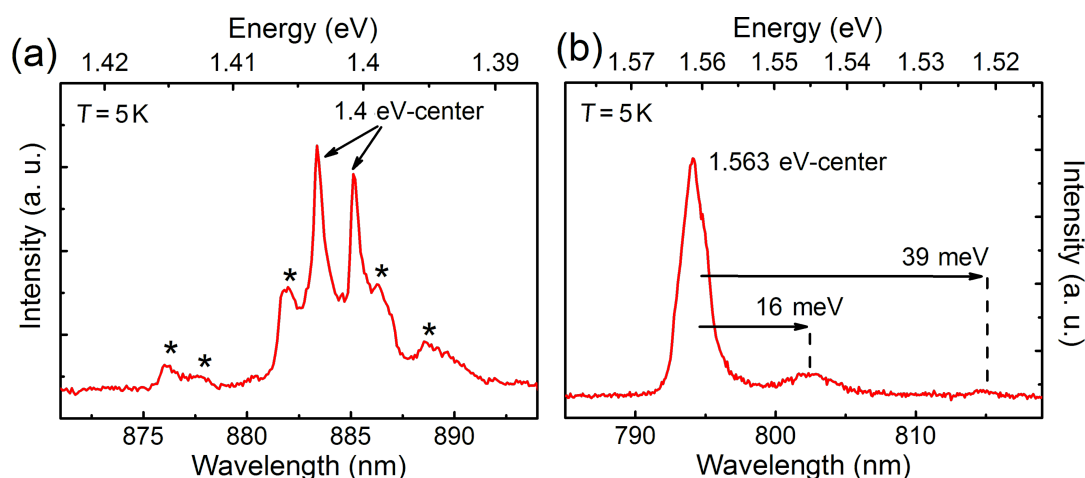
Figure 13: Cathodoluminescence spectra measured at a temperature of 5 K on a nickel-doped single-crystal diamond layer. (a) Emission lines of the 1.4 eV center at 883.4 nm and 885.1 nm, verifying nickel incorporation. Origins of accompanying lines marked with an asterisk are unknown. (b) Luminescence of the 1.563 eV center ("NE8-defect") observed in the same diamond layer. Reproduced with permission of the author from [25].
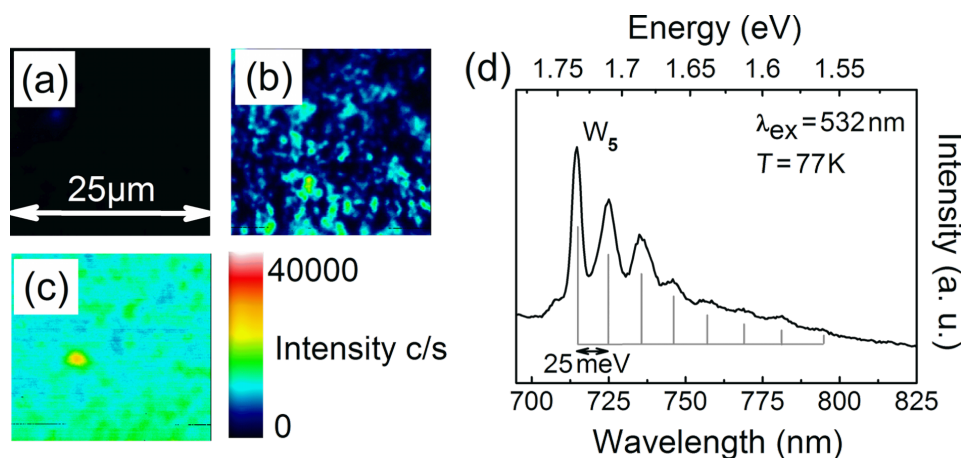
Figure 14: (a–c) Room-temperature PL mapping excited at a wavelength of 660 nm on (111) diamond layers grown by MWPECVD with different additions of $W(CO)_6$: (a) no addition (reference layer); (b) with a mole fraction of 1.1×10^{-6} $W(CO)_6$ in the process gas; (c) with a mole fraction of 1×10^{-5} $W(CO)_6$ in the process gas. (d) Photoluminescence spectrum obtained from a tungsten-doped single-crystal diamond layer; acquired at 77 K with 532 nm laser excitation. The tungsten-related W_5-luminescence at a wavelength of 714 nm together with several pronounced phonon sidebands is visible. Reproduced with permission of the author from [25].

Figure 14b to Figure 14c. The intensity of the W_5-luminescence increases accordingly. Moreover, no dark areas without W_5-center luminescence are visible in Figure 14c.

5.5 Silicon–vacancy centers in as-grown nanodiamonds

Seeding and overgrowth of dispersed nanodiamonds on silicon - We seeded nanodiamond particles with diameters below 10 nm from a colloidal solution onto a silicon wafer [26]. By controlling the surface chemistry of the particles it was possible to achieve an average distance of ca. 1 μm between two adjacent particles. The low particle density guaranteed that every particle could be addressed individually afterwards by confocal microscopy [27]. The nanodiamonds acted as seed crystals in the subsequent overgrowth in the MWPECVD plasma process. In this manner, we produced particles with diameters up to 700 nm, as shown in Figure 15a. Because of the harsh plasma environment the silicon substrate is slightly etched and the plasma is enriched with silicon. Silicon atoms are therefore also incorporated into the growing nanodiamond particles.
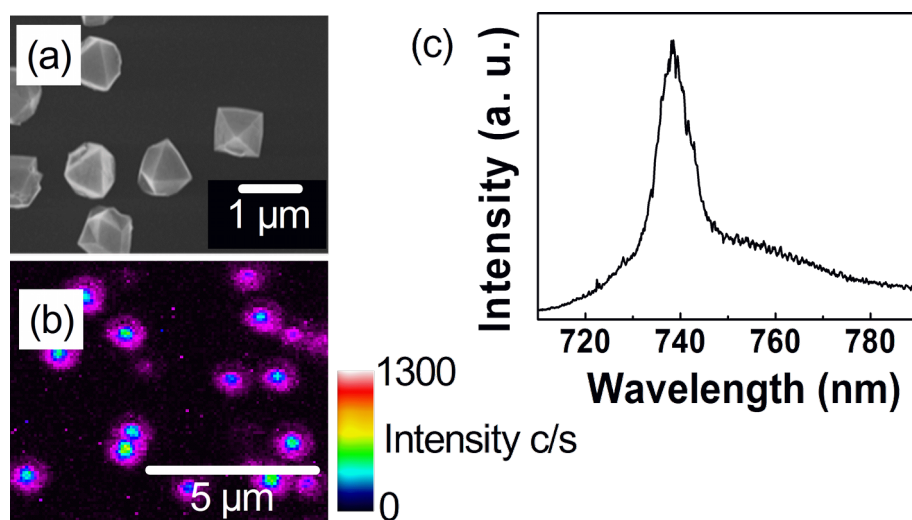
Figure 15: (a) As-grown nanodiamond particles on a silicon substrate. (b) Confocal photoluminescence mapping (660 nm excitation wavelength), recorded at room temperature. The integrated intensity emitted in the spectral window between 725 and 755 nm was measured. Bright areas in the scan correlate with nanodiamond particles. (c) Spectrally resolved PL emission from a particle in (b). The SiV luminescence verifies the successful incorporation of silicon during growth.

Photoluminescence characterization - The presence of silicon-related color centers in the as-grown nanodiamond particles was investigated by micro-photoluminescence measurements. Figure 15b shows a typical PL mapping over a 20×20 µm² region. The bright areas correlate with nanodiamond particles. Origin of the PL signal is the luminescence of the SiV center. A typical PL spectrum of the SiV center is shown in Figure 15c. In order to enhance the yield of fluorescent silicon defects, we varied the temperature during the MWPCVD growth process. Diamond growth below 600 °C is comparatively slow. However, even small nanodiamonds exhibit SiV luminescence. Nanodiamonds grown above 600 °C exhibited a lower SiV yield. Especially small particles showed no luminescence.

Conclusion

We have performed a series of key experiments towards strong coupling of solid-state quantum emitters to plasmonic and dielectric optical resonators. First, we have demonstrated controlled creation of nitrogen–vacancy centers in diamond with nanometer spatial control by ion implantation through suitable masks. Using high-aspect-ratio mica masks, we have shown that high-energy deep implants can be created with nanometer spatial precision. Subsequently, we have demonstrated the coupling of diamond nanocrystals to plasmonic resonators. Emitter–resonator coupling was achieved for different aluminium resonator geometries, with a shortening of the excited state lifetime six times. By using dielectric diamond hemispheres, the photon collection efficiency was increased by a factor of up to six. Dielectric pillar microcavities with embedded diamond nanocrystals containing single NV centers have been manufactured by sputtering and focused ion beam milling. Photon antibunching from a NV center inside a dielectric pillar cavity could be observed. In addition, a reproducible gas-phase doping approach to incorporate nickel and tungsten atoms during MWPECVD growth of single-crystal diamond films has been demonstrated. Our experiments mark a firm step towards strong coupling of solid-state quantum emitters to plasmonic and dielectric resonators by using integrated plasmonic nanophotonics and dielectric diamond optics.

Acknowledgements

References

1. Hwang, J.; Pototschnig, M.; Lettow, R.; Zumofen, G.; Renn, A.; Götzinger, S.; Sandoghdar, V. *Nature* **2009,** *460,* 76–80. doi:10.1038/nature08134
2. Hedges, M. P.; Longdell, J. J.; Li, Y.; Sellars, M. J. *Nature* **2010,** *465,* 1052–1056. doi:10.1038/nature09081
3. Kurtsiefer, C.; Mayer, S.; Zarda, P.; Weinfurter, H. *Phys. Rev. Lett.* **2000,** *85,* 290–293. doi:10.1103/PhysRevLett.85.290
4. Pezzagna, S.; Rogalla, D.; Becker, H.-W.; Jakobi, I.; Dolde, F.; Naydenov, B.; Wrachtrup, J.; Jelezko, F.; Trautmann, C.; Meijer, J. *Phys. Status Solidi A* **2011,** *208,* 2017–2022. doi:10.1002/pssa.201100455
5. Ziegler, J. F. *The Stopping and Range of Ions in Matter.* 2012; http://www.srim.org/.
6. Rittweger, E.; Wildanger, D.; Hell, S. W. *EPL* **2009,** *86,* 14001. doi:10.1209/0295-5075/86/14001
7. Hanke, T.; Krauss, G.; Träutlein, D.; Wild, B.; Bratschitsch, R.; Leitenstorfer, A. *Phys. Rev. Lett.* **2009,** *103,* 257404. doi:10.1103/PhysRevLett.103.257404
8. Hanke, T.; Cesar, J.; Knittel, V.; Trügler, A.; Hohenester, U.; Leitenstorfer, A.; Bratschitsch, R. *Nano Lett.* **2012,** *12,* 992–996. doi:10.1021/nl2041047
9. Dregely, D.; Lindfors, K.; Dorfmüller, J.; Hentschel, M.; Becker, M.; Wrachtrup, J.; Lippitz, M.; Vogelgesang, R.; Giessen, H. *Phys. Status Solidi B* **2012,** *249,* 666–677. doi:10.1002/pssb.201100781
10. Siyushev, P.; Kaiser, F.; Jacques, V.; Gerhardt, I.; Bischof, S.; Fedder, H.; Dodson, J.; Markham, M.; Twitchen, D.; Jelezko, F.; Wrachtrup, J. *Appl. Phys. Lett.* **2010,** *97,* 241902. doi:10.1063/1.3519849
11. Robledo, L.; Childress, L.; Bernien, H.; Hensen, B.; Alkemade, P. F. A.; Hanson, R. *Nature* **2011,** *477,* 574–578. doi:10.1038/nature10401
12. Siyushev, P.; Pinto, H.; Gali, A.; Jelezko, F.; Wrachtrup, J. Low temperature studies of charge dynamics of nitrogen–vacancy defect in diamond. 2012, arXiv:1204.4898v1 [quant-ph].
13. Kahl, M.; Thomay, T.; Kohnle, V.; Beha, K.; Merlein, J.; Hagner, M.; Halm, A.; Ziegler, J.; Nann, T.; Fedutik, Y.; Woggon, U.; Artemyev, M.; Pérez-Willard, F.; Leitenstorfer, A.; Bratschitsch, R. *Nano Lett.* **2007,** *7,* 2897–2900. doi:10.1021/nl071812x
14. Thomay, T.; Hanke, T.; Tomas, M.; Sotier, F.; Beha, K.; Knittel, V.; Kahl, M.; Whitaker, K. M.; Gamelin, D. R.; Leitenstorfer, A.; Bratschitsch, R. *Opt. Express* **2008,** *16,* 9791–9794. doi:10.1364/OE.16.009791
15. Aharonovich, I. Novel single photon emitters based on color centers in diamond. Ph.D. Thesis, School of Physics, University of Melbourne, Australia, 2010.
16. Zaitsev, A. M. *Optical Properties of Diamond – A Data Handbook;* Springer: Berlin Heidelberg New York, 2001.
17. Gaebel, T.; Popa, I.; Gruber, A.; Domhan, M.; Jelezko, F.; Wrachtrup, J. *New J. Phys.* **2004,** *6,* 98. doi:10.1088/1367-2630/6/1/098
18. Steinmetz, D.; Neu, E.; Meijer, J.; Bolse, W.; Becher, C. *Appl. Phys. B: Lasers Opt.* **2011,** *102,* 451–458. doi:10.1007/s00340-011-4402-x
19. Wolfer, M.; Kriele, A.; Williams, O. A.; Obloh, H.; Leancu, C.-C.; Nebel, C. E. *Phys. Status Solidi A* **2009,** *207,* 2012–2015. doi:10.1002/pssa.200982231
20. Wolfer, M.; Obloh, H.; Williams, O. A.; Leancu, C.-C.; Kirste, L.; Gheeraert, E.; Nebel, C. E. *Phys. Status Solidi A* **2010,** *207,* 2054–2057. doi:10.1002/pssa.201000364
21. Rabeau, J. R.; Chin, Y. L.; Prawer, S.; Jelezko, F.; Gaebel, T.; Wrachtrup, J. *Appl. Phys. Lett.* **2005,** *86,* 131926. doi:10.1063/1.1896088
22. Wu, E.; Rabeau, J. R.; Roger, G.; Treussart, F.; Zeng, H.; Grangier, P.; Prawer, S.; Roch, J.-F. *New J. Phys.* **2007,** *9,* 434. doi:10.1088/1367-2630/9/12/434

23. Lal, S.; Dallas, T.; Yi, S.; Gangopadhyay, S.; Holtz, M.; Anderson, F. G.
Phys. Rev. B **1996,** *54,* 13428–13431.
doi:10.1103/PhysRevB.54.13428

24. Füner, M.; Wild, C.; Koidl, P. *Appl. Phys. Lett.* **1998,** *72,* 1149–1151.
doi:10.1063/1.120997

25. Wolfer, M. Mikro-Photolumineszenz an fluoreszierenden Defektzentren
in CVD-gewachsenen einkristallinen Diamantschichten. Ph.D. Thesis,
University of Freiburg, Germany, 2012.

26. Hees, J.; Kriele, A.; Williams, O. A. *Chem. Phys. Lett.* **2011,** *509,*
12–15. doi:10.1016/j.cplett.2011.04.083

27. Layevski, E. Characterization and enhancement of luminescent defects
in CVD diamond. Master Thesis, University of Freiburg, Germany,
2011.

Plasmonic oligomers
in cylindrical vector light beams

Mario Hentschel[1,2], Jens Dorfmüller[1], Harald Giessen[*1], Sebastian Jäger[3],
Andreas M. Kern[3], Kai Braun[3], Dai Zhang[3] and Alfred J. Meixner[3]

Abstract

We investigate the excitation as well as propagation of magnetic modes in plasmonic nanostructures. Such structures are particularly suited for excitation with cylindrical vector beams. We study magneto-inductive coupling between adjacent nanostructures. We utilize high-resolution lithographic techniques for the preparation of complex nanostructures consisting of gold as well as aluminium. These structures are subsequently characterized by linear optical spectroscopy. The well characterized and designed structures are afterwards studied in depth by exciting them with radial and azimuthally polarized light and simultaneously measuring their plasmonic near-field behavior. Additionally, we attempt to model and simulate our results, a project which has, to the best of our knowledge, not been attempted so far.

Introduction

Plasmonics is the optics of metal nanoparticles. If an external light field impinges on a metal nanoparticle, collective oscillations of the quasi-free conduction electrons are excited. The electron charge cloud is displaced with respect to the fixed ionic background and thus causes local electric fields. The main benefit afforded by plasmonics is its ability to concentrate incoming electromagnetic energy into deep subwavelength volumes, so-called hot spots. The local electric-field strength

can surpass the incoming field strength by orders of magnitude. The process is moreover surprisingly efficient as the plasmonic resonances couple extremely well to an external light field due to the huge resonant dipole moment, which is fundamentally connected to the large number of free conduction electrons.

Just as atoms join together in order to form molecules, plasmonic particles can couple to one another and form collective

states. In molecular physics this coupling is mediated via the electron wavefunctions, which mix and hybridize giving rise to new collective orbitals [1]. In plasmonics this coupling is mediated by the plasmonic near fields. In contrast to molecular physics, plasmonics allows us to nearly arbitrarily change the spatial arrangement, the number, and the properties of the constituent particles [2,3]. We can thus tailor the light–matter interaction at will and create novel optical components and devices [4-8].

We investigated the excitation as well as propagation of magnetic modes in such plasmonic nanostructures. We studied the magneto-inductive coupling between adjacent nanostructures and derived the necessary prerequisites for the efficient launch of magnetic plasmon propagation. In our experiments we utilized high-resolution electron-beam lithography for the fabrication of the nanostructures. In order to study the excitation of magnetic modes we used a home-built combined near-field scanning and confocal microscope. The structures were excited with azimuthally and radially polarized light, which allows for an efficient excitation of the fundamental magnetic modes. All these concepts and devices are going to be introduced and discussed in detail in the following.

Results and Discussion
Azimuthal and radial fields: theoretical description

Azimuthal and radial laser modes, also known as cylindrical vector beams, create unique field distributions when focused by high numerical aperture (NA) parabolic mirrors or objective lenses, as depicted in Figure 1. In such a high-NA focus of an azimuthally polarised beam, only in-plane polarized fields are present. By focusing the radially polarized laser beam, a distinctively different field distribution is present. Here a strong *z*-polarized field is present in the center surrounded by a weak in-plane polarized field. The ratio between the *z*- and in-plane polarized field is directly correlated with the NA [9,10].

The calculation of the interaction of radially and azimuthally polarized light with plasmonic nanostructures is a surprisingly complex problem. The mainly utilized methods, such as FDTD, are particularly suited and optimized for plane-wave excitation. Radial and azimuthal fields, however, require a special basis set as they can no longer be described with a single *k*-vector but show a strong variation in direction and magnitude of the *k*-vector contributions in the tight focus of the incoming radiation. Simulation techniques such as Fourier-modal methods, however, are covered by extended fields with discrete *k*-vectors. Thus, the problem cannot be implemented by using these simulation techniques. The huge computational power that would be required to solve the resulting multiscale problems is simply unavailable.

Starting from this need, we developed two sets of techniques in order to tackle the problem at hand. One possibility relies on the so-called multiple-multipole method (MMP). It is a semi-analytical simulation theory based on Mie scattering. The simulated field distribution is described by a sum of distributed expansions, which are analytical solutions of Maxwell's equations, and the coefficients of the expansions are solved at the

Figure 1: (a) and (b) show sketches of simulated focus patterns (E^2 in *xz* plane) in the parabolic mirror and their intensity profile. Adapted from [11].
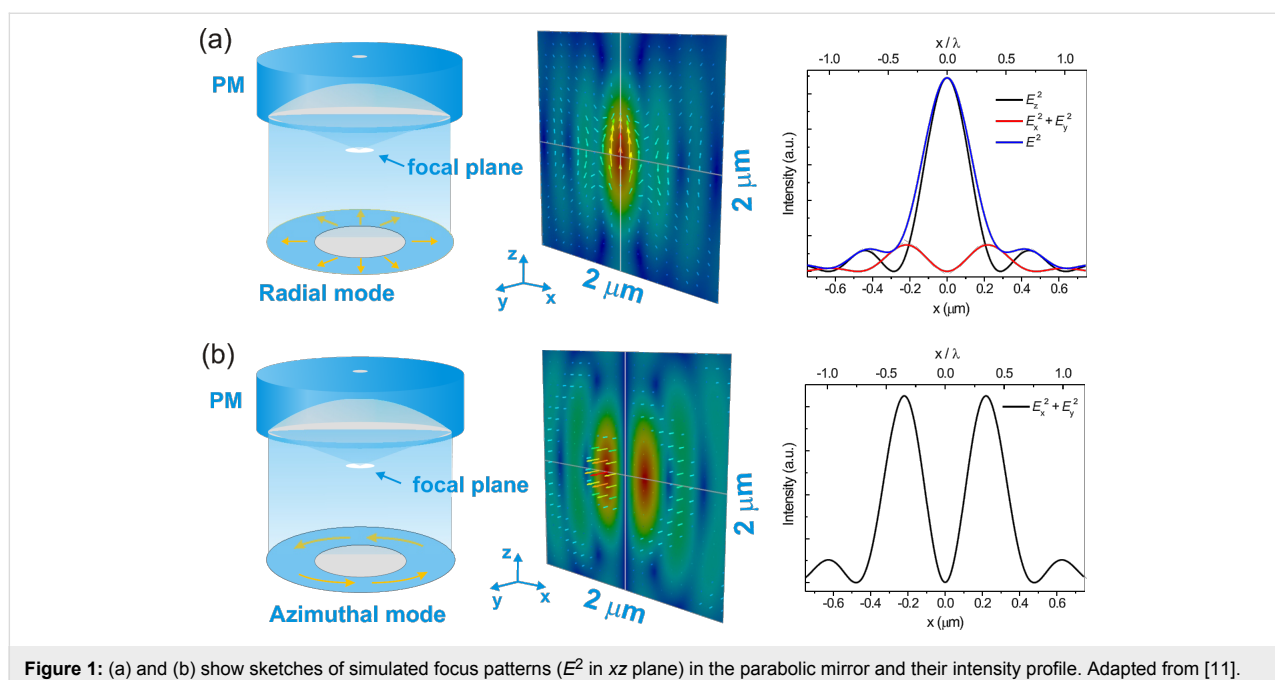
boundaries. In particular, the technique takes advantage of the high symmetry of the clusters, which significantly eases the required computational power. Once the correct expansion has been found, the field distributions as well as the far-field scattering spectra can be calculated from the analytical solutions of Mie theory.

Another description has been developed by using the surface integral equation (SIE) method. This approach uses Green's functions to describe the propagation of an electromagnetic field in homogeneous media and can thus reduce the computational domain to material interfaces. Enforcing the boundary conditions at the material boundaries, the surface fields can be computed for arbitrary incident conditions. Given these surface fields, the field distribution in the surrounding space can then be derived.

A big advantage of the SIE method is the use of continuous basis functions to describe the surface fields. This leads to a physical solution of a boundary value problem at the interfaces, yielding accurate field distributions even in the extreme near field of the particles. Due to the definition of the Green's functions up to infinite distances, the field distribution is accurately reproduced in the far field as well. In addition, as the space surrounding the particles does not need to be discretized, implementation of arbitrary incident conditions, such as cylindrical vector beams, is a simple task.

Plasmonic oligomers

Originally, we intended to utilize split-ring resonators (SRR) as magnetic atoms. These U-shaped nanostructures support a plasmonic mode which is associated with a strong magnetic moment. Arranging SRRs in a chain and thus coupling these modes would allow for a magnetic-plasmon propagation and hence for efficient and low-loss energy propagation on the nanoscale. Yet, the experimental realization of such structures

that exhibit a resonant response in the required wavelength regime around 630 nm proved to be too challenging.

We thus developed an alternative route, which proved to be highly fruitful, cf. Figure 2. By replacing the closed metal-rings of the SRRs by individual but strongly coupled metal nanoparticles, we were able to retain a number of the described properties of the SRRs and yet drastically blue-shift the resonant optical response of the resulting clusters. The ring-shaped arrangements of the gold nanoparticles are ideally matched to the radially and azimuthally polarized excitation and form collective plasmonic modes exhibiting electric as well as magnetic nature. Moreover, these clusters support a multitude of *tunable collective modes*, which justify studying these kinds of plasmonic artificial molecules themselves in detail, even under linearly polarized light [12-16].

In the following we briefly review earlier work on plasmonic oligomers [13]. In order to investigate the evolution of the coupling behavior in plasmonic oligomers, we studied the optical response of a series of nanoparticle oligomers with various interparticle gap distances, cf. Figure 3. The interparticle gap distance g was decreased from 130 to 20 nm. For excitation of the structures, we used normal incident light with linear polarization, as shown in Figure 3, left column. The experimental spectra of the samples and their corresponding SEM images are displayed in the same figure. The spectrum of the gold monomer is plotted as a black curve in the bottom row. A single dipolar resonance is observed around 700 nm (the curve is magnified by a factor of 5 for better comparability). Turning toward the heptamer with a large interparticle gap distance ($g = 130$ nm), the spectrum shows approximately the same behavior as the isolated nanoparticle due to the well-separated nanoparticle configuration. This would correspond in molecular chemistry to the situation of uncoupled atoms before they start to form molecular bonds. As the interparticle gap dis-

Figure 2: (a) Replacing the split ring resonators with individual plasmonically coupled gold dots allows us to spectrally shift the supported modes while retaining most of the optical properties. (b) Additionally, ring-like arrangements of gold nanoparticles are particularly suited for experiments with radially and azimuthally polarized light as they are perfectly matched to their high spatial symmetry.

tance is reduced (*g* = 60 nm), a second peak starts to form around 800 nm. The two peaks are separated by a pronounced dip. As the interparticle gap distance is further reduced towards *g* = 20 nm, the spectral features red-shift successively. In the ring-like hexamer (*g* = 40 nm), which we display for comparison (see the top black spectrum), the shorter-wavelength peak around 700 nm is also present. In contrast to the heptamers, no pronounced dip is visible in the hexamer. We rather observe a long and unstructured tail toward the long-wavelength region.

the experimental and simulated results is also partially due to the assumption of a nanosphere shape for the trapezoidal nanoparticles in the simulation. Nevertheless, all the main spectral features including the distinct resonance dip are clearly predicted.

In order to elucidate the character of the resonances, field distributions at the respective spectral positions are shown in Figure 4. In the hexamer structure, at spectral positions 1, 2, and 3, the currents in the six nanoparticles always oscillate in-phase, manifesting the excitation of the collective dipolar plasmon resonance in the ringlike hexamer. In the heptamer structure, when a central nanoparticle is brought into close proximity with the six satellite nanoparticles, the dipolar plasmon of the central nanoparticle hybridizes with the hexamer dipolar plasmon, giving rise to the formation of a bright super-radiant collective mode and a dark subradiant collective mode. For the super-radiant mode, the oscillating plasmons in the seven nanoparticles are in-phase (see field distributions at spectral positions 1 and 3), exhibiting significant mode broadening due to radiative damping.

Figure 3: Extinction spectra of a gold monomer, a gold hexamer, and gold heptamers with different interparticle gap separations. The spectra are shifted upward for clarity. (left column) Experimental extinction spectra (1 − transmittance). (middle column) SEM images of the corresponding samples with indicated interparticle gap distances. The scale-bar dimension is 500 nm. (right column) Simulated extinction cross-section spectra by using the multiple-multipole method. Adapted with permission from [13]. Copyright (2010) American Chemical Society.

It is worth mentioning that the peak position of the super-radiant mode cannot be exactly determined from the spectrum due to the presence of the resonance dip. Nevertheless, the resonant behavior at positions 1 and 3 is a good indication for the super-radiant mode. For the subradiant mode, the net sum of the plasmon polarizations of the six satellite nanoparticles oscillates oppositely with respect to the plasmon polarization in the central nanoparticle (see field distribution at spectral position 2). The unique symmetry of the heptamer allows for similar yet opposite dipole moments of the central nanoparticle and the ringlike hexamer, thus leading to a narrow mode. The formation of the distinct dip in the spectrum is due to the destructive interference between the narrow subradiant mode and the broad super-radiant mode, which is called a Fano resonance [18-20].

The oligomeric design strategy is highly tunable and allows us to nearly arbitrarily manipulate the optical spectra. Figure 5a depicts SEM micrographs and spectra of exemplary oligomers. Changing the number, size, and spatial arrangement of the individual particles, allows for the tuning of the strength and spectral position of the transparency window. Under certain conditions, the Fano resonance even vanishes completely [21].

Figure 3 as well presents the simulated extinction spectra for different structures. The spectra have been calculated by using the MMP method [17]. It is apparent that the experimental results show a good qualitative agreement with the numerical predictions. The overall red shift of the experimental spectra with respect to the simulated spectra is due to the presence of the glass substrate in the experiment. The difference between

Electron-beam lithography is a highly controllable top-down technique that can be utilized in order to fabricate the structures. Nearly every manipulation in the design of the cluster can be easily implemented. Figure 5b depicts a collection of SEM micrographs that demonstrate our ability to create nearly every arrangement imaginable [22-26].
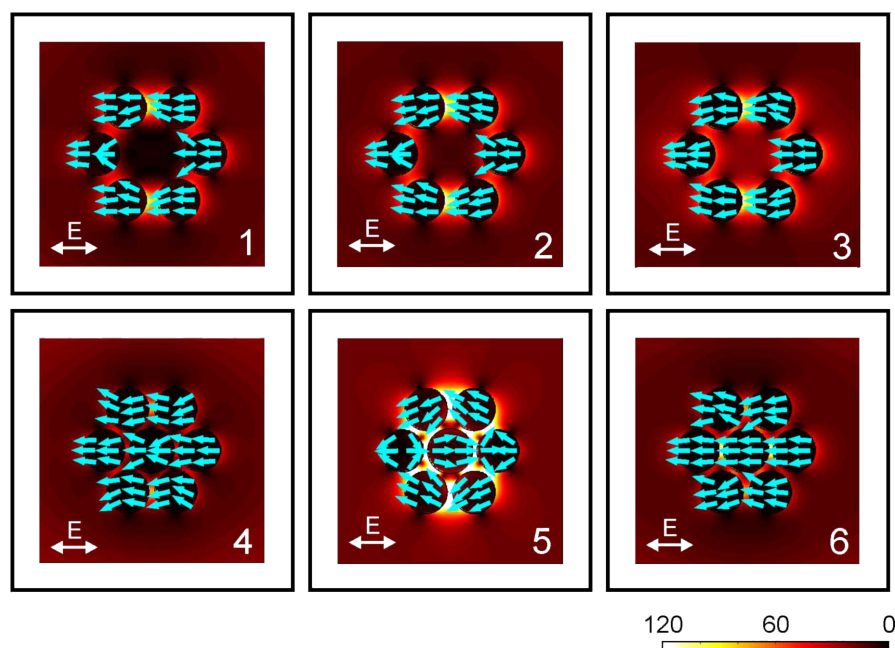
Figure 4: Simulated field distributions and local electric currents (blue arrows) for the gold hexamer and heptamer at the respective spectral positions (as indicated by the arrows in the simulated spectra) by using the multiple-multipole method. The color scale indicates the absolute value of the electric field relative to the external exciting field strength. It is notable that at spectral position 5 in the heptamer, similar yet opposite oscillating plasmons are excited in the central nanoparticle and the ringlike hexamer, thus leading to a subradiant mode. The destructive interference between the subradiant mode and the broad super-radiant mode results in the Fano resonance. In the absence of the central nanoparticle, the nanoparticles in the hexamer always oscillate in phase, leading to a collective dipolar mode. Adapted with permission from [13]. Copyright (2010) American Chemical Society.
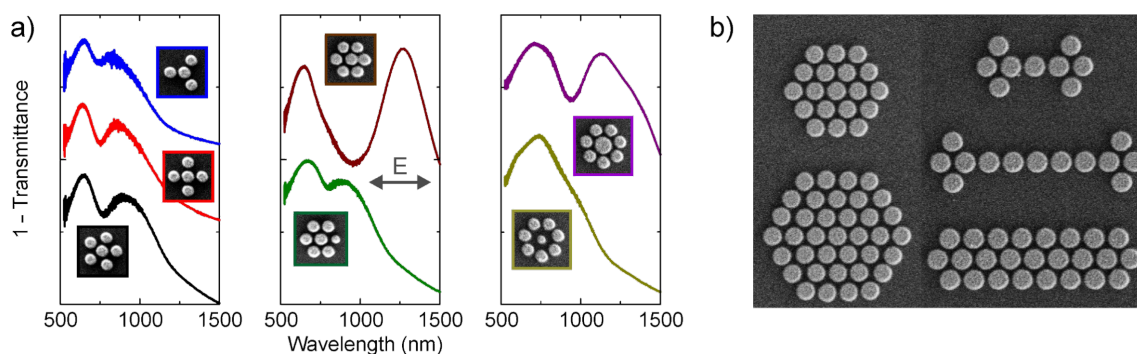
Figure 5: (a) Examples of complex plasmonic oligomers with tailorable optical properties. Adapted with permission from [21]. Copyright (2011) American Chemical Society. (b) Scanning-electron micrographs of oligomers clusters, demonstrating the unique capability of electron-beam lithography to create many of the different spatial arrangements imaginable.

The optical near-field microscope

The studies of the optical behavior of the plasmonic oligomers with focused radially and azimuthally polarized laser beams were performed on home-built combined near-field scanning and confocal microscopes. The exciting laser is in both cases a 632.8 nm HeNe laser, where the beam is transformed by a mode conversion into radially or azimuthally polarized cylindrical vector beams. One of the microscopes uses an oil immersion objective lens (NA of 1.25) for focusing. The other microscope

uses a parabolic mirror with an NA of 0.998 as the focusing element (Figure 6). Based on these confocal microscopes, in combination with a home-built shear force AFM system and the use of sharp gold or glass-fiber tips, we operate a versatile scanning near-field optical microscope (SNOM) system.

To measure the near field generated from the plasmonic oligomers, one single oligomer is placed inside the radially or azimuthally polarized focus. A sharp gold tip (tip radius smaller

Figure 6: Schematic of two optical microscopic configurations using a parabolic mirror for focusing (a, adapted from [27]) and an objective lens for focusing (b). Shear-force SNOM configurations can be obtained by integrating a glass fiber (c) or a gold tip (d) to the confocal optical microscopes.
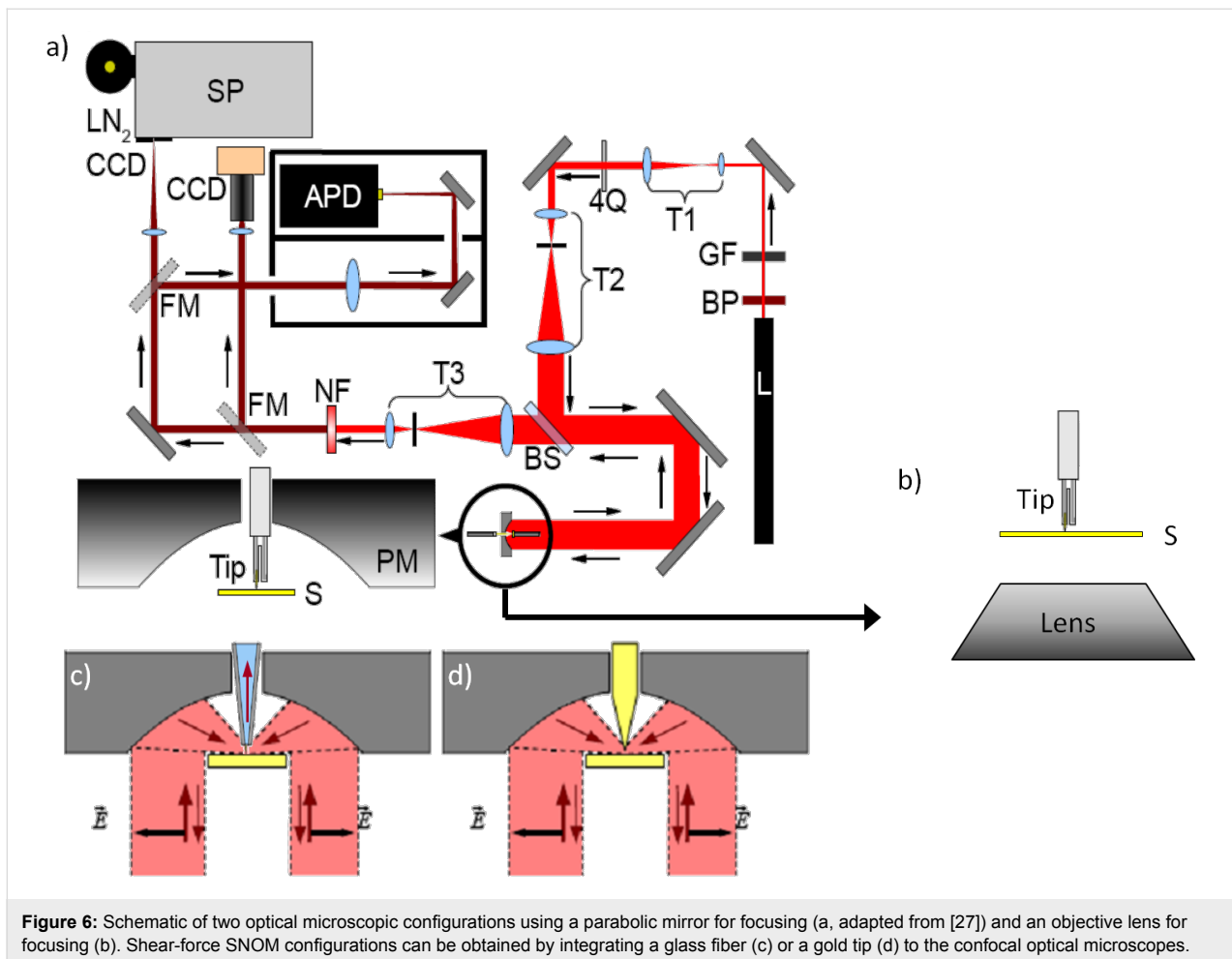
than 15 nm) is used to scan over the structure, collecting the near-field responses. Notably, the sharp gold tip also gives a strong photoluminescence signal, whose intensity is linearly proportional to the local field strength at the plasmonic structures.

Experiments and simulation of near-field imaging of plasmonic oligomer rings using gold luminescence

We excited the plasmonic oligomer rings with radially and azimuthally polarized light at 632.8 nm. The excitation was performed by utilizing a parabolic mirror with an NA = 0.998. The detection was performed by confocal microscopy and the collected signal is one-photon photoluminescence.

Figure 7 depicts examples of these kinds of measurements on closed and open oligomer ring structures. One observes a strong interaction of the light field with the plasmonic nanostructures, resembling a "magnetic focusing", featuring a central spot of enhanced intensity with a diameter of ca. 340 nm. The reason for this behavior is as follows: The luminescence signal is

generated by the individual gold dots, which in turn have been excited by the external light filed. Thus, the signal strength is given by the superposition of the excitation spot and its intensity distribution with the geometry of the oligomer rings. A convolution of these two quantities describes the observed phenomenon.

Near-field microscopy of aluminium heptamers

During the progress of our experiments we found that the gold structures show substantial photoluminescence [28-30]. For some of the conducted experiments, as discussed above, this phenomenon is beneficial, yet, it turned out to be mostly bothersome. In order to circumvent this problem, we designed oligomer structures consisting of aluminium. The new material affords two benefits: on the one hand the photoluminescence of aluminium is significantly smaller than the one of gold. On the other hand the significantly higher plasma frequency of aluminium causes the plasmonic resonances to blue-shift for identical particle sizes, easing fabrication. Figure 8 depicts spectra, SEM, and optical micrographs of these structures.

Figure 7: Oligomer rings composed of gold nanodots, SEM images on the left, confocal luminescence images under azimuthally polarized illumination on the right. Lower row: Simulations based on a planar convolution of the exciting light field with the structure geometry. The left image depicts the one-photon photoluminescence image upon azimuthal excitation. This geometry corresponds to the measured configuration shown in the upper row. The right image shows the predicted signal upon radial excitation. The lowest row depicts once more a simplified sketch of the used polarization states.

Figure 8: Oligomer structures consisting of aluminium. (a) The formation of collective behavior in the clusters is visible by the formation of a well-pronounced Fano resonance. (b) Varying the number of ring particles allows us to study the evolution of the spectra. Starting from a certain number of ring particles one expects the spectral evolution to saturate, similarly to the transition from a molecule to a solid. (c) The individual clusters are surrounded by marker structures, allowing easy location of the structures on the substrate during measurement.

Simulation of the near-fields of plasmonic oligomers under radially and azimuthally polarized excitation

Utilizing the above-discussed surface-integral method [31-33] we were able to calculate the electric near-field distributions of a plasmonic oligomer under radial and azimuthal excitation. The upper row of Figure 9 depicts the near-field intensity distribution within the symmetry plane of the cluster; the lower row shows a 3-D plot of the same data. In both excitation geometries we observe a strong near-field enhancement resembling the high symmetry of the cluster itself. The strong enhancement, as well as the strong local fields, is proof that we indeed excite the cluster with its eigenpolarizations. Such near-field patterns, in strength as well as spatial distribution, are not obtainable upon linear polarized excitation. The field enhancement for azimuthal excitation is significantly stronger as it perfectly matches the nanoscale gaps at the circumference of the cluster. The field is mostly concentrated within these gaps, whereas nearly no field localization is associated with the center particle. This behavior is in striking contrast to the case of linear-polarized excitation (cf. Figure 2, right column). In the case of radial excitation the near fields are mostly confined to the gap between the outer particles and the center one. Overall, the field distribution again resembles the cluster symmetry.
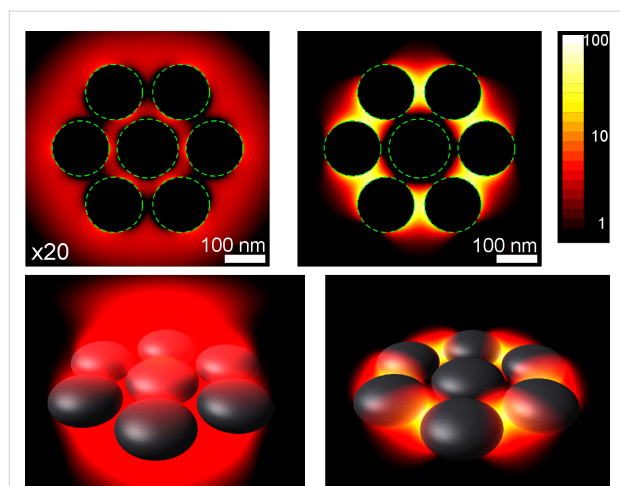

Figure 9: Simulated near-fields of heptamer structures under radial (left, multiplied by 20 for a better comparability) and azimuthal (right) excitation. The upper row depicts the field strength in the center plan, whereas the lower row depicts the same data as a 3-D plot. One can clearly observe the strong enhancement of the electric fields between, within the nanoscale gaps. The overall field strength is significantly higher for azimuthal excitation as this perfectly fits the symmetry of the cluster and the arrangement of the gaps.

Magnetic plasmon propagation along oligomer chains

Oligomers support magnetic modes. Hence, it is a straightforward idea to combine these kinds of structures to form chains, which then in turn allow for the coupling between these modes and thus the transport of energy along the chains. As the coupling will be mediated by the coupling between magnetic dipoles, the transport is expected to show low loss [34,35]. However, measuring such magnetic plasmon propagation requires local excitation at one of its ends and the near-field distributions to be measured along the whole chain [36-38]. This measurement technique requires the separation of the excitation and collection foci, which is experimentally extremely challenging.

Conclusion

We presented a route to create magnetic excitations and propagation on the nanoscale by utilizing individual yet strongly near-field coupled plasmonic atoms. These atoms join together and form collective plasmonic modes which are associated with strong magnetic moments. Arranging these plasmonic molecules in a chain and thus coupling these modes allows for magnetic plasmon propagation and, hence, for efficient and low-loss energy propagation on the nanoscale.

We have demonstrated our ability to create plasmonic molecules with tailorable optical properties. We studied these molecules using far- and near-field measurement techniques. In particular, we observed the transition from isolated to collective modes upon decreasing the interparticle gap. We were able to directly measure the near-field distributions of our plasmonic molecules with cylindrical vector light beams, which, to the best of our knowledge, had not been demonstrated before.

Moreover, we have developed simulation techniques in order to model our results on these complex structures, which constitute a significant advance in the understanding of the interaction of our unconventional states of polarization with the complex plasmonic structures.

Acknowledgements

References

1. Haken, H.; Wolf, H. C. *Molecular physics and elements of quantum chemistry;* Springer: Berlin, 2003.
2. Halas, N. J.; Lal, S.; Chang, W.-S.; Link, S.; Nordlander, P. *Chem. Rev.* **2011,** *111,* 3913–3961. doi:10.1021/cr200061k
3. Liu, N.; Giessen, H. *Angew. Chem., Int. Ed.* **2010,** *49,* 9838–9852. doi:10.1002/anie.200906211
4. Ament, I.; Prasad, J.; Henkel, A.; Schmachtel, S.; Sönnichsen, C. *Nano Lett.* **2012,** *12,* 1092–1095. doi:10.1021/nl204496g
5. Zijlstra, P.; Paulo, P. M. R.; Orrit, M. *Nat. Nanotechnol.* **2012,** *7,* 379–382. doi:10.1038/nnano.2012.51

6. Gansel, J. K.; Thiel, M.; Rill, M. S.; Decker, M.; Bade, K.; Saile, V.; von Freymann, G.; Linden, S.; Wegener, M. *Science* **2009,** *325,* 1513–1515. doi:10.1126/science.1177031

7. Niesler, F. B. P.; Gansel, J. K.; Fischbach, S.; Wegener, M. *Appl. Phys. Lett.* **2012,** *100,* 203508. doi:10.1063/1.4714741

8. Rodríguez-Lorenzo, L.; de la Rica, R.; Álvarez-Puebla, R. A.; Liz-Marzán, L. M.; Stevens, M. M. *Nat. Mater.* **2012,** *11,* 604–607. doi:10.1038/nmat3337

9. Lieb, M. A.; Meixner, A. J. *Opt. Express* **2001,** *8,* 458–474. doi:10.1364/OE.8.000458

10. Novotny, L.; Hecht, B. *Principles of Nano Optics;* Cambridge University Press: Cambridge, New York, 2006. doi:10.1017/CBO9780511813535

11. Wang, X. Confocal and Near-field Optical Microscopy and Spectroscopy of Organic Materials: from Molecules to Thin Solid Films. Ph.D. Thesis, University of Tübingen, Germany, 2011.

12. Fan, J. A.; Wu, C.; Bao, K.; Bao, J.; Bardhan, R.; Halas, N. J.; Manoharan, V. N.; Nordlander, P.; Shvets, G.; Capasso, F. *Science* **2010,** *328,* 1135–1138. doi:10.1126/science.1187949

13. Hentschel, M.; Saliba, M.; Vogelgesang, R.; Giessen, H.; Alivisatos, A. P.; Liu, N. *Nano Lett.* **2010,** *10,* 2721–2726. doi:10.1021/nl101938p

14. Lassiter, J. B.; Sobhani, H.; Fan, J. A.; Kundu, J.; Capasso, F.; Nordlander, P.; Halas, N. J. *Nano Lett.* **2010,** *10,* 3184–3189. doi:10.1021/nl102108u

15. Frimmer, M.; Coenen, T.; Koenderink, A. F. *Phys. Rev. Lett.* **2012,** *108,* 077404. doi:10.1103/PhysRevLett.108.077404

16. Rahmani, M.; Lei, D. Y.; Giannini, V.; Lukiyanchuk, B.; Ranjbar, M.; Liew, T. Y. F.; Hong, M.; Maier, S. A. *Nano Lett.* **2012,** *12,* 2101–2106. doi:10.1021/nl3003683

17. Hafner, C. *Phys. Status Solidi B* **2007,** *244,* 3435–3447. doi:10.1002/pssb.200743165

18. Luk'yanchuk, B.; Zheludev, N. I.; Maier, S. A.; Halas, N. J.; Nordlander, P.; Giessen, H.; Chong, C. T. *Nat. Mater.* **2010,** *9,* 707–715. doi:10.1038/nmat2810

19. Zentgraf, T.; Zhang, S.; Oulton, R. F.; Zhang, X. *Phys. Rev. B* **2009,** *80,* 195415. doi:10.1103/PhysRevB.80.195415

20. Linden, S.; Kuhl, J.; Giessen, H. *Phys. Rev. Lett.* **2001,** *86,* 4688–4691. doi:10.1103/PhysRevLett.86.4688

21. Hentschel, M.; Dregely, D.; Vogelgesang, R.; Giessen, H.; Liu, N. *ACS Nano* **2011,** *5,* 2042–2050. doi:10.1021/nn103172t

22. Dregely, D.; Hentschel, M.; Giessen, H. *ACS Nano* **2011,** *5,* 8202–8211. doi:10.1021/nn202876k

23. Liu, S.-D.; Yang, Z.; Liu, R.-P.; Li, X.-Y. *ACS Nano* **2012,** *6,* 6260–6271. doi:10.1021/nn3017052

24. Artar, A.; Yanik, A. A.; Altug, H. *Nano Lett.* **2011,** *11,* 3694–3700. doi:10.1021/nl201677h

25. Wen, F.; Ye, J.; Liu, N.; Van Dorpe, P.; Nordlander, P.; Halas, N. J. *Nano Lett.* **2012,** *12,* 5020–5026. doi:10.1021/nl302799h

26. Cui, Y.; Zhou, J.; Tamma, V. A.; Park, W. *ACS Nano* **2012,** *6,* 2385–2393. doi:10.1021/nn204647b

27. Sackrow, M. Confocal and near-field measurements with a parabolic mirror. Ph.D. Thesis, University of Tübingen, Germany, 2008.

28. Castro-Lopez, M.; Brinks, D.; Sapienza, R.; van Hulst, N. F. *Nano Lett.* **2011,** *11,* 4674–4678. doi:10.1021/nl202255g

29. Bouhelier, A.; Bachelot, R.; Lerondel, G.; Kostcheev, S.; Royer, P.; Wiederrecht, G. P. *Phys. Rev. Lett.* **2005,** *95,* 267405. doi:10.1103/PhysRevLett.95.267405

30. Wang, H.; Huff, T. B.; Zweifel, D. A.; He, W.; Low, P. S.; Wei, A.; Cheng, J.-X. *Proc. Natl. Acad. Sci. U. S. A.* **2005,** *102,* 15752–15756. doi:10.1073/pnas.0504892102

31. Gallinet, B.; Martin, O. J. F. *Photonics Nanostruct.* **2010,** *8,* 278–284. doi:10.1016/j.photonics.2010.05.003

32. Gallinet, B.; Kern, A. M.; Martin, O. J. F. *J. Opt. Soc. Am. A* **2010,** *27,* 2261–2271. doi:10.1364/JOSAA.27.002261

33. Kern, A. M.; Martin, O. J. F. *IEEE Trans. Antennas Propag.* **2010,** *58,* 2158–2161. doi:10.1109/TAP.2010.2046870

34. Liu, N.; Mukherjee, S.; Bao, K.; Brown, L. V.; Dorfmüller, J.; Nordlander, P.; Halas, N. J. *Nano Lett.* **2012,** *12,* 364–369. doi:10.1021/nl203641z

35. Liu, N.; Mukherjee, S.; Bao, K.; Li, Y.; Brown, L. V.; Nordlander, P.; Halas, N. J. *ACS Nano* **2012,** *6,* 5482–5488. doi:10.1021/nn301393x

36. Esteban, R.; Vogelgesang, R.; Dorfmüller, J.; Dmitriev, A.; Rockstuhl, C.; Etrich, C.; Kern, K. *Nano Lett.* **2008,** *8,* 3155–3159. doi:10.1021/nl801396r

37. Dorfmüller, J.; Vogelgesang, R.; Khunsin, W.; Rockstuhl, C.; Etrich, C.; Kern, K. *Nano Lett.* **2010,** *10,* 3596–3603. doi:10.1021/nl101921y

38. Dorfmüller, J.; Vogelgesang, R.; Weitz, R. T.; Rockstuhl, C.; Etrich, C.; Pertsch, T.; Lederer, F.; Kern, K. *Nano Lett.* **2009,** *9,* 2372–2377. doi:10.1021/nl900900r

Effect of normal load and roughness on the nanoscale friction coefficient in the elastic and plastic contact regime

Aditya Kumar[*§], Thorsten Staedler and Xin Jiang

Abstract

The influence of applied normal load and roughness on the tribological behavior between the indenter and sample surface during nanoindentation-based scratching has been experimentally investigated by using different surfaces (fused silica and diamond-like carbon) featuring various degrees of roughness. At a sufficiently low applied normal load, wherein the contact is elastic, the friction coefficient is constant. However, at increased normal loads the contact involves plastic deformation and the friction coefficient increases with increasing normal load. The critical load range for a transition from predominantly elastic to plastic contact, between the indenter and sample surface, increases with increasing size of indenter and decreases with roughness. Distinct differences between the present experimental results and the existing theoretical models/predictions are discussed.

Introduction

Understanding the contact phenomena underlying tribological processes is fundamental to many basic and applied problems, such as wetting, capillarity, adhesion, lubrication, sealing, hardness, micro/nanoindentation, atomic-scale probing, surface modification and manipulation [1-3]. The contact of two bodies may be defined by the influential parameters such as the applied load or contact force between the contacting bodies, real contact area, real contact pressure and its distribution over the contacting surface, and actual separation between both bodies.

Engineered surfaces are not perfectly smooth and possess finite roughness. Many of the existing models of rough surface topography are based on the relative distribution of asperities within the contact. In order to understand the effect of roughness, statistical rough surface contact modes have been introduced starting from the very early work of Abbot and Firestone in 1933 [4] for purely plastic contact and the classical work of Greenwood and Williamson in 1966 (GW model [5,6]) for purely elastic contact. According to the GW model, the estab-

lishment of elastic or plastic contact is independent of the applied normal load and only influenced by the physical properties of the contacting bodies. To account for elastic–plastic asperity contacts, Chang (CEB model [7,8]) extended the GW model to an elastic–plastic regime assuming the volume conservation law for asperities. However, the CEB model neglects the higher plasticity of the contact in resistance to the additional tangential loading. Later, Kogut and Etsion (KE model [9]) improved the CEB model by accounting for the resistance to sliding of plastically deformed asperities using the finite element method. According to them, the contact parameters, such as separation, real area of contact, and real contact pressure, are functions of the plasticity index and contact load. Their recent work [10] showed that the static friction coefficient (ratio of friction force and normal load) depends on the external force and nominal contact area. Recently, FEM based work by Flores et al. [11] showed that the apparent friction coefficient at a low level of normal load, featuring a predominantly elastic contact, is constant; and at a high level of load, featuring a predominantly plastic contact, is increased. However, this model underestimates the apparent friction coefficient, especially for the ultralow load regime, as the apparent friction coefficient decreases here with increasing load following Hertzian behavior. Another study [12] shows the effect of normal load on the friction coefficient. In this work the friction coefficient is defined as the slope of the friction force with respect to normal load [13]; it is observed that the coefficient of friction in the low load region of elastic deformation is less than that detected in the high load region of plastic deformation. Despite being based on physical and chemical principles as well as the huge amount of experimental work that has been carried out, up to now no complete understanding of the behavior of the friction force or friction coefficient with respect to the contact regime has been achieved, i.e., the effect of load and/or roughness on the friction coefficient is not fully understood for different contact modes. Today the technological progress in scanning-probe techniques opens up the potential to study contact phenomena on the single-asperity level [14]. Here scanning nanoindentation in particular allows for quantitative assessment of the forces involved.

In this paper, various scratch tests with different linearly increasing normal loads for surfaces featuring different roughness values (fused silica (FS) and diamond-like carbon (DLC)) have been carried out. Aside from the normal load, the tip radius of the conical diamond indenter has been varied in these experiments. The friction coefficients were measured and compared to the GW and the KE model as well as the FEM-based model mentioned above. The goal was to study the effect of the applied normal load and roughness on the friction coefficient and the critical normal load regime for a transition from a

predominantly elastic to a plastic contact between the indenter and surface of the sample during a nanoindentation-based scratch test with linearly increasing load.

Experimental

Samples: As mentioned above, fused silica and DLC were chosen as sample materials. The fused silica was provided as a standard sample by Hysitron Inc. The DLC samples, 1μm thick films on Si(100) wafer, were synthesized by chemical vapor deposition (Balzer BAS 450) utilizing a gas mixture of argon and acetylene at a bias voltage of −950 and −350 V, respectively.

Topographical characterization: The surface morphology was characterized by atomic force microscopy (AFM, Park Systems Corp. XE-100). Noncontact AFM was used to obtain detailed information about surface topography and surface roughness. The samples were imaged with commercial tips featuring a nominal tip radius of 10 nm in a feedback-controlled mode on all three axes. Five 8×8 μm^2 images with a pixel resolution of 512×512 were taken at different surface positions on each sample in order to derive the corresponding RMS roughness. The appropriate topography of the conical indenters utilized in the present work was also characterized. The resulting roughness of the 1 μm conical indenter was found to be negligible. The 20 μm conical indenter featured topography aside from the overall macroscopic conical one (with spherical end cap). However, its characteristic length scale was significantly larger than that of the samples studied here. For these reasons, we refrained from taking the indenter roughness into account in both cases.

Mechanical and tribological characterization: The mechanical and tribological sample characterization was carried out by a transducer-based scanning nanoindenter (TriboIndenter, Hysitron Inc.) in a laboratory environment (RT and 50% RH). The mechanical properties of the samples were evaluated with a Berkovich diamond tip following the procedure proposed by Oliver and Pharr [15,16]. The samples were probed at three different spots. At each spot 25 indents were placed in a grid pattern (5×5 indents with 20 μm spacing) varying in final load from 10 mN to 200 μN (100 μN/s loading and unloading rate, 5 s hold time at maximum load). Preceding the mechanical analysis, tribological tests were carried out with two conical diamond tips featuring nominal tip radii of 1 μm and 20 μm (90° cone opening angle). The corresponding real tip radii, determined by fitting of a Hertzian contact to low-load indents into fused silica, are 0.7 μm and 4.5 μm, respectively. Later on these real radii will be used in the context of all calculations. As preliminary testing confirmed that results are not influenced by the fashion of load ramping, i.e., increasing or decreasing load

during scratching, only unidirectional scratch tests with linearly increasing load were performed. One load and lateral displacement scheme of a scratch segment, which will be described below, is shown in Figure 1. For all scratch tests in the work presented here the scratch speed, minimum distance between two scratches, and number of scratches for a particular load were set to 1 µm/sec, 20 µm, and 10, respectively.
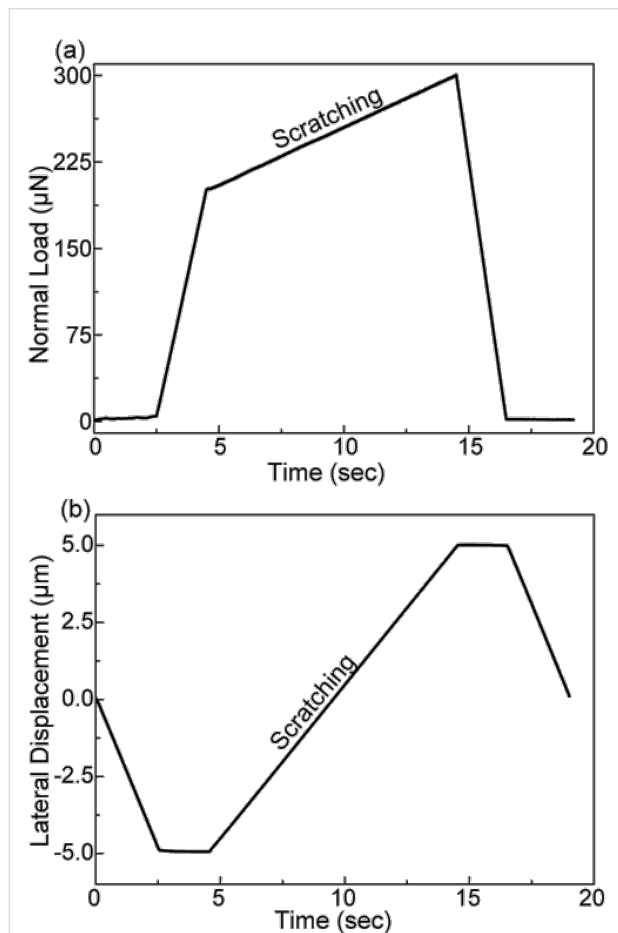
Figure 1: Example for a load (a) and displacement scheme (b) of one of the individual scratch segments used in this work.

In order to identify the suitable normal-load range, i.e., the range that did not feature any artifacts that may be dominated by instrumental boundary conditions, the total normal-load range of each scratch was divided into segments. For practical reasons these segments had to be small but at the same time had to contain an adequate number of data points to be analyzed. In this present case the segment size ranged from 300 µN to 20 µN depending on sample roughness and indenter radius. Here the 300 µN segment size corresponds to a scratch test of the smooth fused silica sample carried out with the large conical indenter, and the 20 µN segment size corresponds to a test of the rough DLC sample utilizing the small conical indenter. The suitable

load range was then defined as the range from the minimum normal load of 10 µN up to either the maximum normal load of the instrument, i.e., 10 mN, or the first segment that featured a maximum lateral-load difference larger than its segment size. The latter case usually can be attributed to some stick–slip event, which will contain a strong influence of the properties of the transducers spring setup. Therefore, such segments in the present work will not be considered. Once the normal load range was established, the slope of a linear trend line fit to each segment was taken as the coefficient of friction of the segment at a normal load equal to the center of the segments. This procedure ensures the elimination of any nonzero measured friction force that may be present at a normal load of zero, see Figure 2. This is usually explained by an additional load term due to an intrinsic adhesive force and/or artifacts generated by the equipment. The adhesion force term itself consists of various attractive forces such as capillary, electrostatic, van der Waals, and others.
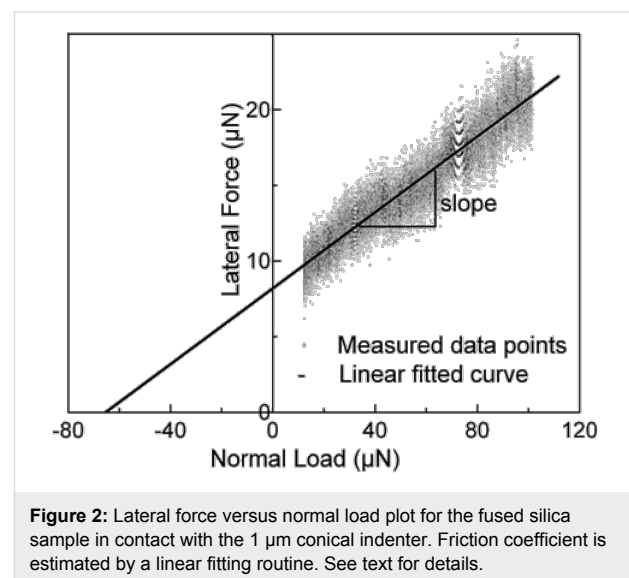
Figure 2: Lateral force versus normal load plot for the fused silica sample in contact with the 1 µm conical indenter. Friction coefficient is estimated by a linear fitting routine. See text for details.

Results

The roughnesses along with the mechanical properties of the samples are given in Table 1. Analyzing the tribological data, some distinct differences in the behavior of the three samples that are the subject of this work are revealed. In order to take a detailed look at the behavior of the friction coefficient with respect to the applied normal load, the corresponding results have been plotted for all three samples and are shown in Figure 3, Figure 4, and Figure 5. These figures also show the error bars that were measured from multiple test data. The friction coefficient for all three samples was always higher for the 20 µm radius conical indenter than for the 1 µm radius conical indenter. Generally a low friction coefficient is observed at an early stage of each scratch, i.e., low applied normal loads. An

Table 1: Topographical and mechanical properties of the fused silica, the smooth, and the rough DLC sample.

sample	hardness H (GPa)	reduced Young's modulus E^* (GPa)	roughness σ_s (nm)	curvature constant $k_s \times 10^{-3}$ (nm^{-1})	hardness coefficient K
FS	9.21 ± 0.29	69.55 ± 1.15	0.62 ± 0.02	2.93 ± 0.35	0.5237[a]
smooth DLC	21.44 ± 3.01	169.39 ± 11.82	4.05 ± 0.06	6.46 ± 0.21	0.577[b]
rough DLC	23.27 ± 5.58	187.26 ± 26.23	11.69 ± 0.66	4.06 ± 0.58	0.577[b]

[a]Poisson ratio v = 0.17; [b]v = 0.30
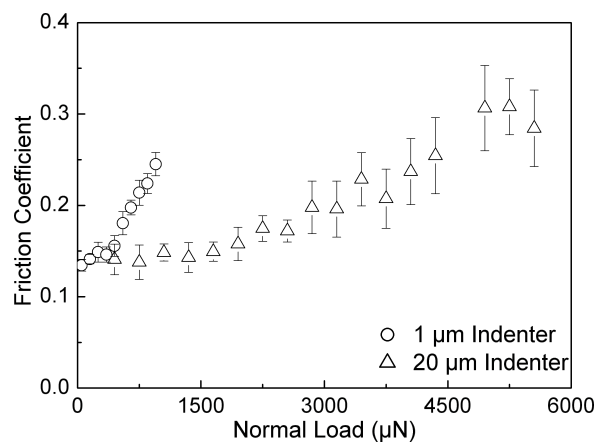
Figure 3: Friction coefficient versus normal load for the fused silica sample derived with both conical indenters. The error bars show the standard deviation of data.
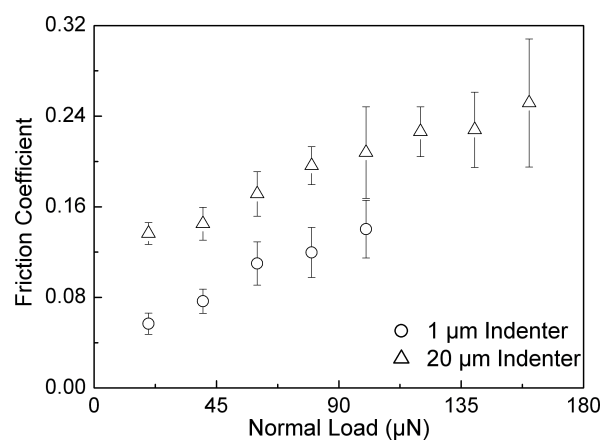
Figure 5: Friction coefficient versus normal load for the rough DLC sample derived for both conical indenters. The error bars show the standard deviation of the data.
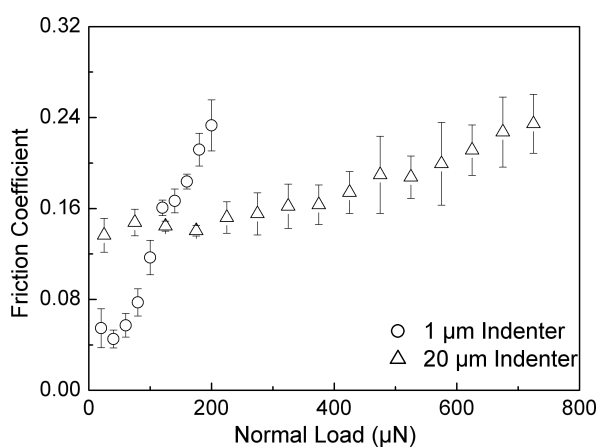
Figure 4: Friction coefficient versus normal load for the smooth DLC sample derived for both conical indenters. The error bars show the standard deviation of the data.

increase of the normal load during scratching typically results in an increased coefficient of friction. This increase can be either continuous as in case of the rough DLC sample, see Figure 5, or the increase is found only if the normal load exceeds some certain critical load. The actual critical load of a transition from a low, apparently constant coefficient of friction to the linearly increasing one depends on the sample material and the roughness as well as the indenter used.

It is generally accepted that these transitions correspond to a transition from a predominantly elastic to a predominantly plastic contact between the sample and the indenter. For this reason it is obviously not possible to provide precise normal-load numbers for such a transition, as the contact between two rough surfaces will typically feature asperities that are deformed elastically along with those that are already plastically deformed. Table 2 (see below) gives the appropriate ranges of normal loads during scratching for which the above-mentioned transitions have been observed in the experiments carried out here. Silica as well as the smooth DLC sample shows a transition between a predominantly elastic and a predominantly plastic contact. The observed values here are 400–500 μN and 1800–2100 μN as well as 50–70 μN and 200–250 μN for tests carried out with the 1 μm and the 20 μm conical diamond indenter on silica (Figure 3) as well as on the smooth DLC sample (Figure 4), respectively. For the rough DLC sample any load regimes featuring a predominantly elastic contact were not identified. Therefore, no transition was observed and a predomi-

Table 2: Plasticity indices and critical load ranges for the fused silica, the smooth DLC, and the rough DLC sample.

sample	plasticity index[a]	plasticity index[b]	1 µm indenter		20 µm indenter		approximated critical load range (µN)	
			$25\varepsilon^2R^2\sigma$ (µN)	$225\varepsilon^2R^2\sigma$ (µN)	$25\varepsilon^2R^2\sigma$ (µN)	$225\varepsilon^2R^2\sigma$ (µN)	1 µm indenter	20 µm indenter
FS	0.32 ± 0.02	0.39 ± 0.02	68.55	616.95	2832.98	25496.77	400–500	1800–2100
smooth DLC	1.28 ± 0.03	1.41 ± 0.03	136.76	1230.83	5651.77	50965.98	50–70	200–250
rough DLC	1.75 ± 0.13	1.93 ± 0.14	136.66	1238.95	5647.68	51201.50	—	—

[a]Greenwood and Williamson model; [b]Kogut and Etsion model.

nantly plastic contact is established already at very low loads (Figure 5). It was also observed that the critical load range increases with increasing indenter size. These findings show that the combination of mechanical properties, sample roughness, and indenter radius are key parameters in determining the contact characteristics, i.e., whether the indenter is in a predominantly elastic or plastic contact, at a given normal load.

In order to take a closer look at the influence of roughness on the contact characteristics we calculated various plasticity indices that have been proposed in the literature. The first here is the one given by the GW model [5,6], $(E^*/H)(\sigma_s k_s)^{1/2}$, where H is the hardness, E^* is the reduced Young's modulus, σ_s is the surface roughness, and k_s is the curvature constant. In the case of the fused silica it was found to be less than unity, whereas both DLC samples feature plasticity indices greater than unity (Table 2). Another modified plasticity index given by the KE model [9] was calculated as $(2E^*/\pi KH)(\sigma_s k_s)^{1/2}$, where K represents the hardness coefficient ($K = 0.454 + 0.41\nu$) and ν is the Poisson ratio. In the present case, following these calculations, the plasticity index of 0.39 for silica ($\nu = 0.17$) and plasticity indices of 1.41 and 1.93 for smooth and rough DLC ($\nu = 0.30$), respectively, were obtained as shown in Table 2. The FEM-based work presented by Flores et al. [11] provides critical loads for a predominantly elastic (normal load $< 25\varepsilon^2R^2\sigma$) and predominantly plastic contact (normal load $> 225\varepsilon^2R^2\sigma$), where ε is yield strain, σ is yield strength, and R is the indenter radius. At intermediate normal loads ($25\varepsilon^2R^2\sigma$ to $225\varepsilon^2R^2\sigma$) the contact characteristic is a mixture between the two. These critical values for all three samples and both indenters are calculated. The results are also shown in Table 2. Although, the general trend of the friction coefficient with increasing normal load is experimentally verified, i.e., initial constant low value followed by a linearly increasing coefficient of friction after a critical normal-load range has been exceeded, the absolute values of the calculated and experimentally found load boundaries differ significantly. The most striking differences in this context are the load boundaries in the case of the smooth and rough DLC samples. The calculations lead to very similar boundaries for

both DLC samples, whereas the experimental tests show huge differences between the two. Here the smooth DLC sample showed a predominantly plastic contact regime. The rough DLC sample on the other hand featured no such regime in the normal-load range tested in this work.

Discussion

In this work the tribological contact behaviors between two conical diamond indenters and fused silica as well as diamond-like carbon samples featuring different roughness during nanoindentation-based scratch test carried out with linearly increasing normal load were investigated. The friction coefficients were segmentally calculated from the slope of a linear fit to the lateral force versus normal load. The friction coefficient is found to increase with the size of indenter due to obvious reasons of increasing contact area, and hence the critical load regime will change accordingly. The results were compared with predictions by the GW as well as the KE model. In both cases the models estimate a predominantly elastic contact for the tests on fused silica and predominantly plastic contact for both DLC samples. This could not be verified by experiments as the fused silica sample showed a transition from predominantly elastic to plastic contact and the smooth DLC sample featured a predominantly elastic contact regime. Therefore, both observations are in contradiction to the models.

The general trend of a transition from a predominantly elastic contact regime featuring a low constant friction coefficient, to a predominantly plastic contact characterized by an increasing friction coefficient with increasing load, suggested by FEM calculations of Flores et al., was experimentally reproduced. However, the load boundaries predicted by the FEM model significantly overestimate the ones that were experimentally found. In addition to that, the FEM model fails to reproduce the significant differences between the two DLC samples of different roughness.

In summary the results presented here show that to date the existing contact models are not able to simulate the behavior of

the friction coefficient during nanoindentation-based scratch tests. Especially the influence of sample roughness is not well understood. Therefore, the authors are in the process of carrying out a series of systematic tests on various samples featuring roughness variations allowing for a more detailed analysis of the effect of roughness on the load dependence of the coefficient of friction. The findings will be the content of a future publication.

Conclusion

In this work, the influence of the applied normal load and roughness on the tribological behavior between the indenter and sample surface using a nanoindenter has been studied. The transition from a predominantly elastic contact regime featuring a constant coefficient of friction to a predominantly plastic contact characterized by an increasing coefficient of friction with increasing load was experimentally observed. It was found that the critical load range for a transition from predominantly elastic to plastic contact increases with increasing size of indenter and decreases with surface roughness. The experimental results were compared with the predictions of the model by Greenwood and Williamson and the one by Kogut and Etsion, as well as the FEM-based model by Flores et al. None of the presently available theoretical models was able to quantitatively describe the experimental results.

Acknowledgements

References

1. Bhushan, B.; Israelachvili, J. N.; Landman, U. *Nature* **1997,** *374,* 607–616. doi:10.1038/374607a0
2. Gao, J.; Luedtke, W. D.; Gourdon, D.; Ruths, M.; Israelachvili, J. N.; Landman, U. *J. Phys. Chem. B* **2004,** *108,* 3410–3425. doi:10.1021/jp036362l
3. Bhushan, B. *Handbook of micro/nanotribology,* 2nd ed.; CRC Press: Boca Raton, FL, 1999.
4. Abbott, E. J.; Firestone, F. A. *Trans. ASME* **1933,** *55,* 569–572.
5. Greenwood, J. A.; Williamson, J. B. P. *Proc. R. Soc. London, Ser. A* **1966,** *295,* 300–319. doi:10.1098/rspa.1966.0242
6. Greenwood, J. A. Contact of Rough Surfaces. In *Fundamentals of Friction: Macroscopic and Microscopic Processes;* Singer, I. L.; Pollock, H. M., Eds.; Kluwer: Dordrecht, Boston, 1992; pp 37–56. doi:10.1007/978-94-011-2811-7_3
7. Chang, W. R.; Etsion, I.; Bogy, D. B. *J. Tribol.* **1987,** *109,* 257–263. doi:10.1115/1.3261348
8. Chang, W. R.; Etsion, I.; Bogy, D. B. *J. Tribol.* **1988,** *110,* 57–63. doi:10.1115/1.3261575
9. Kogut, L.; Etsion, I. *Tribol. Trans.* **2003,** *46,* 383–390. doi:10.1080/10402000308982641
10. Kogut, L.; Etsion, I. *J. Tribol.* **2004,** *126,* 34–40. doi:10.1115/1.1609488
11. Flores, S. E.; Pontin, M. G.; Zok, F. W. *J. Appl. Mech.* **2008,** *75,* No. 061021. doi:10.1115/1.2966268
12. Bhushan, B.; Kulkarni, A. V. *Thin Solid Films* **1996,** *278,* 49–56. doi:10.1016/0040-6090(95)08138-0
13. *Research in surface forces, Vol. 2;* Deryagin, B. V., Ed.; Consultants Bureau: New York, NY, 1996; p 312.
14. Binnig, G.; Quate, C. F.; Gerber, C. *Phys. Rev. Lett.* **1986,** *56,* 930–933. doi:10.1103/PhysRevLett.56.930
15. Fischer-Cripps, A. C. *Nanoindentation,* 2nd ed.; Springer: New York, NY, 2004.
16. Oliver, W. C.; Pharr, G. M. *J. Mater. Res.* **1992,** *7,* 1564–1583. doi:10.1557/JMR.1992.1564

Controlled deposition and combing of DNA across lithographically defined patterns on silicon

Zeinab Esmail Nazari and Leonid Gurevich[*]

Abstract

We have developed a new procedure for efficient combing of DNA on a silicon substrate, which allows reproducible deposition and alignment of DNA molecules across lithographically defined patterns. The technique involves surface modification of Si/SiO$_2$ substrates with a hydrophobic silane by using gas-phase deposition. Thereafter, DNA molecules are aligned by dragging the droplet on the hydrophobic substrate with a pipette tip. Using this procedure, DNA molecules were stretched to an average value of 122% of their contour length. Furthermore, we demonstrated combing of ca. 900 nm long stretches of genomic DNA across nanofabricated electrodes, which was not possible by using other available combing methods. Similar results were also obtained for DNA–peptide conjugates. We suggest this method as a simple yet reliable technique for depositing and aligning DNA and DNA derivatives across nanofabricated patterns.

Introduction

DNA is the subject of many investigations in different areas of nanotechnology research, ranging from genomic and biological studies [1,2] to the development of nanomachines and nanocircuits [3]. However, native double-stranded (ds) DNA is a flexible polymer that forms a random coil in aqueous solutions, hence hindering direct access for investigations and manipulations on DNA molecules unless they are straighten and immobi-

lized on an appropriate substrate. In this context, Bensimon et al. introduced a so-called molecular combing technique in 1994 as an effective way to achieve ordered alignments of DNA molecules stretched on a solid surface [4]. The alignment occurs in two major steps: first, a random-coiled dsDNA floating in solution is partially melted at the ends. The ends with the exposed hydrophobic core are then readily adsorbed to the

hydrophobic surface, hence anchoring the DNA molecules. Second, the meniscus is moved and the movement of the receding air–water interface leaves DNA behind, stretched on the dry substrate [4-6]. Once DNA is deposited and stretched on the surface, a wide variety of further manipulations on DNA become possible [7].

A number of different protocols have been devised based on the original technique proposed by Bensimon et al. They involve evaporation of a DNA solution [8,9], pulling a functionalized coverslip out of a DNA solution [10], using a filter paper [11], using a flow of nitrogen gas [12], pipette sucking [13], etc. Furthermore, several methods have been introduced that involved a combination of molecular combing with other techniques such as lithographic patterning [7]. For instance, Guan et al. used a combination of molecular combing with contact printing and soft lithography. With this method, it was possible to generate complex patterns of DNA on the substrate [14]. An important advantage of the combing method is that it does not require any prior modification of DNA. This makes it an excellent choice for the stretching of DNA on solid substrates for a variety of different applications. In addition to extensive applications in physics and nanoelectronics [7,8,15,16], many biomedical and genomic studies employ molecular combing as an effective tool for the generation of highly ordered alignments of DNA for various investigations, including gene mapping, DNA sequencing, and analysis [17,18].

Most combing methods reported so far involve substrates such as mica, glass, plastic, etc., which are more convenient for DNA deposition and DNA studies, whereas only a few have attempted to adapt the technique to silicon surfaces [11]. However, since silicon is the most common material in micro- and nanofabrication, the dream of DNA-based chips [15] will not come true unless techniques for the manipulation of DNA are optimized for silicon substrates. This inspired us to develop a more "silicon-technology-friendly" variation of a combing method that involves the use of modified silicon substrates and lithographic methods. In this procedure, silicon substrates are coated with a thin layer of a hydrophobic silane by gas-phase deposition. Figure 1 is a representation of the combing procedure used in this experiment.

In the method proposed here, the applied meniscus force is large enough to allow efficient combing of DNA across nanofabricated patterns as well. Stretching of DNA across nano-electrodes has been previously achieved by methods such as electric field immobilization [19,20]; yet no report has been published on the immobilization of DNA on electrodes by molecular combing. We also successfully applied this combing technique to achieve stretching of various DNA–peptide conju-
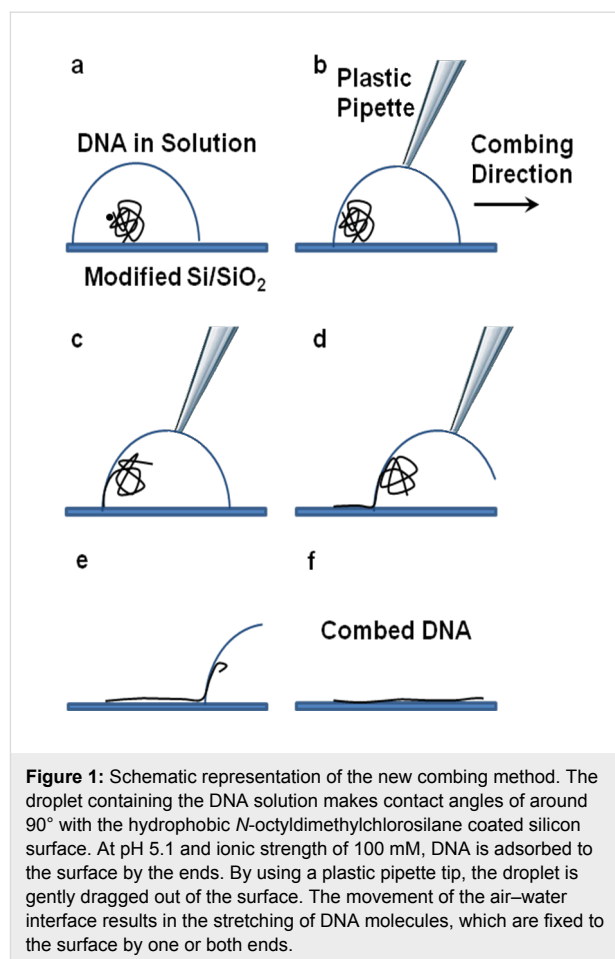
Figure 1: Schematic representation of the new combing method. The droplet containing the DNA solution makes contact angles of around 90° with the hydrophobic *N*-octyldimethylchlorosilane coated silicon surface. At pH 5.1 and ionic strength of 100 mM, DNA is adsorbed to the surface by the ends. By using a plastic pipette tip, the droplet is gently dragged out of the surface. The movement of the air–water interface results in the stretching of DNA molecules, which are fixed to the surface by one or both ends.

gates. These nanomaterials have been recently prepared by our team and are composed of a dsDNA core and peripheral coating layer of self-assembled cationic peptides [21,22].

Results and Discussion

As was mentioned above, DNA molecules acquire a relatively compact coiled configuration in aqueous solution. If DNA is attracted from the solution towards the surface, e.g., electrostatically by introducing positive charge on the surface by APTMS functionalization, the final geometry of DNA molecules on the surface reflects this coiled configuration, as shown in Figure 2a. Deposition of DNA molecules across the electrodes is problematic in this case, even for relatively long DNA (the contour length of the DNA used was about 900 nm assuming B-DNA conformation). This situation is further aggravated by the fact that the negatively charged DNA is predominantly attracted to the positively charged modified area between the electrodes. On the other hand, as demonstrated in Figure 2b, the new variation of the combing method resulted in highly aligned DNA molecules oriented along the direction of the moving meniscus in an orderly and highly reproducible fashion. The average percentage of stretching was calculated as 122%, which is
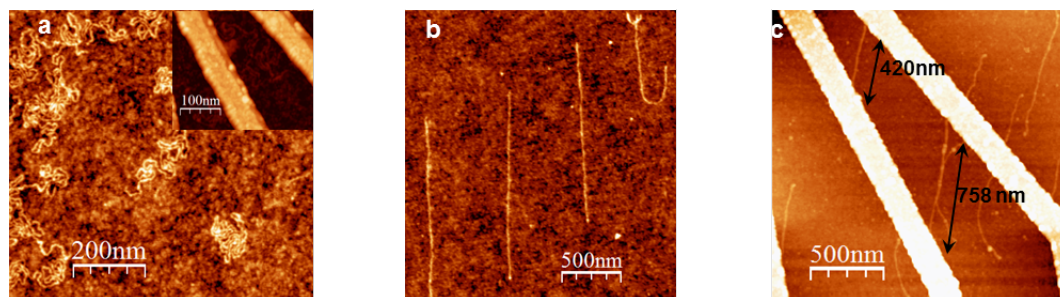
Figure 2: AFM topographic images of dsDNA molecules deposited on silicon substrates. (a) DNA deposited on APTMS-functionalized silicon substrates. The insert shows DNA in the area with nanoelectrodes. (b) DNA molecules combed on hydrophobically modified silicon substrates by using the proposed variation of the combing method. (c) DNA combed across nanofabricated electrodes. The typical observed dsDNA height was 0.7 ± 0.2 nm, in line with other experiments.

comparable to most values reported in earlier studies [23]. Using the new procedure, it was also possible to comb DNA across fabricated nanostructures, as shown in Figure 2c.

Interestingly, the new method was also efficient in combing DNA–peptide conjugates, while the original recipe was proven to be ineffective for combing these materials [11]. Figure 3 represents the topography of combed dsDNA conjugated with various peptides. Combing across nanoelectrodes was also possible for DNA–peptide conjugates (Figure 3e).

The gas-phase deposition of *N*-octyldimethylchlorosilane on silicon substrates used in this study was a key step to achieve hydrophobic and clean surfaces, ideal for deposition and combing of DNA. This procedure did not increase substrate roughness (average RMS ≈ 0.25 nm on modified substrates versus average RMS ≈ 0.3 nm before gas-phase deposition). Interestingly, on the nanoelectrodes, the observed density of deposited and combed DNA was significantly lower than that on flat silicon. This could be mainly attributed to the absence of silane functionalization on the platinum electrodes, which is also indicated by the absence of an additional tunnel barrier observed in [21,22].

The proposed variation of the combing method resulted in significant improvement in the quality of combed dsDNA on silicon. In addition to achieving more ordered alignments, we found the new method to be highly reproducible. We also observed that there is a narrow range of pH between 5.0 and 5.5 required for successful deposition and combing on the hydrophobic substrate, which was in agreement with earlier reports on combing [8,9]. The new procedure was also effective in combing DNA–peptide conjugates, while other commonly used combing recipes were ineffective for combing these materials. In the case of nanoelectrodes, despite the fact that the movement of the meniscus is disturbed when passing
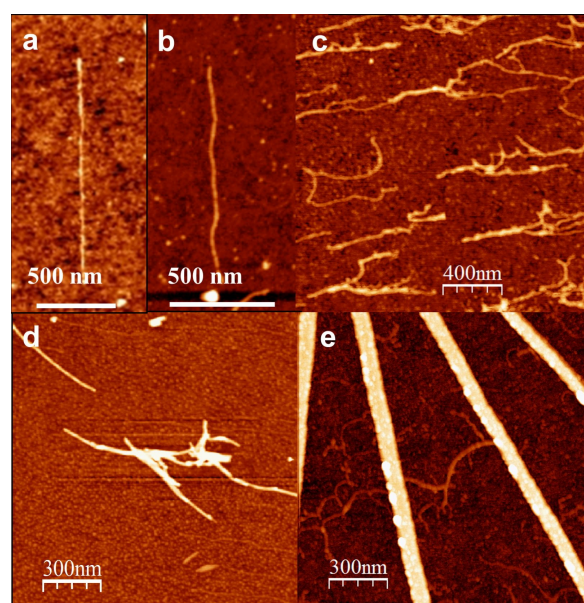
Figure 3: AFM topographic images demonstrating combing of dsDNA and DNA–peptide conjugates on hydrophobically modified silicon substrates. Vertical scale varies for different images. (a) Single dsDNA molecule, shown for comparison. (b) Single DNA–KA$_6$ conjugate, height 3.4 ± 0.4 nm. (c) IL-coated DNA molecules aligned in the direction of combing; typical height is 2–5 nm depending on the bundle size. (d) DNA–KA$_5$ conjugates; typical height of a single complex 5.6 ± 0.4 nm. (e) DNA–KA$_6$ conjugates combed across nanoelectrodes; height 3–5 nm depending on the bundle size.

over the electrodes, DNA molecules were still combed across them in the desired direction, i.e., perpendicular to the electrodes.

Conclusion

In this study, we combined gas-phase deposition and lithographic methods with a new variation of the combing technique in order to achieve high-quality alignments of DNA both on a

flat silicon dioxide surface and across nanoelectrodes. The gas-phase deposition procedure together with choice of the buffer and *N*-octyldimethylchlorosilane to modify the surface provided optimal conditions for stretching of DNA up to 160% of its original contour length. The average percentage of stretching was calculated as 122%, which corresponds to the combing force of ≈2.4 nN. Furthermore, it was possible to achieve 900 nm long stretches of dsDNA deposited across nanoelectrodes. Not only successful in combing dsDNA with high quality and reproducibility, the new technique was also able to comb a number of DNA derivatives, which was not possible with other combing methods. The results of this study offer an efficient and reliable method for the aligned deposition of DNA and DNA derivatives for further applications in DNA nanotechnology.

Experimental

The experiments were performed on a "random" sequence genomic DNA (pUC19/SmaI digest, 25 ng/μL, Fermentas Life Sciences). Pure ammonium acetate solution (20 mM, pH 5.1, Sigma Aldrich) was used as a buffer in all the procedures described here. The DNA solution was buffer exchanged to ammonium acetate before use, to guarantee that only "volatile" ions are present on the substrate. The following peptides were used to form DNA–peptide conjugates: indolicidin, abbreviated as IL, (Ile-Leu-Pro-Trp-Lys-Trp-Pro-Trp-Trp-Pro-Trp-Arg-Arg), IL4 (Ile-Leu-Pro-Trp-Lys-Leu-Pro-Leu-Leu-Pro-Leu-Arg-Arg), KA_5 (Lys-Ala-Ala-Ala-Ala-Ala) KA_6 (Lys-Ala-Ala-Ala-Ala-Ala-Ala), and KA_6W (Lys-Ala-Ala-Ala-Ala-Ala-Ala-Trp). All the peptides used in the experiments were produced in-house by using solid-phase synthesis (Activo-P11, Activotec) and purified by HPLC before usage.

Two types of substrates were used during this experiment: clean silicon substrates (highly doped p-type silicon with 100 nm of thermal oxide, Nova Wafers, USA), as well as those with nanofabricated electrodes. Nanoelectrodes were fabricated by using a combination of optical and e-beam lithography followed by lift-off. In this way, we could achieve thin (5–10 nm) continuous Pt/Cr electrodes with a width of 30–40 nm and electrode spacing down to 40 nm. Prior to functionalization, both types of substrates were thoroughly cleaned and treated for 15–20 min in UV-ozone cleaner (BioForce Nanoscience). For gas-phase deposition, a solution of *N*-octyldimethylchlorosilane (Sigma-Aldrich) in toluene (1:3) was introduced into an evacuated chamber (≈100 mbar) containing the substrates for two hours. This resulted in a thin film of the hydrophobic silane on top of the SiO_2 layer. On these surfaces, water droplets exhibited average contact angles of about 90° as determined by the sessile droplet method. Positively charged silicon surfaces (used for the reference experiment shown in Figure 2a) were

produced by the same technique but with 3-aminopropyltrimethoxysilane (Sigma-Aldrich) and one hour incubation time.

The optimal conditions for combing were achieved with 20 mM ammonium acetate at pH 5.1 and *N*-octyldimethylchlorosilane surface modification. Molecular combing of DNA was performed according to the following procedure: A droplet of dsDNA solution in buffer (with the final concentration corresponding to absorption at 260 nm wavelength, *A*(260 nm), in the range 0.001–0.01, depending on the density of molecules on the surface required) was deposited on a silanized substrate followed by ≈6 min incubation time at room temperature. On a sufficiently functionalized substrate, the droplet produces a contact angle of ≈90°, which makes it easy to gently move the droplet along the surface. In this experiment, we used a plastic pipette tip to drag the droplet out of the substrate.

Preparation of DNA–peptide conjugates was performed in two different ways depending on the peptide. For peptides KA_5, KA_6, and KA_6W the following procedure was used: The stock peptide solutions of KA_5 (8 mM), KA_6 (4 mM), and KA_6W (4 mM) in buffer were sonicated for 30 min prior to mixing in a ratio 2:1 with DNA solution (*A*(260 nm) ≈ 0.05), followed by 2 h incubation of the mixture at room temperature. Combing of the DNA–peptide solution was performed with the same method as described for dsDNA but with longer (8–10 min) incubation times.

Combing of DNA conjugates with IL and IL4 was performed in two steps. First, DNA solution (*A*(260 nm) ≈ 0.05) was combed on a silanized substrate as described before. Then, the substrates were treated again with a second droplet containing peptide solution (8 min incubation). The droplet was then dragged out of the surface by the same combing technique, in the same direction. IL (680 μM) and IL4 (20 μM) were used without sonication. The same procedure was carried out in order to deposit and comb DNA and DNA–peptide conjugates on platinum nanoelectrodes.

Atomic Force Microscopy (AFM) was carried out on a Nanoscope IIIa (Bruker, USA), operating in tapping mode. OMCL-AC200TS, OMCL-AC240TS (Olympus), and HR-SCC (Team Nanotec GmbH) cantilevers were used for AFM imaging. The images were processed by using the WSxM software package [24].

Acknowledgements

References

1. Herrick, J.; Bensimon, A. Introduction to Molecular Combing: Genomics, DNA Replication, and Cancer. In *DNA Replication: Methods and Protocols;* Vengrova, S.; Dalgaard, J. Z., Eds.; Methods in Molecular Biology, Vol. 521; Humana press: New York, 2009; pp 71–101. doi:10.1007/978-1-60327-815-7

2. Herrick, J.; Bensimon, A. *Chromosome Res.* **1999,** *7,* 409–423. doi:10.1023/A:1009276210892

3. Zamora, F.; Amo-Ochoa, M. P.; Sanz Miguel, P. J.; Castillo, O. *Inorg. Chim. Acta* **2009,** *362,* 691–706. doi:10.1016/j.ica.2008.02.029

4. Bensimon, D.; Croquette, V.; Bensimon, A.; Simon, A. J. *Phys. Rev. Lett.* **1995,** *74,* 4754–4757. doi:10.1103/PhysRevLett.74.4754

5. Strick, T.; Allemand, J. F.; Croquette, V.; Bensimon, D. *Prog. Biophys. Mol. Biol.* **2000,** *74,* 115–140. doi:10.1016/S0079-6107(00)00018-3

6. Bensimon, A.; Simon, A.; Chiffaudel, A.; Croquette, V.; Heslot, F.; Bensimon, D. *Science* **1994,** *265,* 2096–2098. doi:10.1126/science.7522347

7. Klein, D. C. G.; Gurevich, L.; Janssen, J. W.; Kouwenhoven, L. P.; Carbeck, J. D.; Sohn, L. L. *Appl. Phys. Lett.* **2001,** *78,* 2396–2398. doi:10.1063/1.1365099

8. Zheng, H.-Z.; Pang, D.-W.; Lu, Z.-X.; Zhang, Z.-L.; Xie, Z.-X. *Biophys. Chem.* **2004,** *112,* 27–33. doi:10.1016/j.bpc.2004.06.011

9. Allemand, J. F.; Bensimon, D.; Jullien, L.; Bensimon, A.; Croquette, V. *Biophys. J.* **1997,** *73,* 2064–2070. doi:10.1016/S0006-3495(97)78236-5

10. Stewart, A. *Trends Mol. Med.* **1998,** *4,* 2. doi:10.1016/S1357-4310(97)01169-6

11. Zhang, J.; Ma, Y.; Stachura, S.; He, H. *Langmuir* **2005,** *21,* 4180–4184. doi:10.1021/la050129s

12. Deng, Z.; Mao, C. *Nano Lett.* **2003,** *3,* 1545–1548. doi:10.1021/nl034720q

13. Nakao, H.; Hayashi, H.; Yoshino, T.; Sugiyama, S.; Otobe, K.; Ohtani, T. *Nano Lett.* **2002,** *2,* 475–479. doi:10.1021/nl025528b

14. Guan, J.; Lee, L. J. *Proc. Natl. Acad. Sci. U. S. A.* **2005,** *102,* 18321–18325. doi:10.1073/pnas.0506902102

15. Porath, D.; Lapidot, N.; Gomez-Herrero, J. Charge Transport in DNA-based Devices. In *Introducing Molecular Electronics;* Cuniberti, G.; Richter, K.; Fagas, G., Eds.; Springer: Berlin, New York, 2005; pp 411–439. doi:10.1007/b101525

16. Cohen, H.; Nogues, C.; Naaman, R.; Porath, D. *Proc. Natl. Acad. Sci. U. S. A.* **2005,** *102,* 11589–11593. doi:10.1073/pnas.0505272102

17. Michalet, X.; Ekong, R.; Fougerousse, F.; Rousseaux, S.; Schurra, C.; Hornigold, N.; van Slegtenhorst, M.; Wolfe, J.; Povey, S.; Beckmann, J. S.; Bensimon, A. *Science* **1997,** *277,* 1518–1523. doi:10.1126/science.277.5331.1518

18. Caburet, S.; Conti, C.; Bensimon, A. *Trends Biotechnol.* **2002,** *20,* 344–350. doi:10.1016/S0167-7799(02)01990-X

19. Lin, H.-Y.; Tsai, L.-C.; Chi, P.-Y.; Chen, C.-D. *Nanotechnology* **2005,** *16,* 2738–2742. doi:10.1088/0957-4484/16/11/046

20. Hölzel, R.; Gajovic-Eichelmann, N.; Bier, F. F. *Biosens. Bioelectron.* **2003,** *18,* 555–564. doi:10.1016/S0956-5663(03)00024-1

21. Esmail Nazari, Z. Electrostatic Force Microscopy and Conductivity Measurements of DNA and DNA Derivatives for Applications in Molecular Electronics. Master's Thesis, Aalborg University, Denmark, 2012.

22. Esmail Nazari, Z.; Gurevich,L. Formation of Conductive DNA-Based Nanowires via Conjugation of dsDNA with Cationic Peptide, in preparation.

23. Cerf, A.; Thibault, C.; Geneviève, M.; Vieu, C. *Microelectron. Eng.* **2009,** *86,* 1419–1423. doi:10.1016/j.mee.2009.01.057

24. Horcas, I.; Fernández, R.; Gómez-Rodríguez, J. M.; Colchero, J.; Gómez-Herrero, J.; Baro, A. M. *Rev. Sci. Instrum.* **2007,** *78,* No. 013705. doi:10.1063/1.2432410

Electronic and transport properties of kinked graphene

Jesper Toft Rasmussen, Tue Gunst, Peter Bøggild, Antti-Pekka Jauho
and Mads Brandbyge[*]

Abstract

Local curvature, or bending, of a graphene sheet is known to increase the chemical reactivity presenting an opportunity for templated chemical functionalisation. Using first-principles calculations based on density functional theory (DFT), we investigate the reaction barrier reduction for the adsorption of atomic hydrogen at linear bends in graphene. We find a significant barrier lowering (≈15%) for realistic radii of curvature (≈20 Å) and that adsorption along the linear bend leads to a stable linear kink. We compute the electronic transport properties of individual and multiple kink lines, and demonstrate how these act as efficient barriers for electron transport. In particular, two parallel kink lines form a graphene pseudo-nanoribbon structure with a semimetallic/semi-conducting electronic structure closely related to the corresponding isolated ribbons; the ribbon band gap translates into a transport gap for electronic transport across the kink lines. We finally consider pseudo-ribbon-based heterostructures and propose that such structures present a novel approach for band gap engineering in nanostructured graphene.

Introduction

Nanostructures based on graphene have an enormous potential for applications. Especially in future electronic devices compatible with and extending silicon technology, due to the outstanding electronic transport properties of graphene [1]. However, it is crucial to modify the semimetallic electronic structure of graphene to exploit its full potential for many elec-

tronic applications: a band gap can be introduced by nanostructuring graphene.

A common approach towards engineering the electronic structure is to form quasi-1D graphene in the form of nanoribbons (GNR) [2]. The electronic structure of GNRs depends on width,

direction and edge structure – all parameters that to some degree can be controlled. GNRs can be formed by etching [2], by unzipping carbon nanotubes (CNTs) [3], or ultimately be grown with atomic-scale precision by using self-assembly of precursor molecules on metal substrates [4]. However, for electronic applications this approach requires a structure-preserving means of releasing and transferring the structures to an insulating substrate. Bonding of H or other species to graphene with large coverage opens an insulating band gap at the adsorption sites due to sp^3 hybridisation [5]. Periodically ordered clusters of adsorbed hydrogen can be formed on graphene in patterns dictated by the Moiré lattice mismatch between graphene and the metal substrate, which opens a semiconducting band gap [6]. Finally, regular perforations, known as a graphene antidot lattice (GAL) [7], or a nanoscale mesh of holes [8-10] can have neck widths [10,11] down to 5 nm corresponding to band gaps of the order of 1 eV [2].

Graphene consists entirely of surface atoms and is thus exceedingly sensitive to the surroundings. In particular, the van der Waals (vdW) interaction with the substrate is of importance. The substrate interactions, which make graphene cling to small features, may be exploited by manufacturing nanostructures in the substrate. Periodic steps in a Cu substrate has been used to induce "wrinkles" or ripples in graphene with period and height on the order of 10 nm [12]. Recently, Hicks et al. [13] demonstrated how arrays of 1D large band gap, semiconducting graphene nanoribbons corresponding to a width of ≈1.4 nm can be formed in graphene on a step-patterned SiC substrate. The substrate interactions can clamp a graphene sheet while partly suspended across small holes, so that a pressure difference between the in- and outside leads to the formation of bubbles or "blisters" in the sheet [14]. Also, linear folds, where the graphene sheet is bulging up from the substrate, have been induced for graphene suspended over trenches by using heat treatment [15]. Thus, the sheet can obtain significant bends at certain places induced by the substrate interaction, substrate nanostructuring, and subsequent treatments [16]. Calculations by Low et al. [17] showed how a sharp step of height 1 nm in a SiC substrate, comparable to experimental values [13], can induce a linear bend in the graphene sheet with a radius of curvature down to around 1 nm.

The ability to accurately control sharp local curvatures of graphene presents opportunities for strain-assisted modification of the local electronic structure and chemical reactivity in the graphene sheet, and may open a route to band gap engineered devices [13,18-21]. Very recently, Wu et al. [21] showed how graphene on a Si substrate decorated with SiO_2 nanoparticles induced local regions of strain and increased reactivity in a selective manner. Atomic hydrogen or other chemical species

do not easily react with flat graphene when dosed from a single side [22]. However, at positions where there is a substantial local bending, rippling or strain of the graphene sheet the reactivity changes significantly [5,23]. So far there have been only a few theoretical studies of the atomic geometry of hydrogenated ripple structures in unsupported, strain-induced, graphene ripples [24-26]. However, to the best of our knowledge, no studies have addressed the reactivity of bends or the transport through hydrogenated ripples, or discussed the possibility of stabilising nonplanar structures by hydrogenation.

In this paper we consider the reactivity of linear bends in a graphene sheet, and the electronic transport properties of kinks resulting from the hydrogenation of bends. Our starting point is the generic graphene structure shown in Figure 1a, which is inspired by the experimental observation of trench formation [15]. The bulging of this structure results from shortening the distance between two separated, clamped regions in the sheet. The remaining sections of the paper are organised as follows: Section "System setup" describes our computational method and setup. In the subsequent section we present our results. First, we describe the adsorption barriers for the reaction with single atomic H on the graphene bend at positions with different local curvature (positions I–VIII in Figure 1a). Then we show how a linear bend transforms into a kink when decorated by H

Figure 1: (a) Smooth ripple-like structure where the first and last six rows of carbon-dimers are surface-clamped regions with a separation of *L* = 90 Å. Atomic hydrogen is adsorbed at positions I–VIII. (b) The resulting kinked graphene structure after hydrogen is adsorbed in lines at the most reactive position (II) corresponding to the smallest local radius of curvature. The four kinks divide the structure into five sections, S_1–S_5.

along the most reactive (most curved) line (Figure 1b), and we present the electronic transmission through a single kink in the subsection "Single kink". The kink acts as an effective barrier with its transmission depending on the kink-angle, φ. In the subsection "Two kinks" we study how two parallel kinks lead to the formation of a pseudo-ribbon-type electronic structure. Finally, in subsection "Multiple kinks" we demonstrate the opening of a transport gap for multikink systems, such as the one shown in Figure 1b.

System setup

The bend we consider in Figure 1a is created along the armchair direction by fixing the first and last six rows of carbon atoms and shortening the separation L, while the rest of the atoms are allowed to relax. A separation of $L = 90$ Å is chosen in order to obtain realistic curvatures [17]. We first assessed the reactivity of the structure at positions with different local curvature, see positions I–VIII in Figure 1a. Subsequently we relaxed the structure where lines of hydrogen (Figure 1b) have been placed at the points of lowest radius of curvature, i.e., the points of highest local reactivity. This particular system is meant to illustrate the potential of the hydrogen adsorption mechanism, and to gain insight into the modification of the electronic properties due to the hydrogen lines. In a corresponding experimental setup we can imagine placing graphene across a trench, which allows hydrogen adsorption on either side of the sheet.

The atomic and electronic structure calculations are based on density functional theory (DFT) using the SIESTA [27] code, and the PBE-GGA exchange-correlation [28] functional. We employ periodic boundary conditions (PBC) in the direction along the bend with a cell-width of four carbon dimers, and 10 Monkhorst–Pack k-points. We use a mesh cut-off of 500 Ry throughout. When calculating reactivity in the form of reduced reaction barriers the unit-cell is chosen so that the distance between single hydrogen atoms is larger than 8.5 Å. This ensures low hydrogen–hydrogen interaction, which is known to impact reaction barriers [29]. In the total energy calculations of relaxed atomic geometries and reaction barriers, we also use PBC transverse to the bend (5 k-points). We use a TZP basis-set for hydrogen and a SZ basis for carbon, except in the reaction barrier calculations where we compare calculations using a DZP and SZP basis for the four carbon atoms nearest to the hydrogen. In the barrier determinations we furthermore use spin-polarised calculations because of unpaired electrons. For the relaxed geometries a force tolerance of 0.01 eV/Å is used, and the final energies are corrected for basis-set-superposition errors (BSSE) [30].

Based on the computed atomic and electronic structures we subsequently use the TranSIESTA [31] method to calculate the electronic conductance per unit-cell width transverse to the bend. To this end we attach semi-infinite flat graphene electrodes to each side of the selected kinks, i.e., replace sections S_1 and S_2 in Figure 1b by semi-infinite electrodes in order to calculate the transmission through the single kink separating S_1 and S_2. In the conductance calculations we employ a dense transverse k-point grid of 400 points.

Results and Discussion
Adsorption barrier

Adsorption of hydrogen on graphene involves a reaction barrier that needs to be overcome before the single hydrogen atom sticks to the graphene sheet. Several investigations based on DFT calculations show that atomic hydrogen adsorbs on-top on flat graphene with a barrier about 0.2 eV and binding energy in the range of 0.7–1.0 eV [22,32-34]. Thus a minimum kinetic energy for the first hydrogen to react [32,33] is required, in an out-of-equilibrium situation such as in an atomic beam [34]. Casolo et al. [35] calculated the reaction barrier and adsorption energy for multiple hydrogen atoms on flat graphene. In agreement with other studies they found decreased barriers to sticking for the second H atom, compared to the barrier for adsorbing a single H atom on a clean surface [36].

Here, we first focus on the trends in the change in adsorption barrier as a function of the local curvature of the graphene sheet. To this end we have considered atomic hydrogen absorption at the on-top carbon positions at points with different curvature on the bent structure, see Figure 1a (positions I–VIII). The barrier is determined by calculating the total energy for each position of hydrogen above graphene as the hydrogen is moved successively closer to the graphene. Following the adsorption investigations on flat graphene by Ivanovskaya et al. [37] we perform, in each step, a relaxation of the hydrogen-bonded carbon atom and its three nearest neighbours. Using the method described above we obtain a reaction barrier of 0.22 eV on locally flat graphene. This is comparable to results obtained by several groups using DZP or plane wave basis sets and the PW91 functional [22,29,32,33]. We find that a SZP basis set for the relaxed carbon atoms yields a reduced barrier height of 0.18 eV (both basis sets with orbital range corresponding to an energy shift of 0.01 eV). Hence, we use the SZP basis in the following reaction-barrier calculations in order to lower the computation time.

For the positions (I-VIII) we obtain the reaction barrier for adsorption of hydrogen as a function of the local radius of curvature (RoC) shown in Figure 2. The second least curved position (VIII), resulting in a large RoC, reduces the barrier by roughly 3% compared to flat graphene (position I). The most curved position (II) in our considered structure has a minimum

RoC of ≈20 Å resulting in a barrier reduction of roughly 16%. For comparison, this RoC roughly corresponds to the radius of a (25,25) nanotube. Experiments by Ruffieux et al. [38] compare hydrogen adsorption on C_{60} molecules, CNTs, and graphite to show that reactivity is increased with curvature. In our case we find that the local electronic density of states changes little for the atoms on the pristine bent graphene sheet (as in Figure 1a). Thus, we conclude that the lowering of the adsorption barrier for the moderate RoC of about 20 Å is mainly due to the mechanical strain in the bend shifting the carbon atoms out of the graphene plane in the direction of the hydrogen. We note that an additional increase in reactivity may result from the change in electronic structure for highly bent graphene. Thus, we expect an increase in reactivity for the graphene with a linear bend, and a simple Arrhenius estimate using our data yields a factor of 3–4 at room temperature (300 K). We have also performed calculations using the less rigorous DFTB method [39] and obtained results in agreement with the trend in reaction-barrier reduction obtained above.
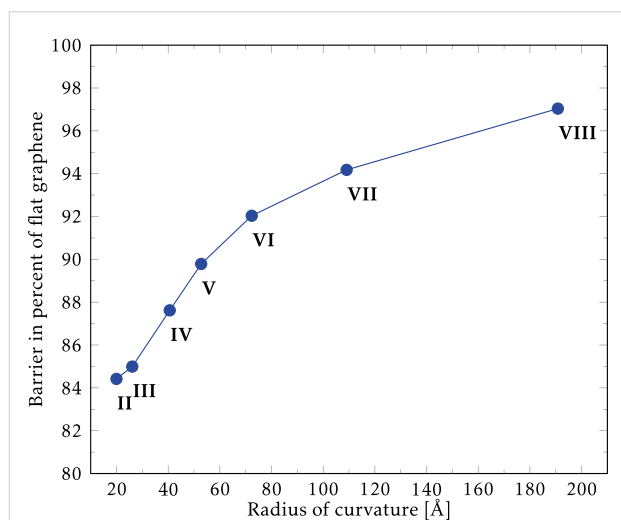
Figure 2: Calculated reaction barriers for hydrogenation of bent graphene as a function of the local radius of curvature (II–VIII in Figure 1a). Flat graphene (position I) has an infinite radius of curvature and is used to normalise the barriers. Calculations are spin-polarised and allow for atomic relaxation.

We may understand the reaction barrier and its change with curvature by considering the changes in carbon bond lengths. The barrier is due to the fact that the reacting carbon atom has to be pulled out of the graphene plane, stretching the strong carbon–carbon bonds, when reacting with the incoming hydrogen atom. When the graphene sheet is curved the carbon atom is already slightly out of the plane, and thus the energy required to pull the atom further out of plane is decreased compared to flat graphene. The ortho- and para-locations in the graphene hexagon have been shown to be the preferred loca-

tions for hydrogen adsorption in studies of flat graphene [22,29,40]. With this in mind as well as the curvature-related reduction of reaction barriers, we conclude that the considered system allows the adsorption of hydrogen atoms in single lines along armchair-edges. The kink in the atomic structure due to the sp^3-binding of a single H makes the graphene curve even more in its vicinity, which in turn, preferentially lowers the barrier for absorption of a H along the linear bend. This suggests a mechanism in which the hydrogen adsorption is propagating and leads to the decoration of the entire linear bend turning it into a kink line. It may be viewed as analogous to crack-formation mechanisms, where the breaking of a bond increases the stress on neighbouring bonds; only in this case, the graphene is hydrogenated rather than broken or destroyed.

Single kink

Next, we examine the energetic and transport properties of kink-lines in the armchair direction. We first consider a single kink with angle φ, e.g., between sections S_1 and S_2 in Figure 1b. The kink-angle φ is varied in the range 0°…90°, while the three nearest unit cells on each side of the kink are allowed to relax. The total energy per H is shown as a function of φ in the inset of Figure 3, showing a minimum energy for φ ≈ 50°. This angle roughly corresponds to the angle in an sp^3 configuration where 2φ = 109.5°. The adsorption of H causes local changes in the geometry, i.e., only the carbon atoms very close to the kink are moved, while the remaining structure remains unperturbed. For this reason, the adsorption of hydrogen atoms can be considered as a process that locally pins the bend.
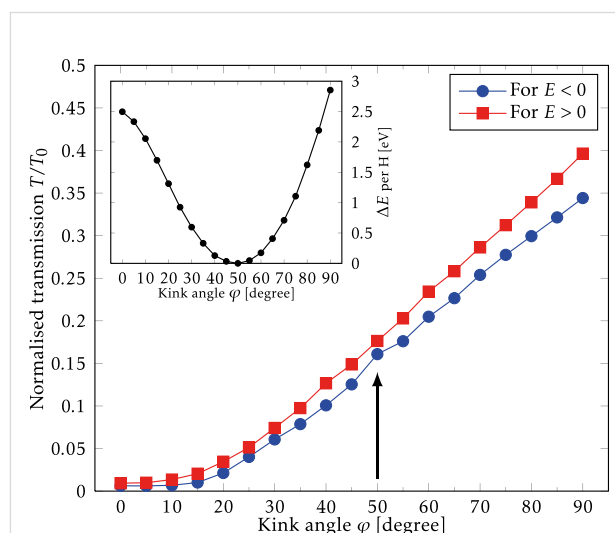
Figure 3: Electronic transmission through a single kink normalised by the transmission of pristine graphene (T_0) as a function of the kink angle, φ, for electrons ($E > 0$) and holes ($E < 0$). The arrow indicates the normalised transmission at the equilibrium angle determined from the total energy calculations shown in the inset.

The electron transmission per unit-cell width is linear in energy for pristine graphene in a energy range around the charge neutrality point ($E = 0$), e.g., $T_0 \propto E$. We find similarly that the calculated kink-transmission curves are also linear, and therefore we express the results for the transmissions in terms of the roughly energy-independent ratio $T/T_0 = $ const. The kink breaks the electron–hole symmetry, and we fit $E > 0$ and $E < 0$ separately, as shown in Figure 3. Larger kink angles result in an increase in the overall transmission, which may be attributed to a better π-orbital overlap across the kink. For the equilibrium angle, $\varphi = 50°$, the ratio T/T_0 is close to 0.17 in both regions (indicated by the arrow in Figure 3), corresponding to a transmission reduction of 83%. Thus, we see that the hydrogen-induced kinks in graphene can be used to form effective electron barriers. We now turn to the effect of multiple barriers and periodic kink structures in order to examine resonant tunnelling phenomena and band gap formation.

Two kinks

Band-structure calculations show that periodic nanoscale rippling of the graphene is not sufficient to create a band gap [24] due to the low scattering by the elastic deformation [17]. In contrast, periodic arrangements of adsorbed hydrogen can indeed induce a semiconducting band gap [24,26]. The electronic band structures of hydrogen lines on flat graphene have been examined by Chernozatonskii et al. [25,26], and recently also for nanoscale-rippled graphene [24]. Here we show how two parallel kinks lead to a local electronic structure that resembles that of an isolated GNR between the kinks. Such structures could be produced experimentally by using the techniques described by Pan et al. [12]. Hydrogen-terminated armchair GNRs are semiconducting but have a small energy gap when the width in atomic lines is $N = 3L − 1$, where L is an integer [41]. In Figure 4 we compare the electronic bandstructure for armchair GNRs (aGNRs) (left panel) to the electronic transmis-

sion through two kinks separated by the corresponding aGNR width (right panel). In the present case the initial width (or, kink separation) is $N = 17$ atomic lines of carbon, which shows a semimetallic behaviour in the transmission spectrum with a small transport gap. In accordance with isolated aGNRs the next two widths $N = 18, 19$ are semiconducting, while the last investigated width $N = 20$ is semimetallic again (not shown). The close correspondence between the electronic band structure for the GNR and the transmission gap for the double-kink system allows us to consider the structure between two kinks as a pseudo-ribbon.

For the semiconducting pseudo-ribbons transport gaps surrounded by van Hove-type 1D behaviour are seen in the transmission functions (Figure 4, right panel). The transport gaps, $E_{gap} = 0.4$ eV and $E_{gap} = 0.5$ eV, are in reasonable agreement with the power-law scaling of E_{gap} with width found for aGNRs [41]. We note that the pseudo-ribbon breaks the electron–hole symmetry: For the $N = 18$ case a larger van Hove resonance is seen at the valence band edge, while for $N = 19$ a larger resonance is seen at the conduction band edge. There are small transmission values within the electronic band gap due to leakage through the barriers, which we expect to introduce shifts in the energies between the real and pseudo aGNR.

Multiple kinks

In order to illustrate the behaviour of systems with more kinks we consider a system consisting of four hydrogen-induced kinks, as illustrated in Figure 1b and Figure 5. The sections S_1/S_5 are now replaced by left/right infinite-lead structures, and the "top" S_3 pseudo-ribbon is connected to the leads via the "side" S_2, S_4 pseudo-ribbons. We keep S_2, S_3 identical for simplicity and determine the transmission across the kinks (in the z-direction in Figure 5), which is experimentally more feasible. We now investigate how the different sections influ-

Figure 4: (Left) Band structures for H-passivated armchair ribbons with varying width, *N*. The ribbons are a zero-gap semiconductor, a semiconductor with band gap $E_{N+1} = 0.4$ eV, and a semiconductor with band gap $E_{N+2} = 0.5$ eV for widths *N*, *N* + 1, *N* + 2, respectively. All widths are based on the number of carbon atom lines *N* = 17. The band gaps are indicated by arrows and are highlighted. (Right) The electronic transmission functions for the corresponding pseudo-ribbons, i.e., across two parallel kinks of varied separation as shown in the inset.

Figure 5: Projected band structure and transmission through structures with multiple kinks. The top (section S_3) and connecting pseudo-ribbons (sections S_2/S_4) are varied in width, changing their electronic properties. The projected band structure along the pseudo-ribbons (i.e., k_x) is shown by using filled circles with radii proportional to the weight on section S_3. Semimetallic (M) pseudo-ribbons corresponding to $N = 17$ are shown in blue, while semiconducting (SC) ribbons of width $N + 1$ are shown in red. Band gaps of the top sections E_{gap}^{top} and connecting sections E_{gap}^{side} are highlighted. These are $E_{gap}^{side} = 0.39$ eV (b), $E_{gap}^{top} = 0.42$ eV (c), and $E_{gap}^{top} = 0.35$ eV, $E_{gap}^{side} = 0.27$ eV (d). The transmission $T(E)$ (per simple transverse unitcell) is determined across all kinks in the z-direction, and transmission gaps comparable to the band gaps are observed in subfigures b and d.

ence the total transport for the four possible combinations of semiconducting (SC) and semimetallic (M), corresponding to the pseudo-ribbon widths N, $N + 1$ used in Figure 4.

In order to analyse the transmission we single out the band structure projected on to the top section, S_3 (excluding carbon and hydrogen atoms at the kink), in the band structure along the pseudo-ribbon direction. The weight on S_3 is represented by a circle of radius R_{nk},

$$R_{nk} \propto \sum_{i \in S_3} \left| \Psi\left(n, k_x, i\right) \right|^2. \qquad (1)$$

Here Ψ is the wave function at k_x ($k_z = 0$) with n (i) being the band (orbital) index. The obtained projected band structures are shown in the left parts of each subfigure in Figure 5. Generally, some bands have no weight (no circles), while others have significant weight indicating that there is little mixing between the orbitals from section S_3 and other sections.

In Figure 5a and Figure 5b we consider pseudo-ribbons with semimetallic top regions, namely $S_2/S_3/S_4$ being M/M/M and SC/M/SC, respectively. For the all-metal pseudo-ribbons, M/M/M, an almost energy-independent transmission function is

seen with a transmission close to that of the metallic double-kink in the previous subsection. The SC/M/SC structure shows a transport gap similar to that of the single SC pseudo-ribbon with van Hove resonances, while the S_3-projected band structure reveals isolated metallic states within the gap. We note that the transmission at the resonances for the SC/M/SC structure is larger than the corresponding M/M/M transmission. For the case of semiconducting top pseudo-ribbons in Figure 5c and Figure 5d, we note that M/SC/M show a greatly reduced transport gap compared to the single pseudo-ribbon case (also, note the scaling of the transmission axis), while the SC/SC/SC structure shows a complete extinction of the transmission in the electronic gap, as expected. Generally, we find that the main behaviour of the transmission is controlled by the connecting sections S_2, S_4, i.e., there is a good correspondence between the side section band gaps E_{gap}^{side} and the transmission gaps.

Conclusion

The presented investigations show that linear kink-line structures may form in graphene by reacting with atomic hydrogen along a linear bend in the sheet. The adsorption barrier is lowered in the close vicinity of the bend, which can be exploited to form the kink. In particular, we have shown that a radius of curvature of $\approx$20 Å reduces the hydrogen adsorption barrier by roughly 16% compared to H adsorption on pristine

graphene. The calculations suggest that once a single hydrogen atom has been adsorbed, the induced local kink and resulting increase in local curvature makes it easier for the following H to adsorb, thus creating a propagating kink formation. A full line of hydrogen atoms pins the structure and divides the electronic systems into different regions. We have shown that the electronic transmission through a single kink is reduced by 83% compared to pristine graphene, meaning that the kink-line acts as an efficient barrier for electron motion. We have demonstrated how two close-by parallel kinks form a pseudo graphene nanoribbon with similar behaviour of the electronic structure to that for isolated nanoribbons. The transmission function displays transport gap features corresponding to the isolated nanoribbon band gaps.

The present work thus suggests that it may be feasible to template functional electronic nanostructures by using the conformation of graphene, e.g., to the substrate, and that this in turn induce changes in local reactivity. Our work clearly calls for extensions in a number of directions. First of all more calculations are needed in order to investigate the kink-line propagation reaction proposed by our results. To this end it is important to include a realistic description of the actual substrate. It is also interesting to consider other adsorbate species, possibly introducing doping of the pseudo-ribbons and electronic gating. Finally, decoration and pinning of the edges of other geometries such as "bubbles" or "blisters" is of interest, e.g., in order to produce GAL-like structures [7] without perforating the graphene sheet. Calculations have shown how the adsorption of hydrogen is correlated over a length scale involving several of the unit cells employed in this work [22,35,42,43]. Thus the adatom–adatom interaction will play a significant role in the kink-line propagation along the step and will be addressed in a future study.

Acknowledgements

References

1. Novoselov, K. S.; Fal'ko, V. I.; Colombo, L.; Gellert, P. R.; Schwab, M. G.; Kim, K. *Nature* **2012,** *490,* 192–200. doi:10.1038/nature11458
2. Han, M. Y.; Özyilmaz, B.; Zhang, Y.; Kim, P. *Phys. Rev. Lett.* **2007,** *98,* 206805. doi:10.1103/PhysRevLett.98.206805
3. Xie, L.; Wang, H.; Jin, C.; Wang, X.; Jiao, L.; Suenaga, K.; Dai, H. *J. Am. Chem. Soc.* **2011,** *133,* 10394–10397. doi:10.1021/ja203860a
4. Cai, J.; Ruffieux, P.; Jaafar, R.; Bieri, M.; Braun, T.; Blankenburg, S.; Muoth, M.; Seitsonen, A. P.; Saleh, M.; Feng, X.; Müllen, K.; Fasel, R. *Nature* **2010,** *466,* 470–473. doi:10.1038/nature09211
5. Elias, D. C.; Nair, R. R.; Mohiuddin, T. M. G.; Morozov, S. V.; Blake, P.; Halsall, M. P.; Ferrari, A. C.; Boukhvalov, D. W.; Katsnelson, M. I.; Geim, A. K.; Novoselov, K. S. *Science* **2009,** *323,* 610–613. doi:10.1126/science.1167130
6. Balog, R.; Jørgensen, B.; Nilsson, L.; Andersen, M.; Rienks, E.; Bianchi, M.; Fanetti, M.; Lægsgaard, E.; Baraldi, A.; Lizzit, S.; Sljivancanin, Z.; Besenbacher, F.; Hammer, B.; Pedersen, T. G.; Hofmann, P.; Hornekær, L. *Nat. Mater.* **2010,** *9,* 315–319. doi:10.1038/NMAT2710
7. Pedersen, T. G.; Flindt, C.; Pedersen, J.; Mortensen, N. A.; Jauho, A.-P.; Pedersen, K. *Phys. Rev. Lett.* **2008,** *100,* 136804. doi:10.1103/PhysRevLett.100.136804
8. Kim, M.; Safron, N. S.; Han, E.; Arnold, M. S.; Gopalan, P. *Nano Lett.* **2010,** *10,* 1125–1131. doi:10.1021/nl9032318
9. Liang, X.; Jung, Y.-S.; Wu, S.; Ismach, A.; Olynick, D. L.; Cabrini, S.; Bokor, J. *Nano Lett.* **2010,** *10,* 2454–2460. doi:10.1021/nl100750v
10. Bai, J.; Zhong, X.; Jiang, S.; Huang, Y.; Duan, X. *Nat. Nanotechnol.* **2010,** *5,* 190–194. doi:10.1038/NNANO.2010.8
11. Shimizu, T.; Nakamura, J.; Tada, K.; Yagi, Y.; Haruyama, J. *Appl. Phys. Lett.* **2012,** *100,* 023104. doi:10.1063/1.3675547
12. Pan, Z.; Liu, N.; Fu, L.; Liu, Z. *J. Am. Chem. Soc.* **2011,** *133,* 17578–17581. doi:10.1021/ja207517u
13. Hicks, J.; Tejeda, A.; Taleb-Ibrahimi, A.; Nevius, M. S.; Wang, F.; Shepperd, K.; Palmer, J.; Bertran, F.; Le Fèvre, P.; Kunc, J.; de Heer, W. A.; Berger, C.; Conrad, E. H. *Nat. Phys.* **2013,** *9,* 49–54. doi:10.1038/nphys2487
14. Bunch, J. S.; Dunn, M. L. *Solid State Commun.* **2012,** *152,* 1359–1364. doi:10.1016/j.ssc.2012.04.029
15. Bao, W.; Miao, F.; Chen, Z.; Zhang, H.; Jang, W.; Dames, C.; Lau, C. N. *Nat. Nanotechnol.* **2009,** *4,* 562–566. doi:10.1038/nnano.2009.191
16. Neek-Amal, M.; Peeters, F. M. *Phys. Rev. B* **2012,** *85,* 195445. doi:10.1103/PhysRevB.85.195445
17. Low, T.; Perebeinos, V.; Tersoff, J.; Avouris, P. *Phys. Rev. Lett.* **2012,** *108,* 096601. doi:10.1103/PhysRevLett.108.096601
18. Levy, N.; Burke, S. A.; Meaker, K. L.; Panlasigui, M.; Zettl, A.; Guinea, F.; Castro Neto, A. H.; Crommie, M. F. *Science* **2010,** *329,* 544–547. doi:10.1126/science.1191700
19. Guinea, F.; Katsnelson, M. I.; Geim, A. K. *Nat. Phys.* **2010,** *6,* 30–33. doi:10.1038/NPHYS1420
20. Ortolani, L.; Cadelano, E.; Veronese, G. P.; Degli Esposti Boschi, C.; Snoeck, E.; Colombo, L.; Morandi, V. *Nano Lett.* **2012,** *12,* 5207–5212. doi:10.1021/nl3023737
21. Wu, Q.; Wu, Y.; Hao, Y.; Geng, J.; Charlton, M.; Chen, S.; Ren, Y.; Ji, H.; Li, H.; Boukhvalov, D. W.; Piner, R. D.; Bielawski, C. W.; Ruoff, R. *Chem. Commun.* **2013,** *49,* 677–679. doi:10.1039/C2CC36747E
22. Hornekær, L.; Rauls, E.; Xu, W.; Šljivančanin, Ž.; Otero, R.; Stensgaard, I.; Lægsgaard, E.; Hammer, B.; Besenbacher, F. *Phys. Rev. Lett.* **2006,** *97,* 186102. doi:10.1103/PhysRevLett.97.186102
23. Srivastava, D.; Brenner, D. W.; Schall, J. D.; Ausman, K. D.; Yu, M.; Ruoff, R. S. *J. Phys. Chem. B* **1999,** *103,* 4330–4337. doi:10.1021/jp990882s
24. Wang, Z. F.; Zhang, Y.; Liu, F. *Phys. Rev. B* **2011,** *83,* 041403(R). doi:10.1103/PhysRevB.83.041403

25. Chernozatonskii, L. A.; Sorokin, P. B. *J. Phys. Chem. C* **2010,** *114,* 3225–3229. doi:10.1021/jp9100653

26. Chernozatonskii, L. A.; Sorokin, P. B.; Brüning, J. W. *Appl. Phys. Lett.* **2007,** *91,* 183103. doi:10.1063/1.2800889

27. Soler, J. M.; Artacho, E.; Gale, J. D.; García, A.; Junquera, J.; Ordejón, P.; Sánchez-Portal, D. *J. Phys.: Condens. Matter* **2002,** *14,* 2745–2779. doi:10.1088/0953-8984/14/11/302

28. Perdew, J. P.; Burke, K.; Ernzerhof, M. *Phys. Rev. Lett.* **1996,** *77,* 3865–3868. doi:10.1103/PhysRevLett.77.3865

29. Kerwin, J.; Jackson, B. *J. Chem. Phys.* **2008,** *128,* 084702. doi:10.1063/1.2868771

30. We note that our correction is not a proper BSSE correction, since we only calculate the energy of a relaxed (bent) graphene sheet (as in Figure 1a) with nearby hydrogen ghost atoms, instead of the graphene structure relaxed in the presence of hydrogen. Our analyses show that this simpler approach underestimates the found reaction barriers by a few tens of meV.

31. Brandbyge, M.; Mozos, J.-L.; Ordejón, P.; Taylor, J.; Stokbro, K. *Phys. Rev. B* **2002,** *65,* 165401. doi:10.1103/PhysRevB.65.165401

32. Jeloaica, L.; Sidis, V. *Chem. Phys. Lett.* **1999,** *300,* 157–162. doi:10.1016/S0009-2614(98)01337-2

33. Sha, X.; Jackson, B. *Surf. Sci.* **2002,** *496,* 318–330. doi:10.1016/S0039-6028(01)01602-8

34. Xia, Y.; Li, Z.; Kreuzer, H. J. *Surf. Sci.* **2011,** *605,* L70–L73. doi:10.1016/j.susc.2011.07.009

35. Casolo, S.; Løvvik, O. M.; Martinazzo, R.; Tantardini, G. F. *J. Chem. Phys.* **2009,** *130,* 054704. doi:10.1063/1.3072333

36. Šljivančanin, Z.; Rauls, E.; Hornekær, L.; Xu, W.; Besenbacher, F.; Hammer, B. *J. Chem. Phys.* **2009,** *131,* 084706. doi:10.1063/1.3187941

37. Ivanovskaya, V. V.; Zobelli, A.; Teillet-Billy, D.; Rougeau, N.; Sidis, V.; Briddon, P. R. *Eur. Phys. J. B* **2010,** *76,* 481–486. doi:10.1140/epjb/e2010-00238-7

38. Ruffieux, P.; Gröning, O.; Bielmann, M.; Mauron, P.; Schlapbach, L.; Gröning, P. *Phys. Rev. B* **2002,** *66,* 245416. doi:10.1103/PhysRevB.66.245416

39. Aradi, B.; Hourahine, B.; Frauenheim, T. *J. Phys. Chem. A* **2007,** *111,* 5678–5684. doi:10.1021/jp070186p

40. Šljivančanin, Z.; Andersen, M.; Hornekær, L.; Hammer, B. *Phys. Rev. B* **2011,** *83,* 205426. doi:10.1103/PhysRevB.83.205426

41. Barone, V.; Hod, O.; Scuseria, G. E. *Nano Lett.* **2006,** *6,* 2748–2754. doi:10.1021/nl0617033

42. Buchs, G.; Krasheninnikov, A.; Ruffieux, P.; Gröning, P.; Foster, A. S.; Nieminen, R. M.; Gröning, O. *New J. Phys.* **2007,** *9,* 275. doi:10.1088/1367-2630/9/8/275

43. Boukhvalov, D.; Katsnelson, M.; Lichtenstein, A. I. *Phys. Rev. B* **2008,** *77,* 035427. doi:10.1103/PhysRevB.77.035427

Catalytic activity of nanostructured Au: Scale effects versus bimetallic/bifunctional effects in low-temperature CO oxidation on nanoporous Au

Lu-Cun Wang[1], Yi Zhong[2], Haijun Jin[3], Daniel Widmann[1], Jörg Weissmüller[2,4] and R. Jürgen Behm[*1]

Address:
[1]Institute of Surface Chemistry and Catalysis, Ulm University, D-89069 Ulm, Germany, [2]Institut für Werkstoffforschung, Helmholtz-Zentrum Geesthacht, D-21502 Geesthacht, Germany, [3]Institute of Metal Research, Chinese Academy of Sciences, 110016, Shenyang, P.R. China and [4]Institut für Werkstoffphysik und Werkstofftechnologie, TU Hamburg-Harburg, D-21073 Hamburg, Germany

Email:
R. Jürgen Behm[*] - juergen.behm@uni-ulm.de

* Corresponding author

Abstract

The catalytic properties of nanostructured Au and their physical origin were investigated by using the low-temperature CO oxidation as a test reaction. In order to distinguish between structural effects (structure–activity correlations) and bimetallic/bifunctional effects, unsupported nanoporous gold (NPG) samples prepared from different Au alloys (AuAg, AuCu) by selective leaching of a less noble metal (Ag, Cu) were employed, whose structure (surface area, ligament size) as well as their residual amount of the second metal were systematically varied by applying different potentials for dealloying. The structural and chemical properties before and after 1000 min reaction were characterized by scanning electron microscopy (SEM), X-ray diffraction (XRD) and X-ray photoelectron spectroscopy (XPS). The catalytic behavior was evaluated by kinetic measurements in a conventional microreactor and by dynamic measurements in a temporal analysis of products (TAP) reactor. The data reveal a clear influence of the surface contents of residual Ag and Cu species on both O_2 activation and catalytic activity, while correlations between activity and structural parameters such as surface area or ligament/crystallite size are less evident. Consequences for the mechanistic understanding and the role of the nanostructure in these NPG catalysts are discussed.

Introduction

Porous metallic materials with well-controlled morphologies and surface properties have attracted considerable attention in both fundamental research and technological applications owing to their unique physical and chemical properties, for applications, e.g., in optics, catalysis or as sensors [1,2]. Among these materials, monolithic gold with nanoporous structures as well as high surface areas is of particular interest for catalysis research in view of its self-supporting nature [3-7]. This kind of material is generally synthesized by corrosion techniques, either by chemical corrosion in acidic solutions [3-7] or by electrochemical etching at anodic potentials [8-10]. Using the latter method, electrochemical dealloying, nanoporous gold (NPG) materials with ligament sizes of less than 6 nm can be effectively fabricated [5,10]. Zielasek et al. [4] and Xu et al. [11] reported that nanoporous gold, prepared by the selective dissolution of Ag from a AuAg alloy, exhibits a remarkably high activity for CO oxidation with molecular oxygen at low temperatures, and recent experiments in our laboratory arrived at comparable conclusions [12,13]. In the meantime, high catalytic activities of NPG catalysts were reported also for other reactions, such as oxidative coupling of methanol [14], aerobic oxidation of alcohols [15], and oxidation of organosilanols [16].

Until recently, high activities for the CO oxidation over Au catalysts were only reported for gold nanoparticles of a few nanometers in diameter, which are supported on reducible metal oxides such as TiO_2, CeO_2 and Fe_2O_3 [17-24]. For these oxide-supported Au catalysts, various parameters, such as the gold particle size, the chemical state of the gold nanoparticles or the nature and morphology of the support material have been shown to influence the catalytic activity [19,21]. Especially the nature of the supporting material was found to be decisive for the catalytic activity, with high activities only for catalysts supported on active, reducible metal oxides and only very low activities for those based on inert, nonreducible metal oxides [19,25]. For this reason, the finding of high activities for unsupported NPG was somewhat unexpected, since contributions from a support material are not possible here. As a consequence, the physical origin of the catalytic activity of the unsupported NPG materials has been under debate ever since.

The absence of the oxide support, however, can also be considered as an advantage for the understanding of the mechanisms responsible for the catalytic activity of NPG catalysts, and hence the catalytic behavior of nanoscaled Au, without the complications brought about by the interactions between the support material and the Au nanoparticles and the direct involvement of the support material in the catalytic reaction. Accordingly, earlier studies aiming at the understanding of the reaction mechanism and the physical origin of the high catalytic

activity of NPG materials discussed this mainly in terms of structural effects and related modifications in the local electronic properties [4,5]. In these studies, gold atoms with low coordination numbers at surface defect sites, e.g., steps, corners and kinks, whose concentration increases with decreasing Au particle size or, for NPG, Au ligament size, were proposed as active sites for the activation of molecular oxygen, which is the key step for gold-catalyzed oxidation reactions [26,27]. Furthermore, quantum size effects, which have been proposed by Chen and Goodman for oxide-supported Au catalysts [28], may also be relevant for NPG catalysts considering the nanometer size of the Au ligaments. More recently, residual amounts of the second, less noble metal in the Au alloy used for NPG formation, such as Ag [13,29,30], Cu [6] or Al [31], which cannot be fully removed during dealloying [29], were proposed to be responsible for the unexpected high catalytic activity of NPG catalysts [4,32,33]. This would agree also with earlier proposals for Ag-contaminated submicron-size Au nanoparticles [34] and highly active mesoporous oxide-supported AuAg catalysts [35,36]. From calculations based on density functional theory, Moskaleva et al. found a significant reduction of the barrier for O_2 dissociation in the vicinity of Ag surface atoms in a bimetallic AuAg surface [37]. On the other hand, Haruta considered the NPG catalyst as an inversely supported gold catalyst, where the junction perimeters between gold and Ag_2O accounts for the high catalytic activity. A similar bifunctional effect was proposed also for CO oxidation on oxide-supported AuCu catalysts [38]. A recent study reported a NPG(Cu) catalyst to be very active for CO oxidation as well, but did not provide any mechanistic explanations [6]. Hence, in these pictures the NPG materials can be considered either as a bimetallic or as a bifunctional catalyst, where the second metal modifies the electronic and therefore also chemical properties of the Au surface atoms, or where oxidation of the second metal leads to a local metal–oxide interface.

To clarify whether one of these effects is dominating, and if so which, it would be best to completely separate these two aspects by using NPG samples that are completely free of the second metal or to vary the structural properties of the nanostructured NPG material, such as surface area or crystallite/ligament size, at a constant (surface) content of the respective second metal. Both of these approaches are not possible from experimental reasons, since it is not possible to completely remove all of the less noble metal, such as Ag and Cu, from the starting alloy [10], and also since these impurities sensitively affect the structural properties of the resulting NPG materials [13]. Therefore, these aspects have to be explored in a more indirect way, e.g., by comparing the effect of different residual metals on the catalytic properties of the NPG materials over a wide range of

structural parameters and (surface) content of the respective second metal.

This is the topic of the present paper, in which we compare results on the low-temperature CO oxidation behavior of NPG catalysts with two different residual materials, Ag and Cu, and with different (surface and bulk) contents of these residues, focusing on differences and similarities in the role of these metals on the reaction behavior. A more extensive account of the experimental procedures and of the results on the Ag-containing NPG catalysts can be found in [12]. By applying different potentials during the electrochemical dealloying of AuAg and AuCu alloys, a series of NPG(Ag) and NPG(Cu) catalysts with varying Au ligament sizes and residual Ag(Cu) contents were obtained. The resulting samples were characterized by scanning electron microscopy (SEM), powder X-ray diffraction (XRD) and X-ray photoelectron spectroscopy (XPS) with respect to their morphology, structure and chemical composition. In order to unravel possible structure–activity relationships, the measurements were performed both on the fresh NPG samples and after reaction at atmospheric pressure for 1000 min. Measurements of the catalytic activity for CO oxidation of the NPG catalysts were performed in a conventional microreactor at atmospheric pressure and in a temporal analysis of products (TAP) reactor under ultrahigh vacuum (UHV) conditions. Further information on similarities and differences of the two different types of NPG catalysts in the reaction mechanism was obtained from multipulse TAP reactor measurements, which give access to the ability of the NPG catalysts to activate molecular O_2 and to deposit stable adsorbed active oxygen species on the surface. The results are discussed in a comprehensive picture, in an attempt to combine both structural effects ("structure-activity correlations") and the role of the second, less noble metal.

Experimental
Nanoporous gold sample preparation
NPG(Ag): Nanoporous gold samples were prepared by electrochemical etching (dealloying) of an Ag–Au alloy, as reported previously [13,39,40]. In short, the master alloy $Ag_{75}Au_{25}$ (atom %) was prepared by arc melting of high purity Au and Ag wires (Au 99.9985% and Ag 99.99%, Chempur) and subsequent homogenization at 950 °C for 70 h (sealed in a quartz tube). The ingots were rolled to 0.5 mm thick disks and annealed at 500 °C for two hours in vacuum for recovery. Electrochemical etching (dealloying) was performed in 1 M $HClO_4$ aqueous solution under potentiostatic control. In order to obtain samples with different amounts of residual Ag, different potentials were applied for the dealloying procedure: 1.280 V_{SHE} (NPG(Ag)-1), 1.330 V_{SHE} (NPG(Ag)-2), and 1.380 V_{SHE} (NPG(Ag)-3 and NPG(Ag)-4). The potential was measured by a

pseudo Ag/AgCl reference electrode (in 1 M $HClO_4$), but is quoted versus that of a standard hydrogen electrode (SHE), whose potential is 0.53 V lower than that of the Ag/AgCl electrode. Dealloying was stopped when the current fell to 10 μA. After dealloying, the electrolyte was replaced by fresh base electrolyte and a higher potential (either 1.530 V_{SHE} for NPG(Ag)-1, NPG(Ag)-2 and NPG(Ag)-3 or 1.480 V_{SHE} for NPG(Ag)-4) was applied to the sample for about one hour to further remove the Ag ions, which had remained in the pore channels (see below in Table 1). Subsequently, the nanoporous gold samples were repeatedly rinsed with pure water for cleaning. The NPG(Ag) disks were dried, crushed and gently ground into powder before use, with grain sizes in the range of 20 to 100 μm.

NPG(Cu): Similar to the NPG(Ag) catalysts, a series of NPG samples containing varying amounts of residual Cu was prepared by electrochemical dealloying of a $Au_{25}Cu_{75}$ (atom %) alloy. The master alloy was prepared by arc melting of high purity Au and Cu wires (Au 99.995% and Cu 99.99%, Chempur) and subsequent homogenization at 900 °C for 4 days (sealed in a quartz tube), followed by quenching in water. The ingot was rolled to 0.2 mm thickness and annealed at 600 °C for 2 h in vacuum for recovery. Dealloying was performed in 1 M $HClO_4$ aqueous solution (using deionized ultrapure water with electrical resistivity of 18.2 MΩ cm²/cm), at potentials of 1.430, 1.480 and 1.530 V_{SHE} (Ag/AgCl reference electrode placed directly in the 1 M $HClO_4$ electrolyte close to the sample) for approximately one day. To minimize copper contamination in the sample compartment, the coiled-Cu wire counter electrode (CE) and the reference electrode (RE) were separated from the main cell by placing them in a tube filled with the same solution and mounted with its opening close to the sample. Also in this case, dealloying was stopped when the current fell to 10 μA. Further treatment of the NPG(Cu) samples resembled that for NPG(Ag) described above.

Catalyst characterization
As mentioned previously [13], it is not possible to determine the surface area of the NPG samples under the normal conditions of a BET measurement, since its microstructure is thereby destroyed. For this reason we determined the surface area of the as-prepared NPG catalysts by the electrochemical capacitance ratio method [41].

X-ray diffraction (XRD) provided a separate, independent approach towards the structure of the NPG samples. The measurements were performed on a PANalytical MPD PRO instrument by using Cu Kα radiation (λ = 0.154 nm). The structural coherency was evaluated through the width of the Au(111) diffraction peaks by means of the Scherrer equation, $D_{Scherrer} =$

($K\cdot\lambda$)/($\beta\cdot\cos\theta$), where $K = 0.89$ is the Scherrer constant, λ the wavelength of the X-rays, and β the FWHM. In the idealized case of nanoscale crystallites that are free of strain, $D_{Scherrer}$ approximates the crystal size. NPG consists of crystals with a size on the order of 10 to 100 µm, which are porous on the much smaller nanometer scale [39,42]. The width of the diffraction peaks and the defect structure of the material [39,42] imply that the contribution of lattice defects/lattice strain to the reflection broadening may not be neglected. Overall, the Scherrer equation is therefore not an appropriate way of determining the ligament size. Nonetheless, the width of the Bragg reflections indicates a loss of crystalline coherence on a length-scale on the order of $D_{Scherrer}$, and in this sense, the broadening of the XRD profiles may be discussed as an indicator of structure size. Moreover, if one assumes idealized, cylindrical ligaments with diameter D, the mass-specific surface areas (α) of the NPG samples can be calculated from the ligament size by the relation $\alpha = 4/(\rho\cdot D)$ [40], where ρ is the mass density of gold (19.32 g·cm^{-3}). Our results even indicate a quantitative correlation between the specific surface area as measured by the capacitance method and the value inferred by using $D_{Scherrer}$ as the ligament size and assuming cylindrical ligaments (see below, Results and Discussion, subsection 1.1). Keeping in mind that this is an empirical relation, we will use the term *apparent ligament size* for the value derived from $D_{Scherrer}$, and use this for the characterization of samples after the catalytic reaction, which cannot be characterized by the capacitance ratio method.

For further characterization of the samples, scanning electron microscopy (SEM) and energy dispersive X-ray spectroscopy (EDX) measurements were performed to determine the surface morphology, microstructure and the bulk concentration of Ag/Cu, respectively. In order to determine the surface concentration of residual Ag or Cu, respectively, X-ray photoelectron (XP) spectra were recorded on the NPG powder samples by using a PHI 5800 ESCA system (Physical Electronics) with monochromatic Al Kα radiation for excitation. The binding energies of the Au(4f), Ag(3d) and Cu(2p) states were calibrated with respect to the C(1s) peak at 284.6 eV. The Au, Ag and Cu surface concentrations were calculated from the measured intensities of the Au(4f), Ag(3d) and Cu(2p) signals, respectively, by using tabulated sensitivity factors. It should be noted that this procedure assumes a constant composition of the top few layers. Repeated XPS measurements on the same samples and also on samples before grinding them into powder revealed that the error for the resulting surface Ag content is less than 5% (relative).

Catalytic activities: Flow reactor measurements
In a similar manner to the measurements in [12,13], the catalytic activities of the NPG catalysts for CO oxidation were measured in a microreactor with a length of 300 mm, an outer diameter of 6 mm, and an inner diameter of 4 mm at atmospheric pressure and a reaction temperature of 30 °C, without applying any pretreatment prior to the measurements. The catalysts were diluted with α-Al$_2$O$_3$ in order to obtain differential reaction conditions, with reactant conversions of below 15% throughout the measurements. The temperature of the catalyst bed was measured by a thermocouple attached to the outer wall of the reactor, in the central area of the catalyst bed. The flow rate of the reactant gas was 60 NmL·min^{-1} (1% CO, 1% O$_2$, rest N$_2$), and both influent and effluent gases were analyzed by on-line gas chromatography (Chrompack CP9001). For further details of the setup and the evaluation see [19,43].

Catalytic activities: TAP reactor measurements
The pulse experiments were carried out in a home-built TAP reactor [44], which is largely based on the TAP-2 approach of Gleaves et al. [45], using a similar approach as was described previously in [12,13]. In short, piezoelectric pulse valves were used to generate gas pulses of typically ~1 × 10^{16} molecules per pulse. For all measurements presented, these pulses contained 50% Ar as an internal standard to enable quantitative evaluation on an absolute scale. The gas pulses were directed into a quartz-tube microreactor with a length of 90 mm, an outer diameter of 6 mm, and an inner diameter of 4 mm. The catalyst bed was located in its central part, fixed by two stainless steel sieves (Haver & Boecker OHG, transmission 25%). For all measurements, we used a three-zone catalyst bed containing 2 mg of NPG catalyst diluted with 20 mg SiO$_2$ as the central zone and two layers of SiO$_2$ as the outer zones (total mass 150 mg). All pulse experiments were performed at 30 °C reaction temperature. Also here, the catalyst was used as received, with no additional pretreatment prior to the measurements. After passing through the reactor, the gas pulses were analyzed by a quadrupole mass spectrometer (QMG 700, Pfeiffer) located behind the reactor tube in the analysis chamber. The consumption of CO and O$_2$ in the respective pulses was calculated from the missing mass spectrometric intensity in the pulses compared to the intensity after surface saturation, which is equivalent to the initial intensity. The formation of CO$_2$ could be determined directly from the CO$_2$ pulse intensity. Additionally, (pre)treatment of the catalysts at higher (atmospheric) pressure is possible by separating the reactor from the ultrahigh vacuum (UHV) system by a differentially pumped gate valve and connecting it directly to an adjustable roughing pump.

For testing the catalytic activity for CO oxidation in the TAP reactor, the samples were exposed to simultaneous pulses of CO/Ar and O$_2$/Ar, with a CO/O$_2$ ratio of 1:1, i.e., an excess of oxygen relative to stoichiometric reaction conditions. Prior to these measurements it was checked that the gas mixing unit and

the gas pipes containing the reaction mixture as well as the reactor and the dilution materials were inert; no conversion of CO or O_2 was found under these conditions in control experiments. To identify stable adsorbed surface species on the catalyst surface before and after the reaction, we also performed temperature-programmed desorption (TPD) measurements in the TAP reactor. During these measurements, the catalysts were heated from 30 to 600 °C at a heating rate of 25 °C·min^{-1}. The gaseous desorption/decomposition products are transported by diffusion into the analysis chamber, where they are detected by the mass spectrometer.

The ability to activate O_2, given by the amount of stable adsorbed active oxygen that can be reversibly deposited from interaction with O_2 and reacted away by CO pulses (oxygen storage capacity, OSC), was also determined by TAP reactor measurements. Here, the NPG samples were first exposed to O_2 in a continuous flow of 10% O_2/N_2 with a gas flow of 20 NmL·min^{-1} at atmospheric pressure (30 min at 30 °C); afterwards the amount of stable adsorbed oxygen species active for CO oxidation was titrated by a sequence of CO/Ar pulses under vacuum conditions. The formation of CO_2 originating from the reaction of CO with adsorbed oxygen could be determined directly from the CO_2 pulse intensity, and the OSC was calculated from the total amount of CO_2 produced during a sequence of CO pulsing [12]. Details about the calibration of the mass spectrometric signals on an absolute scale can be found in [44]. Direct evaluation of the OSC by quantification of the O_2 uptake of a reduced sample during O_2 pulses, as performed for supported catalysts [23,25,46], was not possible due to the very low amount of oxygen uptake within single O_2/Ar pulses. After the oxygen species were removed, the catalyst was exposed once again to a mixture of 10% O_2/N_2 at atmospheric pressure, and the process of oxygen deposition and reactive removal by CO was repeated at least three times for all samples in order to check the reversibility of the active oxygen formation.

Results and Discussion
1 Structural and chemical characterization of the NPG catalysts
1.1 NPG(Ag) catalysts
As-prepared samples: The morphology of the NPG materials was characterized by SEM imaging. Figure 1 displays representative SEM images of the NPG(Ag)-4 sample before and after the catalytic reaction. The fresh sample has a foamlike morphology with ligament diameters of below 10 nm (Figure 1a). More detailed structural features, however, are not discernible due to the limited resolution of the SEM image. To gain further information on the structural properties of the bulk phase, XRD measurements were performed on these samples (Figure 2a). Considering the discussion in the Experimental

subsection „Catalyst characterization", the broad diffraction peaks of metallic Au for the three fresh samples, NPG(Ag)-2 to NPG(Ag)-4, indicate that the crystallites are significantly strained, possibly due to a large density of lattice dislocations. On NPG(Ag)-1, the diffraction peaks are significantly sharper, indicating a lower defect density. This goes along with a significantly lower specific surface area of sample NPG(Ag)-1 as determined by the capacitance ratio method (see below). In none of the samples could we detect diffraction peaks characteristic of the Ag-containing phases (metallic silver or silver oxides). Using the Scherrer equation in the sense described before, we determined apparent ligament sizes of 21, 6.4, 4.1 and 4.1 nm for the samples NPG(Ag)-1, NPG(Ag)-2, NPG(Ag)-3 and NPG(Ag)-4, respectively (Table 1).
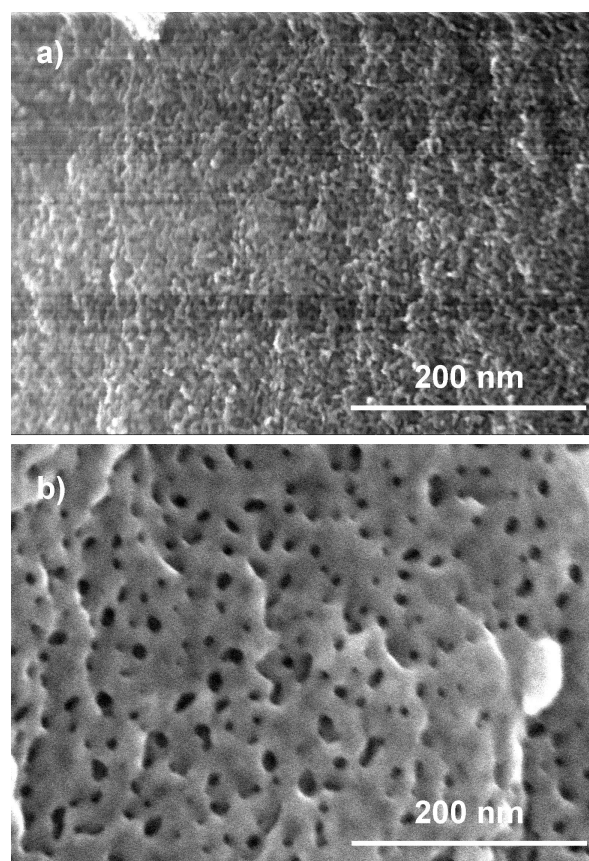
Figure 1: SEM images of the NPG(Ag)-4 catalyst (a) before and (b) after 1000 min on stream.

Figure 3 shows XP detail spectra of the Au(4f) and Ag(3d) regions of an as-prepared NPG(Ag) sample. For brevity, we here show only those of the NPG(Ag)-3 sample; the corresponding spectra for the other three samples are given in Supporting Information File 1 (Figure S1). The characteristic parameters evaluated from these XP spectra are summarized in Table 2. The Au(4f) spectrum contains two sets of distinct
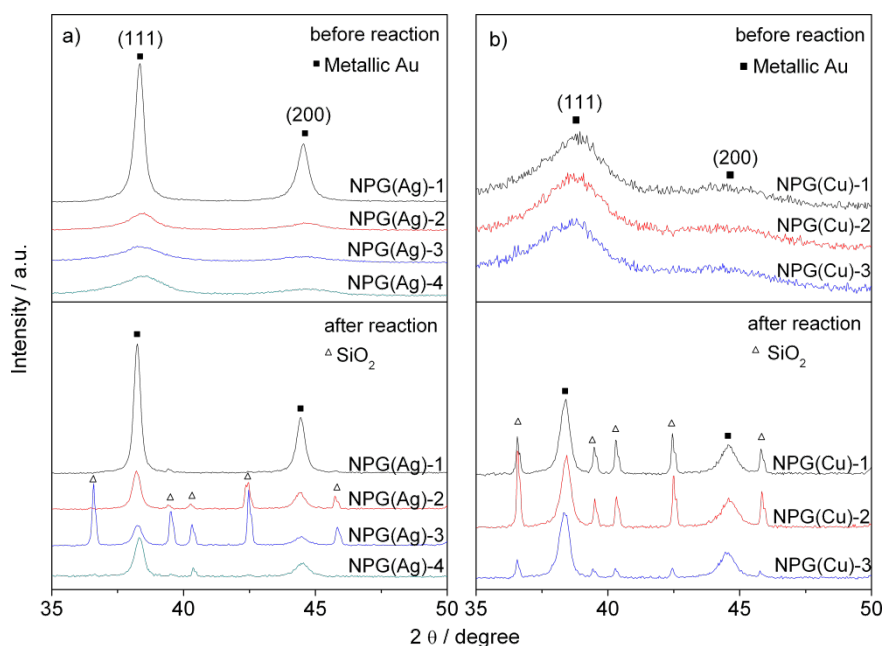
Figure 2: XRD patterns of various NPG catalysts before and after 1000 min on stream: (a) NPG(Ag) and (b) NPG(Cu).

Table 1: Details of the preparation parameters, physical properties and catalytic activity for CO oxidation at 30 °C for various NPG(Ag) catalysts (values taken from [13]).[a]

catalyst	NPG(Ag)-1	NPG(Ag)-2	NPG(Ag)-3	NPG(Ag)-4
potential of dealloying / V_{SHE}	1.280	1.330	1.380	1.380
potential of cleaning / V_{SHE}	1.530	1.530	1.530	1.480
average crystallite size D / nm[b]	21 (28)	6.4 (21)	4.1 (23)	4.1 (21)
surface area / $m^2 \cdot g^{-1}$ [c]	≈10	63	59	75
surface area / $m^2 \cdot g^{-1}$ [d]	10 (7)	31 (10)	51 (9)	50 (10)
bulk Ag / atom %[e]	4.5	13.2	14.4	14.6
surface Ag / atom %[f]	5.4 (16.6)	9.5 (30.0)	10.5 (24.7)	18.6 (25.3)
surface Ag atoms / $10^{20} \cdot g_{cat}^{-1}$	0.06 (0.13)	0.69 (0.34)	0.71 (0.26)	1.6 (0.29)
OSC–stable / 10^{19} O atoms$\cdot g_{Au}^{-1}$	0.03	1.2	0.54	0.86
r_{Au} / 10^{-5} mol$\cdot s^{-1} \cdot g_{Au}^{-1}$	0.4 (0.3)	12.4 (9.2)	3.4 (3.6)	18.2 (6.2)

[a]The data presented in parentheses are obtained from the samples after 1000 min on stream. [b]Estimated from Au(111) diffraction peaks by using the Scherrer equation. [c]Surface areas of the fresh samples measured by the capacitance ratio method. [d]Estimated by assuming idealized, cylindrical ligaments with diameter D. [e]Measured by SEM-EDX. [f]Measured by XPS.

peaks, with the Au($4f_{7/2}$) peaks at 84.6 and 86.2 eV. The binding energy (BE) of the main peak is slightly higher than that for metallic Au^0 (84.0 eV) [47,48]. The shoulder at higher BE can be assigned to Au^{3+} (Au_2O_3) species, following previous assignments [48]; it contributes about 21% to the total Au(4f) intensity based on a deconvolution of the peaks. Similar spectra were also obtained on the NPG(Ag)-2 and NPG(Ag)-4 samples, with contributions of 11% and 12% from Au^{3+} species, respectively. In contrast, no oxidic species were detected on the NPG(Ag)-1 sample. The Ag(3d) XP spectra were also recorded to check the existence of residual Ag and its

chemical state. As shown in Figure 3b, the as-prepared NPG(Ag)-3 sample contains two distinct components of the Ag($3d_{5/2}$) peak with BEs of 368.7 eV and 367.7 eV, respectively. At first glance, the second peak seems to be more characteristic for metallic Ag^0 [35], while the high BE of the first peak does not fit with literature reports [49]. Considering, however, that the final-state effects will lead to a similar up-shift of the BEs as discussed for the Au(4f) peaks, we assign the Ag($3d_{5/2}$) peak at 368.7 eV to metallic Ag, up-shifted by final-state effects, while the 367.7 eV peak is attributed to a similarly up-shifted Ag($3d_{5/2}$) peak related to AgO [49], with a contribu-
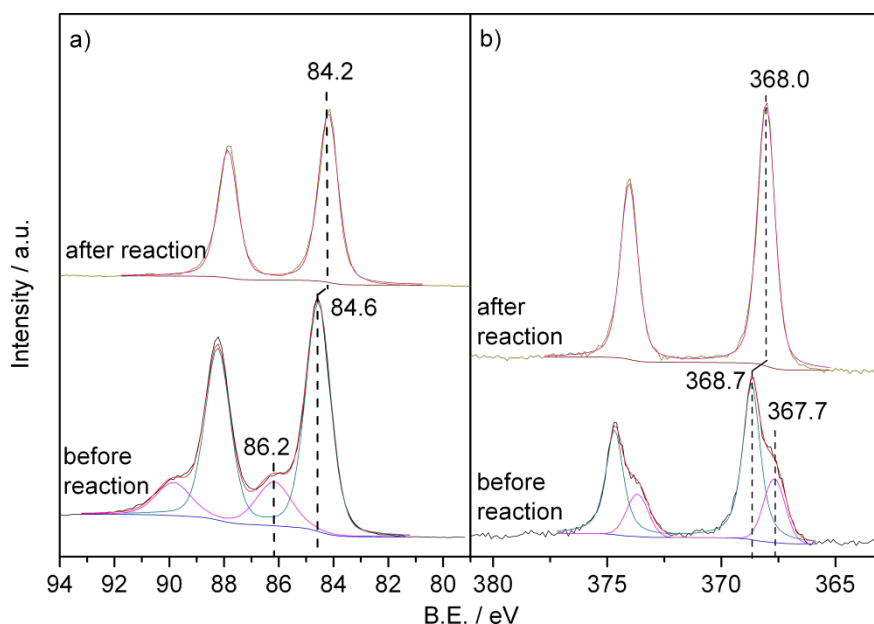
Figure 3: Au(4f) (a) and Ag(3d) (b) XP spectra of the NPG(Ag)-3 catalyst before and after 1000 min on stream.

Table 2: XPS results of various NPG(Ag) samples before and after reaction.

catalyst	B.E. of Au(4f$_{7/2}$) / eV	Au^{3+} / %	B.E. of Ag(3d$_{5/2}$) / eV	AgO / %	surface Ag / atom %
NPG(Ag)-1 fresh	84.5	0	368.3/—	0	5.4
NPG(Ag)-1 used	84.4	0	368.2/—	—	16.6
NPG(Ag)-2 fresh	84.5	11	368.6/367.8	22	9.5
NPG(Ag)-2 used	84.3	0	368.1/—	—	30.0
NPG(Ag)-3 fresh	84.6	21	368.7/367.7	28	10.5
NPG(Ag)-3 used	84.2	0	368.0/—	—	24.7
NPG(Ag)-4 fresh	84.5	12	368.5/367.7	26	18.6
NPG(Ag)-4 used	84.3	0	368.2/—	—	25.3

tion of about 28% to the total Ag(3d) intensity. The corresponding fractions of silver oxide species on the NPG(Ag)-2 and NPG(Ag)-4 catalysts were 22% and 26%, respectively, while only metallic Ag was found on the NPG(Ag)-1 sample.

Table 1 lists the Ag contents (both bulk content (EDX) and content in the near-surface region (XPS)) and the specific surface areas of the different NPG(Ag) samples. Obviously, raising the dealloying potential leads to an increase of the residual (bulk) Ag content in the NPG(Ag) samples, though with a nonlinear relationship. A potential increase from 1.280 V$_{SHE}$ to 1.330 V$_{SHE}$ results in a more significant Ag retention in the bulk phase (4.5 and 13.2 atom % Ag for NPG(Ag)-1 and NPG(Ag)-2, respectively), while for a further potential increase to 1.380 V$_{SHE}$ the changes are less pronounced, with 14.4 and 14.6 atom % Ag for NPG(Ag)-3 and NPG(Ag)-4, respectively.

The surface Ag contents show a similar dependence on the dealloying potential as observed in the bulk phase, with surface Ag contents of 5.4, 9.5, 10.5 and 18.6 atom % Ag for NPG(Ag)-1 to NPG(Ag)-4, respectively (see Table 1). The surface Ag content of the sample NPG(Ag)-4, however, is remarkable, since it is significantly higher compared to that of the NPG(Ag)-3 sample, although it has a comparable bulk Ag content and the same dealloying potential was applied. Most probably, this discrepancy is caused by the lower potential used during the following cleaning procedure. The present data agrees well with a recent study of Ag retention during electrochemical dealloying of AuAg at different pH values by Liu et al. [50]. Those authors also showed that it is possible to obtain samples with significantly different surface Ag content by varying the dealloying potential (at constant dealloying time and sample size) and the subsequent cleaning procedure [50].

The higher dealloying potential not only caused an increase in the Ag content (bulk and near-surface Ag contents) of the NPG(Ag) samples, but also in the surface areas measured directly by the capacitance ratio method. The latter changes are particularly obvious at lower potentials, from 1.280 V_{SHE} to 1.330 V_{SHE}. As described in the Experimental section (subsection „Catalyst characterization"), we also estimated the surface areas from the XRD data, assuming idealized, cylindrical ligaments and using the apparent ligament size. The results are comparable to the data measured directly for the samples NPG(Ag)-1 (10 $m^2 \cdot g_{cat}^{-1}$) and NPG(Ag)-3 (51 $m^2 \cdot g_{cat}^{-1}$), whereas for the samples NPG(Ag)-2 (31 versus 63 $m^2 \cdot g_{cat}^{-1}$) and NPG(Ag)-4 (50 versus 75 $m^2 \cdot g_{cat}^{-1}$) the directly measured surface areas were higher than those derived from the XRD data (see Table 1). This discrepancy underlines the dangers in applying the Scherrer equation to materials with nanoscale pores in micron-scale crystals. In fact, previous TEM investigations revealed a large number of lattice defects in NPG, specifically when the dealloying conditions are set to obtain a very small ligament size [39]. In order to correct for differences/changes in the Ag surface content in the respective NPG samples, we also calculated the total amount of surface Ag atoms per gram of catalyst (see Table 1), assuming a homogeneous vertical distribution of the Ag atoms in the surface regime analyzed by XPS. This was done by multiplying the surface Ag content with the total number of surface atoms, which was determined from the surface area by assuming a surface density of 1.15×10^{15} atoms cm^{-2}. The resulting values are given in Table 1.

Catalysts after reaction: Since the NPG(Ag) catalysts deactivated to different extents during 1000 min on stream (see section 2 "Catalytic activities"), we followed the structural changes during the activity measurements in order to detect possible structure-activity correlations. The NPG(Ag) catalysts were retrieved after reaction for 1000 min and subsequently characterized again. A representative SEM image taken from the NPG(Ag)-4 sample after reaction showed a distinct coarsening of the porous surface structure (see Figure 1b). This is confirmed also by the XRD patterns (see Figure 2a), where exposure to the reaction gas mixture caused a considerable sharpening of the diffraction peaks for all NPG(Ag) catalysts. Hence, restructuring occured also in the bulk region. These peak widths correspond to apparent ligament sizes of 28, 21, 23 and 21 nm for NPG(Ag)-1 to NPG(Ag)-4 after reaction, respectively. A similar reaction-induced ligament size growth for nanoporous gold during CO oxidation (25 h, 30 °C, 66.7 mL·min^{-1}: 1% CO + 10% O_2 + 89% N_2,) was reported also by Xu et al. [5]. Note that since SiO_2 was used as a dilution material during reaction, its sharp peaks can also be identified in the XRD patterns after reaction.

After exposure to the reaction conditions for 1000 min, the higher BE Au($4f_{7/2}$) XPS shoulder completely disappeared, and the main Au($4f_{7/2}$) peak shifted to a lower BE of 84.2 eV (see Figure 3a). This result clearly indicates that the surface Au^{3+} oxide species are reduced under the reaction conditions. The down-shift of the main peaks can originate from the reduction of slightly oxidized Au species (e.g., Au^+ with a BE 0.6 eV higher than that of Au^0 [51,52]) and/or from the significant growth of the ligament size during reaction (from ca. 4.1 nm to ca. 23 nm, as described above). It has been reported that BE shifts of 0.5–0.9 eV relative to the bulk Au^0 value could be obtained as final-state effects in small Au clusters [53,54]. With increasing particle size, the Au(4f) peak would shift back to the metallic Au^0 position. However, in view of the relatively large average Au ligament size (apparent ligament size 4.1 nm) for the fresh sample, larger contributions from final-state effects are considered to be not very likely. Therefore, we favor an explanation that relates the higher BE of the peak at 84.6 eV (before reaction) mainly to positively charged gold species ($Au^{\delta+}$), which are discharged during the reaction. The exact charge of this $Au^{\delta+}$ species, however, cannot be determined from these measurements. Going to the Ag(3d) signals, we find that after reaction for 1000 min the doublet of the Ag(3d) XPS peaks detected on the fresh samples for NPG(Ag)-2 to NPG(Ag)-4 is replaced by a new peak with an intermediate BE of 368.0 eV (see Figure 3b). This corresponds to the normal BE of metallic Ag^0, without further shifts introduced by final state effects [35,49]. Thus, similar to Au, oxidized Ag surface species are reduced during the reaction.

Table 1 also contains the chemical compositions as well as the surface areas of the various NPG(Ag) samples after reaction. Unlike the fresh samples, the surface area of the samples after reaction could not be measured by the capacitance ratio method, since the amounts of NPG(Ag) catalyst used for reaction are very low (2 mg) and the samples were crushed before use. Therefore, the surface areas of the used NPG(Ag) catalysts were estimated from the apparent ligament sizes, as described above. Here we should keep in mind the approximate character of the X-ray diffraction analysis and the deviations between the surface areas determined by different methods, which are expected also for the surface areas determined after reaction. Deviations in the surface areas will directly affect the number of Ag or Au surface atoms per gram of catalyst. Interestingly, the distinct differences in the ligament sizes of the fresh NPG(Ag) catalysts decay significantly during reaction for 1000 min, resulting in much more similar values. Hence, the structure of the NPG(Ag) changes considerably during the reaction, and these changes are much more pronounced for the samples with initially smaller ligaments (NPG(Ag)-2 to NPG(Ag)-4). This finding agrees well with those in previous reports [11].

Based on the XPS measurements, the reaction also caused a significant surface Ag enrichment for all four NPG(Ag) samples. The surface Ag content increased by a factor of 3 to 16.6 and 30.0 atom % for NPG(Ag)-1 and NPG(Ag)-2, respectively, compared with that before reaction. For the samples NPG(Ag)-3 and NPG(Ag)-4 the Ag surface enrichment was lower, and increased only by a factor of 2.4 to 24.7 atom % and by a factor of 1.4 to 25.3 atom %, respectively. Surface enrichment of Ag in bimetallic AuAg systems has previously been detected both experimentally [35,55] and in theoretical simulations [56,57]. For example, in a study of CO oxidation over Au–Ag/TiO$_2$ catalysts, Sandoval et al. [55] observed a surface Ag enrichment upon thermal treatment at high temperatures. The extent of Ag enrichment on the surface of AuAg alloys depends sensitively on temperature, composition and particle size [56]. From a thermodynamic point of view, Ag prefers either to be on the surface or to form interfacial alloys with Au, while Au prefers to segregate at the core due to the lower surface energy of Ag compared to Au in the absence of adsorbates [56,58]. This may be modified by strongly adsorbing species. The number of surface Ag atoms after reaction was also calculated to compare with the data obtained on the fresh samples (see Table 1).

1.2 NPG(Cu) catalysts

For the Cu-containing NPG catalysts, we employed an approach similar to the preparation of NPG(Ag) catalysts to prepare a series of NPG(Cu) samples with different residual Cu contents by using different dealloying potentials in the range of 1.430–1.530 V$_{SHE}$ during the etching process. This potential range was chosen since initial experiments had shown that highly active NPG(Cu) samples with small ligament sizes (see below), which are comparable to those of the samples

NPG(Ag)-2 to NPG(Ag)-4, could only be obtained when the dealloying was performed at potentials higher than 1.380 V$_{SHE}$.

As-prepared samples: The characterization results presented in Table 3 show that, within the range investigated, the dealloying potential had no significant influence on the surface area (58, 68 and 49 m^2·g^{-1} for NPG(Cu)-1 to NPG(Cu)-3, respectively). The rather broad XRD diffraction peaks (see Figure 2b), which are similar for all samples, indicate that there are also no distinct differences in the structural properties; the apparent mean ligament sizes were calculated to be 3.5, 3.3 and 3.3 nm, with the corresponding estimated surface areas of 60, 63 and 62 m^2·g^{-1} for the samples NPG(Cu)-1, NPG(Cu)-2 and NPG(Cu)-3, respectively (see Table 3). The calculated surface areas fit well with the ones measured directly via the capacitance ratio method.

Au(4f) and Cu(2p) XP spectra recorded on the NPG(Cu)-2 sample, which are representative of all three NPG(Cu) samples, are presented in Figure 4. The parameters evaluated from the XP spectra are summarized in Table 4. Similar to the Ag-containing NPG samples, two Au(4f$_{7/2}$) peaks with BEs of 84.4 and 86.0 eV were detected on all three samples investigated, with the fraction of the Au^{3+} oxide species (86.0 eV) being 22, 19 and 24% for NPG(Cu)-1 to NPG(Cu)-3, respectively. The main peak of the Cu(2p) spectra (Figure 4b) consists of two components at ≈932.6 and ≈934.0 eV, accompanied by a distinct satellite peak at ≈942 eV. According to the literature [59-61], the peak at ≈934.0 eV together with the satellite peak is characteristic of Cu^{2+} oxide species, whereas the peak at ≈932.6 eV may arise from copper oxide species with lower oxidation states, most likely Cu$_2$O. An unambiguous assignment, however, requires further information, e.g., from the corres-

Table 3: Details on the preparation parameters, physical properties and catalytic activity for the CO oxidation at 30 °C for various NPG(Cu) catalysts.[a]

catalyst	NPG(Cu)-1	NPG(Cu)-2	NPG(Cu)-3
potential of dealloying / V$_{SHE}$	1.430	1.480	1.530
potential of cleaning / V$_{SHE}$	1.530	1.530	1.530
average crystallite size *D* / nm[b]	3.5 (24)	3.3 (23)	3.3 (22)
surface area / m^2·g^{-1} [c]	58	68	49
surface area / m^2·g^{-1} [d]	60 (9)	63 (9)	62 (10)
bulk Cu / atom %[e]	6.8	6.0	4.5
surface Cu / atom %[f]	3.4 (5.3)	3.7 (5.7)	4.1 (5.4)
amount of surface Au atoms / 10^{20}·g$_{cat}^{-1}$	6.6 (0.96)	7.0 (0.96)	6.9 (1.02)
amount of surface Cu atoms / 10^{19}·g$_{cat}^{-1}$	2.3 (0.54)	2.7 (0. 57)	3.0 (0.58)
OSC–stable / 10^{19} O atoms·g$_{Au}^{-1}$	0.07	0.13	0.23
r_{Au} / 10^{-5} mol·s^{-1} g$_{Au}^{-1}$	0.9 (1.5)	2.4 (2.8)	2.6 (3.5)

[a]The data presented in parentheses are obtained from the samples after 1000 min on stream. [b]Estimated from Au(111) diffraction peaks by using the Scherrer equation. [c]Surface areas of the fresh samples measured by the capacitance ratio method. [d]Estimated by assuming idealized, cylindrical ligaments with diameter *D*. [e]Measured by SEM-EDX. [f]Measured by XPS.
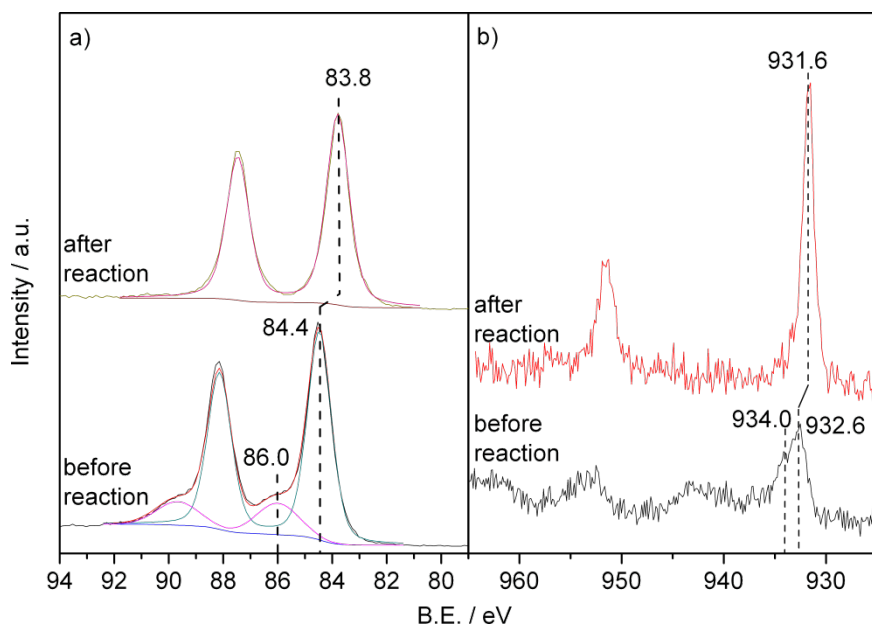
Figure 4: Au(4f) (a) and Cu(2p) (b) XP spectra of the NPG(Cu)-2 catalyst before and after 1000 min on stream.

Table 4: XPS results of various NPG(Cu) samples before and after reaction.

catalyst	B.E. of Au(4f$_{7/2}$) / eV	Au^{3+} / %	B.E. of Cu(2p$_{3/2}$) / eV	surface Cu / atom %
NPG(Cu)-1 fresh	84.5	22	934.1/932.7	3.4
NPG(Cu)-1 used	84.7	0	932.7	5.3
NPG(Cu)-2 fresh	84.4	19	934.0/932.6	3.7
NPG(Cu)-2 used	83.8	0	931.6	5.7
NPG(Cu)-3 fresh	84.5	24	934.2/932.7	4.1
NPG(Cu)-3 used	83.5	0	931.4	5.4

ponding Auger spectra [60]. The elemental analysis showed an increasing surface Cu content with increasing dealloying potential, i.e., 3.4, 3.7 and 4.1 atom % for samples NPG(Cu)-1 to NPG(Cu)-3, respectively. These values are somewhat lower than the corresponding Cu contents in the bulk phase determined by EDX (6.8, 6.0 and 4.5 atom % for NPG(Cu)-1 to NPG(Cu)-3, respectively, see Table 3). This result differs from the trends for the fresh NPG(Ag) samples, where two of the catalysts had a lower and two a higher surface Ag content than the bulk (see Table 1). The physical origin for this discrepancy, however, is not clear yet.

Samples after reaction: The diffractograms of the used catalysts (Figure 2b) show a significant sharpening of the diffraction peaks for all three samples after reaction for 1000 min, pointing to a pronounced coarsening of the bulk structure. The apparent ligament sizes were determined to be 24, 23 and 22 nm for NPG(Cu)-1 to NPG(Cu)-3 (see Table 3), respectively, close

to the values obtained for the NPG(Ag) samples after reaction. The surface areas of these samples are calculated to be 9, 9 and 10 m$^2 \cdot$g^{-1}. XP spectra recorded after 1000 min on stream resolved only metallic Au surface species on all three samples, with the BE of Au(4f$_{7/2}$) down-shifted to ≈83.8 eV for NPG(Cu)-2 (see Figure 4) and NPG(Cu)-3, again comparable to the findings for NPG(Ag) samples, while it stays almost constant for NPG(Cu)-1. For the surface Cu species, the satellite peaks disappeared after exposure to the reaction conditions, and the main Cu(2p) peak shifted to lower BE, to ≈931.6 eV for all NPG(Cu) samples, indicating the formation of metallic copper or Cu$^+$ species [59,61,62]. Due to the presence of the dominant Au(4d$_{5/2}$) peak at 335.0 eV, we cannot distinguish between these two species from their Cu LMM Auger peaks at 335.0 eV (Cu^0) or 337.5 eV (Cu$^+$), respectively (see also the discussion on the TPD results below, subsection 2.2). Finally, also in this case the XP spectra indicate a reaction-induced surface enrichment of Cu for all three NPG(Cu) samples, with

5.3, 5.7 and 5.4 atom % for the samples NPG(Cu)-1 to NPG(Cu)-3, respectively, although to a much lesser extent compared with the NPG(Ag) materials. This can be simply explained by the lower surface energy of Au compared to that of Cu [63].
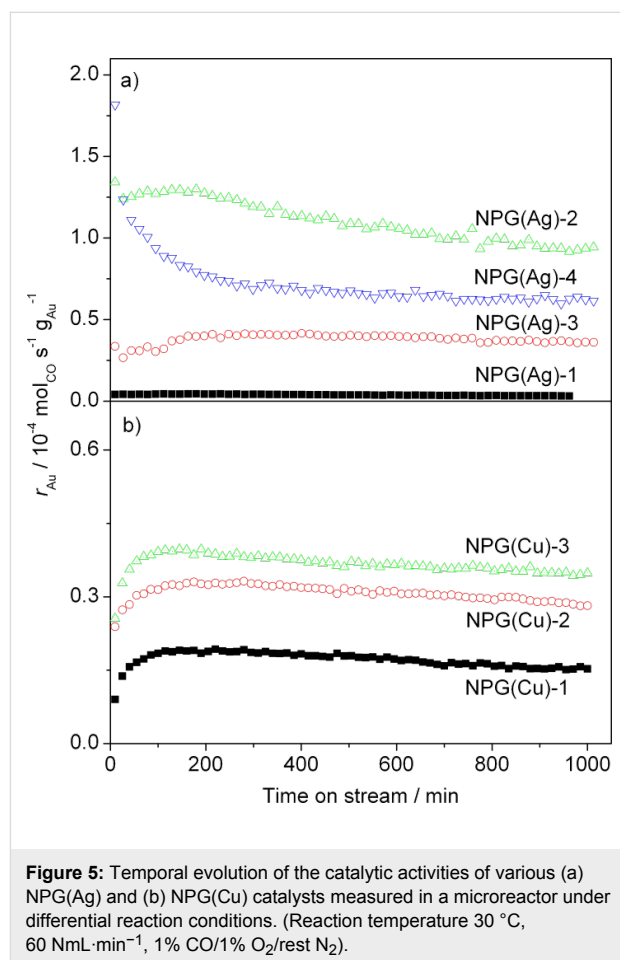
2 Catalytic activities
2.1 Catalytic activities in the microreactor

NPG(Ag): The catalytic activities of the NPG catalysts for CO oxidation were first determined in the commonly used approach, by kinetic measurements at atmospheric pressure in a microreactor under differential reaction conditions. Note that for the nanoporous Au material the kinetic parameters may be significantly influenced by the mass transport limitation by pore diffusion [29]. For the diluted powders of NPG samples used in this work, however, diffusion limitations are much less likely than for NPG disks used in a previous study [29]. In fact, by using the method described before [29], the Thiele modulus is estimated to be less than 3, where the influence of mass transport limitations is negligible.

Figure 5a shows the CO oxidation activity of the four NPG(Ag) catalysts, in terms of Au mass-normalized reaction rates, and their temporal evolution in a standard reaction mixture (1% CO, 1% O_2, rest N_2) at 30 °C reaction temperature. Among the four samples investigated, the NPG(Ag)-4 catalyst showed the highest initial activity (1.8×10^{-4} $mol_{CO} \cdot s^{-1} \cdot g_{Au}^{-1}$), with a continuous decay over time during the first 200 min (60%), followed by an almost constant activity up to 1000 min on stream. This closely resembles the behavior of Au/TiO_2 catalysts during CO oxidation [64,65]. In contrast, the other three NPG(Ag) catalysts exhibited a distinctly different reaction behavior. For these samples, the activity first increased steadily, for 2–3 h, and afterwards decayed by 20–30% (see Figure 5a). After 1000 min on stream, approximately steady-state activities are reached, which amount to 0.3, 9.2, 3.6, and 6.2 × 10^{-5} $mol_{CO} \cdot s^{-1} \cdot g_{Au}^{-1}$ for NPG(Ag)-1 to NPG(Ag)-4, respectively (see also Table 1). Note that despite the comparable surface areas under steady-state conditions, the NPG(Ag)-2 sample is more active than samples NPG(Ag)-3 and NPG(Ag)-4. The observation of an initial activation phase closely resembles findings by Wittstock et al., who reported an activation period of approximately 2–3 h on a NPG disk catalyst (ligament size 30–50 nm) for CO oxidation at 80 °C [29]. These authors related the activation to the removal of moisture in the pores or of contaminants stemming from the leaching process. The first suggestion, removal of moisture, appears to be unlikely considering the results of additional kinetic measurements performed in our laboratory, in which we used an additional drying pretreatment and dry feed gas [13]. These experiments revealed that while the activities are lower for all

catalysts than under "normal" reaction conditions, the catalytic behavior is essentially unaltered (for details see [13]). Hence, the presence of moisture in the reaction gas mixture, even of the trace impurities as present in commercial gases and on the catalyst, raises the activity of NPG(Ag) catalysts, but does not change their typical reaction behavior with time on stream. The increase in activity even extends to higher moisture contents as evidenced by recent findings by Wittstock et al. [33] who observed that adding 10000 ppm water to the gas feed enhances the catalytic activity of NPG catalyst in CO oxidation, in their case by more than 100%.

Figure 5: Temporal evolution of the catalytic activities of various (a) NPG(Ag) and (b) NPG(Cu) catalysts measured in a microreactor under differential reaction conditions. (Reaction temperature 30 °C, 60 NmL·min^{-1}, 1% CO/1% O_2/rest N_2).

NPG(Cu): Similar kinetic measurements performed on the three NPG(Cu) catalysts showed that the catalytic behavior closely resembles that of the NPG(Ag)-2 and NPG(Ag)-3 samples, showing an activation period of ca. 2 h followed by a continuous decay until reaching a quasi-steady-state after 1000 min on stream (see Figure 5b). Since the apparent ligament size and surface area for all Cu- and Ag-containing samples is almost the same after reaching the steady state, we use the stable activities to compare the NPG(Cu) and NPG(Ag) samples. Although the amount of Cu residues at the surface of

NPG(Cu) catalysts is much lower compared to that of Ag in all NPG(Ag) catalysts (ca. 5.5% surface Cu content compared to 16.6–30.0% surface Ag content), the stable catalytic activities of the NPG(Cu) samples for CO oxidation reaction at 30 °C are even higher (NPG(Ag)-1) or comparable (NPG(Ag)-3) compared with those of the two less active NPG(Ag) catalysts (see Table 3). This indicates a higher efficiency of Cu in oxygen activation under the reaction conditions compared with that of Ag, considering the comparable particle sizes (≈20 nm) and assuming that Cu plays a similar role to that of Ag.

2.2 TAP reactor measurements

In a second approach, the catalytic activities of the NPG catalysts for CO oxidation were examined in the TAP reactor under UHV conditions, starting with a fresh catalyst without any pretreatment.

NPG(Ag): In these experiments, the sample was exposed to a sequence of simultaneous pulses of CO/Ar and O_2/Ar at 30 °C reaction temperature. Typical results of these measurements obtained on the NPG(Ag)-4 sample are illustrated in Figure 6a. Apparently, the CO uptake, which is quantitatively identical to the amount of CO_2 formation, decreased continuously, until after ca. 1100 pulses for 2.0 mg of catalyst it was below the detection level (CO uptake < 1% of the incoming intensity). Meanwhile, no measurable O_2 uptake could be detected during the whole pulse experiment. Apparently, in this experiment CO oxidation proceeds by a noncatalytic process, through reaction of CO molecules with active oxygen species that were already present on the fresh NPG catalyst. Similar results were obtained also on the other three NPG(Ag) catalysts, with different amounts of CO/O_2 pulses required to remove the precovered surface oxygen species. In contrast to these findings for the NPG catalysts, steady catalytic activities can be achieved when performing similar single-pulse TAP reactor measurements on supported Au catalysts such as Au/TiO_2 catalysts [23,46]. The very low catalytic activity of the NPG catalysts in the TAP reactor compared to that of Au/TiO_2 catalysts under low pressure conditions points to a very low probability for O_2 activation under these reaction conditions. Most simply, this can be explained by a highly nonlinear pressure dependence for O_2 activation on the NPG catalysts [12].

In order to determine the nature and the amount of oxygen species present on the NPG(Ag) catalyst surface before and after the pulse reaction, we performed TPD experiments on the fresh NPG(Ag)-4 catalyst as well as after reaction by simultaneous pulses of CO and O_2 (for details see [12]). Desorption spectra of O_2 (m/z = 32) recorded on the fresh NPG(Ag)-4 catalyst showed a pronounced O_2 desorption peak at around 270 °C (see Figure 7a), which we assigned to the desorption of atomic
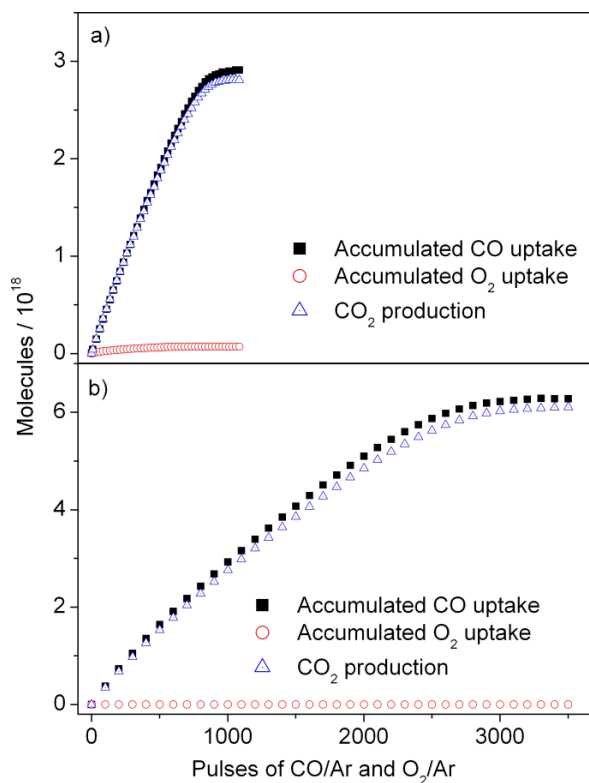
Figure 6: Accumulated uptake of CO and O_2 as well as CO_2 formation during simultaneous pulsing of CO/Ar and O_2/Ar on the fresh (a) NPG(Ag)-4 and (b) NPG(Cu)-2 catalyst in the TAP reactor (2.0 mg NPG catalyst diluted with SiO_2 (1:10), temperature 30 °C, 1 × 10^{16} molecules per pulse, with CO/Ar and O_2/Ar = 1:1).

Figure 7: TPD spectra of oxygen species (m/z = 32) recorded before reaction and after the simultaneous pulsing experiment on the (a) NPG(Ag)-4 and (b) NPG(Cu)-1 catalysts.

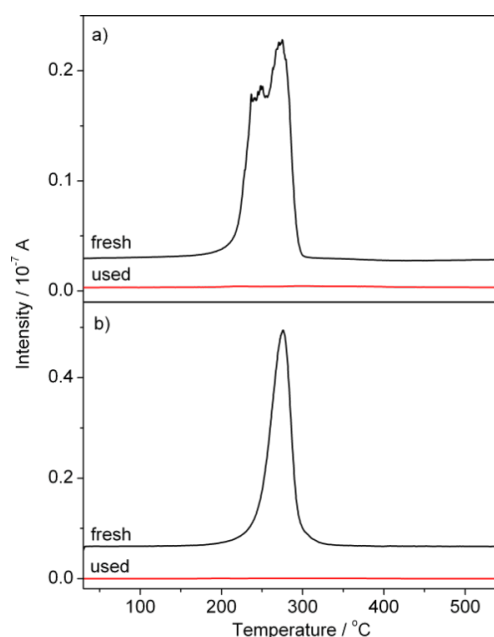oxygen species chemisorbed on Au surface sites [12]. In the spectrum recorded after the pulse reaction, however, this peak is essentially absent (see Figure 7a), indicating that the related oxygen species was removed by reaction with CO molecules. The desorption temperature, which is close to that reported for the desorption of atomic oxygen from Au surfaces (270–300 °C [66-69]) and lower than that for the desorption of oxygen from Ag surfaces (322 ± 25 °C [70-72]), points to atomic oxygen species adsorbed on Au sites as the origin for this peak (for the exact nature of the oxygen species see below). This agrees with the conclusions derived from the pulse measurements. Quantitative evaluation of the TPD spectra yields nominal oxygen coverages of 1.5 and 0.04 monolayers (ML) for the fresh and the used NPG(Ag)-4 catalyst, respectively, assuming a specific surface area of 75 $m^2 \cdot g^{-1}$, and a Au surface atom density of 1.4×10^{15} atoms·cm^{-2} (surface density on Au(111)) [13]. For the other three NPG(Ag) samples, the results are qualitatively similar, differing only in the amount of oxygen for different fresh samples. In all cases, the active oxygen species already present on the freshly prepared sample surfaces were almost completely depleted after pulse reaction.

NPG(Cu): For comparison, we performed similar pulse reaction measurements in the TAP reactor on the NPG(Cu) samples, as representatively illustrated in Figure 6b for NPG(Cu)-2. Again, no measurable catalytic activity was observed, only removal of the precovered surface oxygen species by reaction with CO molecules. The absolute amount of removed surface oxygen, however, is significantly higher than that on the NPG(Ag) samples. For the same amount of NPG catalyst (2 mg), the uptake of CO molecules of the NPG(Cu)-2 sample is about twice as high as that on the NPG(Ag)-4 sample. Considering the comparable surface area, this result is in reasonable agreement with the XPS results, showing an almost doubled fraction of Au^{3+} oxide species on the surface of the NPG(Cu)-2 sample.

Following the pulse reaction, the amount and bond strength of the (remaining) surface oxygen on the NPG(Cu) catalysts was determined in O_2-TPD experiments. A typical oxygen desorption spectrum on the NPG(Cu)-1 sample is shown in Figure 7b. For comparison, we again include a spectrum of the fresh sample. Similar to our findings for the NPG(Ag) catalysts, essentially all of the surface oxygen was removed on the used sample by reaction with CO. The fresh sample exhibits a single sharp desorption peak with a maximum at 275 °C, equal to that on the NPG(Ag)-4 catalyst (see Figure 7a). Vacuum-annealing-induced reduction of fully oxidized copper films (2 nm thick, grown by physical vapor deposition) has shown that CuO started to form Cu_2O at around 200 °C and complete reduction to Cu began at 400 °C [73]. On the other hand, temperature-

programmed desorption (TPD) experiments performed on Au_2O_3 compounds revealed that O_2 evolves in a temperature range from ca. 250–370 °C, with the highest rate of oxygen evolution at ca. 320 °C, and with no evidence of an intermediate oxidation state of gold, e.g., Au_2O or AuO [74]. In combination with the rather low content of residual Cu in the NPG(Cu) sample, the peak observed in our TPD measurement (at 275 °C) should be assigned to desorption of atomic oxygen species chemisorbed on Au sites or decomposition of an Au oxide (for details see below).

TPD experiments on the other two NPG(Cu) samples have shown that the desorption temperatures are significantly higher with almost doubled peak intensities (see Supporting Information File 1, Figure S2). Hence, the desorption temperature of the surface oxygen species is strongly affected by the oxygen coverage, i.e., higher coverage leads to higher desorption temperature. This finding is somewhat unexpected, since higher coverages usually destabilize the adsorbed species, resulting in a shift to lower temperatures with increasing coverage. A similar coverage-dependent desorption behavior, however, has also been reported by Gottfried et al. [75] during O_2-TPD experiments on a Au(110)-(1×2) surface with varying oxygen coverages, i.e., from ca. 0.50 to 1.80 ML. They explained this behavior by an autocatalytic desorption process, based on the assumption that at high oxygen coverages the surface is predominantly covered with O islands possessing a low local desorption rate (tc-phase) [75]. The same may be true in our case; however, an influence of residual Cu on the oxygen desorption from Au cannot be ruled out.

So far we have not specified the nature of the atomic surface oxygen species identified as the active species above. Different types have been proposed. Baker et al. proposed the existence of chemisorbed oxygen in threefold hollow sites, of a 2D surface oxide and of a (subsurface) oxide on Au(111) on the basis of vibrational spectroscopy data and density functional theory based calculations and molecular dynamics simulations [76]. (Interestingly, these authors also remarked that there is no clear definition of the surface oxide and subsurface oxide in the literature.) In a recent high-resolution photoelectron spectroscopy study, Schaefer et al. [77] could indeed identify three different types of atomic oxygen upon interaction of oxygen with nanoporous Au, which they associated with the above species. Considering the onset of oxygen desorption at ca. 200 °C in our TPD measurements, both the chemisorbed oxygen and surface oxide discussed in the paper by Schaefer et al. would be compatible with our findings (little/small loss after 15 min annealing at 150 °C). More information on the nature of this oxygen species, however, cannot be obtained from our results.

2.3 Physical origin of the catalytic activity of NPG catalysts

In the following, we wish to discuss the mechanistic findings derived from the similarities and characteristic differences in the reaction behavior of the NPG(Ag) and NPG(Cu) catalysts. Characteristic features of both NPG(Ag) and NPG(Cu) catalysts are

1. their relatively high activities for reaction under atmospheric pressure conditions in combination with their much lower activity for the activation of O_2 towards stable adsorbed, atomic oxygen,
2. the pronounced dependence of the reaction rate on the surface content of the less noble metal (Ag, Cu), while the surface area seems to play only a minor role,
3. the distinct initial activation behavior in the initial reaction phase at current reaction conditions, followed by a slow deactivation with time on stream, in combination with an equally pronounced coarsening behavior of the NPG ligament structure and loss of surface area, and variable extents of surface enrichment of the Ag or Cu species during reaction,
4. and finally, the presence of predominantly metallic Ag and Cu species in NPG(Ag) and NPG(Cu) materials under the present reaction conditions.

Consequences arising from these characteristic features shall be discussed in the following.

To (1.): The CO oxidation activity of the NPG catalysts is relatively high, about 3–30% of that of highly active Au/TiO_2 catalysts when based on the Au mass, and 4–200% when based on the TOF rate (0.28 s^{-1} for 3 wt % Au/TiO_2 with a mean Au particle size of 3.0 nm). This demonstrates that contributions from a reactive support, e.g., by metal-support interactions or by formation of active sites at the perimeter of the interface between metal and support, are not necessarily required for the reaction. On the other hand, the activation of molecular O_2 to form stable adsorbed oxygen, which can be regarded as an analogue to the stable surface lattice oxygen proposed as the reactive oxygen species for a number of Au/oxide catalysts under comparable reaction conditions [24,25], is much less efficient on NPG catalysts than on Au/oxide catalysts. In our previous report on the formation of active oxygen on the NPG(Ag)-2 catalyst, we calculated the maximum uptake of oxygen within one pulse to be around 4×10^{13} O atoms for 2 mg NPG(Ag), assuming that 10% of the total oxygen deposition during O_2 pulses occurs in the first pulse [12]. One should note that this maximum uptake of oxygen within one pulse was estimated from a multipulse experiment with 200 O_2 pulses on a fresh NPG(Ag) sample [12]. For reacted samples (after reaction

for 1000 min) or after higher doses of O_2 (higher amount of O_2 pulses or O_2 gas flow at atmospheric pressure) this value is always lower [12,13]. Hence, formation of active oxygen under pulse conditions is at least a factor of 20 less efficient than on supported Au/oxide catalysts under comparable reaction conditions, for which the oxygen uptake within a single O_2 pulse reaches up to 5×10^{15} O atoms (for 10 mg catalyst). Moreover, estimating from these pulse measurements the total amount of reactive atomic oxygen that can be deposited per time unit during the reaction, based on these assumptions, this is at least a factor of 10 lower than the total amount of CO_2 formed during continuous reaction for NPG(Ag) [12]. The difference is even larger for AuCu-based NPG samples than for the AuAg-based ones. For NPG(Ag), we had previously interpreted this discrepancy as an indication of a pronounced nonlinear pressure effect, leading to a more efficient active oxygen deposition during reaction at atmospheric pressure than during O_2 pulsing [13]. It is equally possible, however, that different from the reaction mechanism proposed for oxide-supported Au catalysts for reaction above 50 °C, CO oxidation on NPG catalysts does not proceed via a stable adsorbed atomic oxygen species as a reaction intermediate, but by another mechanism. Most likely this would be a mechanism via a $CO_{ad}\cdots O_{2,ad}$ intermediate and a CO_{ad} induced dissociation of the adsorbed O_2, as is likely to occur for oxide-supported catalysts at much lower temperatures [78]. In that case, however, this reaction intermediate was stabilized by the Au-oxide interface ("dual adsorption sites"), which is not present for the NPG catalysts. Therefore, the question of the dominant reaction pathway and the active oxygen species on NPG catalysts is still unresolved. However, the present data provide clear proof that reaction by formation and reactive removal of a stable adsorbed atomic oxygen species is at least a minority pathway.
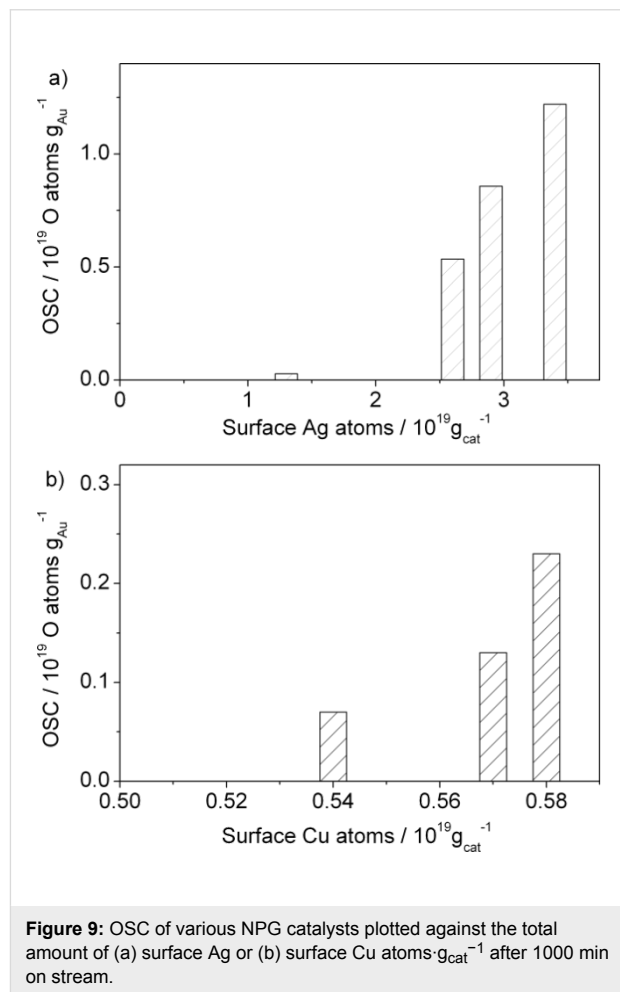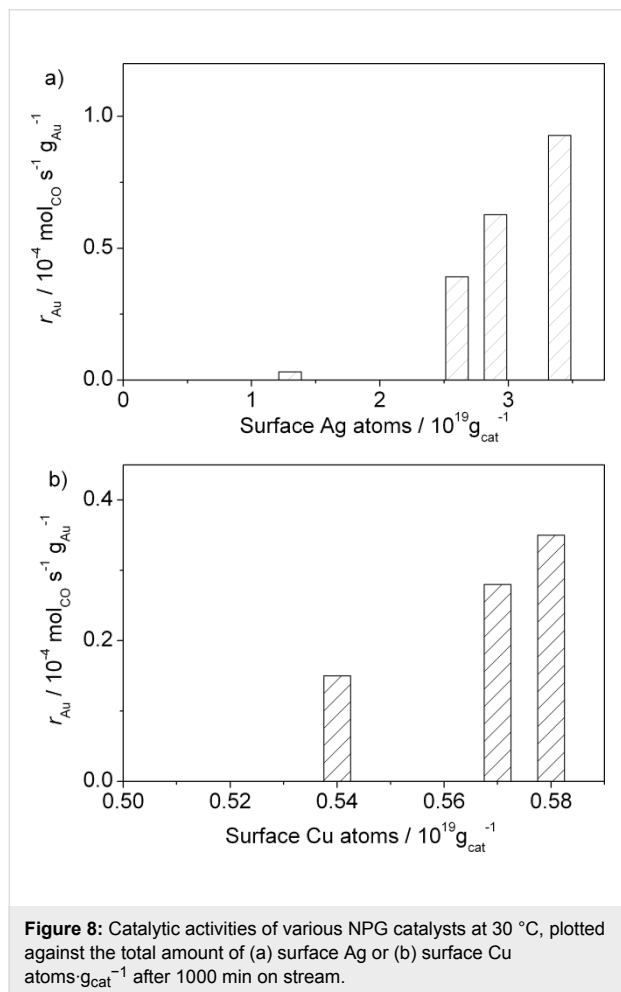
To (2.): The above data indicate that the concentration of less noble residues from the original alloy plays an important role in the range of surface contents investigated. To illustrate the influence of surface Ag or Cu atoms on the catalytic activity more quantitatively, we plotted the reaction rates of the different catalysts in the steady state against the corresponding total number of Ag or Cu atoms present on the catalyst surface (after reaction). As shown in Figure 8, there is an almost linear correlation between these two quantities, pointing to the important role of surface Ag or Cu atoms in the catalytic properties of the NPG catalysts. Only the sample NPG(Ag)-1 with the lowest concentration of surface Ag atoms does not fit to this linear trend. Although its activity is rather low compared to that of the other samples, it is still higher than expected from the linear relation of the other three NPG(Ag) samples. Tentatively this may be attributed to an intrinsic activity of Au itself, without major contributions from Ag surface atoms. Obviously, the

variation in Cu surface concentrations is too small for an unambiguous identification of a surface concentration effect, but the trend fits well to that observed for NPG(Ag). Interestingly, this also shows that although the activities of the NPG(Cu) catalysts are significantly lower than those of the NPG(Ag) catalysts on average, they are considerably higher than that of the NPG(Ag)-1 sample with the lowest Ag surface content. (Note that the surface Ag content in the latter sample is still almost double that of the surface Cu content of the NPG(Cu) samples.) Surface area effects can be ruled out, since the surface areas under steady-state conditions are comparable for all catalysts.

A similar comparison can be performed for the oxygen storage capacity of the various NPG catalysts after reaction for 1000 min. This was measured by exposing the catalysts to a flow of 10% O_2/N_2 (20 mL·min^{-1}) for 30 min, followed by titration with CO pulses in the TAP reactor. The results are presented in Table 1 and Table 3 and also plotted against the corresponding total number of surface Ag or Cu atoms on the stable catalyst (after reaction) in Figure 9. Again, an almost

identical linear correlation was obtained between the OSC and the absolute amount of surface Ag or Cu atoms, and this result strongly suggests that the surface Ag or Cu atoms are directly involved in the activation of molecular oxygen during the oxidation reaction, thus promoting the catalytic activity.

To (3.): Based on the results of the structural characterization described above, we tentatively attribute the initial activity enhancement of the NPG catalysts to the structural rearrangement induced by the removal of the pre-existent oxide species on the fresh samples, where the latter occurs on a much faster time scale, i.e, within a couple of minutes. The pre-existent oxygen species plays an important role in stabilizing the structure of the NPG material [30,40]. It has been suggested that the removal of surface oxygen may lead to two coinciding processes, first the creation of a large transient population of mobile gold adatoms during the reduction process and second, on a longer timescale, the creation of a gold surface that is free of the constraints on diffusivity [40]. In this study, the surface areas of all the Ag- and Cu-containing NPG samples decreased significantly during reaction, by a factor of up to about 7. This

Figure 8: Catalytic activities of various NPG catalysts at 30 °C, plotted against the total amount of (a) surface Ag or (b) surface Cu atoms·g$_{cat}$$^{-1}$ after 1000 min on stream.

Figure 9: OSC of various NPG catalysts plotted against the total amount of (a) surface Ag or (b) surface Cu atoms·g$_{cat}$$^{-1}$ after 1000 min on stream.

yields comparable surface areas after reaction for 1000 min, which, obviously, can neither explain the activation phase in the beginning of the reaction nor the discrepancies in the catalytic activities of various NPG catalysts under steady-state conditions. Hence, the absence of a clear correlation between the activity for CO oxidation and the catalyst surface area indicates that the (total) surface area plays no dominant role in the activity of these samples.

To (4.): Considering the TAP, TPD and XPS results it is likely that under reaction conditions both Ag and Cu are present as metallic species and not as local (surface) oxides, despite the much higher affinity of Cu towards oxygen as compared to Ag. In this case, the NPG catalysts can be considered as bimetallic catalysts, where the presence of the second metal modifies the chemical properties of the main component (Au) and at the same time also introduces its own functionality [79,80]. In fact, the important role of the guest metals Ag or Cu, for example as an active center for O_2 activation, as a part of active mixed Au_xMe_y ensembles (Me = Ag, Cu), or as a modifier for the Au surface atoms, has been discussed already by both theoretical and experimental research. For instance, Moskaleva et al. [37,81] have investigated the role of Ag in NPG catalysts theoretically by DFT calculations and concluded that Ag plays a decisive role in the activation of oxygen [37]. Experimental studies by several groups have also underlined the role of Ag in AuAg bimetallic systems, including both NPG catalysts [14,30] and supported Au catalysts [35,36]. Significant effects of the Cu content were also reported for AuCu systems [6,38,82]. If the Ag (Cu) atoms (Ag (Cu) ensembles) act as active centers for O_2 activation, they would take the role of the metal–oxide interface in oxide-supported catalysts [24,83,84]. In that case, the NPG catalysts could be considered as bifunctional catalysts, with the Au atoms supporting CO adsorption/oxidation and Ag (Cu) surface atoms/ensembles supporting O_2 activation.

Conclusion

Based on detailed continuous and dynamic reaction measurements of the CO oxidation reaction on unsupported NPG catalysts with systematically varied structural parameters (surface area, ligament size) and surface composition (nature and content of the residual amounts of the less noble metal), we arrived at the following conclusions regarding the mechanism of the CO oxidation reaction on these surfaces and on the physical effects responsible for the activity of these catalysts:

1. The NPG catalysts are highly active for CO oxidation at atmospheric pressure, with Au-mass based activities that are between 3 and 30% of those of highly active Au/TiO2 catalysts with 3 nm Au particle size. Hence, the absence of oxide support does not necessarily lead to poor activity for Au catalysts under ambient pressure conditions.

2. In contrast, for reaction in the TAP reactor, the activity decreased to below the detection limit after removal of the precovered surface oxygen.

3. In both cases, the reaction leads to rapid reduction of the pre-existent surface oxygen species present after electrochemical dealloying, until steady-state conditions are reached.

4. The reaction results in a steady coarsening of the NPG structure, evident by a strong increase in the Au ligament size, and enrichment of residual Ag or Cu on the surface, in particular at lower surface contents.

5. For the NPG(Ag) catalysts, the OSC as well as the activity of the NPG catalysts for CO oxidation scale approximately linearly with the number of surface atoms in the stable state after the reaction for 1000 min. Based on these results, we propose that the residual Ag in the NPG catalysts plays an important role in the activation of molecular oxygen and thus the catalytic performance.

6. Correlations between the activity for CO oxidation and the catalyst surface area are weak, considering that the activities of the NPG catalysts are hardly affected by the initial significant loss of surface area, in particular when comparing with the pronounced effects imposed by the surface Ag or Cu content. Obviously, the total surface area plays a less important role for the activity of the NPG samples.

7. Comparison between Ag- and Cu-containing NPG samples suggests that also for NPG(Cu) catalysts the catalytic activity is determined mainly by the amount of the residual less noble metal, but with a higher efficiency for oxygen activation under reaction conditions for Cu compared with Ag.

Moisture in the feed gas has a distinct influence on the catalytic activity of the NPG samples, but neither alters the relative activities of the catalysts, relative to each other, nor the temporal evolution of the activity. The latter is different from observations on supported Au/TiO2 catalysts, where the presence of trace amounts of moisture in the feed gas has a clear effect on the deactivation behavior.

Supporting Information

Supporting Information File 1
Additional XPS and TPD spectra
[http://www.beilstein-journals.org/bjnano/content/supplementary/2190-4286-4-13-S1.pdf]

Acknowledgements

References

1. Polarz, S.; Smarsly, B. *J. Nanosci. Nanotechnol.* **2002,** *2,* 581. doi:10.1166/jnn.2002.151
2. Ding, Y.; Chen, M. *MRS Bull.* **2009,** *34,* 569. doi:10.1557/mrs2009.156
3. Erlebacher, J.; Aziz, M. J.; Karma, A.; Dimitrov, N.; Sieradzki, K. *Nature* **2001,** *410,* 450. doi:10.1038/35068529
4. Zielasek, V.; Jürgens, B.; Schulz, C.; Biener, J.; Biener, M. M.; Hamza, A. V.; Bäumer, M. *Angew. Chem., Int. Ed.* **2006,** *45,* 8241. doi:10.1002/anie.200602484
5. Xu, C.; Su, J.; Xu, X.; Liu, P.; Zhao, H.; Tian, F.; Ding, Y. *J. Am. Chem. Soc.* **2007,** *129,* 42. doi:10.1021/ja0675503
6. Kameoka, S.; Pang Tsai, A. *Catal. Lett.* **2008,** *121,* 337. doi:10.1007/s10562-007-9344-x
7. Déronzier, T.; Morfin, F.; Massin, L.; Lomello, M.; Rousset, J.-L. *Chem. Mater.* **2011,** *23,* 5287. doi:10.1021/cm202105k
8. Li, R.; Sieradzki, K. *Phys. Rev. Lett.* **1992,** *68,* 1168. doi:10.1103/PhysRevLett.68.1168
9. Cortie, M. B.; Maaroof, A. I.; Smith, G. B. *Gold Bull.* **2005,** *38,* 14. doi:10.1007/BF03215223
10. Weissmüller, J.; Newman, R. C.; Jin, H.-J.; Hodge, A. M.; Kysar, J. W. *MRS Bull.* **2009,** *34,* 577. doi:10.1557/mrs2009.157
11. Xu, C.; Xu, X.; Su, J.; Ding, Y. *J. Catal.* **2007,** *252,* 243. doi:10.1016/j.jcat.2007.09.016
12. Wang, L. C.; Jin, H.-J.; Widmann, D.; Weissmüller, J.; Behm, R. J. *J. Catal.* **2011,** *278,* 219. doi:10.1016/j.jcat.2010.12.007
13. Wang, L. C.; Zhong, Y.; Widmann, D.; Weissmüller, J.; Behm, R. J. *ChemCatChem* **2012,** *4,* 251. doi:10.1002/cctc.201100297
14. Wittstock, A.; Zielasek, V.; Biener, J.; Friend, C. M.; Bäumer, M. *Science* **2010,** *327,* 319. doi:10.1126/science.1183591
15. Asao, N.; Hatakeyama, N.; Menggenbateer, X.; Minato, T.; Ito, E.; Hara, M.; Kim, Y.; Yamamoto, Y.; Chen, M.; Zhang, W.; Inoue, A. *Chem. Commun.* **2012,** *48,* 4540. doi:10.1039/c2cc17245c
16. Asao, N.; Ishikawa, Y.; Hatakeyama, N.; Menggenbateer, X.; Yamamoto, Y.; Chen, M.; Zhang, W.; Inoue, A. *Angew. Chem., Int. Ed.* **2010,** *49,* 10093. doi:10.1002/anie.201005138
17. Haruta, M.; Kobayashi, T.; Sano, H.; Yamada, N. *Chem. Lett.* **1987,** *16,* 405. doi:10.1246/cl.1987.405
18. Haruta, M. *Catal. Surv. Jpn.* **1997,** *1,* 61. doi:10.1023/A:1019068728295
19. Schubert, M. M.; Hackenberg, S.; van Veen, A. C.; Muhler, M.; Plzak, V.; Behm, R. J. *J. Catal.* **2001,** *197,* 113. doi:10.1006/jcat.2000.3069
20. Haruta, M. *CATTECH* **2002,** *6,* 102. doi:10.1023/A:1020181423055
21. Bond, G. C.; Louis, C.; Thompson, D. T. *Catalysis by Gold;* Imperial College Press: London, 2006.
22. Aguilar-Guerrero, V.; Gates, B. C. *Catal. Lett.* **2009,** *130,* 108. doi:10.1007/s10562-009-9906-1
23. Kotobuki, M.; Leppelt, R.; Hansgen, D. A.; Widmann, D.; Behm, R. J. *J. Catal.* **2009,** *264,* 67. doi:10.1016/j.jcat.2009.03.013
24. Widmann, D.; Behm, R. J. *Angew. Chem., Int. Ed.* **2011,** *50,* 10241. doi:10.1002/anie.201102062
25. Widmann, D.; Liu, Y.; Schüth, F.; Behm, R. J. *J. Catal.* **2010,** *276,* 292. doi:10.1016/j.jcat.2010.09.023
26. Remediakis, I. N.; Lopez, N.; Nørskov, J. K. *Angew. Chem.* **2005,** *117,* 1858. doi:10.1002/ange.200461699
27. Janssens, T. V. W.; Clausen, B. S.; Hvolbaek, B.; Falsig, H.; Christensen, C. H.; Bligaard, T.; Nørskov, J. K. *Top. Catal.* **2007,** *44,* 15. doi:10.1007/s11244-007-0335-3
28. Chen, M. S.; Goodman, D. W. *Science* **2004,** *306,* 252. doi:10.1126/science.1102420
29. Wittstock, A.; Neumann, B.; Schaefer, A.; Dumbuya, K.; Kübel, C.; Biener, M. M.; Zielasek, V.; Steinrück, H. P.; Gottfried, J. M.; Biener, J.; Hamza, A.; Bäumer, M. *J. Phys. Chem. C* **2009,** *113,* 5593. doi:10.1021/jp808185v
30. Wittstock, A.; Wichmann, A.; Biener, J.; Bäumer, M. *Faraday Discuss.* **2011,** *152,* 87. doi:10.1039/c1fd00022e
31. Xu, J.; Wang, Y.; Zhang, Z. *J. Phys. Chem. C* **2012,** *116,* 5689. doi:10.1021/jp210488t
32. Haruta, M. *ChemPhysChem* **2007,** *8,* 1911. doi:10.1002/cphc.200700325
33. Wittstock, A.; Biener, J.; Bäumer, M. *Phys. Chem. Chem. Phys.* **2010,** *12,* 12919. doi:10.1039/c0cp00757a
34. Iizuka, Y.; Kawamoto, A.; Akita, K.; Daté, M.; Tsubota, S.; Okumura, M.; Haruta, M. *Catal. Lett.* **2004,** *97,* 203. doi:10.1023/B:CATL.0000038585.12878.9a
35. Wang, A.-Q.; Liu, J.-H.; Lin, S. D.; Lin, T.-S.; Mou, C.-Y. *J. Catal.* **2005,** *233,* 186. doi:10.1016/j.jcat.2005.04.028
36. Yen, C.-W.; Lin, M.-L.; Wang, A.; Chen, S.-A.; Chen, J.-M.; Mou, C.-Y. *J. Phys. Chem. C* **2009,** *113,* 17831. doi:10.1021/jp9037683
37. Moskaleva, L. V.; Röhe, S.; Wittstock, A.; Zielasek, V.; Klüner, T.; Neyman, K. M.; Bäumer, M. *Phys. Chem. Chem. Phys.* **2011,** *13,* 4529. doi:10.1039/c0cp02372h
38. Liu, X.; Wang, A.; Li, L.; Zhang, T.; Mou, C.-Y.; Lee, J. F. *J. Catal.* **2011,** *278,* 288. doi:10.1016/j.jcat.2010.12.016
39. Parida, S.; Kramer, D.; Volkert, C. A.; Rösner, H.; Erlebacher, J.; Weissmüller, J. *Phys. Rev. Lett.* **2006,** *97,* 035504. doi:10.1103/PhysRevLett.97.035504
40. Jin, H. J.; Parida, S.; Kramer, D.; Weissmüller, J. *Surf. Sci.* **2008,** *602,* 3588. doi:10.1016/j.susc.2008.09.038
41. Trasatti, S.; Petrii, O. A. *Pure Appl. Chem.* **1991,** *63,* 711. doi:10.1351/pac199163050711
42. Jin, H. J.; Kurmanaeva, L.; Schmauch, J.; Rösner, H.; Ivanisenko, Y.; Weissmüller, J. *Acta Mater.* **2009,** *57,* 2665. doi:10.1016/j.actamat.2009.02.017
43. Kahlich, M. J.; Gasteiger, H. A.; Behm, R. J. *J. Catal.* **1997,** *171,* 93. doi:10.1006/jcat.1997.1781
44. Leppelt, R.; Hansgen, D.; Widmann, D.; Häring, T.; Bräth, G.; Behm, R. J. *Rev. Sci. Instrum.* **2007,** *78,* 104103. doi:10.1063/1.2791948
45. Gleaves, J. T.; Yablonskii, G. S.; Phanawadee, P.; Schuurman, Y. *Appl. Catal., A* **1997,** *160,* 55. doi:10.1016/S0926-860X(97)00124-5
46. Tost, A.; Widmann, D.; Behm, R. J. *J. Catal.* **2009,** *266,* 299. doi:10.1016/j.jcat.2009.06.020
47. Wertheim, G. K.; DiCenzo, S. B.; Youngquist, S. E. *Phys. Rev. Lett.* **1983,** *51,* 2310. doi:10.1103/PhysRevLett.51.2310
48. Pireaux, J.-J.; Liehr, M.; Thiry, P. A.; Delrue, J. P.; Caudano, R. *Surf. Sci.* **1984,** *141,* 221. doi:10.1016/0039-6028(84)90207-3
49. Hoflund, G. B.; Hazos, Z. F.; Salaita, G. N. *Phys. Rev. B* **2000,** *62,* 11126. doi:10.1103/PhysRevB.62.11126

50. Liu, Y.; Bliznakov, S.; Dimitrov, N. *J. Electrochem. Soc.* **2010,** *157,* K168–K176. doi:10.1149/1.3454753

51. Fu, Q.; Saltsburg, H.; Flytzani-Stephanopoulos, M. *Science* **2003,** *301,* 935. doi:10.1126/science.1085721

52. Deng, W.; Carpenter, C.; Yi, N.; Flytzani-Stephanopoulos, M. *Top. Catal.* **2007,** *44,* 199. doi:10.1007/s11244-007-0293-9

53. Haruta, M.; Tsubota, S.; Kobayashi, T.; Kageyama, H.; Genet, M. J.; Delmon, B. *J. Catal.* **1993,** *144,* 175. doi:10.1006/jcat.1993.1322

54. Boyen, H.-G.; Ethirajan, A.; Kästle, G.; Weigl, F.; Ziemann, P.; Schmid, G.; Garnier, M. G.; Büttner, M.; Oelhafen, P. *Phys. Rev. Lett.* **2005,** *94,* 016804. doi:10.1103/PhysRevLett.94.016804

55. Sandoval, A.; Aguilar, A.; Louis, C.; Traverse, A.; Zanella, R. *J. Catal.* **2011,** *281,* 40. doi:10.1016/j.jcat.2011.04.003

56. Deng, L.; Hu, W.; Deng, H.; Xiao, S.; Tang, J. *J. Phys. Chem. C* **2011,** *115,* 11355. doi:10.1021/jp200642d

57. Shibata, T.; Bunker, B. A.; Zhang, Z.; Meisel, D.; Vardemann, C. F., II; Gezelter, J. D. *J. Am. Chem. Soc.* **2002,** *124,* 11989. doi:10.1021/ja026764r

58. Li, Z. Y.; Wilcoxon, J. P.; Yin, F.; Chen, Y.; Palmer, R. E.; Johnston, R. L. *Faraday Discuss.* **2008,** *138,* 363. doi:10.1039/b708958a

59. Alejo, L.; Lago, R.; Peña, M. A.; Fierro, J. L. G. *Appl. Catal., A* **1997,** *162,* 281. doi:10.1016/S0926-860X(97)00112-9

60. Agrell, J.; Birgersson, H.; Boutonnet, M.; Melián-Cabrera, I.; Navarro, R. M.; Fierro, J. L. G. *J. Catal.* **2003,** *219,* 389. doi:10.1016/S0021-9517(03)00221-5

61. Matter, P. H.; Braden, D. J.; Ozkan, U. S. *J. Catal.* **2004,** *223,* 340. doi:10.1016/j.jcat.2004.01.031

62. Dai, W.-L.; Sun, Q.; Deng, J.-F.; Wu, D.; Sun, Y.-H. *Appl. Surf. Sci.* **2001,** *177,* 172. doi:10.1016/S0169-4332(01)00229-X

63. Ferrando, R.; Jellinek, J.; Johnston, R. L. *Chem. Rev.* **2008,** *108,* 845. doi:10.1021/cr040090g

64. Schumacher, B.; Denkwitz, Y.; Plzak, V.; Kinne, M.; Behm, R. J. *J. Catal.* **2004,** *224,* 449. doi:10.1016/j.jcat.2004.02.036

65. Denkwitz, Y.; Schumacher, B.; Kučerová, G.; Behm, R. J. *J. Catal.* **2009,** *267,* 78. doi:10.1016/j.jcat.2009.07.018

66. Sault, A. G.; Madix, R. J.; Campbell, C. T. *Surf. Sci.* **1986,** *169,* 347. doi:10.1016/0039-6028(86)90616-3

67. Saliba, N.; Parker, D. H.; Koel, B. E. *Surf. Sci.* **1998,** *410,* 270. doi:10.1016/S0039-6028(98)00309-4

68. Deng, X.; Min, B. K.; Guloy, A.; Friend, C. M. *J. Am. Chem. Soc.* **2005,** *127,* 9267. doi:10.1021/ja050144j

69. Min, B. K.; Alemozafar, A. R.; Pinnaduwage, D.; Deng, X.; Friend, C. M. *J. Phys. Chem. B* **2006,** *110,* 19833. doi:10.1021/jp0616213

70. Grant, R. B.; Lambert, R. M. *Surf. Sci.* **1984,** *146,* 256. doi:10.1016/0039-6028(84)90241-3

71. Campbell, C. T. *Surf. Sci.* **1985,** *157,* 43. doi:10.1016/0039-6028(85)90634-X

72. Rehren, C.; Isaac, G.; Schlögl, R.; Ertl, G. *Catal. Lett.* **1991,** *11,* 253. doi:10.1007/BF00764316

73. Lee, S. Y.; Mettlach, N.; Nguyen, N.; Sun, Y. M.; White, J. M. *Appl. Surf. Sci.* **2003,** *206,* 102. doi:10.1016/S0169-4332(02)01239-4

74. Soares, J. M. C.; Bowker, M. *Appl. Catal., A* **2005,** *291,* 136. doi:10.1016/j.apcata.2005.02.049

75. Gottfried, J. M.; Schmidt, K. J.; Schroeder, S. L. M.; Christmann, K. *Surf. Sci.* **2003,** *525,* 184. doi:10.1016/S0039-6028(02)02560-8

76. Baker, T. A.; Xu, B.; Xiaoying, L.; Kaxiras, E.; Friend, C. M. *J. Phys. Chem. C* **2009,** *113,* 16561. doi:10.1021/jp9052192

77. Schaefer, A.; Ragazzon, D.; Wittstock, A.; Walle, L. E.; Borg, A.; Bäumer, M.; Sandell, A. *J. Phys. Chem. C* **2012,** *116,* 4564. doi:10.1021/jp207638t

78. Green, I. X.; Tang, W.; Neurock, M.; Yates, J. T. *Science* **2011,** *333,* 736. doi:10.1126/science.1207272

79. Groß, A. *J. Phys.: Condens. Matter* **2009,** *21,* 084205. doi:10.1088/0953-8984/21/8/084205

80. Behm, R. J. *Z. Phys. Chem.* **2009,** *223,* 9. doi:10.1524/zpch.2009.6022

81. Moskaleva, L. V.; Zielasek, V.; Klüner, T.; Neyman, K. M.; Bäumer, M. *Chem. Phys. Lett.* **2012,** *525–526,* 87. doi:10.1016/j.cplett.2011.12.050

82. Liu, X.; Wang, A.; Zhang, T.; Su, D. S.; Mou, C.-Y. *Catal. Today* **2011,** *160,* 103. doi:10.1016/j.cattod.2010.05.019

83. Haruta, M.; Daté, M. *Appl. Catal., A* **2001,** *222,* 427. doi:10.1016/S0926-860X(01)00847-X

84. Fujitani, T.; Nakamura, I. *Angew. Chem., Int. Ed.* **2011,** *50,* 10144. doi:10.1002/anie.201104694

Functionalization of vertically aligned carbon nanotubes

Eloise Van Hooijdonk[*1], Carla Bittencourt[*2], Rony Snyders[2,3] and Jean-François Colomer[1]

Abstract

This review focuses and summarizes recent studies on the functionalization of carbon nanotubes oriented perpendicularly to their substrate, so-called vertically aligned carbon nanotubes (VA-CNTs). The intrinsic properties of individual nanotubes make the VA-CNTs ideal candidates for integration in a wide range of devices, and many potential applications have been envisaged. These applications can benefit from the unidirectional alignment of the nanotubes, the large surface area, the high carbon purity, the outstanding electrical conductivity, and the uniformly long length. However, practical uses of VA-CNTs are limited by their surface characteristics, which must be often modified in order to meet the specificity of each particular application. The proposed approaches are based on the chemical modifications of the surface by functionalization (grafting of functional chemical groups, decoration with metal particles or wrapping of polymers) to bring new properties or to improve the interactions between the VA-CNTs and their environment while maintaining the alignment of CNTs.

Introduction

Carbon nanotubes (CNTs) have stirred the curiosity of the scientific community for two decades now. They consist of layers of graphene rolled up on themselves in order to form cylinders often closed at the two ends by fullerenic caps. Either they are encased one in another in a coaxial way and are called multiwalled carbon nanotubes (MWCNTs) [1], or they consist of a single layer and are categorized as single-walled carbon nanotubes (SWCNTs) [2]. SWCNTs are generally assembled in two-dimensional, compact, wide ropes called bundles [3]. The structure of the nanotubes determines the majority of their properties. Their symmetry is related to the orientation of the hexagonal lattice with respect to the axis of the tube (chirality).

Depending on the chirality, a carbon nanotube shows either metallic or semiconductor behavior [4]. Thus, this allotrope of carbon exhibits exceptional morphological, physical and chemical properties: high aspect ratio (a length-to-diameter ratio greater than 10 000 and as high as 132 000 000) [5], an extremely high conductance [6], a high structural flexibility [7], and a high thermal conductance [8]. With a high tensile strength [9] and elastic modulus [10], CNTs form the strongest and stiffest material that humans have created. These properties offer a wide range of potential applications [11,12], for electronic devices, energy storage and transport, nanocomposite materials, and nanomedicine.

The as-synthesized product is macroscopically seen as a black powder whereas microscopically the CNTs are randomly oriented in an entangled spaghetti-like configuration. Until recently, practical applications of CNTs had been limited by issues related to their synthesis. The first important research outcomes in this area were the synthesis on a large scale, the reproducibility, and the control of the diameter and number of walls of the CNTs using different synthesis techniques such as arc discharge, laser ablation or chemical vapor deposition. After these issues had been addressed, the focus in carbon nanotube research shifted towards obtaining control in the engineering of organized architectures with determined orientations, such as vertically aligned carbon nanotubes (VA-CNTs). Because of the strong anisotropy of the CNT properties, the orientation of the longitudinal direction of the CNTs is often requested in many applications such as field-emission displays, chemical or biological sensors, or polymer fillers. The advantages of using VA-CNTs include an excellent alignment of the nanotubes, a good electrical and thermal conductivity, and uniform length. Nevertheless, a key challenge to be overcome for achieving actual applications is the tuning of the CNT surface properties. In this context, functionalization (i.e., the grafting of chemical groups (molecules or particles) on the surface of the nanomaterial) has been reported to give excellent results, with the drawback that it negatively impacts on the alignment of the VA-CNT. To date, different functionalization methods have been reported [13], all being well-known and controlled for non-aligned CNTs (single or multiwalled). These methods can be divided into two major functionalization strategies. The first is "endohedral functionalization", in which the CNT functionalization is obtained by filling the inner cavity with guest nanoparticles [14] or molecules [15]. This can be achieved by using colloidal suspensions or applying special thermal or chemical conditions (called "wet chemistry"). In the second strategy, termed "exohedral functionalization", only the external sidewall of the CNTs is functionalized. During the functionalization, functional groups or nanoparticles can form a covalent (chemical) or a non-covalent (physical) bond with the CNT

surface. The covalent functionalization (creation of a chemical bond between the CNT and the functional group or nanoparticle) can occur at the fullerenic caps, which are more reactive than the CNT sidewalls [16], at the defects, or exclusively at the sidewalls of the nanotubes. The non-covalent functionalization (creation of a physical bond between the CNT and the chemical group or particle) involves for instance CNTs wrapped by polymers. Several methods involving the functionalization of the non-aligned CNTs, such as wet-chemistry, are not applicable to VA-CNTs if the alignment of the nanotubes must be preserved. A review devoted to the functionalization of non-aligned CNTs was written by Balasubramanian and Burghard in 2005 [17]. Regarding the VA-CNTs, the functionalization method should be well-controlled, restricting damage to the nanotubes and their arrangement [18-20]. Another, important characteristic of a post-growth treatment is the removal of the amorphous carbon layers that can be often observed on the as-grown CNTs [21]. In this context, physical functionalization, such as plasma treatment where the functionalization features depend on the plasma parameters, has been reported. This technique allows an optimal tunable chemical modification of the CNT surface. A detailed review devoted to the surface treatment of non-aligned carbon nanotubes by different plasma technologies was published by Ruelle et al. [22] in 2011.
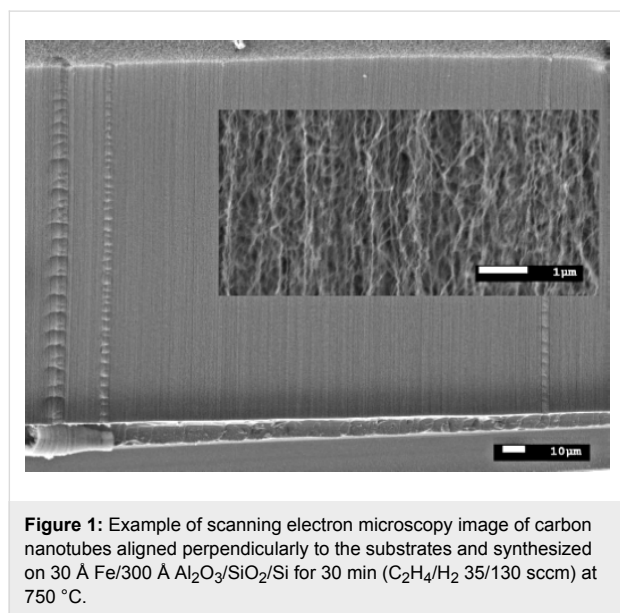
The present review is focused on the different methods available to functionalize vertically aligned carbon nanotubes, including plasma functionalization, wet chemical functionalization, and also dry gas-phase functionalization. Before presenting these methods, we briefly discuss different ways to synthesize vertically aligned carbon nanotubes and the existing approaches to obtain patterning of vertically aligned carbon nanotubes. A part of this review is also dedicated to a frequent consequence of the functionalization (voluntarily searched or not): the bundling of CNTs.

Review
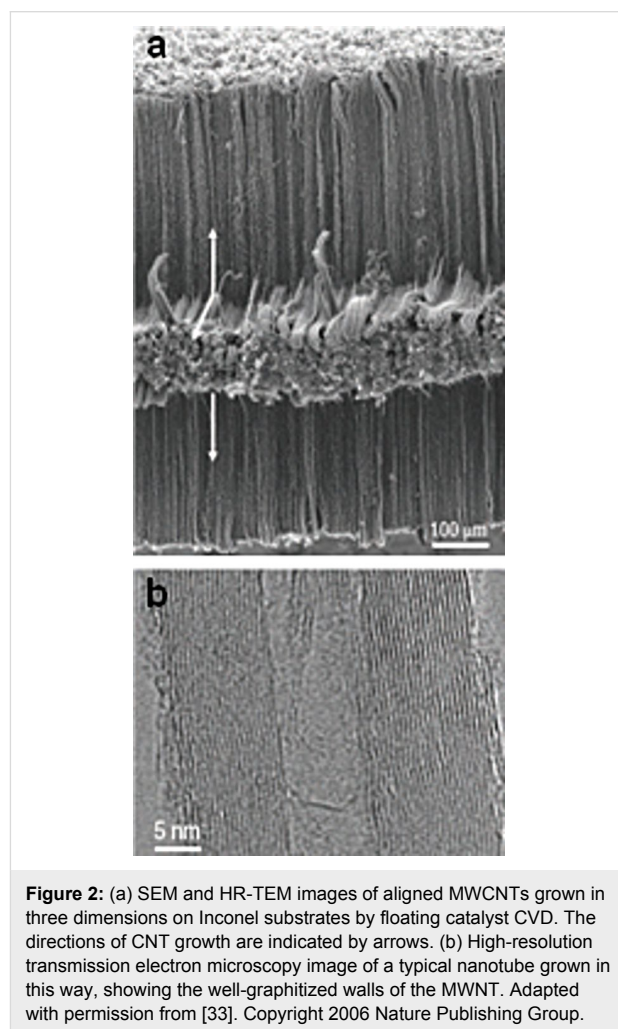## 1 Synthesis of vertically aligned CNT arrays
Considerable progress has been made in the synthesis of vertically aligned CNTs since the first report, in 1996, by Li et al. [23] showing the synthesis of aligned CNTs from acetylene chemical vapor deposition (CVD) catalyzed by iron nanoparticles embedded in mesoporous silica. In that work, the growth direction of not very straight, entangled-CNTs was related to the direction of the pores in the silica substrate, being perpendicular to the substrate surface if the pores were vertical. Later, in 1998, the synthesis of very straight, aligned multiwalled CNTs on nickel-coated glass at temperatures as low as 666 °C was obtained by Ren et al. [24] using plasma-enhanced hot-filament chemical vapor deposition (PE-HF-CVD). Reported in 1999 by Fan et al. [25], a key achievement was the engineering

of vertically oriented CNT-arrays by using CVD of ethylene, size-controlled Fe catalytic particles, and nanotube positioning by substrate patterning. The mechanism of the alignment of the CNTs was proposed to be due to the van der Waals forces where the outer wall of each nanotube interacts with the outer walls of neighboring nanotubes to form large bundles with sufficient rigidity to keep the growth direction. The density of nanotubes promotes the aligned growth (Figure 1). More recently, Hata et al. (2004) reported the growth of superdense, vertically aligned single-wall carbon nanotubes with heights up to several millimeters achieved by increasing the activity and lifetime of the Fe-based catalysts during the ethylene CVD by adding small amounts of water vapor, which acts as an oxidizer [26]. And, in 2006, Yamada et al. reported the selective (85%) growth of double-walled carbon nanotubes also by water-assisted CVD [27]. The development of CNT-based applications requires an easy, secure, inexpensive way of industrialization producing large VA-CNTs surfaces with, obviously, high-quality and well-controlled properties (homogeneity, length, doping, etc.). A great progress in this context has been recently realized by the IRAMIS/SPAM/Francis Perrin laboratory (France) [28]. Using the aerosol-assisted CVD technique, they synthesized VA-CNTs carpets over large surfaces such as a 30 cm in diameter silicon wafer.

synthesis is based on the pyrolysis of organometallic precursors such as metallocenes [29,30]; this method was called "floating catalyst CVD" because it does not require the preparation of catalyst particles. Floating catalyst CVD involves vaporization and sublimation of a catalyst precursor on a substrate that is then introduced in a high-temperature zone where the growth of the CNTs takes place. Whether the CNT growth starts during the floating stage [31], or from metal particles deposited on substrates or on the walls of the reactor leading into the furnace, followed by the tip-base growth mechanism [32] has been the subject of discussion. This technique allows the preparation of well-aligned and three-dimensional architectures of CNTs on conductive as well as nonconductive substrates (Figure 2) [33].

Figure 1: Example of scanning electron microscopy image of carbon nanotubes aligned perpendicularly to the substrates and synthesized on 30 Å Fe/300 Å Al_2O_3/SiO_2/Si for 30 min (C_2H_4/H_2 35/130 sccm) at 750 °C.

Figure 2: (a) SEM and HR-TEM images of aligned MWCNTs grown in three dimensions on Inconel substrates by floating catalyst CVD. The directions of CNT growth are indicated by arrows. (b) High-resolution transmission electron microscopy image of a typical nanotube grown in this way, showing the well-graphitized walls of the MWNT. Adapted with permission from [33]. Copyright 2006 Nature Publishing Group.

Among the different methods used to synthesize non-aligned CNTs, such as chemical vapor deposition (CVD), electrical arc discharge, or laser ablation, CVD has been reported to be the best for the synthesis of VA-CNTs. Different versions of CVD for the synthesis of VA-CNTs have been used, which can be mainly divided in two types: those involving a single synthesis step and those requiring double step synthesis. The single-step

In the double-step synthesis, firstly catalytic nanoparticles with controlled size and distribution are prepared, and then the growth of CNTs is performed. The nanoparticles can be obtained by physical methods (for example, Physical Vapor Deposition (PVD)) or chemical methods by using precursor solutions for the catalysts, which are then deposited by dip or

spin coating or, alternatively, are filled into nanoporous architectures serving as templates for the CNT growth.

Plasma vapor deposition is an efficient method for the preparation of thin films of metal catalysts with well-defined thicknesses. The catalytic nanoparticles are formed by annealing the film; the size and distribution of the nanoparticles are controlled by the thickness of the deposited film, the annealing parameters, and the type of the substrate (and added buffer layers) used for depositing the films [34,35]. In the case of chemical methods for catalyst particle production, the chemistry of the catalyst solution is crucial for determining the size of the nanoparticles, whereas their distribution is mainly determined by the deposition technique, for example spin [36] or dip [37] coating. The most common solutions consist of metal salts diluted in alcoholic solutions; however, stable solutions by using surfactants [38] or applying a sol–gel process [39] can be also used. The main disadvantage of the chemical method is the difficulty of optimizing the catalyst solution. The template-based approach in which the catalysts are deposited within the pores of nanoporous templates (for example, anodic aluminum oxide (AAO) membranes) allows design of a wide range of nanostructures with particular geometries, including aligned and monodispersed CNTs [40].

After the catalyst preparation, the next step is the synthesis of the VA-CNTs. This can be performed by thermal chemical vapor deposition (CVD) or plasma enhanced chemical vapor deposition (PECVD). The PECVD includes different plasma techniques, such as DC plasma [41], radio-frequency plasma [42], or microwave plasma [43]. The main difference is that the plasma in the PECVD provides a highly reactive environment compared with thermal CVD, allowing lower synthesis temperatures. An activation energy of about 1.2–1.8 eV [44,45] characterizes the thermal CVD while a lower activation energy of ≈0.3 eV [46] was reported for the PECVD. These energies are defined taking into account the four fundamental steps occurring during the CVD growth of CNTs: adsorption of the gas precursor molecule on the catalyst surface, dissociation of the precursor molecule, diffusion of the growth species in/on the catalyst particle, and nucleation and incorporation of carbon into the growing structure. Hoffman et al. [47] demonstrated that the limiting step in the determination of the activation energy for thermal CVD is the dissociation of the precursor molecule and, for PECVD, is the carbon diffusion on the catalyst. Thanks to the low temperatures in PECVD compared to the temperatures in thermal CVD, substrates that could be damaged at high temperature (for example glass) can be used as a support for VA-CNTs or their synthesis can be performed directly integrated in devices [48]. The CVD involves the decomposition of hydrocarbon gas molecules on the surfaces of catalyst nanoparticles, followed by carbon diffusion through the nanoparticles resulting in carbon precipitation at the surface and the nanotube growth. Two growth mechanisms were proposed: tip or base related growth [46]. In the first case, the catalyst nanoparticle comes off the substrate and, after synthesis, is observed at the top of the CNT. In the second case, the particle remains attached to the substrate. The common explanation for this difference is based on the adhesion force between the catalyst and the substrate. It is reported that a strong (weak) interaction furthers the base (tip) related mode. However, Gohier et al. [49] demonstrated that, during the catalytic chemical vapor deposition growth process, the particle size also plays a key role in the determination of the growth mechanism. For a given substrate/catalyst pairing, tip-related growth is favored when the catalyst particles are large (>>5 nm), giving multiwalled CNTs (>10 walls); while base-related growth is promoted for small particles (<5 nm), producing single or few-wall CNTs (typically less than seven walls). Gauthier et al. explained the shift between both growth modes using two different pathways for carbon diffusion [49].

The main constraint for the growth of CNTs is the poisoning of the catalyst due to encapsulation by amorphous carbon. In 2004, Hata et al. [26] reported the growth of VA-CNTs with millimeter length (Figure 3). By adding a small amount of an oxidizer during the CVD synthesis the poisoning of catalyst nanoparticles is prevented, extending the catalyst lifetime [50]. Another positive effect of the use of the oxidant is the inhibition of Ostwald ripening if injected during the annealing treatment of the catalyst film; the Ostwald ripening causes the formation of large particles thus reducing the yield of the CNT synthesis [51]. The usual oxidizer agent employed is water vapor, but in general oxygen-containing compounds such as alcohols or ethers are efficient. Alternatively the synthesis of VA-CNTs can be performed by using an alcohol as a carbon source with the advantages that the alcohol serves also as a weak oxidizer [52]. The two leading methods currently used to synthesize vertically aligned carbon nanotubes are the ferrocene-catalyzed growth of aligned multiwalled carbon nanotubes reported by Talapatra et al. [33] and the (super)-growth of ultrahigh-aligned single- (double-)walled carbon nanotubes on the catalytic system composed of thin Al_2O_3/Fe metal layers proposed by K. Hata, and co-workers [26,27].

In 2012, Zhu et al. [53] reported the synthesis of a hybrid material formed by VA-SWCNTs covalently bonded to graphene. The synthesis strategy is as follows. A sandwich consisting of a graphene substrate/catalyst layer/alumina layer is used. During the CNT growth, the catalyst and alumina layers are lifted up and the CNTs grow vertically aligned, directly on the graphene layer. As a result of this strategy, no seam exists between the
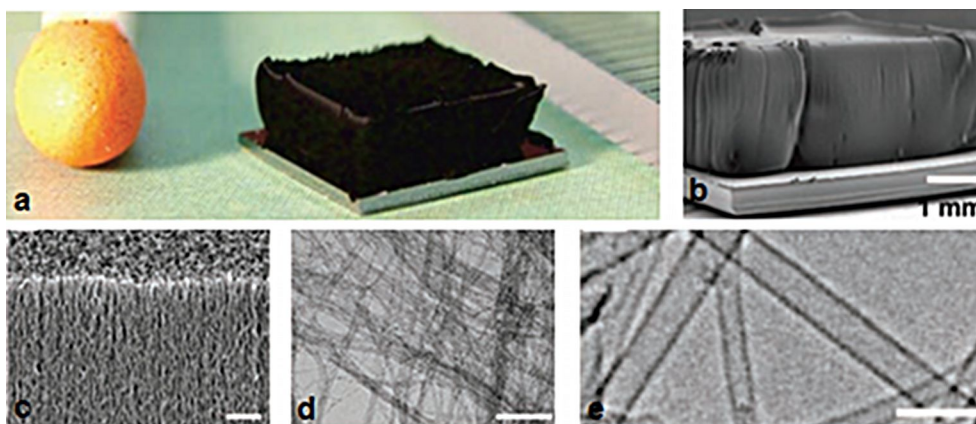
Figure 3: SWCNT forest grown with water-assisted CVD. (a) Picture of a 2.5 mm tall SWCNT forest on a 7 mm by 7 mm silicon wafer. A matchstick on the left and ruler with millimeter markings on the right is for size reference. SEM images of the same SWCNT forest with scale bars of 1 mm (b) and 1 μm (c), respectively. TEM images of the nanotubes with scale bars of 100 nm (d) and 5 nm (e), respectively. Adapted with permission from [26]. Copyright 2004 American Association for the Advancement of Science.

graphene and the nanotubes carpet. The introduction of the top alumina floating buffer layer is a crucial step, it allows the control of the CNTs diameter while forming a covalent bond between both elements. The particularity of this hybrid material is that it extends to three dimensions the excellent electrical conductivities and the large specific surface areas (SSA) of SWCNTs and graphene. The covalent bond between both elements leads to an ohmic contact at the junction. In parallel to this efficient electrical contact, a SSA between 2,000 and 2,600 $m^2 \cdot g^{-1}$ was measured. This work opens perspectives for potential applications in energy storage and nanoelectronic devices.

Outstanding progress in the synthesis of aligned carbon nanotubes has been reported; several studies show promising results in the control of the density, the length, the diameter, number of walls, and alignment of the vertically aligned nanotubes. We intended to give a brief overview of the synthesis techniques and the main achievements in this field. For further reading, detailed literature can be found in [54].

2 Patterning of VA-CNT arrays

For optimal engineering in applications such as field emitters or sensors, the location of the VA-CNTs and the design of their growth area are of primary importance. Two main strategies have been used to pattern VA-CNTs: the first is pre-patterning of the catalysts/substrates in order to form islands with desired size and shape and, thus, to pattern the growing VA-CNTs; the second is to directly pattern the VA-CNTs arrays by selective etching.

Most of the reported strategies are related to the first method in which the pre-patterning of the substrate is obtained by using shadow masks, photolithography and electron-beam-lithography (e-beam lithography). The first example, was given by Fan et al. [25]. These authors synthesized aligned carbon nanotubes in tower-like arrays by patterning the substrate with Fe films using electron beam evaporation through shadow masks, patterned with squared openings of well-defined size. The shape and size of the holes in the shadow masks determine the resulting shape of the patterned aligned nanotubes. For example, columns of aligned nanotubes can be obtained by using substrates patterned with catalyst dots. High lateral resolution in the patterning of the substrate for site-selective growth of VA-CNTs can be achieved by photolithography with the use of high-contrast films as photomasks with features on the microscale [55,56]. The use of other lithographic techniques such as soft-lithographic approach [57] or e-beam lithography [58], to pattern VA-CNTs, have been reported.

The soft-lithographic approach consists of micro- or nanopatterning processes mainly using two methods applied for aligned carbon nanotubes: microcontact printing and solvent-assisted micromolding techniques. Microcontact printing involves the use of a poly(dimethylsiloxane) (PDMS) stamp with self-assembled monolayer (SAM) coating to print the substrate surface by transfer of the SAM (e.g., alkylsiloxane). A photoresist solution is deposited in the areas not covered by the SAM, patterning the resulting polymer [57]. After the removal of SAM and the carbonization step of the PDMS, aligned carbon nanotubes can grow in the areas from which the SAM was removed. This technique has also been use to print catalysts, instead of SAMs, to synthesize free-standing SWCNTs on regularly patterned silicon with tower-like structures [59] or aligned multiwalled carbon nanotubes [60]. The second method, solvent-assisted micromolding consists of printing a drop of

photoresist solution by pressing with a PDMS stamp with a patterned relief structure on its surface. After drying, a patterned polymer is obtained and, consequently, after the carbonization step, patterned aligned carbon nanotubes can grow [57,61]. The disadvantage of the use of polymer in the lithography techniques described previously is the carbonization step, that is necessary to transform the polymer into carbon black areas, which then remains on the surface of the substrate to impede the growth of aligned nanotubes in these regions. To overcome this problem, plasma patterning can be employed to polymerize a resin in a patterned way. The obtained plasma-patterned substrate is then subjected to a pyrolysis of iron(II) phthalocyanine (FePc) under Ar/H$_2$ atmosphere at 800–1100 °C, which leads to the growth of vertically aligned carbon nanotubes in the plasma-patterned polymer-free regions. The highly cross-linked structure of the plasma-patterned polymer films guarantees the integrity of the polymer layer, remaining stable at the high temperatures involved in the CNTs growth process from FePc. The carbonization step, i.e., the inconvenient stage when using polymers in lithography techniques, can therefore be skipped with this method [62].

An alternative technique used to pattern aligned carbon nanotubes is e-beam lithography. It allows the selective growth of single free-standing aligned multiwalled carbon nanotubes [58]. For that purpose, the catalyst film is deposited precisely in selected regions; the density of catalytic nanoparticles in the region can be controlled, with a remarkable demonstration of writing, using patterned aligned nanotubes (Figure 4) [63]. An interesting example of patterned aligned carbon nanotubes is the engineering of gecko-foot-mimetic dry adhesives. Patterning is employed to effectively reproduce the setae of gecko composed of many lobes, aimed at obtaining the remarkable self-cleaning abilities and the same properties, i.e., high shear and peeling forces (Figure 5) [64-66].

A further step in patterning VA-CNTs is the engineering of 3D-architectures. The formation of 3D-aligned carbon nanotube patterns is obtained by growing VA-MWCNTs with different lengths and packing densities on specific regions, with covered and uncovered photoresist films using a photolithographic approach. The surface areas covered and uncovered by the film lead to a difference in the aligned CNTs growth on these two regions and consequently to the formation of 3D aligned carbon nanotube patterns [67].

Photolithography followed by dry and/or wet etching can be used to pattern silicon oxide in different shapes and thickness allowing the design of a wide range of organized nanotube structures. An example is the beautiful patterns of multiply oriented, organized, flower-like structures of nanotubes
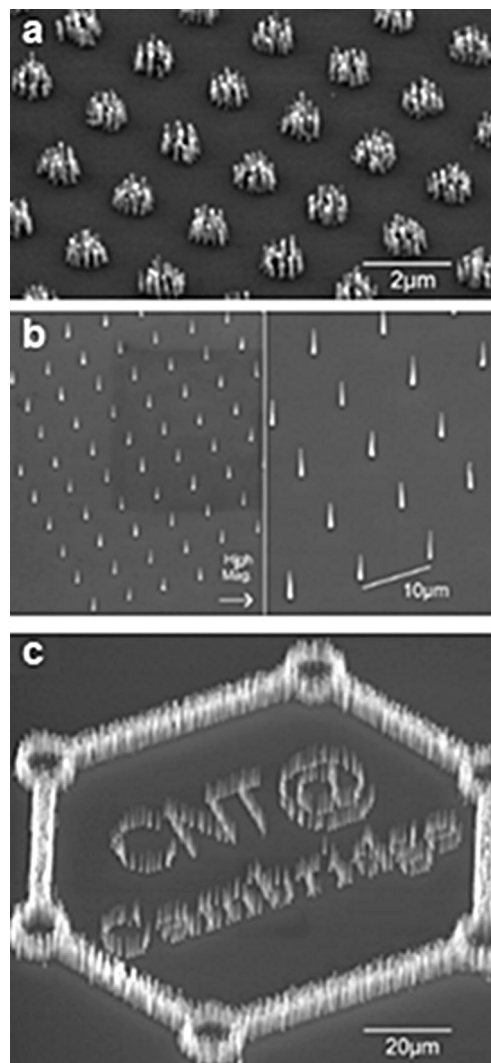

Figure 4: Various examples of nanotube arrays grown on Ni dots. (a) Bunches of nanotubes (about 100 nm in diameter) are deposited on 1 μm nickel dots, because the nickel catalyst film breaks up into nanoparticles. (b) Single nanotubes will grow when the size of the Ni dot is reduced to 100 nm, as only a single nanoparticle is formed from such a dot. (c) Demonstration of high yield, uniform, and selective growth of nanotubes at different densities. Adapted with permission from [63]. Copyright 2001 American Institute of Physics.

(Figure 6) [68,69]. A different method is the so-called "contact transfer" for producing micropatterns of the aligned carbon nanotubes by pressing on the adhesive layer of Scotch tape pre-patterned with a non-adhesive layer, followed by peeling the Scotch tape off to obtain positive and negative patterns [70]. 3D multicomponent micropatterns were synthesized by direct growth using masks produced by contact transfer [71]. Another example is the patterned growth of 3D interposed VA-SWCNTs and VA-MWCNTs by activating selective regions of iron substrates used for the synthesis of VA-MWCNTs with a thin layer of Al for the growth of VA-SWCNTs [72].
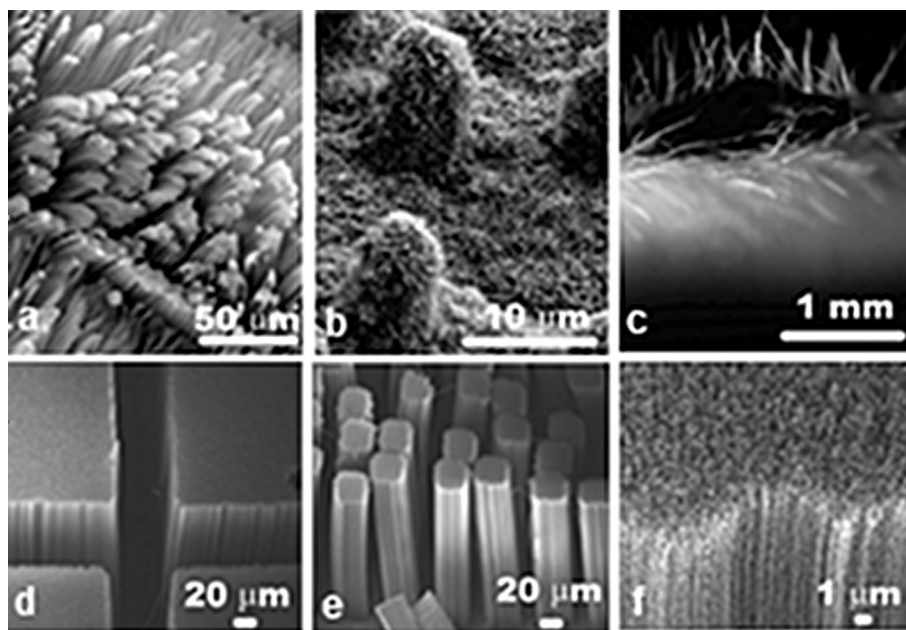
Figure 5: SEM images of natural (a) gecko setae, (b) a lotus leaf with hierarchical roughness, and (c) the hairy structure of lady's mantle leaf. SEM images of synthetic setae made of micropatterned aligned carbon nanotubes where they act as spatulas (d-f). Adapted with permission from [66]. Copyright 2008 American Chemical Society.
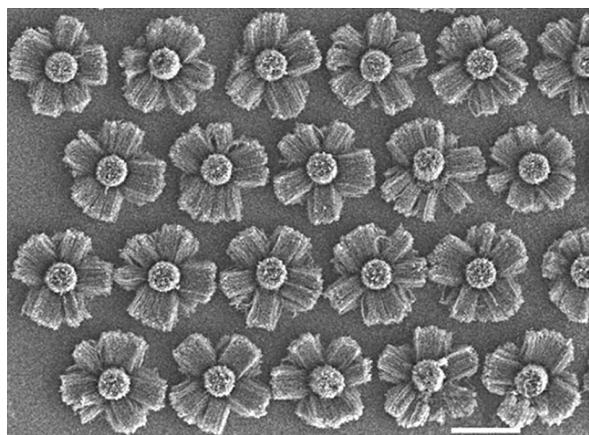

Figure 6: SEM image of beautiful repeating patterns of multiply oriented, organized nanotube structures on deep (about 5 μm) silica features (circular cross section), machined on silicon substrates. Growth in the vertical direction occurs from the top silica surface (seen as arrays emanating from the center of each pattern); growth on the sides occurs as horizontal arrays (sideways growth seen on each pattern) (scale bar, 50 μm). Adapted with permission from [69]. Copyright 2002 Nature Publishing Group.

Aligned carbon nanotubes can be directly etched by laser irradiation. A pruning method using a focused laser beam can be used to fabricate different 3D architectures. The spread of the beam causes the removal of a thin layer of aligned CNTs, and movable flaps of CNTs can be created by undercutting the CNT sidewalls (Figure 7) [73]. The patterning of VA-CNTs in large areas was obtained by using laser trimming. The use of a mask allows one to shield part of the VA-CNTs from the intense laser beam while the exposed CNTs are burnt away [74]. Alternatively, the VA-CNTs can be micromachined with the focused pulsed laser beams to produce columns with controlled size and shapes [75].

To conclude this part, the preparation of micropatterned VA-CNTs has been widely studied and significant advances in the methodology have been achieved in order to match the needs for device applications. Two strategies have been developed: the selective growth of VA-CNTs on pre-patterned substrates, and the post-patterning of CNTs films by using laser beams to selectively trench them, leaving the desired pattern behind.

3 Functionalization of VA-CNTs

We now focus on the functionalization of vertically aligned carbon nanotube samples. First, we describe the grafting of fluorine-, oxygen- and nitrogen-containing chemical groups at the VA-CNT surface. Next, we review the functionalization of CNTs with nanoparticles such as Cu, Ag, Au, Pt, Pd or TiO_2. Then, we present polymer-based functionalization and the grafting of biomolecules (DNA molecules, glucose molecules, proteins, etc.) on VA-CNTs for biological applications. Finally, we present some less-common functionalization methods.
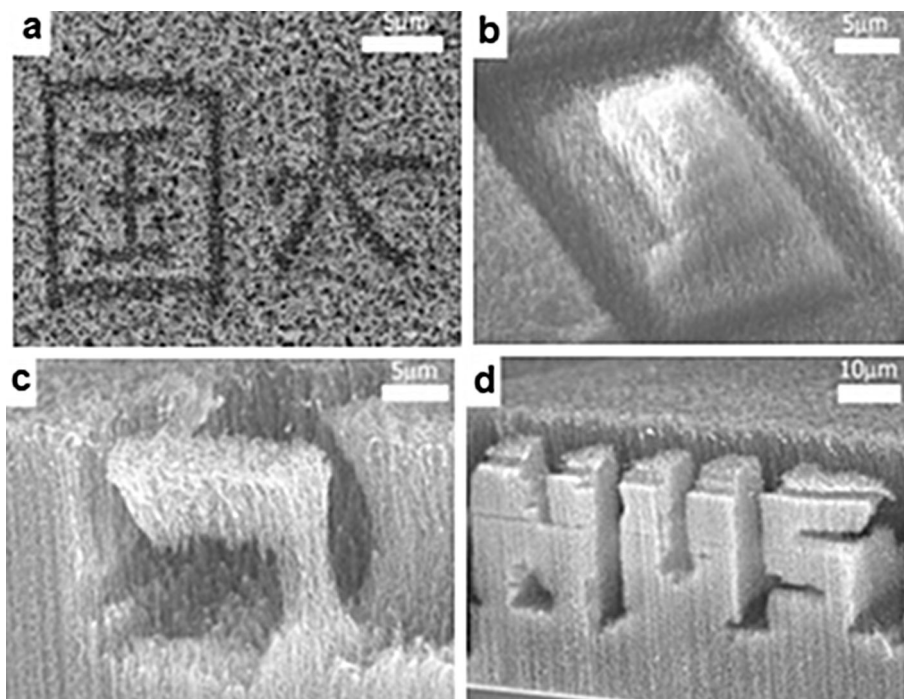
Figure 7: SEM images of (a) Chinese characters cut in 2D on a mat of CNTs, (b) a pyramidal structure cut by focusing the laser to different depths and scanning over the predetermined areas, (c) an inverted "L", and (d) 3D letters "NUS" produced in a two-step process: cutting first from the side and then with the sample in face-up configuration. Adapted with permission from [73]. Copyright 2003 John Wiley and Sons.

3.1 Functional groups

Fluorination of VA-CNTs: During the past decade, fluorinated non-aligned carbon nanotubes have been intensively investigated because of their potential applications [76]. Fluorination has been reported to impact on the morphology and on the physical and chemical properties of the CNTs, which can be used, for instance, as new precursors for chemical synthesis due to their better solubility and the creation of weaker C–F bonds [76]. Fluorinated CNTs are better electron acceptors, i.e., more prone to interact than pristine CNTs because both the Fermi energy level and conduction bands shift towards lower energy upon fluorination.

Regarding VA-CNTs, Dickrell et al. showed that the friction coefficient of oriented MWCNTs films depends on the temperature of the sample and the chemical groups at the surface [77]. In 2007, this problematic stirred the curiosity of Ler et al. [78]. Their work revealed the dependence of the friction coefficient on other parameters (CNT functionalization or CNT sidewall morphology, for instance). This value is determined by using a frictional force microscopy (FFM). The principle is the following: an atomic force microscopy (AFM) tip is pushed vertically into the film, between the nanotubes, and the lateral force experienced as the tip moves through the film laterally is measured [79]. Under this condition, it is clear that the CNT

sidewall plays a key role in determining the coefficient of friction. Moreover, the CNTs being hydrophobic [80], the water meniscus between the AFM tip and the CNT sidewall can be a hindrance to the tip displacement through the CNT forest and can disturb the measurement. To clarify these points, they accomplished a comparison between friction coefficient measurements for VA-CNTs modified by CF_4- or O_2-plasma treatment, under normal room humidity or reduced ambient humidity. The data revealed that the functionalization incorporates chemical species into the VA-CNTs film and modifies the wettability of the sample as well as the CNTs arrangement (according to the gas used in the plasma chamber). Consequently, the value of the coefficient of friction is modified. By contrast, the effect of the humidity on the coefficient of friction was found to be insignificant.

Because of their high aspect ratio and high chemical stability, carbon nanotubes can also find practical applications as electron-field emitters in flat-panel displays [81,82]. The major inconvenience is the weak field-emission performance. However, it was demonstrated that a fluorine-based functionalization of carbon nanomaterials such as diamond films [83] or amorphous carbon nanoparticle films [84] increases the yield of the phenomenon. The fluorination of carbon nanofibers [85] and SWCNTs [86] was also underlined. Chung et al. extended it

to aligned MWCNTs samples [87]. The proposed solution consists of a layer-by-layer deposition method, involving alternately the deposition of a thin layer of carbon nanotubes and the exposure of its surface to a CF_4 plasma. The advantage of these combined techniques is the continuous elimination of the unwanted amorphous-carbon and graphite phases forming in the film, resulting in the production of high quality CNTs at low substrate temperatures. Moreover, the CF_4 treatment opens the ends of the nanotubes, leading to an increase of the emission currents. A similar study was performed by Zhu et al. (Figure 8) [88]. They exposed VA-CNTs films to CF_4 plasma and evaluated the dependence of the field-emission properties on the exposure time. Results highlighted an optimal exposure time of two minutes, giving the higher field emission current, as well as a modification of the physical and chemical properties of the CNTs due to the plasma process (i.e., fluorination in CF_4 of the CNTs, defect-density increase and opening of the CNT caps).
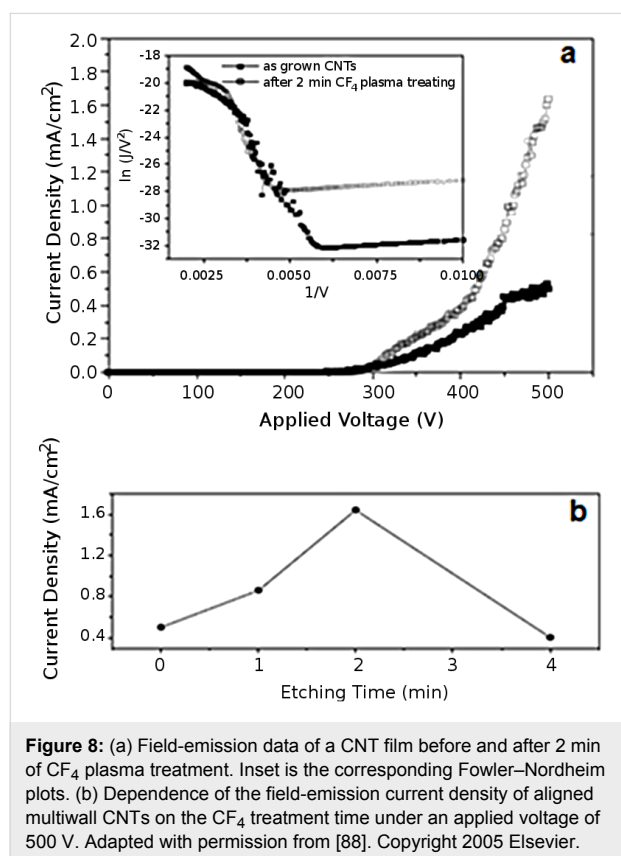

Figure 8: (a) Field-emission data of a CNT film before and after 2 min of CF_4 plasma treatment. Inset is the corresponding Fowler–Nordheim plots. (b) Dependence of the field-emission current density of aligned multiwall CNTs on the CF_4 treatment time under an applied voltage of 500 V. Adapted with permission from [88]. Copyright 2005 Elsevier.

Oxidation of VA-CNTs: As-grown VA-CNTs are superhydrophobic [89]. In 2010, Ramos et al. [90] emphasized that a post-treatment by using oxygen pulsed direct-current (DC) plasma can modify radically the wettability of VA-CNTs. The plasma treatment allows the grafting of oxygen-containing groups onto the VA-CNTs tips, altering the polarity of the sample and leading to a more hydrophilic surface. Ramos et al.

showed that a CO_2 laser irradiation post-treatment can reverse the phenomenon. It totally removes the grafted groups and re-establishes the hydrophobic character of the sample. They reported the ability to control the VA-CNTs wettability (from superhydrophilicity to superhydrophobicity) by combining both techniques. The change in the wettability of the VA-CNTs by grafting oxygen groups was also demonstrated by Lobo et al. [91] (Figure 9). They showed that an oxygen DC plasma etching post-treatment can modify radically the wettability of VA-CNTs films (oxygen flow rate of 1 sccm, at a pressure of 85 mTorr, −700 V, at a repetition rate of 20 kHz). The peculiarity of this treatment is the extremely brief treatment time (1, 2 or 5 min).
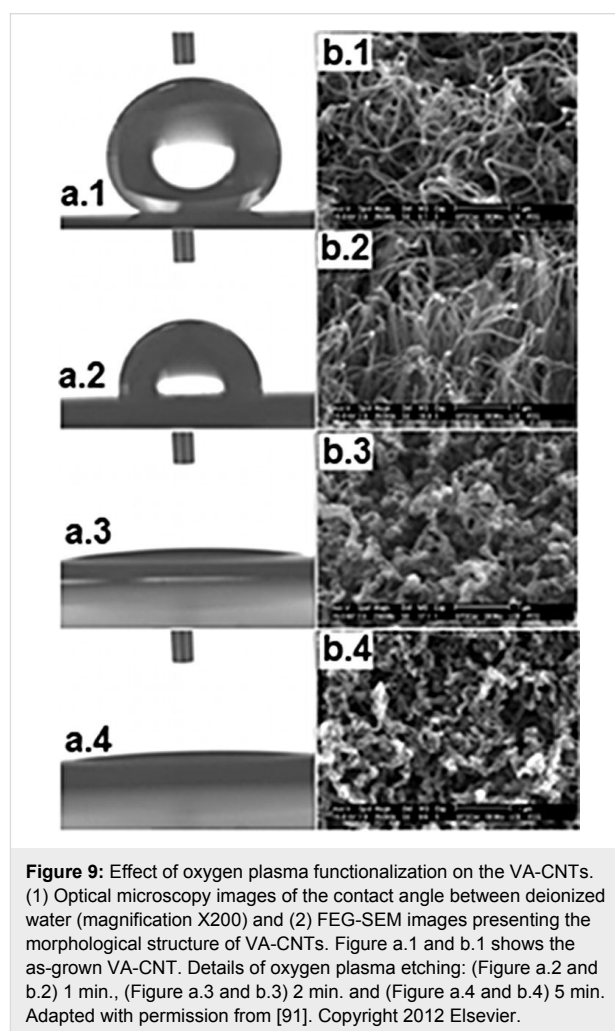

Figure 9: Effect of oxygen plasma functionalization on the VA-CNTs. (1) Optical microscopy images of the contact angle between deionized water (magnification X200) and (2) FEG-SEM images presenting the morphological structure of VA-CNTs. Figure a.1 and b.1 shows the as-grown VA-CNT. Details of oxygen plasma etching: (Figure a.2 and b.2) 1 min., (Figure a.3 and b.3) 2 min. and (Figure a.4 and b.4) 5 min. Adapted with permission from [91]. Copyright 2012 Elsevier.

Many transport applications (e.g., controlled drug delivery or molecular sensing [92]) require nanoporous membranes with a precise pore diameter, a perfect vertical orientation of the pores and a high uniformity. Until now, their manufacturing represents a complex challenge. Using a VA-CNT film, the inner core diameter of the tubes can be set by the catalytic particle

size [93] and the perfect vertical orientation is guaranteed [94,95]. Based on these synthesis characteristics, Majumder et al. [96] reported the engineering of VA-CNTs membranes in four steps: (i) growth of aligned MWCNTs by chemical vapor deposition, (ii) CNT filling with polystyrene, (iii) HF etching in order to separate the composite film from the substrate, and (iv) H_2O plasma oxidation in order to remove excess surface polymer and Fe nanocrystals at the CNT tips. The final product was a nanoporous membrane with carboxylate functions at the CNT tips. After further chemical functionalization, the nanoporous membrane showed an improvement of the selectivity of the chemical transport across its peculiar architecture. The attachment of oxygen-containing groups on CNTs is often a preliminary step before subsequent functionalizations, since they form active sites where other chemical groups will preferentially graft [97].

We have mentioned the interest in oxygen-containing groups grafting onto VA-CNTs to improve the wettability and the transport properties. Let us focus now on the electrical properties. Kim et al. [98] carried out mild oxygen plasma treatment on SWCNTs aligned between two electrodes. They found that the structural defect density on the sample surface increased linearly with the plasma treatment time. In parallel, they observed an exponential dependence of the resistance. No significant modification of the carrier concentration and tube–tube interaction was noticed. Considering that the electronic transport is driven by the localization mechanism (i.e., a localization of the electron states at the defect sites), Kim et al. explained the correspondence between (i) the linear behavior of the structural defect density with time and (ii) the exponential behavior of the resistance. This observation is important for different electrical devices. Ye et al. [99] electrodeposited molybdenum oxide (MoO_x) on VA-VNTs forests to develop electrochemical sensors for the detection of bromate. Brown et al. [100] investigated the potential use of VA-CNTs as neural stimulation electrodes. They performed flash oxidation (short exposition time of 20 min) of the VA-CNTs in O_2 (100 sccm) at various temperatures (between 200 °C and 500 °C) aiming at improving their charge storage properties. Various approaches were tested: (i) purify CNTs by removing carbonaceous impurities, (ii) create active sites for the grafting of hydrophilic oxygenated groups, (iii) attach oxygenated groups on the surface, and (iv) heat the sample. The consequences were an improvement of the electrolyte penetration as well as the wettability, the capacitance, and the charge-storage properties.

Rechargeable lithium-ion (Li-ion) batteries are based on the motion of lithium ions from the negative electrode to the positive electrode when being used, and inversely when charging. Their current limitation comes from their poor performance in terms of energy and power densities, safety and lifetime. Much attention is focused on the electrodes and electrolyte technology. Lu et al. [101] developed vertically aligned carbon nanotubes with and without a coaxial layer of vanadium oxide (V_2O_5) as cathode and anode, respectively. Due to their unique properties (e.g., large surface area, electrical conductivity, regular pore structure, electrolyte accessibility, charge transport), they are candidates for replacing traditional electrodes. Instead of traditional organic electrolytes, they used ionic liquids because of their nonflammability, nonvolatility, nontoxicity, large electrochemical window, and wide liquid-phase range. Practically, VA-CNTs were etched by H_2O plasma in order to open the extremities of the nanotubes prior to an electrochemical deposition of V_2O_5 on the sidewalls of the tubes. Opening the tips facilitates the penetration of the electrolyte inside the composite electrode.

Oxygen-based functionalization by plasma techniques can lead to morphological and chemical modifications of the nanomaterials [102,103] (Figure 10). Functionalization of vertically aligned MWCNTs performed by using atomic oxygen, generated by a microwave plasma, was reported to graft oxygen functional groups onto the tips of the VA-MWCNTs, without perturbation of the CNT alignment and structure. The CNT tips are more reactive than the CNT sidewalls [104,105]. In consequence, an opening of the VA-CNTs was observed. Radiofrequency Ar/O_2 plasma is also able to bring about modifications of the atomic composition and the structure of CNT forests. Zhao et al. [106] performed a detailed experimental investigation of the influence of the plasma parameters (work pressure, gas flow ratio, and plasma power among others) on the surface morphology and the chemical composition of VA-CNTs. As opposed to the wet chemical treatment, the plasma treatment does not destroy the vertical alignment of the nanotubes. By contrast, a significant surface morphology alteration is perceptible: nanotube tips agglomerate together, leading to the appearance of small nanotube bundles. It was proven that the agglomeration is independent of the oxygen concentration in the plasma chamber, but depends strongly on the work pressure and the plasma power. Besides, it was shown that the oxygen-containing compounds are exclusively grafted on the outer surface of the VA-CNT forest. A radio-frequency glow-discharge H_2O-plasma etching method was used in 2002 by Huang and Dai [21], to purify the VA-CNTs. During VA-CNT synthesis, a thin layer of amorphous carbon covers the aligned nanomaterial film [107] constituting an obstacle for certain applications. Water plasma etching was used to purify the sample and to remove the amorphous parasitic layer. When the plasma conditions are optimal, this method does not cause observable CNT structure or arrangement spoilage. On the contrary, when the conditions become harsh, a selective
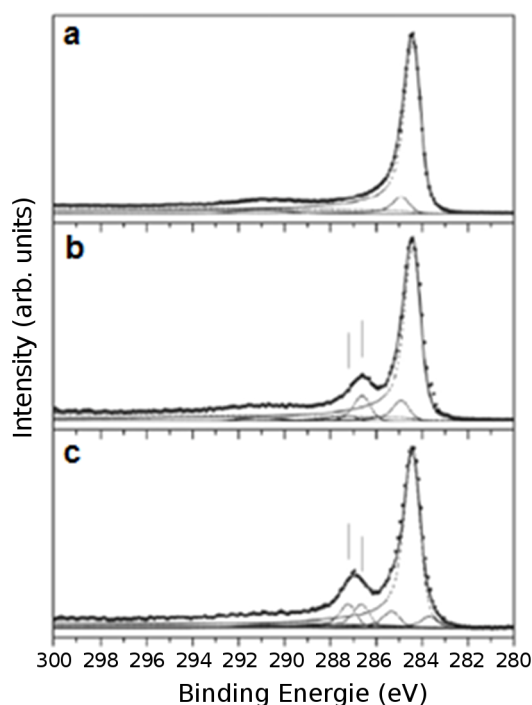
Figure 10: XPS analysis of (a) pristine vertically aligned MWCNTs and oxygen-plasma-treated MWCNTs for (b) 5 min and (c) 30 min. Vertical lines indicate the components associated with the oxygen functionalization. Adapted with permission from [102]. Copyright 2011 American Chemical Society.

Figure 11: Percentage weight loss of amorphous carbon as a function of the H_2O-plasma etching time. The H_2O-plasma etching was performed at 250 kHz, 30 W, and 0.62 Torr. Adapted with permission from [21]. Copyright 2002 American Chemical Society.

opening of the top end caps of the VA-CNTs is observed. Similar results were demonstrated both for VA-CNT continuous films and VA-CNT micropatterned films (Figure 11). Recently, water-vapor plasma was likewise used by Hussain et al. [108]. They showed that the plasma treatment (i) introduced defects in the CNT structure, (ii) removed catalyst molecules present at the CNT tips after the CNT synthesis, and (iii) decreased the CNT diameter. Depending on the plasma parame-
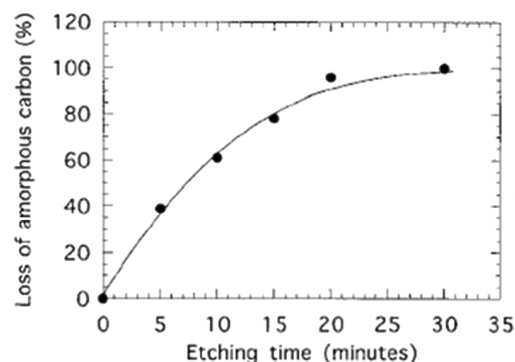
ters, it was possible to choose the grafted functional group between carboxyl and hydroxyl, thus tuning the electrochemical properties of the VA-CNTs.

Nitration of VA-CNTs: Fluorination of VA-CNTs increases their field-emission performance. Another solution lies in the utilization of post-growth nitrogen plasma treatment. This method was proposed by Lai et al. [109] in 2009. Patterned VA-CNTs, with an ideal hexagon arrangement, were used. Nitrogen doping was incorporated in the CNT bundles by nitrogen RF-plasma treatment (20 W of power, at a pressure of 27 Pa) with various exposure times (10–100 min), indicating the correlation between the duration of the nitrogen plasma treatment, i.e., an optimal doping concentration of impurities and the threshold electric field. (Figure 12) Lai et al. recorded the lowest threshold electric field (with a value of 2.3 V/μm) for the highest nitrogen content of CNTs (4.08 atom %), i.e., for a
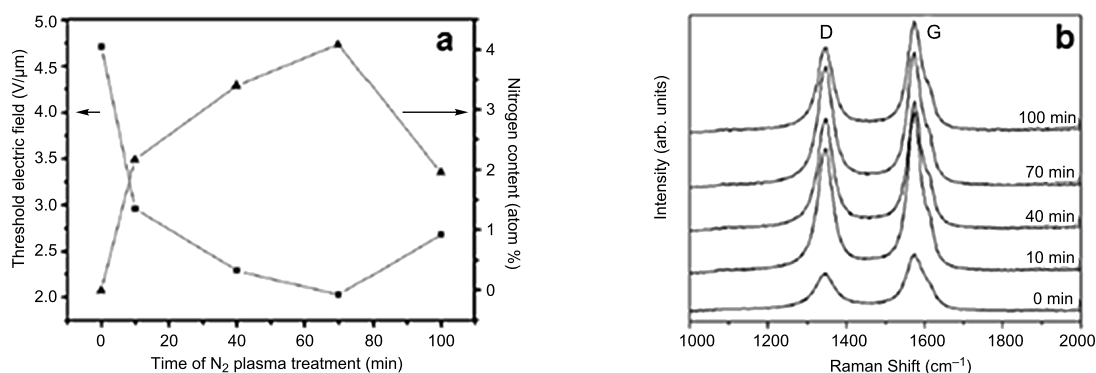

Figure 12: (a) Variation of threshold electric field and nitrogen content with the duration of the nitrogen plasma treatment. (b) Raman spectra of the CNTs after different times of nitrogen plasma treatment. Adapted with permission from [109]. Copyright 2009 Elsevier.

70 min nitrogen plasma treatment. The field emission characteristics of CNTs depend on their structural defects [110].

The fuel cell [111], discovered in 1839 by Sir William Grove [112], is a device in which the production of electricity is due to oxidation on a fuel reducer electrode coupled to the reduction of an oxidant on the other electrode. The oxygen reduction reaction plays a key role in the performance of the cell [113,114]. The traditional cell has many drawbacks including high fabrication costs and the spoilage of the platinum electrode with time [115]. VA-CNTs functionalized with electron-accepting nitrogen atoms prove to be a potential candidate to replace traditional Pt-electrodes [116-118].

3.2 Nanoparticles

In 2006, Qu et al. [119] developed a method to decorate selectively the walls and the tips of CNTs with metallic nanoparticles (NPs) controlled in size and shape (e.g., Cu, Ag, Au, Pt and Pd nanoparticles). The principle is the following: VA-CNTs are produced by the template-synthesis method by using alumina membrane templates with a pore size of about 200–500 nm; the assembly is then immerged in an aqueous solution, in which the NPs production will occur. Depending on the conditions (metal salt concentration, exposure time), the shape and size of the NPs can be controlled. A subsequent dissolution of the alumina template in aqueous HF retrieves individual nanotubes for

further manipulations. For instance, it is possible to obtain an asymmetric functionalization by attaching one kind of NPs on the inner wall of the CNTs and another kind of NPs on the outer wall (Figure 13).

TiO_2 stirs the curiosity of scientists because of its remarkable semiconducting and photoelectronic properties. Hence, integrated systems combining CNTs and TiO_2 NPs are potential candidates for photocatalytic or optoelectronic systems, taking advantages of both materials. Yang et al. [120] carried electrophoretic coating of VA-CNTs with TiO_2 NPs in order to create coaxial nanowires. In parallel, they synthesized aligned TiO_2 nanotubes and nanomembranes, using the VA-CNT film as a template. All these products have novel photocurrent and photoinduced properties.

More recently, the functionalization of VA-CNTs arrays with platinum nanoparticles was examined by Soin et al. [121]. A method combining microwave-plasma-enhanced chemical vapor deposition and DC sputtering was employed in order to synthesize such samples. The alignment of tubes was not perturbed, no physical damage and no etching were observed. Dispersed NPs with diameters close to 2–3 nm were formed at the tip of the tubes. In contrast, at the middle of the tube, NPs with diameters close to 3–5 nm or NPs clusters were observed (Figure 14). The NP spatial distribution depends on the defect
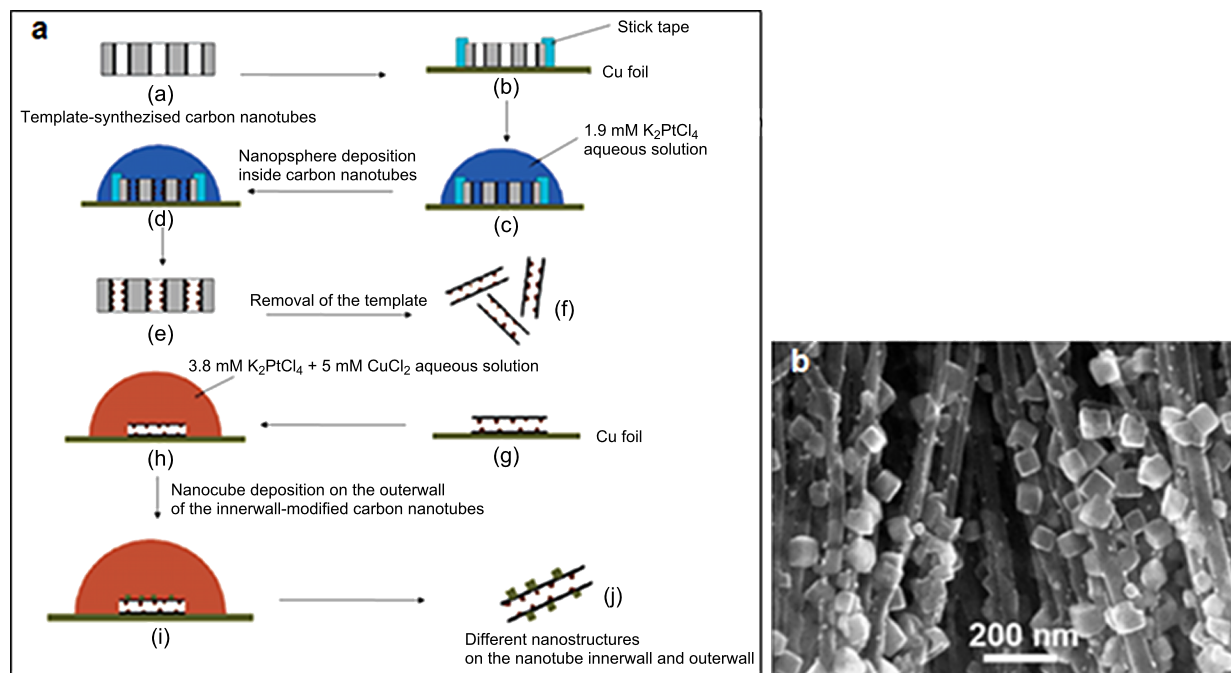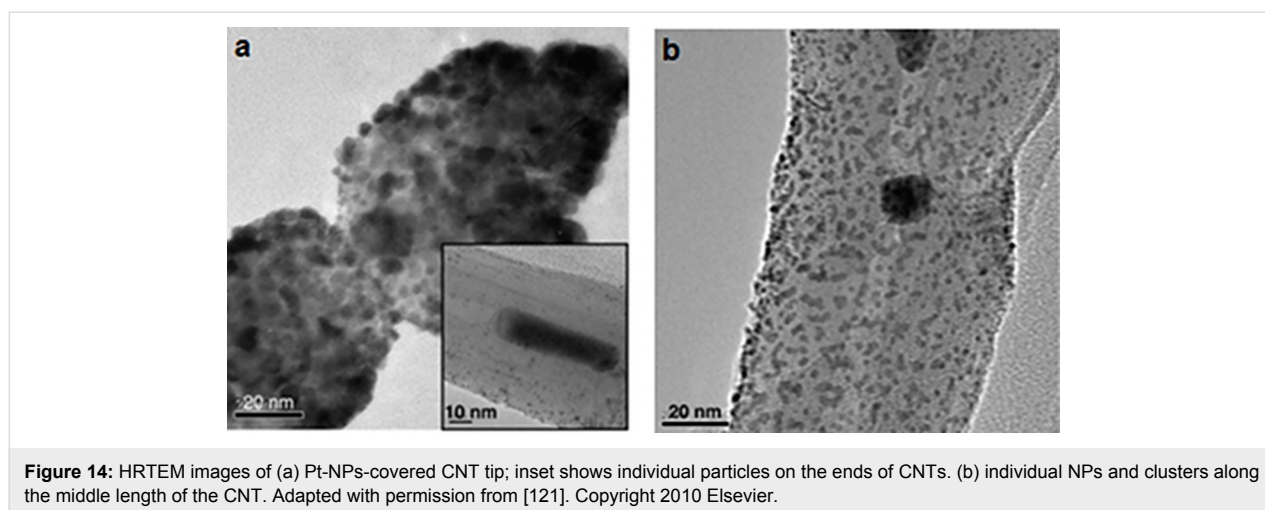

Figure 13: (a) Procedures for the nanotube inner wall modification and the asymmetric modification of the nanotube inner wall with Pt nanospheres and the outer wall with nanocubes. For the sake of clarity, only a few of the many CNTs on the Cu foil are shown. (b) SEM image of aligned CNTs decorated with Pt nanocubes. Adapted with permission from [119]. Copyright 2006 American Chemical Society.

Figure 14: HRTEM images of (a) Pt-NPs-covered CNT tip; inset shows individual particles on the ends of CNTs. (b) individual NPs and clusters along the middle length of the CNT. Adapted with permission from [121]. Copyright 2010 Elsevier.

density distribution along the length of the tube, since defects are nucleation sites for NP growth [122]. Functionalization of VA-CNT arrays with platinum nanoparticles is promising in fuel-cell development [123]. Similar samples, i.e., platinum decorated VA-CNTs, were produced by Dameron et al. [124] using atomic layer deposition (ALD). First the VA-CNTs were modified by chemical functionalization with a trimethylaluminium (TMA) monolayer or ex-situ Ar, O_2 or Ar/O_2 RF-plasma functionalization. Then, platinum was deposited by ALD. The gas-phase functionalization route was preferred in order to control the nucleation sites and to improve the Pt coverage and uniformity on the CNTs. The authors showed that the preliminary treatment, especially the O_2 plasma treatment, is effective to create nucleation sites and to favor the deep Pt infiltration inside the CNTs array.

3.3 Polymers

In recent decades, many publications have gathered together the tremendous progress made in the understanding of polymer functionalization of VA-CNTs. The success in this field offers a wide range of technological opportunities in a myriad of applications. For instance, in order to enhance the field-emission properties of VA-CNTs, a two-step method can be applied [125]. It consists of sheathing the nanotubes with a thin layer of polymer coating by means of a radio-frequency hexane-plasma treatment, followed by a water-induced restructuring. Another example is the synthesis of conducting coaxial nanowires, useful for optoelectronic and sensing applications. Aligned carbon nanotubes were coated uniformly by electrochemical deposition with an appropriate conducting polymer [126,127].

In order to manufacture plastic solar cells, transparent and flexible conductors are required. Traditionally, indium tin oxide (ITO) is deposited on flexible substrates. The inconvenience is the weak resistance to acid, the weak resistance after repeated

strain and the weak conductivity in comparison to glass [128]. Peng [129] developed a CNTs/polymer composite material by spin-coating a polymer solution onto a VA-CNTs sample, followed by the evaporation of the solvent. The product has high optical transparency, robust flexibility and good conductivity.

Chen et al. [130] used a radio-frequency glow-discharge treatment and chemical reactions post-treatment to graft polysaccharide chains onto a VA-CNT surface. After functionalization, the sample is highly hydrophilic and biocompatible, and presents little perturbation of the CNT structure. This highly hydrated coating offers possibilities to use VA-CNTs in biological systems (Figure 15).

The wettability properties of VA-CNTs can be changed by grafting oxygen functional groups, but also by polymer functionalization. Lau et al. [131] favored a bio-inspired approach to the problem and mimicked designs found in nature. In certain plants such as the lotus leaf, water droplets roll on the surface and remove dust particles; this is a self-cleaning behavior and is called the Lotus effect [132]. The origin is the peculiar roughness and the intrinsic hydrophobic behavior of the surface. Based on this observation, the authors enhanced the superhydrophobic effect on CNTs by combining two elements: the coating of VA-CNTs with hydrophobic poly(tetrafluoroethylene) (PTFE) and the nanoscale roughness inherent to the sample (Figure 16).

The enhancement of the thermal conductivity of a composite enclosure in the direction of its thickness is another illustration of the application of VA-CNT polymer functionalization. Sihn et al. [133] embedded VA-MWCNTs in an adhesive medium (epoxy infused between CNTs) and encapsulated the whole between two adherent media (graphite facesheets). A transition zone made of metallic coatings was inserted between the CNTs
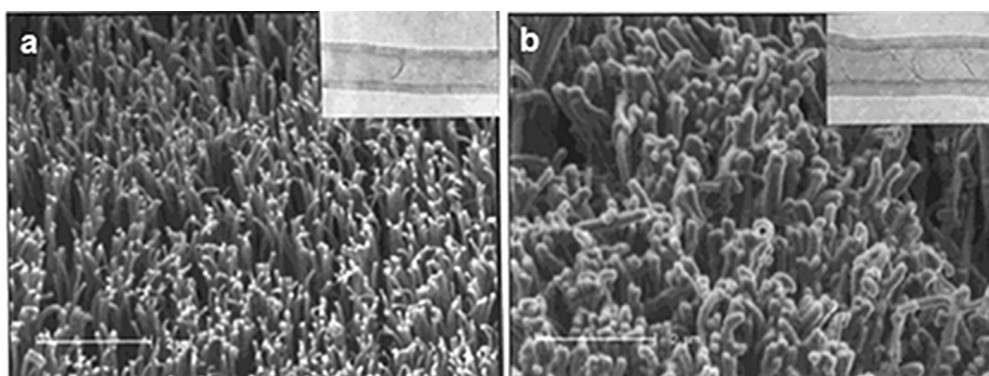
Figure 15: SEM micrographs of the aligned carbon nanotubes (a) before and (b) after plasma polymerization of acetaldehyde. The insets show TEM images of an individual nanotube (a) before and (b) after being coated with a layer of the acetaldehyde-plasma-polymer (optimized conditions for the polymerization of acetaldehyde: 200 kHz, 20 W and a monomer pressure of 0.3 Torr for 5 min). Adapted with permission from [130]. Copyright 2001 American Chemical Society.
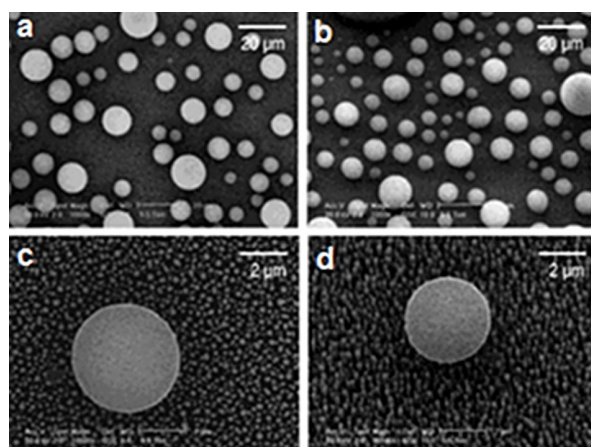

Figure 16: SEM images of water droplets on CNT films. (a) Top-down view of micron-sized water droplets suspended on the PTFE-coated films, (b) 15° tilt view at the same magnification, (c) top-down view of a single suspended water droplet in which the PTFE-coated nanotubes are also visible, and (d) 15° tilt view at the same magnification. Adapted with permission from [131]. Copyright 2003 American Chemical Society.

tips and the surroundings, after their suitable functionalization. The authors evaluated experimentally and numerically the through-thickness thermal conductivity of the composite sample. They reported that the key components influencing the thermal conductivity are, on the one hand, the thermal conductivity and the size of the metallic transition zone and, on the other hand, the use of highly conductive vertically aligned nanotubes. A preliminary study performed by Huang et al. [134] has laid the foundations for this observation. Lin et al. [135] went a step further by adapting VA-CNTs–epoxy nanocomposites to produce thermal interface materials (TIMs) (Figure 17). A process combining in situ functionalization of

VA-CNTs and microwave curing was employed. This device has an ultrasmall coefficient of thermal expansion (CTE), good mechanical load transfer, and good phonon transport across the interface.
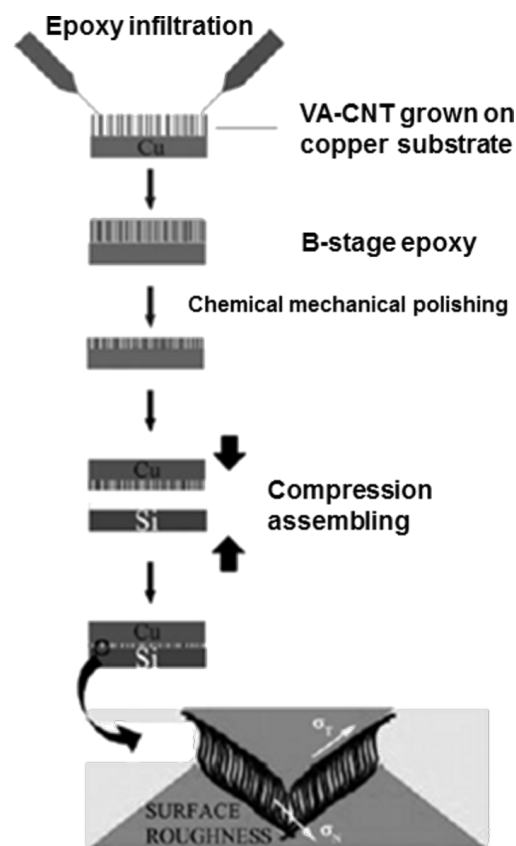

Figure 17: Illustration of the ACNT-epoxy TIM assembly process and the CNT statues at the interface. Adapted with permission from [135]. Copyright 2009 John Wiley and Sons.
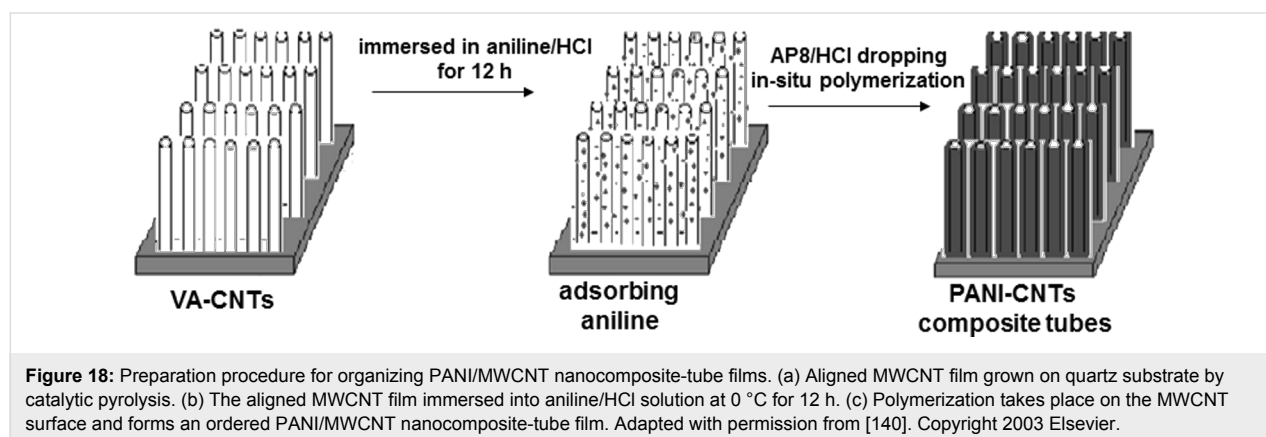
The control of the CNT orientation within the polymer matrix (PM) and the control of the interaction between both components are of paramount importance [136]. VA-CNT films are good candidates matching these requirements. In 2002, Nguyen et al. [137] created CNT–PM samples in two steps: first, a nucleic acid grafting at the CNT tips, leading to the opening of their end caps, and then a spin-on-glass deposition inside the VA-CNT array. Hinds et al. [138] and then Chopra et al. [139] used, instead of a spin-on-glass matrix, a polystyrene (PS) matrix. By means of refined experimental examinations, the first group proved an efficient molecular transport through the CNTs cores, opening perspectives in chemical separation and sensing. The second group showed that encapsulating CNTs in a polystyrene matrix protects their sidewalls against oxidation and favors selective and independent functionalization of each end of the CNTs. Moreover, individual CNTs with a chemical group attached at each end can be retrieved by the dissolution of the PS membrane.

Feng et al. [140] opted for a polyaniline (PANI) matrix. This material is one of the most conducting polymers (Figure 18). Synthesis and characterization of conducting polymer polyaniline nanofibers was reported by Huang [141]. The major issue related to great disorder of the functionalized fibers was solved by Feng et al. who made well-aligned MWCNTs/PANI hybrid materials. The methodology is the following: (i) VA-CNTs are grown on a quartz substrate by catalytic pyrolysis, (ii) the film is immersed in an aniline/HCl solution (0 °C, 12 h), (iii) polymerization on the CNTs surfaces. The products showed a high-quality structural arrangement and an enhanced electrical conductivity. Many physical properties such as morphology, thermal stability, conductivity and charge carrier mobility are disrupted by this treatment. This can be crucial for applications in the photovoltaic field. We can also mention the work of Raravikar et al. [142] who embedded VA-CNTs into a poly(methyl methacrylate) (PMMA) matrix with a two-step strategy. The first step is the fabrication of a VA-CNTs array

followed by a MMA monomer infiltration while the subsequent step is in situ polymerization. Finally, we mention the work of Jung et al. [143] who created flexible CNT–PM samples with soft poly(dimethysiloxane) as the polymer compound. Their product respects the CNTs alignment, is highly flexible and retains its conducting properties even under hard tensile and compressive forces.

As shown in the literature, a large variety of polymer matrices can be used. The principal approach to achieve this CNT–PM mixing is the solution-coating. However, in all these works, the inconvenience was the difficulty in controlling the nanotube length being embedded within the matrix. In 2007, Qu and Dai [144] brought a simple answer: a thin polymer layer is deposited on the surface of a VA-CNT array, followed by heating beyond the melting temperature of the polymer, causing its infiltration inside the array. According to the heating temperature and the exposure time, the resulting composite shows a more or less large polymer-free region (Figure 19). Mechanical insertion of a VA-CNT forest in a spin-cast PM allows the best control of the penetration depth [145]. A post-treatment consisting of the attachment of nanoparticles in the polymer-free region can take place (as discussed in the previous section), the functionalization length being set by the experimental conditions of the synthesis of the VA-CNT–PM composite. Moreover, using the polymer-masking technique twice, it is possible to achieve an asymmetric functionalization of the CNT sidewalls [146]. Finally, using compounds such as iron adds new magnetic properties to the CNT tips.

The polymer-masking methodology was also used to manufacture highly efficient gas sensors [147]. VA-CNTs were embedded in a polymer matrix (e.g., poly(vinyl acetate) or polyisoprene) and two gold electrodes were sputtered onto the surface of the sample. A change of the charge transfer or the capacitance will then indicate the presence of gases in the environment [148-150]. In this context, we mention also the work of
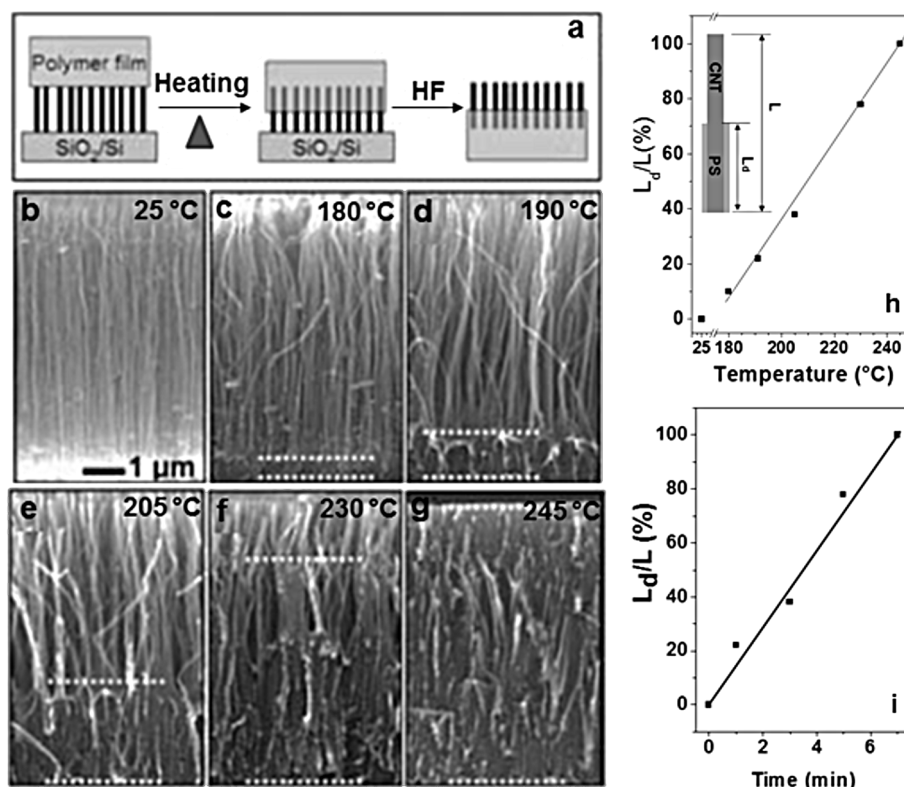

Figure 18: Preparation procedure for organizing PANI/MWCNT nanocomposite-tube films. (a) Aligned MWCNT film grown on quartz substrate by catalytic pyrolysis. (b) The aligned MWCNT film immersed into aniline/HCl solution at 0 °C for 12 h. (c) Polymerization takes place on the MWCNT surface and forms an ordered PANI/MWCNT nanocomposite-tube film. Adapted with permission from [140]. Copyright 2003 Elsevier.

Figure 19: (a) Schematic representation of the VA-CNTs embedded into a polymer matrix by thermal infiltration of the melted polymer into the nanotube forest; (b)–(g) SEM images of (b) the pristine VA-CNT array and (c)–(g) the VA-CNT array after being embedded into PS films by heating at different temperatures for 1 min. The gaps between the dashed lines crossing the polymer coated regions show the approximate embedment length for each of the PS-embedded VA-CNTs; (h) and (i) temperature and time dependence of the embedment length for VA-CNTs embedded into the PS matrix (L: nanotube length ($\approx$6 μm), L_d: embedment length, which was estimated from the distance between the two dashed lines in each of the images shown in (c)–(g). Adapted with permission from [144]. Copyright 2007 Royal Society of Chemistry.
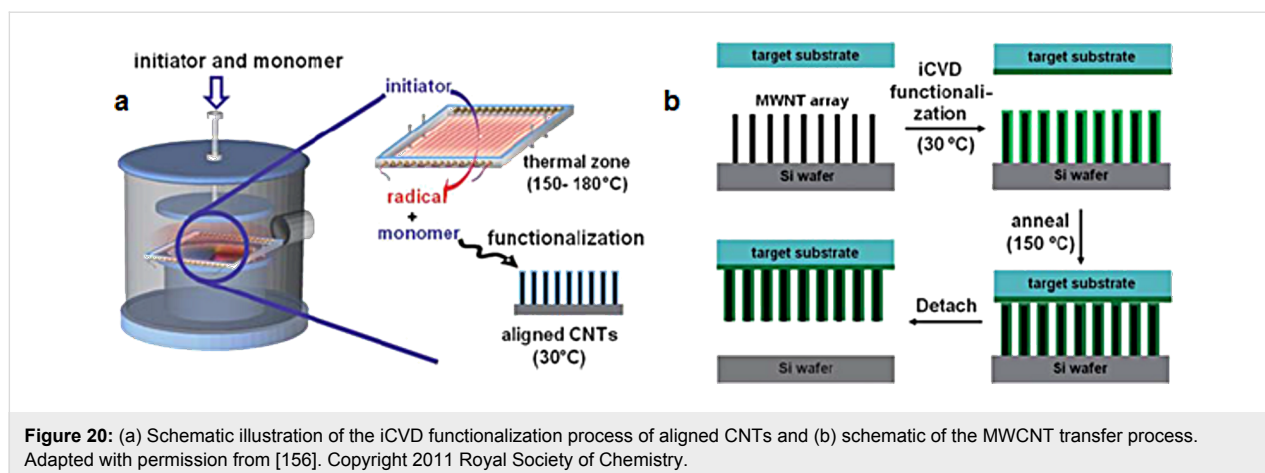
Chen et al. [151]. They integrated temperature-responsive polymers in an array of VA-CNTs to produce composite systems with self-cleaning capabilities and/or with abilities to controllably release objects trapped within the systems. For example, we can imagine the production of antifouling devices, gecko-like artificial devices, functional membranes, or sensors.

Wardle et al. [152] assessed the density of VA-CNTs that it is possible to insert in a PM with a two-step technique (a mechanical densification of VA-CNT forests followed by a capillarity-driven wetting along the axis of the CNTs). They revealed that the theoretical limit can be approached, i.e., a distance between two neighboring nanotubes close to the typical length of the polymer chains. The morphological features of the sample (CNT alignment and distribution, polymer morphology) seem to be conserved despite this close packing.

Based on the interaction between carbon nanotubes and polymer or ceramic (e.g., silicon nitride), membranes including VA-CNTs can be fabricated with potential applications in novel ultrafiltration and sized-based exclusion separation devices.

These membranes present many advantages in comparison with traditional membranes. Indeed, studies highlighted an enhancement of the properties of the flow of liquids or gases through the CNTs cores [153]. In the case of CNTs being used as transport channels, we draw the attention of the reader to the fact that the VA-CNTs must be opened (by example by plasma oxidation) and that this treatment introduces functional groups modifying the transport properties [154].

In this section, various techniques allowing functionalization of VA-CNTs were presented, such as the polymer-impregnation technique, polymer-masking technique, sheathing technique and in situ polymerization. The vapor-based technique, a solventless method, was also presented. In 2005, He et al. [155] deposited uniformly thin carbon fluorine films on the surface of aligned carbon nanotubes by means of a plasma-polymerization treatment. In 2011, Ye et al. [156] applied initiated the chemical vapor deposition (iCVD) method, a one-step polymer deposition method without any liquid medium (Figure 20). Initiator molecules thermally break down into radicals at relatively low temperature. Then, a radical polymerization of the specific

Figure 20: (a) Schematic illustration of the iCVD functionalization process of aligned CNTs and (b) schematic of the MWCNT transfer process. Adapted with permission from [156]. Copyright 2011 Royal Society of Chemistry.
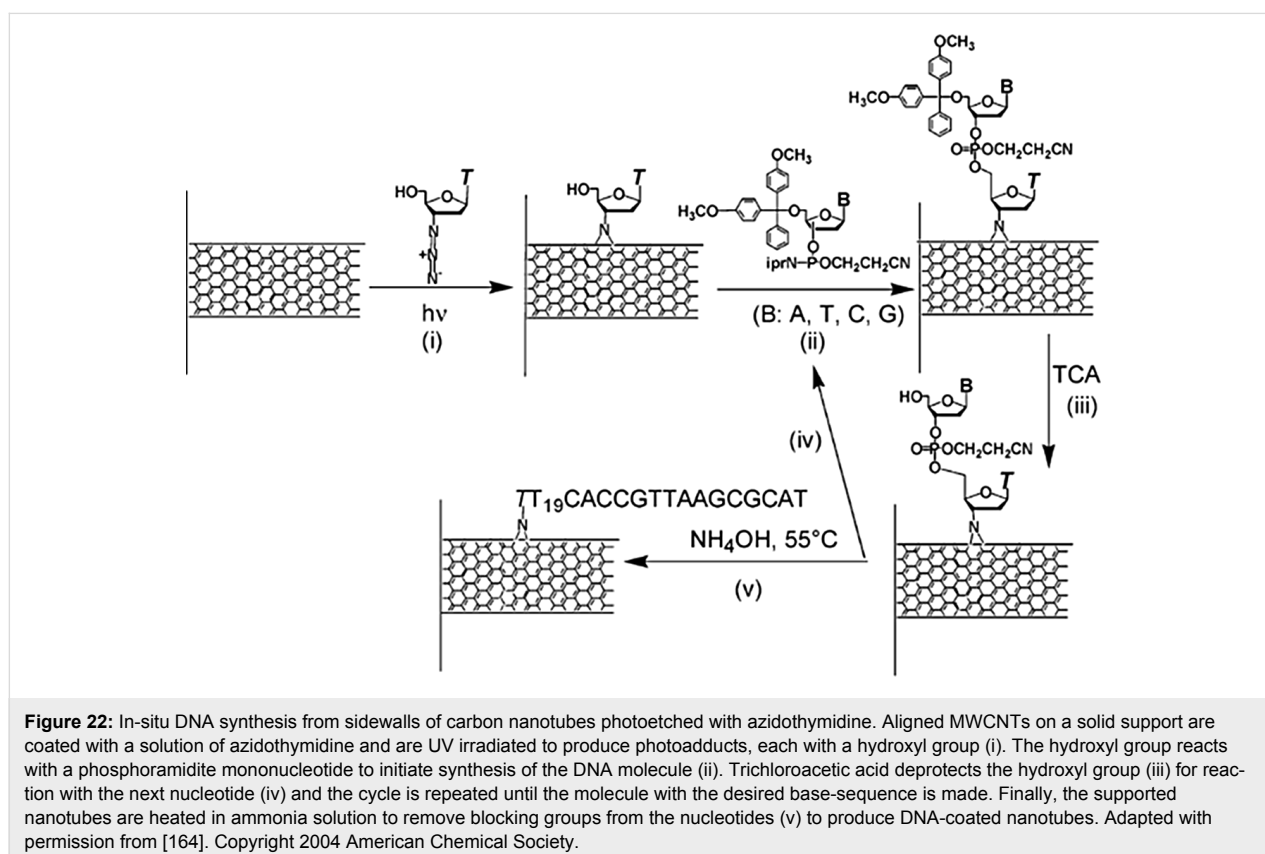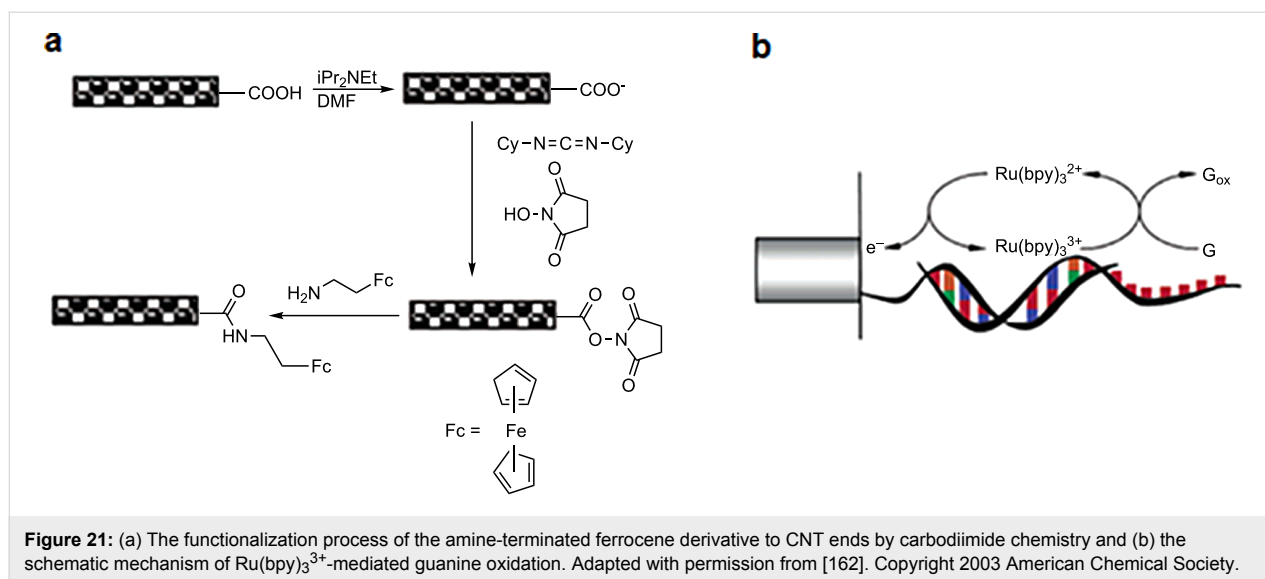
monomers begins at the surface of the substrate. In their work, Ye et al. used an array of VA-CNTs on a silicon wafer, a *tert*-butyl peroxide (TBP) initiator, and a glycidyl methacrylate (GMA) monomer. After iCVD, the CNTs alignment is preserved. Furthermore, the sample porosity and the deposition uniformity along the CNTs sidewalls can be controlled with the exposure time and deposition rate. The restrictions to the VA-CNT growth are the limited choice of substrates and the poor adhesion between both elements. Hence, Ye et al. intended to transfer the functionalized VA-CNT array to another substrate. They performed similar polymerization treatment on the novel substrate, placed the functionalized VA-CNTs array in contact with the novel substrate, and annealed the system under vacuum at 150 °C. The result was the separation of the CNTs array from the silicon substrate and the attachment to the novel substrate. This low temperature flip-over transfer method preserves the CNTs alignment, gives a strong adhesion between the CNTs and the novel substrate, improves the mechanical properties of the system, and enhances the stability towards wetting (Figure 20).

Recent work on the covalent functionalization of VA-CNTs with polystyrene was published by MacDonald et al. [157]. The originality lies in the type of samples they used: instead of using CVD aligned nanotubes, a method reported by Yu et al. [158] was preferred. In this case, VA-CNTs were attached to a silicon(100) substrate by chemical anchoring directly to the surface. The silicon surface was hydroxylated while the surface of the nanotubes was acid treated and functionalized with carboxylic moieties. MacDonald et al. succeeded in modifying the sample in situ. The carboxylic group was derivatized to bis(dithioesther) moieties, which act as a chain transfer agent (CTA), before application of a reversible addition fragmentation chain transfer (RAFT) polymerization of polystyrene on the surface. The results of this work are important for the design of water-treatment membranes, solar cells, or biochemical sensors.

3.4 Biomolecules

A major issue is the fast and reliable detection of minute quantities of enzymes, proteins or DNA molecules for diagnostic purposes. For this reason, devices with an easy measurement method, high sensitivity, high selectivity and low production cost are required. It has been proven that CNT arrays are a good candidate. Dwyer et al. [159] as well as Willams et al. [160] grafted modified DNA strands at the open ends and defect sites of SWCNTs. This was an initial step to the fabrication of self-assembled molecular-scale electronic systems. Thereafter, researchers have moved away from CNT powder and have focused on VA-CNTs. Indeed, VA-CNTs present many advantages such as a large surface area in order to offer a maximized contact with the analyzed sample or ease of device manufacturing. In 2002, Li et al. fabricated an aligned MWCNT array embedded in a SiO_2 matrix [161] and functionalized CNT tips with primary amine-terminated oligonucleotide probes [162]. An electrochemical platform, combining such a CNT nanoelectrode array with $Ru(bpy)_3^{2+}$-mediated guanine oxidation (Figure 21), can detect the hybridization of extremely small amounts of DNA targets (less than a few attomoles).

Gooding et al. [163] showed that a platform composed of VA-SWCNTs and redox protein grafted to the CNTs tips is a good electrical communication channel between the underlying electrode and the proteins. This work represents a major step towards bioelectrical devices. In all these works, only the tip of the nanotubes could be modified. Moghaddam et al. [164], firstly, and He and Dai [165], secondly, proposed a method to attach single-strand DNA chains both to the sidewall and to the tips of the vertically aligned carbon nanotubes. These devices offer novel perspectives in the biosensors domain since they have a high sensitivity and selectivity for probing complementary DNA chains of specific base sequences (Figure 22). In this context, Lin et al. [166] and Pandey et al. [167] fabricated glucose biosensors based on VA-MWCNTs functionalized by

Figure 21: (a) The functionalization process of the amine-terminated ferrocene derivative to CNT ends by carbodiimide chemistry and (b) the schematic mechanism of $Ru(bpy)_3^{3+}$-mediated guanine oxidation. Adapted with permission from [162]. Copyright 2003 American Chemical Society.

Figure 22: In-situ DNA synthesis from sidewalls of carbon nanotubes photoetched with azidothymidine. Aligned MWCNTs on a solid support are coated with a solution of azidothymidine and are UV irradiated to produce photoadducts, each with a hydroxyl group (i). The hydroxyl group reacts with a phosphoramidite mononucleotide to initiate synthesis of the DNA molecule (ii). Trichloroacetic acid deprotects the hydroxyl group (iii) for reaction with the next nucleotide (iv) and the cycle is repeated until the molecule with the desired base-sequence is made. Finally, the supported nanotubes are heated in ammonia solution to remove blocking groups from the nucleotides (v) to produce DNA-coated nanotubes. Adapted with permission from [164]. Copyright 2004 American Chemical Society.

glucose oxidase (GOx) molecules. They showed encouraging results in terms of the minimum limit of detection and sensitivity, as well as the possibility for device reuse (up to six months) when stored in a proper environment.

With a high chemical stability, a large surface area easily accessible to molecules in solution, a quasi-perfect vertical arrange-

ment, a nanoscale size, and a facility to synthesize patterned samples, VA-CNTs are ideal for biological detection. Additionally, their high mechanical strength and their small diameter suggest that VA-CNTs are ideal for intracellular detection [168]. Baker et al. [169] manufactured vertically aligned carbon nanofibers (VA-CNFs)-based electrodes as a platform for biological detection. Using a photochemical functionalization,

carboxylic acid functions are grafted on the carbon nanomaterial. Thereafter, these functions act as a preferential site where Cytochrome *c* metalloproteins (small proteins found associated with the inner membrane of the mitochindrion) will be immobilized (Figure 23).

3.5 Other functionalization groups
In the context of the investigation of complex electrocatalytic reactions, Landis et al. [170,171] functionalized VA-CNTs with redox-active molecules (e.g., ferrocene) and studied the electron-transfer properties of the system. They explained that the edge-plane graphite sites along the CNT sidewalls provide anchorage points for the ferrocene molecules. An exclusive study of the role of these sites on the electrochemical properties of carbon nanotubes was also performed [172].

Finally, the properties of VA-CNTs can be changed by doping during the nanotube growth itself. The doping of aligned CNTs has been mostly done with nitrogen [173,174] in order to, for example, enhance the field-emission properties [175], but other elements such as boron have also been studied [176]. The strategy is to use a dopant source with the hydrocarbon compounds during the nanotube growth in order to introduce dopant atoms into the carbon networks composing the nanotube walls. Besides, doping during the nanotube growth itself also activates the nanotube sidewalls and increases their reactivity towards further functionalization. Indeed, a correlation between the crystallinity of nanotube walls and the doping content has been highlighted: the increase of doping content allows a weak crystallinity and a higher defect density (this effect is generally well illustrated by Raman spectroscopy where the D-band (1315 cm^{-1}) related to the defects increases with the doping content) [174]. This high density of defects increases the reactivity of the CNTs towards further functionalization.

3.6 Functionalization and CNTs bundling
As mentioned in this review, the functionalization of VA-CNTs has many consequences, actively sought or otherwise. For instance, the tendency that VA-CNTs have to clump together into bundles could be desirable, as in the case of superhydrophobicity/hydrophilicity studies, but in general, it represents a handicap. Indeed, CNT bundling significantly reduces access to the CNT sidewalls and inhibits an effective and uniform functionalization of the tubes. It seems important to include in this review a discussion dedicated to this topic.

CNTs bundling: In 2004, Bico et al. [177] investigated this bundling topic using an original approach: they dunked a brush of parallel elastic lamellae in a perfectly wetting liquid and, after withdrawal of the brush, they observed the formation of hierarchical bundling patterns. They noted that the lamellae aggregation depended on a balance between the lamellae elasticity and the capillary forces. This coalescence process can take place in the VA-CNT films and influence their structures. This point has been discussed by Joseph et al. [178]. Their concern was the understanding of the influence of the roughness of superhydrophobic surfaces on their hydrodynamic characteristics. Toward this goal, they studied superhydrophobic VA-CNT forests coated by a thin gold layer, functionalized with thiol molecules in gas or liquid phase and included into the microchannels. They reported that the gas-phase mode does not affect the CNTs structure while, in contrast, the liquid-phase mode leads to the bundling of the CNTs, modifying thereby the surface roughness (Figure 24). The bundling was associated to
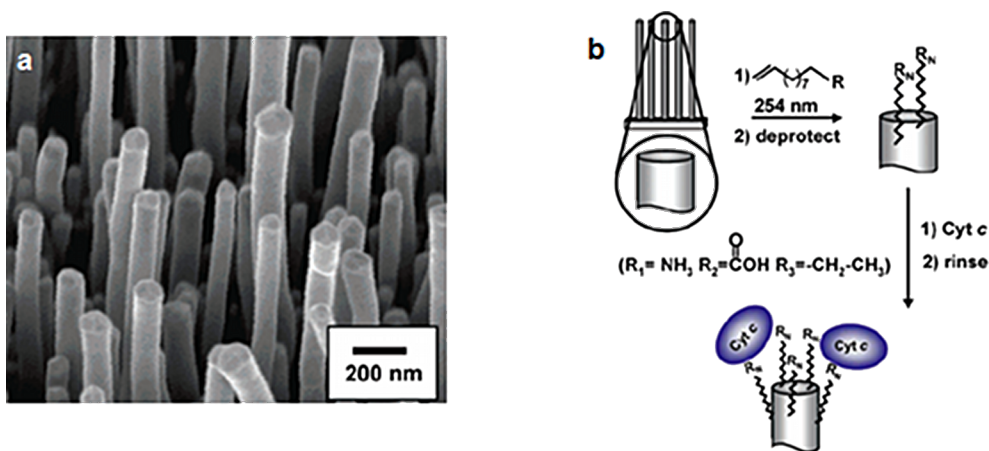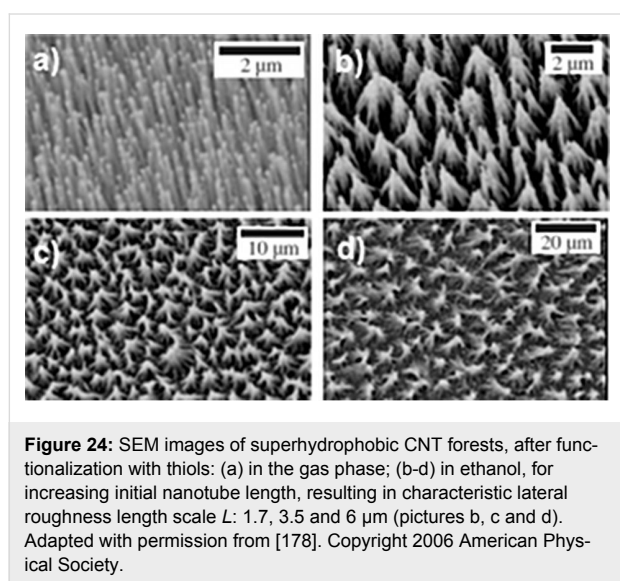

Figure 23: (a) SEM image (taken at a 25° tilt) of a VA-CNFs substrate. (b) Schematic of the functionalization of VA-CNFs with the redox-active protein Cytochrome *c*. Adapted with permission from [169]. Copyright 2006 American Chemical Society.

the capillary adhesion occurring during the evaporative drying of the functionalization solvent (ethanol in this case) in the liquid-phase mode. We can also mention the work of Journet et al. [179]. After Lau et al. in 2003 [131], the superhydrophobicity effect on VA-CNTs forests has also gained their attention. They functionalized such surfaces with the same route as Joseph et al., i.e., through the anchorage of thiol molecules (in the liquid or vapor phase) on a thin gold coating. They inspected the effect of pressure on the contact angle of a water drop on these superhydrophobic surfaces and showed that they are resistant to high excess pressure (>10 kPa), while keeping their low adhesion characteristics.

Figure 24: SEM images of superhydrophobic CNT forests, after functionalization with thiols: (a) in the gas phase; (b-d) in ethanol, for increasing initial nanotube length, resulting in characteristic lateral roughness length scale *L*: 1.7, 3.5 and 6 μm (pictures b, c and d). Adapted with permission from [178]. Copyright 2006 American Physical Society.

Dry gas-phase functionalization: To avoid VA-CNT bundling and obtain a very homogeneous surface functionalization, gas-phase functionalization represents an original and alternative route. In this context, in a recent patent [180], Bismarck et al. proposed a one-step process that has the peculiarity of being carried out in situ, in the growth chamber. The principle is the following [181]: CNTs are submitted to a high-temperature treatment (at 1000 °C for 2 h), before being slowly cooled to room temperature; the thermally activated sample is then exposed to a functional organic reactant in vapor form. With this process, the nanotubes have not been wetted and, hence, do not bundle together. In consequence, the surface functionalization is very homogeneous. Another example of in situ gas-phase functionalization is reported by Lin et al. [182]. The VA-CNT synthesis by chemical vapor deposition (CVD) has the inconvenience of a high growth temperature and few substrate materials available. The solution they proposed consists of the separation of the growth process and the CNT assembly. This new transfer technology is based on the functionalization of VA-CNTs. In comparison to the wet chemical process, this

technology preserves the alignment of CNTs, introduces few defects to the CNTs, and allows patterning, precise length control, and quality control of the samples. The first step is the in situ functionalization of VA-CNTs during their CVD growth. A small amount of Ar is bubbled through H_2O_2 into the furnace chamber during the CVD process. The consequence is the grafting of oxygen-containing compounds onto the sample surface. The second step is the transfer of the functionalized VA-CNT sample onto a novel substrate (metal, polymer or semiconductor substrate) coated by self-assembled monolayers of conjugated thiol molecules on gold surfaces. This transfer technology, characterized by a self-assembled monolayer of conjugated thiol molecules at the interface between the VA-CNTs and the gold surface, is useful for providing both a bonding ligand and the pathway for tunneling or electron transport, and also for phonon transport. Finally, we can also mention the work of Shulga et al. [183]. In 2011, they reported a simple technique to functionalize millimeter-high, aligned carbon nanotubes using nitric acid (HNO_3) vapor at low temperature, leading to the formation of carbonyl and carboxyl groups on the CNTs. According to the process parameters (temperature, exposure time), one can obtain highly uniform functionalization along the CNT sidewalls, preserve the CNT alignment and minimize the CNT destruction.

Conclusion

We have reviewed recent developments on the functionalization of vertically aligned carbon nanotubes. This topic is at the forefront of current scientific research, as demonstrated by the wealth of articles in the literature. Depending on the intended application and required properties, different functionalization of VA-CNT films is possible: uniformly over the nanotubes in their entirety, or selectively for the CNT tips and the CNT sidewalls. Two kinds of functionalization coexist: chemical functionalization and dry chemical functionalization, each method having its advantages and its inconveniences. A large variety of potential applications could be developed in a multitude of fields including electron field emitters, chemical and biological sensors, solar cells, optoelectronic devices, selective nanoporous membranes, self-cleaning films, materials with adaptable-wettability, fuel cells, etc.

Acknowledgements

References

1. Iijima, S. *Nature* **1991,** *354,* 56. doi:10.1038/354056a0
2. Bethune, D. S.; Kiang, C. H.; de Vries, M. S.; Gorman, G.; Savoy, R.; Vazquez, J.; Beyers, R. *Nature* **1993,** *363,* 605. doi:10.1038/363605a0
3. Thess, A.; Lee, R.; Nikolaev, P.; Dai, H.; Petit, P.; Robert, J.; Xu, C.; Lee, Y. H.; Kim, S. G.; Rinzler, A. G.; Colbert, D. T.; Scuseria, G. E.; Tománek, D.; Fischer, J. E.; Smalley, R. E. *Science* **1996,** *273,* 483. doi:10.1126/science.273.5274.483
4. Wilder, J. W. G.; Venema, L. C.; Rinzler, A. G.; Smalley, R. E.; Dekker, C. *Nature* **1998,** *391,* 59. doi:10.1038/34139
5. Wang, X.; Li, Q.; Xie, J.; Jin, Z.; Wang, J.; Li, Y.; Jiang, K.; Fan, S. *Nano Lett.* **2009,** *9,* 3137. doi:10.1021/nl901260b
6. Charlier, J.-C.; Blase, X.; Roche, S. *Rev. Mod. Phys.* **2007,** *79,* 677. doi:10.1103/RevModPhys.79.677
7. Iijima, S.; Brabec, C.; Maiti, A.; Bernholc, J. *J. Chem. Phys.* **1996,** *104,* 2089. doi:10.1063/1.470966
8. Pop, E.; Mann, D.; Wang, Q.; Goodson, K.; Dai, H. *Nano Lett.* **2006,** *6,* 96. doi:10.1021/nl052145f
9. Yu, M.-F.; Lourie, O.; Dyer, M. J.; Moloni, K.; Kelly, T. F.; Ruoff, R. S. *Science* **2000,** *287,* 637. doi:10.1126/science.287.5453.637
10. Treacy, M. M. J.; Ebbesen, T. W.; Gibson, J. M. *Nature* **1996,** *381,* 678. doi:10.1038/381678a0
11. Baughman, R. H.; Zakhidov, A. A.; de Heer, W. A. *Science* **2002,** *297,* 787. doi:10.1126/science.1060928
12. Terrones, M. *Annu. Rev. Mater. Res.* **2003,** *33,* 419. doi:10.1146/annurev.matsci.33.012802.100255
13. Hirsch, A.; Vostrowsky, O. *Top. Curr. Chem.* **2005,** *245,* 193. doi:10.1007/b98169
14. Monthioux, M. *Carbon* **2002,** *40,* 1809. doi:10.1016/S0008-6223(02)00102-1
15. Dujardin, E.; Ebbesen, T. W.; Hiura, H.; Tanigaki, K. *Science* **1994,** *265,* 1850. doi:10.1126/science.265.5180.1850
16. Dai, L. *Polym. Adv. Technol.* **1999,** *10,* 357. doi:10.1002/(SICI)1099-1581(199907)10:7<357::AID-PAT886>3.0.CO;2-9
17. Balasubramanian, K.; Burghard, M. *Small* **2005,** *1,* 180. doi:10.1002/smll.200400118
18. Karousis, N.; Tagmatarchis, N.; Tasis, D. *Chem. Rev.* **2010,** *110,* 5366. doi:10.1021/cr100018g
19. Simmons, J. M.; Nichols, B. M.; Baker, S. E.; Marcus, M. S.; Castellini, O. M.; Lee, C.-S.; Hamers, R. J.; Eriksson, M. A. *J. Phys. Chem. B* **2006,** *110,* 7113. doi:10.1021/jp0548422
20. Okpalugo, T. I. T.; Papakonstantinou, P.; Murphy, H.; Mclaughlin, J.; Brown, N. M. D. *Carbon* **2005,** *43,* 2951. doi:10.1016/j.carbon.2005.06.033
21. Huang, S.; Dai, L. *J. Phys. Chem. B* **2002,** *106,* 3543. doi:10.1021/jp014047y
22. Ruelle, B.; Bittencourt, C.; Dubois, P. *Surface treatment of carbon nanotubes via plasma technology;* Woodhead Publishing Limited: Cambridge, 2011.
23. Li, W. Z.; Xie, S. S.; Qian, L. X.; Chang, B. H.; Zou, B. S.; Zhou, W. Y.; Zhao, R. A.; Wang, G. *Science* **1996,** *274,* 1701. doi:10.1126/science.274.5293.1701
24. Ren, Z. F.; Huang, Z. P.; Xu, J. W.; Wang, J. H.; Bush, P.; Siegal, M. P.; Provencio, P. N. *Science* **1998,** *282,* 1105. doi:10.1126/science.282.5391.1105
25. Fan, S.; Chapline, M. G.; Franklin, N. R.; Tombler, T. W.; Cassell, A. M.; Dai, H. *Science* **1999,** *283,* 512. doi:10.1126/science.283.5401.512
26. Hata, K.; Futaba, D. N.; Mizuno, K.; Namai, T.; Yumura, M.; Iijima, S. *Science* **2004,** *306,* 1362. doi:10.1126/science.1104962
27. Yamada, T.; Namai, T.; Hata, K.; Futaba, D. N.; Mizuno, K.; Fan, J.; Yudasaka, M.; Yumura, M.; Iijima, S. *Nat. Nanotechnol.* **2006,** *1,* 131. doi:10.1038/nnano.2006.95
28. Belkadi, L.; Hibert, E.; Patel, S.; Porterat, D.; Pinault, M.; Boulanger, P.; Mayne, M.; Reynaud, C. to be published.
29. Sen, R.; Govindaraj, A.; Rao, C. N. R. *Chem. Phys. Lett.* **1997,** *267,* 276. doi:10.1016/S0009-2614(97)00080-8
30. Rao, C. N. R.; Sen, R. *Chem. Commun.* **1998,** 1525. doi:10.1039/a802258e
31. Huang, S.; Cai, X.; Du, C.; Liu, J. *J. Phys. Chem. B* **2003,** *107,* 13251. doi:10.1021/jp0364708
32. Chen, Y.; Yu, J. *Carbon* **2005,** *43,* 3181. doi:10.1016/j.carbon.2005.07.015
33. Talapatra, S.; Kar, S.; Pal, S. K.; Vajtai, R.; Ci, L.; Victor, P.; Shaijumon, M. M.; Kaur, S.; Nalamasu, O.; Ajayan, P. M. *Nat. Nanotechnol.* **2006,** *1,* 112. doi:10.1038/nnano.2006.56
34. Yen, J. H.; Leu, I. C.; Lin, C. C.; Hon, M. H. *Diamond Relat. Mater.* **2004,** *13,* 1237. doi:10.1016/j.diamond.2003.11.045
35. Lucas, S.; Colomer, J.-F.; Bittencourt, C.; Moskovkin, P.; Moreau, N. *Appl. Phys. A* **2010,** *99,* 125. doi:10.1007/s00339-010-5566-7
36. Kim, D. Y.; Yoo, J.-B.; Han, I. T.; Kim, H. J.; Kim, H. J.; Jung, J. E.; Jin, Y. W.; Kim, J. M.; Chin, K.-H. *Diamond Relat. Mater.* **2005,** *14,* 2084. doi:10.1016/j.diamond.2005.08.017
37. Murakami, Y.; Chiashi, S.; Miyauchi, Y.; Hu, M.; Ogura, M.; Okubo, T.; Maruyama, S. *Chem. Phys. Lett.* **2004,** *385,* 298. doi:10.1016/j.cplett.2003.12.095
38. Cho, Y.-S.; Choi, G.-S.; Hong, S.-Y.; Kim, D. *J. Cryst. Growth* **2002,** *243,* 224. doi:10.1016/S0022-0248(02)01496-3
39. Terrado, E.; Redrado, M.; Muñoz, E.; Maser, W. K.; Benito, A. M.; Martínez, M. T. *Diamond Relat. Mater.* **2006,** *15,* 1059. doi:10.1016/j.diamond.2005.10.071
40. Kyotani, T.; Tsai, L.-f.; Tomita, A. *Chem. Mater.* **1996,** *8,* 2109. doi:10.1021/cm960063+
41. Amelinckx, S.; Zhang, X. B.; Bernaerts, D.; Zhang, X. F.; Ivanov, V.; Nagy, J. B. *Science* **1994,** *265,* 635. doi:10.1126/science.265.5172.635
42. Täschner, C.; Pácal, F.; Leonhardt, A.; Spatenka, P.; Bartsch, K.; Graff, A.; Kaltofen, R. *Surf. Coat. Technol.* **2003,** *174–175,* 81. doi:10.1016/S0257-8972(03)00712-6
43. Yabe, Y.; Ohtake, Y.; Ishitobi, T.; Show, Y.; Izumi, T.; Yamauchi, H. *Diamond Relat. Mater.* **2004,** *13,* 1292. doi:10.1016/j.diamond.2003.11.067
44. Lee, Y. T.; Park, J.; Choi, Y. S.; Ryu, H.; Lee, H. J. *J. Phys. Chem. B* **2002,** *106,* 7614. doi:10.1021/jp020488l
45. Ducati, C.; Alexandrou, I.; Chhowalla, M.; Amaratunga, G. A. J.; Robertson, J. *J. Appl. Phys.* **2002,** *92,* 3299. doi:10.1063/1.1499746
46. Hofmann, S.; Ducati, C.; Kleinsorge, B.; Robertson, J. *Appl. Phys. Lett.* **2003,** *83,* 4661. doi:10.1063/1.1630167
47. Hofmann, S.; Csányi, G.; Ferrari, A. C.; Payne, M. C.; Robertson, J. *Phys. Rev. Lett.* **2005,** *95,* 036101. doi:10.1103/PhysRevLett.95.036101
48. Choi, Y. C.; Shin, Y. M.; Lee, Y. H.; Lee, B. S.; Park, G.-S.; Choi, W. B.; Lee, N. S.; Kim, J. M. *Appl. Phys. Lett.* **2000,** *76,* 2367. doi:10.1063/1.126348
49. Gohier, A.; Ewels, C. P.; Minea, T. M.; Djouadi, M. A. *Carbon* **2008,** *46,* 1331. doi:10.1016/j.carbon.2008.05.016

50. Yamada, T.; Maigne, A.; Yudasaka, M.; Mizuno, K.; Futaba, D. N.; Yumura, M.; Iijima, S.; Hata, K. *Nano Lett.* **2008,** *8,* 4288. doi:10.1021/nl801981m

51. Sakurai, S.; Nishino, H.; Futaba, D. N.; Yasuda, S.; Yamada, T.; Maigne, A.; Matsuo, Y.; Nakamura, E.; Yumura, M.; Hata, K. *J. Am. Chem. Soc.* **2012,** *134,* 2148. doi:10.1021/ja208706c

52. Maruyama, S.; Einarsson, E.; Murakami, Y.; Edamura, T. *Chem. Phys. Lett.* **2005,** *403,* 320. doi:10.1016/j.cplett.2005.01.031

53. Zhu, Y.; Li, L.; Zhang, C.; Casillas, G.; Sun, Z.; Yan, Z.; Ruan, G.; Peng, Z.; Raji, A.-R. O.; Kittrell, C.; Hauge, R. H.; Tour, J. M. *Nat. Commun.* **2012,** *3,* 1225. doi:10.1038/ncomms2234

54. Seah, C.-M.; Chai, S.-P.; Mohamed, A. R. *Carbon* **2011,** *49,* 4613. doi:10.1016/j.carbon.2011.06.090

55. Yang, Y.; Huang, S.; He, H.; Mau, A. W. H.; Dai, L. *J. Am. Chem. Soc.* **1999,** *121,* 10832. doi:10.1021/ja992945q

56. Huang, S.; Mau, A. W. H. *Appl. Phys. Lett.* **2003,** *82,* 796. doi:10.1063/1.1541939

57. Huang, S.; Mau, A. W. H.; Turney, T. W.; White, P. A.; Dai, L. *J. Phys. Chem. B* **2000,** *104,* 2193. doi:10.1021/jp994152w

58. Ren, Z. F.; Huang, Z. P.; Wang, D. Z.; Wen, J. G.; Xu, J. W.; Wang, J. H.; Calvet, L. E.; Chen, J.; Klemic, J. F.; Reed, M. A. *Appl. Phys. Lett.* **1999,** *75,* 1086. doi:10.1063/1.124605

59. Cassell, A. M.; Franklin, N. R.; Tombler, T. W.; Chan, E. M.; Han, J.; Dai, H. *J. Am. Chem. Soc.* **1999,** *121,* 7975. doi:10.1021/ja992083t

60. Kind, H.; Bonard, J.-M.; Forró, L.; Kern, K. *Langmuir* **2000,** *16,* 6877. doi:10.1021/la0001880

61. Zheng, G.; Zhu, H.; Luo, Q.; Zhou, Y.; Zhao, D. *Chem. Mater.* **2001,** *13,* 2240. doi:10.1021/cm0009726

62. Chen, Q.; Dai, L. *Appl. Phys. Lett.* **2000,** *76,* 2719. doi:10.1063/1.126454

63. Teo, K. B. K.; Chhowalla, M.; Amaratunga, G. A. J.; Milne, W. I.; Hasko, D. G.; Pirio, G.; Legagneux, P.; Wyczisk, F.; Pribat, D. *Appl. Phys. Lett.* **2001,** *79,* 1534. doi:10.1063/1.1400085

64. Ge, L.; Sethi, S.; Ci, L.; Ajayan, P. M.; Dhinojwala, A. *Proc. Natl. Acad. Sci. U. S. A.* **2007,** *104,* 10792. doi:10.1073/pnas.0703505104

65. Qu, L.; Dai, L.; Stone, M.; Xia, Z.; Wang, Z. L. *Science* **2008,** *322,* 238. doi:10.1126/science.1159503

66. Sethi, S.; Ge, L.; Ci, L.; Ajayan, P. M.; Dhinojwala, A. *Nano Lett.* **2008,** *8,* 822. doi:10.1021/nl0727765

67. Chen, Q.; Dai, L. *J. Nanosci. Nanotechnol.* **2001,** *1,* 43. doi:10.1166/jnn.2001.003

68. Wei, B. Q.; Vajtai, R.; Jung, Y.; Ward, J.; Zhang, R.; Ramanath, G.; Ajayan, P. M. *Chem. Mater.* **2003,** *15,* 1598. doi:10.1021/cm0202815

69. Wei, B. Q.; Vajtai, R.; Jung, Y.; Ward, J.; Zhang, R.; Ramanath, G.; Ajayan, P. M. *Nature* **2002,** *416,* 495. doi:10.1038/416495a

70. Yang, J.; Dai, L.; Vaia, R. A. *J. Phys. Chem. B* **2003,** *107,* 12387. doi:10.1021/jp036191k

71. Patil, A.; Toshiyuki, O.; Buldum, A.; Dai, L. *Appl. Phys. Lett.* **2006,** *89,* 103103. doi:10.1063/1.2345253

72. Qu, L.; Dai, L. *J. Mater. Chem.* **2007,** *17,* 3401. doi:10.1039/b703046k

73. Lim, K. Y.; Sow, C. H.; Lin, J.; Cheong, F. C.; Shen, Z. X.; Thong, J. T. L.; Chin, K. C.; Wee, A. T. S. *Adv. Mater.* **2003,** *15,* 300. doi:10.1002/adma.200390072

74. Cheong, F. C.; Lim, K. Y.; Sow, C. H.; Lin, J.; Ong, C. K. *Nanotechnology* **2003,** *14,* 433. doi:10.1088/0957-4484/14/4/305

75. Elmer, J. W.; Yaglioglu, O.; Schaeffer, R. D.; Kardos, G.; Derkach, O. *Carbon* **2012,** *50,* 4114. doi:10.1016/j.carbon.2012.04.059

76. Khabashesku, V. N. *Russ. Chem. Rev.* **2011,** *80,* 705. doi:10.1070/RC2011v080n08ABEH004232

77. Dickrell, P. L.; Pal, S. K.; Bourne, G. R.; Muratore, C.; Voevodin, A. A.; Ajayan, P. M.; Schadler, L. S.; Sawyer, W. G. *Tribol. Lett.* **2006,** *24,* 85. doi:10.1007/s11249-006-9162-0

78. Ler, J. G. Q.; Hao, Y.; Thong, J. T. L. *Carbon* **2007,** *45,* 2737. doi:10.1016/j.carbon.2007.09.038

79. Qi, H. J.; Teo, K. B. K.; Lau, K. K. S.; Boyce, M. C.; Milne, W. I.; Robertson, J.; Gleason, K. K. *J. Mech. Phys. Solids* **2003,** *51,* 2213. doi:10.1016/j.jmps.2003.09.015

80. Barber, A. H.; Cohen, S. R.; Wagner, H. D. *Phys. Rev. Lett.* **2004,** *92,* 186103. doi:10.1103/PhysRevLett.92.186103

81. Talin, A. A.; Dean, K. A.; Jaskie, J. E. *Solid-State Electron.* **2001,** *45,* 963. doi:10.1016/S0038-1101(00)00279-3

82. Bonard, J.-M.; Kind, H.; Stöckli, T.; Nilsson, L.-O. *Solid-State Electron.* **2001,** *45,* 893. doi:10.1016/S0038-1101(00)00213-6

83. Shiomi, H. *Jpn. J. Appl. Phys., Part 1* **1997,** *36,* 7745. doi:10.1143/JJAP.36.7745

84. Lai, S. H.; Huang, K. P.; Pan, Y. M.; Chen, Y. L.; Chan, L. H.; Lin, P.; Shih, H. C. *Chem. Phys. Lett.* **2003,** *382,* 567. doi:10.1016/j.cplett.2003.10.106

85. Zhang, W.; Guérin, K.; Dubois, M.; El Fawal, Z.; Ivanov, D. A.; Vidal, L.; Hamwi, A. *Carbon* **2008,** *46,* 1010. doi:10.1016/j.carbon.2008.02.029

86. Mickelson, E. T.; Huffman, C. B.; Rinzler, A. G.; Smalley, R. E.; Hauge, R. H.; Margrave, J. L. *Chem. Phys. Lett.* **1998,** *296,* 188. doi:10.1016/S0009-2614(98)01026-4

87. Chung, S. J.; Hoon, S.; Jang, L. J. *Thin Solid Films* **2001,** *383,* 73. doi:10.1016/S0040-6090(00)01617-5

88. Zhu, Y. W.; Cheong, F. C.; Yu, T.; Xu, X. J.; Lim, C. T.; Thong, J. T. L.; Shen, Z. X.; Ong, C. K.; Liu, Y. J.; Wee, A. T. S.; Sow, C. H. *Carbon* **2005,** *43,* 395. doi:10.1016/j.carbon.2004.09.029

89. Pavese, M.; Musso, S.; Bianco, S.; Giorcelli, M.; Pugno, N. *J. Phys.: Condens. Matter* **2008,** *20,* 474206. doi:10.1088/0953-8984/20/47/474206

90. Ramos, S. C.; Vasconcelos, G.; Antunes, E. F.; Lobo, A. O.; Trava-Airoldi, V. J.; Corat, E. J. *Diamond Relat. Mater.* **2010,** *19,* 752. doi:10.1016/j.diamond.2010.01.044

91. Lobo, A. O.; Ramos, S. C.; Antunes, E. F.; Marciano, F. R.; Trava-Airoldi, V. J.; Corat, E. J. *Mater. Lett.* **2012,** *70,* 89. doi:10.1016/j.matlet.2011.11.071

92. Martin, C. R.; Kohli, P. *Nature* **2003,** *2,* 29. doi:10.1038/nrd988

93. Cheung, C. L.; Kurtz, A.; Park, H.; Lieber, C. M. *J. Phys. Chem. B* **2002,** *106,* 2429. doi:10.1021/jp0142278

94. Wang, H.; Xu, Z.; Eres, G. *Appl. Phys. Lett.* **2006,** *88,* 213111. doi:10.1063/1.2206152

95. Nessim, G. D.; Hart, A. J.; Kim, J. S.; Acquaviva, D.; Oh, J.; Morgan, C. D.; Seita, M.; Leib, J. S.; Thompson, C. V. *Nano Lett.* **2008,** *8,* 3587. doi:10.1021/nl801437c

96. Majumder, M.; Chopra, N.; Hinds, B. J. *J. Am. Chem. Soc.* **2005,** *127,* 9062. doi:10.1021/ja043013b

97. Cellot, G.; Cilia, E.; Coipollone, S.; Rancic, V.; Sucapane, A.; Giordani, S.; Gambazzi, L.; Markram, H.; Grandolfo, M.; Scaini, D.; Gelain, F.; Casalis, L.; Prato, M.; Giugliano, M.; Ballerini, L. *Nat. Nanotechnol.* **2009,** *4,* 126. doi:10.1038/nnano.2008.374

98. Kim, S.; Kim, H.-J.; Lee, H. R.; Song, J.-H.; Yi, S. N.; Ha, D. H. *J. Phys. D: Appl. Phys.* **2010,** *43,* 305402. doi:10.1088/0022-3727/43/30/305402

99. Ye, J.-S.; Wen, Y.; Zhang, W.-D.; Ciui, H. F.; Xu, G. Q.; Sheu, F.-S. *Nanotechnology* **2006,** *17,* 3994. doi:10.1088/0957-4484/17/15/065

100. Brown, B.; Parker, C. B.; Stoner, B. R.; Grill, W. M.; Glass, J. T. *J. Phys. Chem. C* **2012,** *116,* 19526. doi:10.1021/jp304419a

101. Lu, W.; Goering, A.; Qu, L.; Dai, L. *Phys. Chem. Chem. Phys.* **2012,** *14,* 12099. doi:10.1039/c2cp40726d

102. Bittencourt, C.; Navio, C.; Nicolay, A.; Ruelle, B.; Godfroid, T.; Snyders, R.; Colomer, J.-F.; Lagos, M. J.; Ke, X.; Van Tendeloo, G.; Suarez-Martinez, I.; Ewels, C. P. *J. Phys. Chem. C* **2011,** *115,* 20412. doi:10.1021/jp2057699

103. Colomer, J.-F.; Ruelle, B.; Moreau, N.; Lucas, S.; Snyders, R.; Godfroid, T.; Navio, C.; Bittencourt, C. *Surf. Coat. Technol.* **2011,** *205,* S592. doi:10.1016/j.surfcoat.2011.03.040

104. Ajayan, P. M.; Ebbesen, T. W.; Ichihashi, T.; Iijima, S.; Tanigaki, K.; Hiura, H. *Nature* **1993,** *362,* 522. doi:10.1038/362522a0

105. Colbert, D. T.; Zhang, J.; McClure, S. M.; Nikolaev, P.; Chen, Z.; Hafner, J. H.; Owens, D. W.; Kotula, P. G.; Carter, C. B.; Weaver, J. H.; Rinzler, A. G.; Smalley, R. E. *Science* **1994,** *266,* 1218. doi:10.1126/science.266.5188.1218

106. Zhao, B.; Zhang, L.; Wang, X.; Yang, J. *Carbon* **2012,** *50,* 2710. doi:10.1016/j.carbon.2012.02.029

107. Dai, L.; Mau, A. W. H. *Adv. Mater.* **2001,** *13,* 899. doi:10.1002/1521-4095(200107)13:12/13<899::AID-ADMA899>3.0.CO;2-G

108. Hussain, S.; Amade, R.; Jover, E.; Bertran, E. *Nanotechnology* **2012,** *23,* 385604. doi:10.1088/0957-4484/23/38/385604

109. Lai, Y.-H.; Lian, H.-B.; Lee, K.-Y. *Diamond Relat. Mater.* **2009,** *18,* 544. doi:10.1016/j.diamond.2008.10.011

110. Qin, Y.; Hu, M. *Appl. Surf. Sci.* **2008,** *254,* 1757. doi:10.1016/j.apsusc.2007.07.174

111. Steele, B. C. H.; Heinzel, A. *Nature* **2001,** *414,* 345. doi:10.1038/35104620

112. Grove, W. R. *Phil. Mag. Ser. 3* **1839,** *14,* 127. doi:10.1080/14786443908649684

113. Stamenkovic, V. R.; Fowler, B.; Mun, B. S.; Wang, G.; Ross, P. N.; Lucas, C. A.; Marković, N. M. *Science* **2007,** *315,* 493. doi:10.1126/science.1135941

114. Zhang, J.; Vukmirovic, M. B.; Xu, Y.; Mavrikakis, M.; Adzic, R. R. *Angew. Chem., Int. Ed.* **2005,** *44,* 2132. doi:10.1002/anie.200462335

115. Yu, X.; Ye, S. *J. Power Sources* **2007,** *172,* 145. doi:10.1016/j.jpowsour.2007.07.048

116. Gong, K.; Du, F.; Xia, Z.; Durstock, M.; Dai, L. *Science* **2009,** *323,* 760. doi:10.1126/science.1168049

117. Yang, J.; Liu, D.-J.; Kariuki, N. N.; Chen, L. X. *Chem. Commun.* **2008,** 329. doi:10.1039/B713096A

118. Wang, S.; Yu, D.; Dai, L. *J. Am. Chem. Soc.* **2011,** *133,* 5182. doi:10.1021/ja1112904

119. Qu, L.; Dai, L.; Osawa, E. *J. Am. Chem. Soc.* **2006,** *128,* 5523. doi:10.1021/ja060296u

120. Yang, Y.; Qu, L.; Dai, L.; Kang, T.-S.; Durstock, M. *Adv. Mater.* **2007,** *19,* 1239. doi:10.1002/adma.200602181

121. Soin, N.; Roy, S. S.; Karlsson, L.; McLaughlin, J. A. *Diamond Relat. Mater.* **2010,** *19,* 595. doi:10.1016/j.diamond.2009.10.029

122. Bittencourt, C.; Hecq, M.; Felten, A.; Pireaux, J. J.; Ghijsen, J.; Felicissimo, M. P.; Rudolf, P.; Drube, W.; Ke, X.; Van Tendeloo, G. *Chem. Phys. Lett.* **2008,** *462,* 260. doi:10.1016/j.cplett.2008.07.082

123. Caillard, A.; Charles, C.; Boswell, R.; Brault, P.; Coutanceau, C. *Appl. Phys. Lett.* **2007,** *90,* 223119. doi:10.1063/1.2745210

124. Dameron, A. A.; Pylypenko, S.; Bult, J. B.; Neyerlin, K. C.; Engtrakul, C.; Bochert, C.; Leong, G. J.; Frisco, S. L.; Simpson, L.; Dinh, H. N.; Pivovar, B. *Appl. Surf. Sci.* **2012,** *258,* 5212. doi:10.1016/j.apsusc.2012.01.139

125. Patil, A.; Vaia, R.; Dai, L. *Synth. Met.* **2005,** *154,* 229. doi:10.1016/j.synthmet.2005.07.058

126. Gao, M.; Huang, S.; Dai, L.; Wallace, G.; Gao, R.; Wang, Z. *Angew. Chem., Int. Ed.* **2000,** *39,* 3664. doi:10.1002/1521-3773(20001016)39:20<3664::AID-ANIE3664>3.0.CO;2-Y

127. Soundarrajan, P.; Patil, A.; Dai, L. *J. Vac. Sci. Technol., A* **2003,** *21,* 1198. doi:10.1116/1.1569926

128. Gaarenstroom, S. W.; Balogh, M. P.; Militello, M. C.; Waldo, R. A.; Wong, C. A.; Kelly, N. A.; Gibson, T. L.; Kundrat, M. D. *Surf. Interface Anal.* **2005,** *37,* 385. doi:10.1002/sia.2010

129. Peng, H. *J. Am. Chem. Soc.* **2008,** *130,* 42. doi:10.1021/ja078267m

130. Chen, Q.; Dai, L.; Gao, M.; Huang, S.; Mau, A. *J. Phys. Chem. B* **2001,** *105,* 618. doi:10.1021/jp003385g

131. Lau, K. K. S.; Bico, J.; Teo, K. B. K.; Chhowalla, M.; Amaratunga, G. A. J.; Milne, W. I.; McKinley, G. H.; Gleason, K. K. *Nano Lett.* **2003,** *3,* 1701. doi:10.1021/nl034704t

132. Barthlott, W.; Neinhuis, C. *Planta* **1997,** *202,* 1. doi:10.1007/s004250050096

133. Sihn, S.; Ganguli, S.; Roy, A. K.; Qu, L.; Dai, L. *Compos. Sci. Technol.* **2008,** *68,* 658. doi:10.1016/j.compscitech.2007.09.016

134. Huang, H.; Liu, C. H.; Wu, Y.; Fan, S. *Adv. Mater.* **2005,** *17,* 1652. doi:10.1002/adma.200500467

135. Lin, W.; Moon, K.-S.; Wong, C. P. *Adv. Mater.* **2009,** *21,* 2421. doi:10.1002/adma.200803548

136. Ajayan, P. M.; Schadler, L. S.; Giannaris, C.; Rubio, A. *Adv. Mater.* **2000,** *12,* 750. doi:10.1002/(SICI)1521-4095(200005)12:10<750::AID-ADMA750>3.0.CO;2-6

137. Nguyen, C. V.; Delzeit, L.; Cassell, A. M.; Li, J.; Han, J.; Meyyappan, M. *Nano Lett.* **2002,** *2,* 1079. doi:10.1021/nl025689f

138. Hinds, B. J.; Chopra, N.; Rantell, T.; Andrews, R.; Gavalas, V.; Bachas, L. G. *Science* **2004,** *303,* 62. doi:10.1126/science.1092048

139. Chopra, N.; Majumder, M.; Hinds, B. J. *Adv. Funct. Mater.* **2005,** *15,* 858. doi:10.1002/adfm.200400399

140. Feng, W.; Bai, X. D.; Lian, Y. Q.; Liang, J.; Wang, X. G.; Yoshino, K. *Carbon* **2003,** *41,* 1551. doi:10.1016/S0008-6223(03)00078-2

141. Huang, J. *Pure Appl. Chem.* **2006,** *78,* 15. doi:10.1351/pac200678010015

142. Raravikar, N. R.; Schadler, L. S.; Vijayaraghavan, A.; Zhao, Y.; Wei, B.; Ajayan, P. M. *Chem. Mater.* **2005,** *17,* 974. doi:10.1021/cm0485254

143. Jung, Y. J.; Kar, S.; Talapatra, S.; Soldano, C.; Viswanathan, G.; Li, X.; Yao, Z.; Ou, F. S.; Avadhanula, A.; Vajtai, R.; Curran, S.; Nalamasu, O.; Ajayan, P. M. *Nano Lett.* **2006,** *6,* 413. doi:10.1021/nl052238x

144. Qu, L.; Dai, L. *Chem. Commun.* **2007,** 3859. doi:10.1039/B707698C

145. Peng, Q.; Qu, L.; Dai, L.; Park, K.; Vaia, R. A. *ACS Nano* **2008,** *2,* 1833. doi:10.1021/nn8002532

146. Lee, K. M.; Li, L.; Dai, L. *J. Am. Chem. Soc.* **2005,** *127,* 4122. doi:10.1021/ja0423670

147. Wei, C.; Dai, L.; Roy, A.; Tolle, T. B. *J. Am. Chem. Soc.* **2006,** *128,* 1412. doi:10.1021/ja0570335

148. Kong, J.; Franklin, N. R.; Zhou, C.; Chapline, M. G.; Peng, S.; Cho, K.; Dai, H. *Science* **2000,** *287,* 622. doi:10.1126/science.287.5453.622

149. Collins, P. G.; Bradley, K.; Ishigami, M.; Zettl, A. *Science* **2000,** *287,* 1801. doi:10.1126/science.287.5459.1801

150. Snow, E. S.; Perkins, F. K.; Houser, E. J.; Badescu, S. C.; Reinecke, T. L. *Science* **2005,** *307,* 1942. doi:10.1126/science.1109128

151. Chen, W.; Qu, L.; Chang, D.; Dai, L.; Ganguli, S.; Roy, A. *Chem. Commun.* **2008,** 163. doi:10.1039/B715079B

152. Wardle, B. L.; Saito, D. S.; García, E. J.; Hart, A. J.; Guzmán de Villoria, R.; Verploegen, E. A. *Adv. Mater.* **2008,** *20,* 2707. doi:10.1002/adma.200800295

153. Noy, A.; Park, H. G.; Fornasiero, F.; Holt, J. K.; Grigoropoulos, C. P.; Bakajin, O. *Nano Today* **2007,** *2,* 22. doi:10.1016/S1748-0132(07)70170-6

154. Van der Bruggen, B. *ISRN Nanotechnol.* **2012,** *2012,* 693485. doi:10.5402/2012/693485

155. He, P.; Shi, G.; Lian, J.; Wang, L. M.; Ewing, R. C.; van Ooij, W.; Li, W. Z.; Ren, Z. F. *Appl. Phys. Lett.* **2005,** *86,* 043107. doi:10.1063/1.1846957

156. Ye, Y.; Mao, Y.; Wang, F.; Lu, H.; Qu, L.; Dai, L. *J. Mater. Chem.* **2011,** *21,* 837. doi:10.1039/c0jm02506b

157. MacDonald, T.; Gibson, C. T.; Constantopoulos, K.; Shapter, J. G.; Ellis, A. V. *Appl. Surf. Sci.* **2012,** *258,* 2836. doi:10.1016/j.apsusc.2011.10.144

158. Yu, J.; Shapter, J. G.; Quinton, J. S.; Johnston, M. R.; Beattie, D. A. *Phys. Chem. Chem. Phys.* **2007,** *9,* 510. doi:10.1039/b615096a

159. Dwyer, C.; Guthold, M.; Falvo, M.; Washburn, S.; Superfine, R.; Erie, D. *Nanotechnology* **2002,** *13,* 601. doi:10.1088/0957-4484/13/5/311

160. Williams, K. A.; Veenhuizen, P. T. M.; de la Torre, B. G.; Eritja, R.; Dekker, C. *Nature* **2002,** *420,* 761. doi:10.1038/420761a

161. Li, J.; Stevens, R.; Delzeit, L.; Ng, H. T.; Cassell, A.; Han, J.; Meyyappan, M. *Appl. Phys. Lett.* **2002,** *81,* 910. doi:10.1063/1.1496494

162. Li, J.; Ng, H. T.; Cassell, A.; Fan, W.; Chen, H.; Ye, Q.; Koehne, J.; Han, J.; Meyyappan, M. *Nano Lett.* **2003,** *3,* 597. doi:10.1021/nl0340677

163. Gooding, J. J.; Wibowo, R.; Liu, J.; Yang, W.; Losic, D.; Orbons, S.; Mearns, F. J.; Shapter, J. G.; Hibbert, D. B. *J. Am. Chem. Soc.* **2003,** *125,* 9006. doi:10.1021/ja035722f

164. Moghaddam, M. J.; Taylor, S.; Gao, M.; Huang, S.; Dai, L.; McCall, M. J. *Nano Lett.* **2004,** *4,* 89. doi:10.1021/nl034915y

165. He, P.; Dai, L. *Chem. Commun.* **2004,** 348. doi:10.1039/b313030b

166. Lin, Y.; Lu, F.; Tu, Y.; Ren, Z. *Nano Lett.* **2004,** *4,* 191. doi:10.1021/nl0347233

167. Pandey, A.; Prasad, A.; Moscatello, J.; Yap, Y. K. *Mater. Res. Soc. Symp. Proc.* **2009,** *1204.* doi:10.1557/PROC-1204-K13-05

168. McKnight, T. E.; Melechko, A. V.; Hensley, D. K.; Mann, D. G. J.; Griffin, G. D.; Simpson, M. L. *Nano Lett.* **2004,** *4,* 1213. doi:10.1021/nl049504b

169. Baker, S. E.; Colavita, P. E.; Tse, K.-Y.; Hamers, R. J. *Chem. Mater.* **2006,** *18,* 4415. doi:10.1021/cm0609000

170. Landis, E. C.; Hamers, R. J. *J. Phys. Chem. C* **2008,** *112,* 16910. doi:10.1021/jp806173d

171. Landis, E. C.; Hamers, R. J. *Chem. Mater.* **2009,** *21,* 724. doi:10.1021/cm802869b

172. Landis, E. C.; Klein, K. L.; Liao, A.; Pop, E.; Hensley, D. K.; Melechko, A. V.; Hamers, R. J. *Chem. Mater.* **2010,** *22,* 2357. doi:10.1021/cm9036132

173. Lee, Y. T.; Kim, N. S.; Bae, S. Y.; Park, J.; Yu, S.-C.; Ryu, H.; Lee, H. J. *J. Phys. Chem. B* **2003,** *107,* 12958. doi:10.1021/jp0274536

174. Liu, H.; Zhang, Y.; Li, R.; Sun, X.; Désilets, S.; Abou-Rachid, M.; Jaidann, M.; Lussier, L.-S. *Carbon* **2010,** *48,* 1498. doi:10.1016/j.carbon.2009.12.045

175. Cui, T.; Lv, R.; Kang, F.; Hu, Q.; Gu, J.; Wang, K.; Wu, D. *Nanoscale Res. Lett.* **2010,** *5,* 941. doi:10.1007/s11671-010-9586-1

176. Chen, C. F.; Tsai, C. L.; Lin, C. L. *Diamond Relat. Mater.* **2003,** *12,* 1500. doi:10.1016/S0925-9635(03)00181-X

177. Bico, J.; Roman, B.; Moulin, L.; Boudaoud, A. *Nature* **2004,** *432,* 690. doi:10.1038/432690a

178. Joseph, P.; Cottin-Bizonne, C.; Benoît, J.-M.; Ybert, C.; Journet, C.; Tabeling, P.; Bocquet, L. *Phys. Rev. Lett.* **2006,** *97,* 156104. doi:10.1103/PhysRevLett.97.156104

179. Journet, C.; Moulinet, S.; Ybert, C.; Purcell, S. T.; Bocquet, L. *EPL* **2005,** *71,* 104. doi:10.1209/epl/i2005-10068-4

180. Bismarck, A.; Shaffer, M. S. P.; Menzel, R.; Tran, M. Q.; Menner, A. Process for the production of a functionalised carbon nanomaterial. U.S. Pat. Appl. 2011/0245384 A1, Oct 6, 2011.

181. Menzel, R.; Tran, M. Q.; Menner, A.; Kay, C. W. M.; Bismarck, A.; Shaffer, M. S. P. *Chem. Sci.* **2010,** *1,* 603. doi:10.1039/c0sc00287a

182. Lin, W.; Xiu, Y.; Jiang, H.; Zhang, R.; Hildreth, O.; Moon, K.-S.; Wong, C. P. *J. Am. Chem. Soc.* **2008,** *130,* 9636. doi:10.1021/ja802142g

183. Shulga, E.; Pohako, K.; Treshchalov, A.; Joost, U.; Kisand, V.; Kink, I. *Micro Nano Lett.* **2011,** *6,* 704. doi:10.1049/mnl.2011.0357

Near-field effects and energy transfer in hybrid metal-oxide nanostructures

Ulrich Herr[*1], Barat Achinuq[1], Cahit Benel[1], Giorgos Papageorgiou[1], Manuel Goncalves[2], Johannes Boneberg[3], Paul Leiderer[3], Paul Ziemann[4], Peter Marek[5] and Horst Hahn[5]

Full Research Paper

Address:
[1]Institute for Micro- and Nanomaterials, Ulm University, Albert-Einstein-Allee 47, 89081 Ulm,Germany, [2]Institut für Experimentelle Physik, Ulm University, Albert-Einstein-Allee 11, 89069 Ulm, Germany, [3]Fachbereich Physik, Universität Konstanz, Universitätsstraße 10. 78457 Konstanz, Germany, [4]Institut für Festkörperphysik,Universität Ulm, Albert-Einstein-Allee 11, 89069 Ulm, Germany and [5]Institut für Nanotechnologie, Karlsruhe Institute of Technology, Hermann-von-Helmholtz-Platz 1,76344 Eggenstein-Leopoldshafen, Germany

Email:
Ulrich Herr[*] - ulrich.herr@uni-ulm.de

* Corresponding author

Abstract

One of the big challenges of the 21st century is the utilization of nanotechnology for energy technology. Nanoscale structures may provide novel functionality, which has been demonstrated most convincingly by successful applications such as dye-sensitized solar cells introduced by M. Grätzel. Applications in energy technology are based on the transfer and conversion of energy. Following the example of photosynthesis, this requires a combination of light harvesting, transfer of energy to a reaction center, and conversion to other forms of energy by charge separation and transfer. This may be achieved by utilizing hybrid nanostructures, which combine metallic and nonmetallic components. Metallic nanostructures can interact strongly with light. Plasmonic excitations of such structures can cause local enhancement of the electrical field, which has been utilized in spectroscopy for many years. On the other hand, the excited states in metallic structures decay over very short lifetimes. Longer lifetimes of excited states occur in nonmetallic nanostructures, which makes them attractive for further energy transfer before recombination or relaxation sets in. Therefore, the combination of metallic nanostructures with nonmetallic materials is of great interest. We report investigations of hybrid nanostructured model systems that consist of a combination of metallic nanoantennas (fabricated by nanosphere lithography, NSL) and oxide nanoparticles. The oxide particles were doped with rare-earth (RE) ions, which show a large shift between absorption and emission wavelengths, allowing us to investigate the energy-transfer processes in detail. The main focus is on TiO_2

nanoparticles doped with Eu^{3+}, since the material is interesting for applications such as the generation of hydrogen by photocatalytic splitting of water molecules. We use high-resolution techniques such as confocal fluorescence microscopy for the investigation of energy-transfer processes. The experiments are supported by simulations of the electromagnetic field enhancement in the vicinity of well-defined nanoantennas. The results show that the presence of the nanoparticle layer can modify the field enhancement significantly. In addition, we find that the fluorescent intensities observed in the experiments are affected by agglomeration of the nanoparticles. In order to further elucidate the possible influence of agglomeration and quenching effects in the vicinity of the nanoantennas, we have used a commercial organic pigment containing Eu, which exhibits an extremely narrow particle size distribution and no significant agglomeration. We demonstrate that quenching of the Eu fluorescence can be suppressed by covering the nanoantennas with a 10 nm thick SiO_x layer.

Introduction

Mankind has faced a growing demand for energy at all times in its history, but the 21st century is characterized by the approaching limits to the exploitation of nonrenewable resources (see, e.g., the present "peak oil" discussion). It is generally agreed now that the solution to the problem of supplying sufficient energy to present and future generations lies in techniques for using renewable energies, such as wind, water and direct sunlight. Direct conversion of sunlight by photovoltaics is an extremely attractive method of energy conversion, since the "final product" is supplied already in a most useful form. On the other hand, the storage of energy is a particularly important issue in this case, since the energy supplied by photovoltaics depends on the local and temporal availability of sunlight. There is again general agreement on the fact that the use of renewable energy sources requires reliable and large-scale energy storage. A most attractive way to this end would be conversion of solar energy directly into chemical energy; this can, for example, be achieved by photocatalytic splitting of water into hydrogen and oxygen, as already demonstrated forty years ago [1]. Nanotechnology holds great promises for the development of new devices in the field of advanced energy conversion. This became very apparent with the development of the dye-sensitized solar cells by M. Grätzel [2] more than 20 years ago. Other than conventional semiconductor photovoltaic cells, which depend on a p-n junction for separating electrons and holes generated by photon absorption, these cells are based on the very different mobility of electrons and holes. The electrons are injected into the conduction band of nanostructured TiO_2, where the nanostructure provides a sufficient contact area between the organic dye molecules and the semiconductor to make the process efficient. The Grätzel cell thus mimics the natural process of photosynthesis, where light harvesting, energy transfer to a reaction center, and conversion to chemical energy by an electron-transfer reaction, take place at different locations in the functional complexes involved. This early success has inspired the scientific community to further elaborate on this type of concept. In particular, it appears attractive to combine structures that interact strongly with light with structures that can transport and store excited states over some time. The strength of the interaction with light is largely dependent on the availability of mobile electrons that may be excited by the electrical field. On the other hand, in systems with a high density of mobile electrons, the excited states may not live long enough to allow conversion or extraction of energy. Plasmonic excitations in metallic nanostructures are a famous example of this. It has been known for decades that the interaction of the electrons of a metal with light can lead to local enhancement of the electrical field, which is utilized in spectroscopy to achieve local sensitivity on the subwavelength scale in Raman spectroscopy and related techniques [3,4]. More recently, the interest of researchers has turned towards applications of plasmonic structures in photovoltaics (for recent reviews, see [5,6]). Possible applications depend on the scattering of light for increasing the absorption, especially in thin-film structures, as well as the exploitation of field enhancements in the near-field region. Another approach reviewed in [6] for "light trapping" in photovoltaics is the excitation of surface plasmon polaritons at the interface between metals and semiconductors. Plasmonic-metal nanostructures are also promising for increasing the conversion efficiency of solar energy directly into chemical energy (see review in [7]), such as in plasmon-enhanced water splitting. These systems depend on the close interaction between metallic nanoparticles and semiconductors. Typically, noble metals are used for the metal nanostructures, since they offer both long term stability and strong resonant enhancements in the range of visible light. A general review of materials aspects in nanotechnology-based approaches in energy technology can be found in [8].

From the examples given, it is clear that the realization of nanotechnology-based approaches to efficient solar-energy conversion depends on a thorough understanding of the individual steps of the energy-transfer processes involved. As already mentioned, these include the absorption process itself, which may be modified by the presence of plasmonic metal structures, but also the transfer of charges (typically in the form

of electrons and holes), which may support either an external flow of charge in the electrical circuit connected to the photovoltaic cell, or a chemical reaction in which the energy carrier is formed (e.g., H_2). Although there are an increasing number of experiments aiming at new advanced energy-conversion systems (see, e.g., [9,10]), further progress depends on a quantitative description and modeling of the individual steps [11]. To this end, we have carried out studies of model systems with well-defined structure and composition of both the metallic and the semiconducting part. In the following, we present results of studies on hybrid nanostructures using regular arrays of nanoantennas formed by lithographic techniques. The optical properties of the metal nanostructures have been characterized by optical techniques, and also modeled by appropriate computer simulations. In a second step, these structures have been combined with oxide nanoparticles that are doped by rare-earth ions, such as Eu^{3+}. Materials of this kind are used for light conversion, e.g., in fluorescent lighting and white LEDs (light-emitting diodes). They are characterized by efficient conversion of short-wavelength photons into longer wavelength emission; the large Stokes shift allows one to clearly distinguish between excitation and emission. In the form of nanoparticles, these materials (also termed "nano-phosphors") allow probing locally the electromagnetic field in the vicinity of the plasmonic metal nanostructures. Also, since nonradiative recombination is an alternative to the radiative emission process in the nanophosphors, we may expect to learn more about the transfer of charge between metal and nonmetal from a possible quenching of the emission of the nanophosphor in the presence of the metal. In this way, the nanophosphor acts as a local probe on the nanoscale for the energy-transfer processes of interest.

The paper is organized as follows. First we describe the preparation of the TiO_2:Eu nanoparticles used in the energy-transfer experiments, together with their relevant optical properties.

Then we report details of the preparation of the Ag nanoantennas. Results of numerical simulations of the electromagnetic field in the vicinity of the nanoantennas are then presented and discussed with respect to the factors influencing the experimental fluorescence measurements. Results of TiO_2:Eu layers on top of Ag nanoantennas prepared in different ways are presented. To further study the effect of agglomeration and fluorescence quenching, we finally present results obtained using a nonagglomerated commercial organic pigment containing Eu.

Results and Discussion
A. TiO_2:Eu nanophosphors

Nanophosphors can be generated by doping a large-band-gap semiconducting oxide with rare-earth (RE) ions such as Ce^{3+}, Eu^{3+} or others. The chemical vapor reaction (CVR) technique has been successfully used for the production of high-purity nanophosphors of this type in the past. Examples include Y_2O_3:Eu nanophosphors [12,13] and $Y_3Al_5O_{12}$:Ce [14]. In this method, metal–organic precursors are evaporated and reacted with oxygen to form nanoparticles of the desired oxide phase. The particle growth can be controlled by process parameters such as the flow rates of gases, precursor temperature, and furnace temperature (Figure 1). The nanoparticles are carried away from the reaction zone by the gas flow and subsequently deposited inside a powder-collection system. For the generation of hybrid nanosystems, metal nanostructures deposited on substrates such as glass, Si wafers or MgO can be coated by introducing them into the powder-collection system.

For the production of TiO_2:Eu nanoparticles (NPs), we used titanium(IV) iso-propoxide (TTIP) and tris(2,2,6,6-tetramethyl-3,5-heptanedionato)europiate(III) [Eu(THMD)$_3$] (both precursors provided by STREM Chemicals Inc.) at temperatures varying between 45 and 50 °C for the TTIP, and 140 to 160 °C

Figure 1: CVR chamber consisting of precursor sources, reaction zone and thermophoretic powder-collection system. The substrates on which the nanoparticles are collected have been placed on the cooling trap below the Quartz lamps.
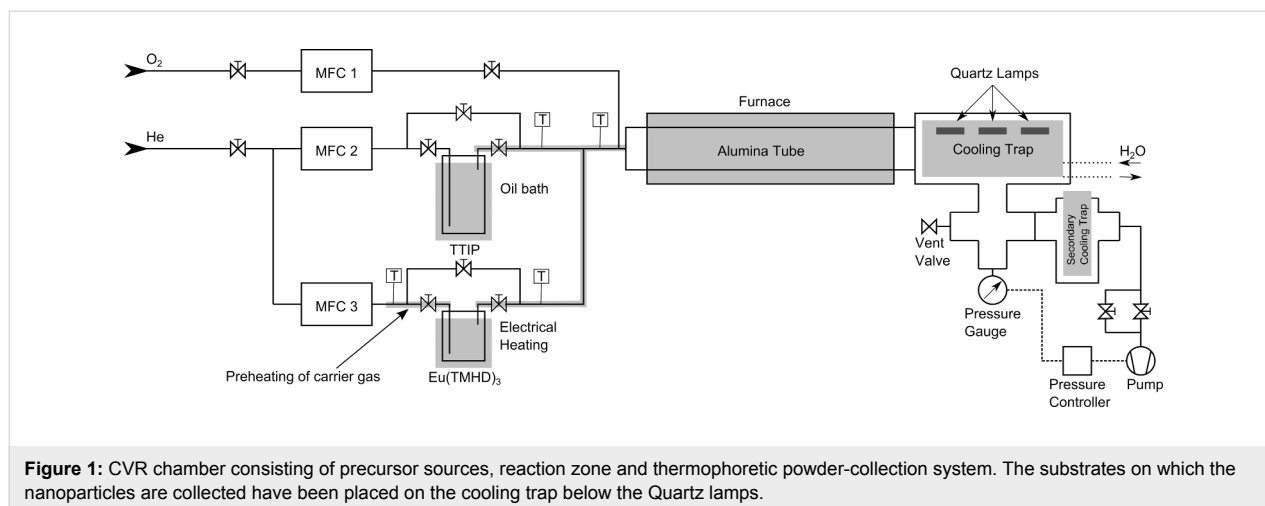
for the Eu(THMD)$_3$. The gas flow rates used were 120 mL/min of He and 800 mL/min of O$_2$ and the pressure was maintained at 50 mbar by a regulation valve. The furnace temperature was kept at 1000 °C during the process. The composition of the NPs was controlled by energy-dispersive X-ray spectroscopy.

Figure 2 shows the X-ray diffraction patterns of the as-prepared TiO$_2$:Eu NPs with varying composition. For Eu concentrations below 0.56 atom % we find predominantly the anatase structure, whereas for higher Eu concentrations an increasing fraction of rutile is visible.

Optical properties of the materials were determined by photoluminescence spectroscopy in a Fluorolog FL3-22 spectrometer (Jobin Yvon) equipped with a Hamamatsu R928P photomultiplier tube. Excitation and emission spectra were measured. Figure 3 shows a typical emission spectrum of a TiO$_2$:Eu sample containing 0.8 wt % Eu under excitation at 330 or 390 nm. The characteristic Eu^{3+} emission lines with the dominating $^5D_0 \rightarrow ^7F_2$ transition at 617 nm can be clearly observed. For excitation with 330 nm, the photon energy (3.76 eV) is larger than the band gap of the TiO$_2$ (3.2 eV), such that excitation through the TiO$_2$ host is possible. This may be the reason for the slight differences in the emission at 330 or 390 nm excitation. The emission properties of our TiO$_2$:Eu are very similar to the results of Li et al. [15] and Ikeda et al. [16] on Eu-doped TiO$_2$ nanoparticles with comparable Eu^{3+} concentration obtained by a plasma-pyrolysis synthesis route.

The excitation spectrum of the TiO$_2$:Eu nanoparticles is shown in Figure 4. The emission intensity at 617 nm was recorded and shows several maxima for excitation at around 400 nm as well as maxima at 467 and 538 nm. According to [15], the maxima at 416, 467 and 538 nm can be attributed to the $^5D \rightarrow ^7F$ transitions of the Eu^{3+} ion. The increase of the intensity at short wavelengths (below 390 nm) can be attributed to indirect excitation through the TiO$_2$ host lattice [15].

To learn more about the excitation processes in the TiO$_2$:Eu nanoparticles, we conducted time-resolved emission measurements using a xenon flash lamp for the excitation. Figure 5 shows the decay of the emission at 617 nm under excitation at 330 nm. We find that the decay of the emission under these conditions is predominantly exponential with a lifetime of 0.87 ± 0.05 ms, which does not vary significantly with the Eu concentration.
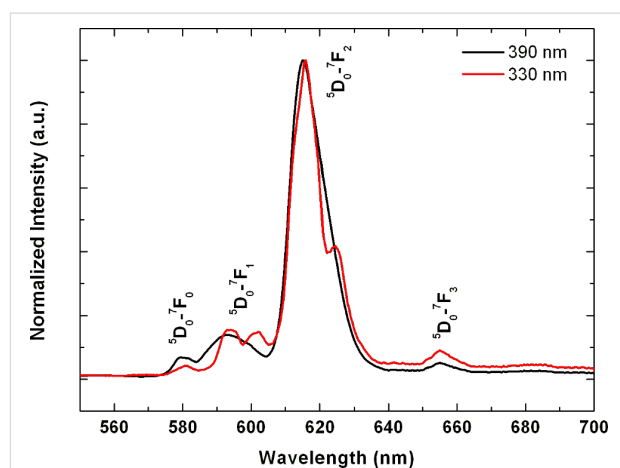
Figure 3: Normalized emission spectra of Eu^{3+} in TiO$_2$ under excitation at 330 or 390 nm.

Figure 2: X-ray diffraction patterns (Cu Kα radiation) from the TiO$_2$:Eu nanophosphors produced by the CVR method. For low Eu concentrations, only the anatase phase is found, whereas for higher concentrations a mixture of anatase and rutile can be observed.
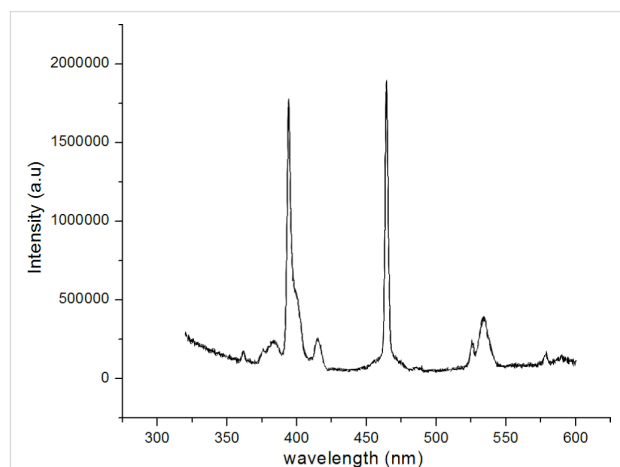
Figure 4: Excitation spectrum of TiO$_2$:Eu nanoparticles detected at 617 nm emission.
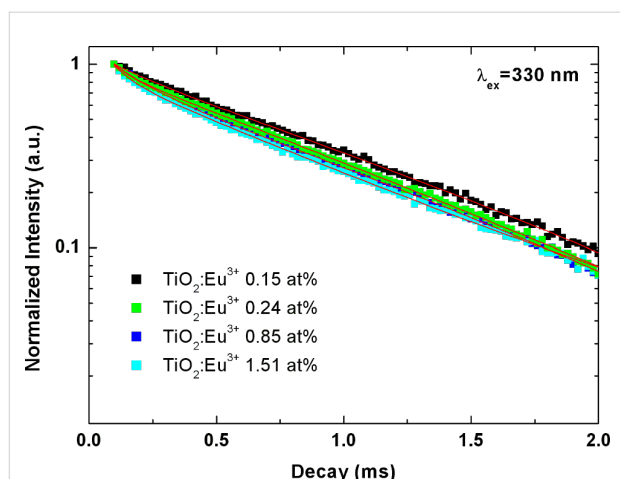
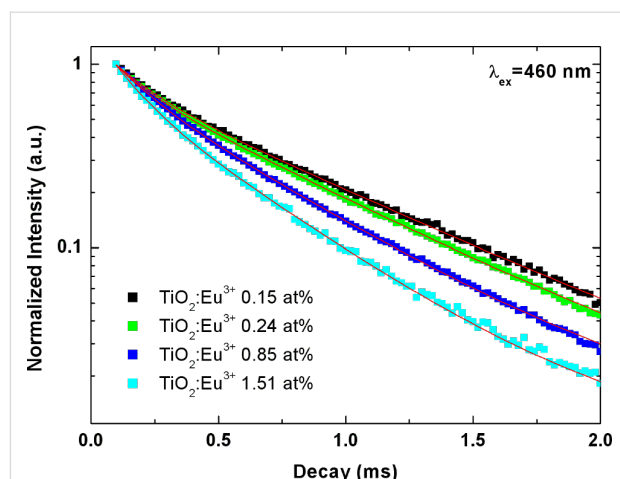**Figure 5:** Decay of the TiO$_2$:Eu emission intensity with time for excitation at 330 nm.

Figure 6: Decay of the TiO$_2$:Eu emission intensity at 617 nm with time for excitation at 460 nm.

Different observations are made for excitation below the band gap of the TiO$_2$. Figure 6 shows the decay curves measured for excitation with 460 nm wavelength. The curves clearly deviate from a single exponential decay, and the decay behavior clearly depends on the Eu^{3+} concentration. The general trend observed is that the decay gets faster with increasing Eu^{3+} content. The lifetime decreases continuously from 0.69 ms for 0.15 atom % Eu to 0.46 ms for 1.51 atom % Eu. This is a fingerprint of the increasing role of energy transfer between the individual Eu^{3+} ions. Since the excited state of the Eu^{3+} can be depopulated both by radiative processes, but also by nonradiative processes fed by the energy transfer from ion to ion, it is plausible that this transfer leads to a faster depopulation of the excited state, which shows up as a reduction of the lifetime in the present experiments. Similar results have been found in earlier experiments on Y$_2$O$_3$:Eu produced by the CVR method [13].

These results show that TiO$_2$:Eu nanoparticles doped with Eu can be synthesized by the CVR methods, and that they show emission from Eu under different excitation conditions. The ion-to-ion energy transfer (most likely by short-ranged Förster transfer) suggests that the surface may play a significant role, e.g., as a preferred site for nonradiative recombination. The influence of the surface may be investigated by modification of the surface of the nanophosphors. Stable oxides may be considered as a suitable solution for such a coating. In principle, two options may be considered in the present context. A coating with a wide-band-gap oxide material, such as Al$_2$O$_3$, could passivate the surface and confine excitations inside the TiO$_2$ core, similar to techniques applied in core–shell semiconductor nanoparticles. Another option would be a coating with undoped TiO$_2$. The lack of Eu in this outer coating shell would effectively suppress the energy transfer to the particle surface, while

not disturbing the lattice structure of the TiO$_2$:Eu core due to the perfect lattice matching possible in the homoepitaxial case. In order to investigate the possibility for generation of such coatings, TiO$_2$:Eu nanoparticles were subjected to a post-processing step in an atomic layer deposition (ALD) chamber supplied with trimethyl aluminium (TMA) and TTIP sources. In both cases, combination with water vapor allows to grow oxides of the respective metal in a layer by layer mode, and achieve a conformal coating of well-defined thickness in this way. The advantage of the ALD process is that this conformal coating can be achieved without using organic surfactants. Results of the ALD post-processing of TiO$_2$:Eu nanoparticles are shown in Figure 7 and Figure 8. Figure 7 shows a STEM image of TiO$_2$:Eu nanoparticles coated with 3 nm of Al$_2$O$_3$. In addition, a thin layer of TiO$_2$ was added at the end of the process in order to test the possibility of generating multishell structures. One can clearly distinguish the TiO$_2$:Eu core from the shell in Figure 7, but it is not possible to distinguish between the Al$_2$O$_3$ and the TiO$_2$ part of the shell.

Figure 8 shows a high-resolution TEM image of TiO$_2$ nanoparticles coated with Al$_2$O$_3$. Lattice fringes can only be observed in the core of the particles, indicating that the TiO$_2$ cores are crystalline. However, the absence of lattice fringes in the region of the Al$_2$O$_3$ shells indicates that the shell is amorphous. The results prove that it is possible to generate potentially passivating coatings by ALD post-processing. However, it has also become obvious that already existing agglomerates will be coated as a whole, therefore not leading to a separate protection of the surface of individual particle. This may be avoided by coating of the particles while they are still being carried in the gas flow of the CVR process. Future work will therefore aim at an integration of the ALD process into the CVR technique.
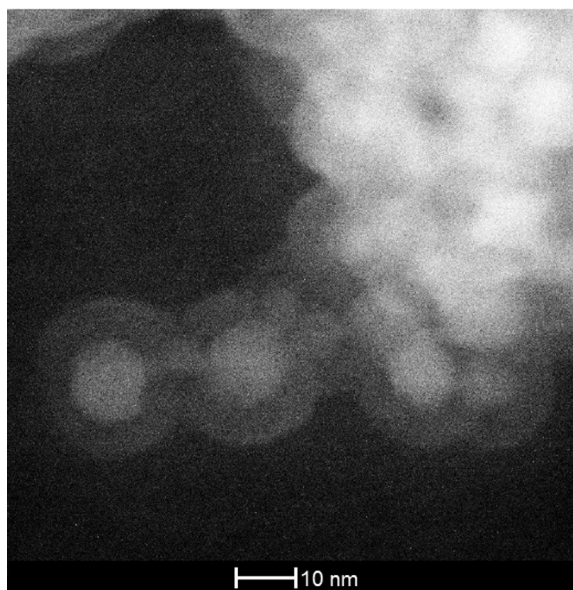
Figure 7: STEM image of TiO$_2$:Eu nanoparticles coated with a shell of 3 nm Al$_2$O$_3$ and TiO$_2$.
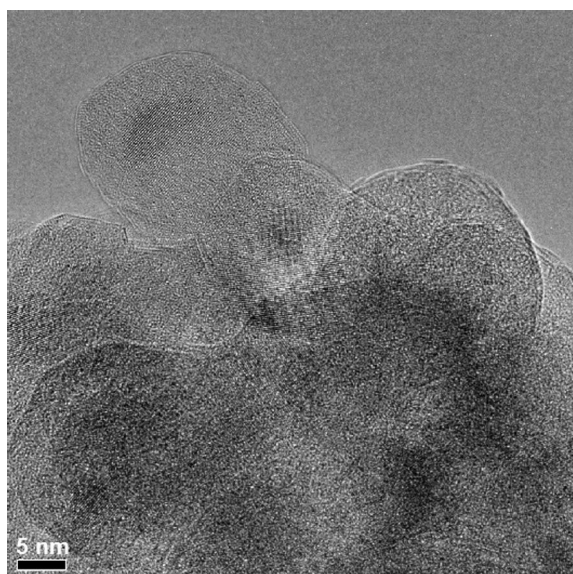

Figure 8: High-resolution TEM image of TiO$_2$ nanoparticles coated with Al$_2$O$_3$ showing that the Al$_2$O$_3$ coating is amorphous, whereas the TiO$_2$ cores exhibit lattice fringes proving that they are crystalline. The length of the scale bar is 5 nm.

B. Systems with Ag nanoantennas from NSL

Nanosphere lithography (NSL) is a well-established technique for the generation of periodic structures on the submicron scale [17]. Colloid spheres, which are commercially available, e.g., as size standards in microscopy, are deposited as part of a suspension onto substrates. After drying, hexagonal close-packed

arrangements of the spheres can be obtained, with periodicities extending over quite large distances. Single layers of such spheres serve as template masks for deposition of materials through the open holes of the layer structure. After removal of the colloid particles, typically arrangements of triangular structures are obtained. The distance between the structures is determined by the size of the original colloid sphere, and can be adjusted over a wide range by the choice of the sphere size. In our study, we have used polystyrene spheres with diameters of 1 μm or 3 μm. The water-based dispersions were dried under constant temperature and air flow to assure a constant evaporation rate of the solvent. In the next step, we deposited Ag films with a thickness of 50 nm by thermal evaporation under vacuum conditions. The spheres were removed afterwards by sonication in ethyl methyl ketone and water. The resulting structures are triangular with a regular spacing over wide regions (the typical size of the ordered regions was several 10 μm). These Ag nanoantennas are then covered with nanophosphors in a second processing step. Figure 9 shows a SEM image of a structure obtained by using 3 μm diameter spheres. The cover layer of TiO$_2$:Eu nanoparticles was obtained by incorporation of the nanoantenna covered substrate into the powder-collection stage of the CVR machine (see Figure 1).

A big advantage of the regular nanoantenna patterns generated in this way is that the positions of the individual antennas can be identified in confocal microscopy, even though the details of the antenna itself may not be resolved. We have used confocal microscopy with excitation by 532 nm laser light to study the optical properties of the nanophosphor-covered Ag nanoantennas. We analyze the light coming from the structure using a spectrometer with a CCD sensor. In this way, we can distinguish between the scattered and reflected primary light, and the fluorescence generated by conversion of the excitation light to
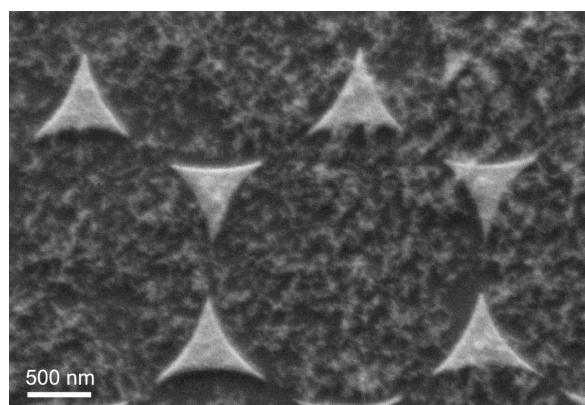
Figure 9: SEM image of Ag nanoantennas from the nanosphere lithography process (using colloid spheres with 3 μm diameter), covered with TiO$_2$:Eu nanophosphors.

photons with 618 nm from the Eu^{3+} ions. Figure 10a and Figure 10b show two confocal microscopy images of the same area of the sample. Figure 10a was obtained by using the wavelength region of 530–535 nm, which contains mainly elastically or quasi-elastically scattered light. In contrast, Figure 10b was obtained using the wavelength region of 605 to 630 nm, where the emission from the Eu^{3+} is concentrated. Several observations can be made from these images. Firstly, the scattered light is concentrated at the nanoantenna structures, with dark areas between the nanoantennas. Secondly, fluorescence occurs all over the sample, but the intensity is higher in the vicinity of the nanoantennas.

The results demonstrate that the regular nanoantenna patterns from NSL offer excellent opportunities for assessment of the

Figure 10: Confocal microscopy images of the Ag nano-antenna structures (produced using 3 µm diameter colloid spheres) covered with TiO_2:Eu nanophosphors under illumination with 532 nm laser light. In (a) intensity in the wavelength region 530–535 nm has been used, whereas in (b) the region 605–630 nm is used. The scale bars mark a length of 3 µm.

coupling of the nanophosphors to the nanoantennas with submicron resolution. However, in order to optimize the resolution it will be necessary to obtain a well-defined arrangement of the phosphor nanoparticles. As can be observed from Figure 9, agglomerates of the nanophosphor do still occur, which will not allow a quantitative measurement of local intensities, since these intensities will not only be determined by the local electrical field strength, but also by the local density of nanophosphor. Therefore, we have investigated alternative ways for deposition of the nanophosphor with the aim of getting more homogeneous particle arrangements. These studies will be reported in section D.

On the other hand, the actual intensity distribution in the near field of the nanoantennas will depend not only on the size and thickness of the antennas, but also on the dielectric properties of its environment, i.e., both the substrate and the nanophosphor cover layer. In addition, the local arrangement of individual nanoantennas with respect to each other (e.g., the gap width between the tips of neighboring antenna triangles) will play a role for the intensity distribution, as well as the orientation towards the plane of polarization of the illuminating light. These effects have been further explored by numerical simulations of the electromagnetic field in model structures, which will be presented in the next section.

C. Numerical simulation of the electrical field distribution

Numerical simulations have been performed using the COMSOL Multiphysics RF module, which solves the Maxwell equations in the frequency domain based on the finite-element method. Bowtie model antenna structures have been defined with geometries close to the experimental ones. The aim was to calculate the relative electrical field enhancement factor E/E_0 of the local field strength E over the field of the incident light wave E_0. Dielectric properties of Ag have been taken from the literature [18]. As an example, Figure 11 shows the field-enhancement factor in the center of the gap between two triangles of a bowtie nanoantenna structure made of a 30 nm thick Ag layer for two different polarizations (the long axis of the bowtie is along the x direction). For comparison, field enhancement factors for two other positions outside the gap region are shown in the same image. The size of the gap is 12 nm, and the tip-to-edge length of the antenna arms (measured from the tip of the triangle to the centre of the opposing base) is 100 nm. Resonances are found, which depend on the size of the antenna but also on the dielectric constants of the environment (substrate and cover layer). The spatial distribution of the enhancement factor in the region of the maximum (around 700 nm) for polarization in the horizontal (x) direction is shown in Figure 12.
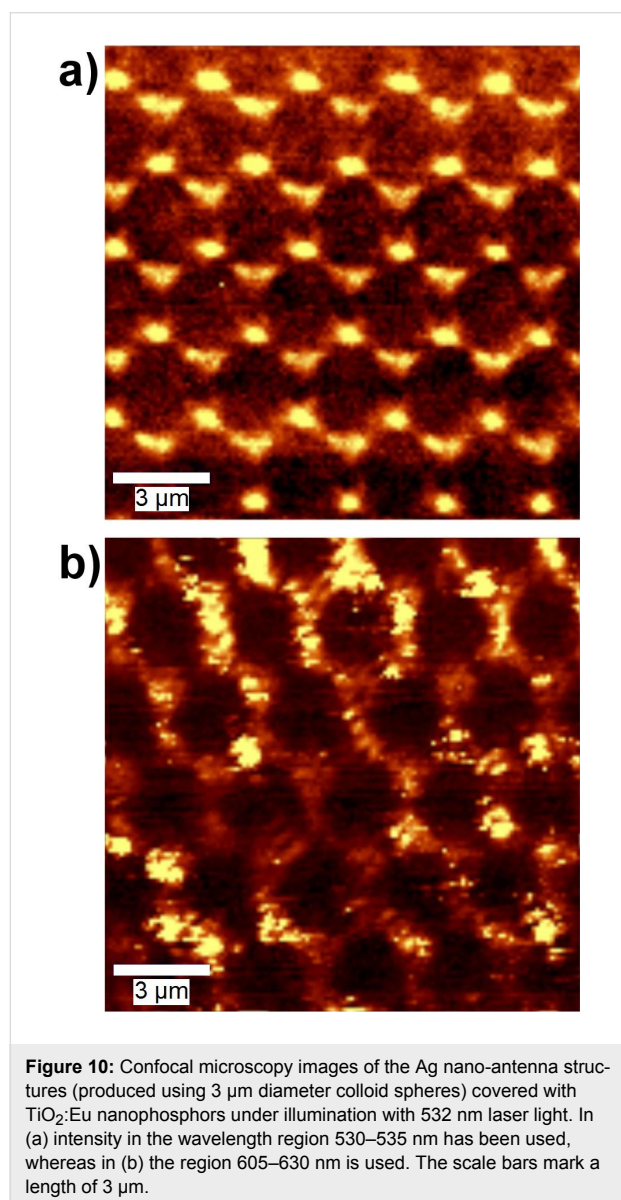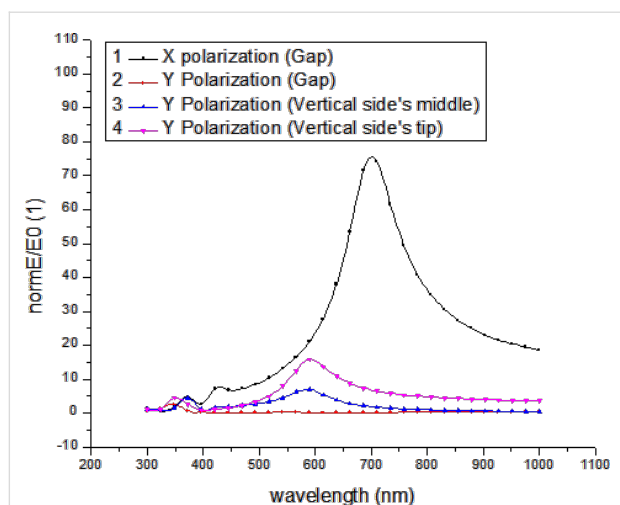
Figure 11: Calculated field-enhancement factor (normalized to the amplitude E_0 of the incident light) for bowtie nanoantennas at different positions and for different polarization of the incident light.
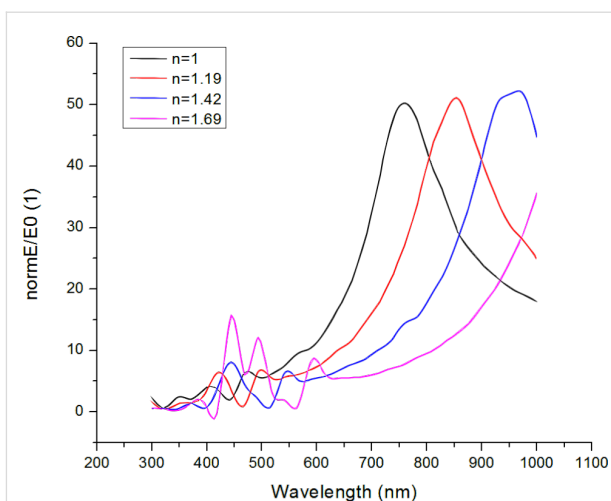

Figure 13: Dependence of the field enhancement in the centre of the gap of a bowtie antenna structure on the index of refraction ($n = \varepsilon^{0.5}$) of the cover layer. The substrate is glass ($n = 1.54$).
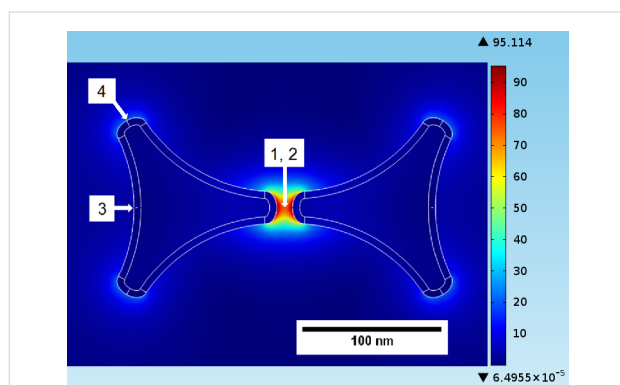

Figure 12: Field enhancement ratio (scale goes from 0 to 90) for Ag bow-tie nano-antennas with tip-to-edge length of 100 nm, thickness 30 nm, and gap size of 12 nm under excitation at 700 nm. The labels 1 to 4 mark the positions for which the field-enhancement curves shown in Figure 11 were calculated.

The dielectric constant ε of the environment depends on the density of the TiO_2 particles in the cover layer. To get an idea about the importance of this effect, we have simulated cover layers with varying average dielectric constant (using an effective-medium approach) and thickness, which aims at mimicking the effect of different packing densities of TiO_2 powder particles in the cover layer. As an example, Figure 13 shows results for the field-enhancement factors in the gap center for a variation of the index of refraction n (we can use $n = \varepsilon^{0.5}$ here).

The simulation results show that the arrangement of the nanophosphor particles in the cover layer is important, since the presence of the nanoparticles has a significant effect on the resonant behavior of the nanoantennas. For a fixed excitation wavelength, the field enhancement factor can vary locally with the local density of the nanophosphor. It is therefore most important to achieve a regular and reproducible arrangement of the nanophosphor inside the cover layer.

Another result of the simulations is that the maximum field enhancement that can be achieved depends on the size of the gap between the antennas. Since the structural dimension and the gap size scale with the diameter of the colloid spheres, the use of smaller spheres is more promising. However, for very small sphere sizes it gets increasingly difficult to identify the positions of individual antennas in the confocal microscope. As a compromise, we chose polystyrene spheres with 1 μm diameter for the following experiments. To obtain realistic values for the expected field enhancements, we performed a simulation of an array of 50 nm thick Ag nanoantennas with tip-to-edge length of 370 nm and a gap size of 60 nm. The individual antenna dimensions correspond to the dimensions of the experimental antennas we obtained when using 1 μm diameter spheres. The results are shown in Figure 14. One can observe significant field enhancement in the gap region, but also at other regions of the individual antennas. Considering the limited resolution of the confocal microscope, we can expect to see the antennas as bright regions in the fluorescence images.

D. Optimization of the nanophosphor layer

In order to homogenize the distribution of the TiO_2:Eu nanoparticles in the cover layer, the nanoparticles collected from the CVR process were dispersed in ethanol solution (95 % ethanol, 5% water), mixed and sonicated with ultrasound. The nanosuspensions obtained in this way were spin-coated on top of glass substrates covered with Ag nanoantennas produced by NSL at a speed of 2000 rpm and a spinning time of 10 s. Figure 15 shows
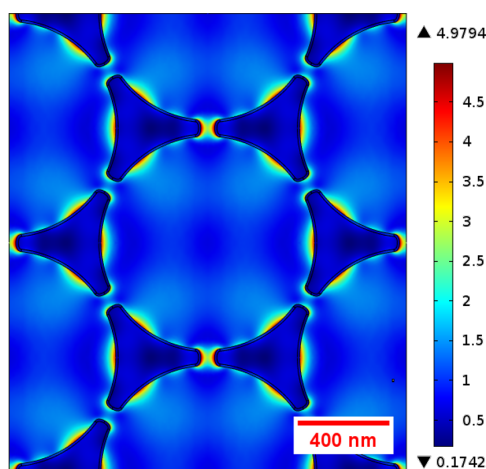
Figure 14: Field enhancement ratio for an array of Ag nanoantenna structures with tip-to-edge length of 370 nm, thickness of 50 nm and gap size of 60 nm calculated for excitation at 532 nm. The polarization direction of the electrical field is horizontal.
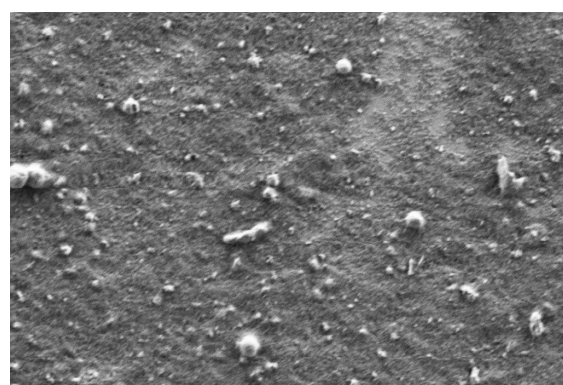

Figure 15: SEM image of spin coated TiO_2:Eu layer on Ag nanoantenna structures.

Figure 16: (a) AFM image of the spin coated TiO_2:Eu layer. The antenna structure is still visible in this region. (b) AFM height profiles along the lines marked in (a) (black line corresponds to line 2 in (a), red line to line 1 in (a)).
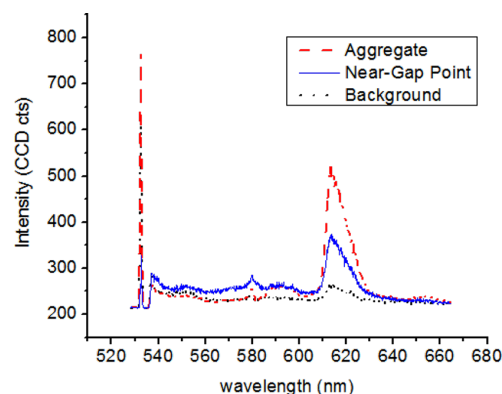
Figure 17: Fluorescent intensity obtained by confocal microscopy of spin-coated nanoantenna structures under excitation with 532 nm radiation.

an SEM image of the spin-coated TiO_2:Eu particles. The surface is characterized by regions of relatively homogeneous particle deposition, but also by the presence of large particles. Good results by confocal fluorescence imaging can only be expected from the smooth regions. Figure 16 shows an AFM image of a smooth region. From the image in Figure 16a and the line profiles in Figure 16b it can be observed that even in the smooth regions agglomerated particles with sizes of more than 100 nm can be found.

The effect of agglomerates becomes evident by comparison of fluorescent intensities from different areas of the sample. Figure 17 shows the intensities taken from a region with a large aggregate (red line), a point near the gap of a bowtie nanoantenna (blue line), and a region without nanoantennas (background intensity, black line). It is observed that the intensity of the large aggregate is higher than that from the near-gap point. This result makes the interpretation of fluorescent intensity enhancements quite difficult. We can conclude here that

although fluorescence intensity enhancements are observed in the vicinity of the Ag nanoantennas, a quantitative interpretation in terms of local field enhancement will require further optimization of the nanoparticle arrangement.

E. Study of quenching effects using organic pigments

The results reported up to know show the importance of obtaining a narrow distribution of nanoparticle sizes. This can be achieved by stabilizing the nanoparticle dispersions with surfactants. In this part of the study, we used a nanosuspension based on a commercial fluorescent organic pigment (VTLUNP by LuminoChem), which exhibits excitation and emission spectra very similar to the ones of the TiO_2:Eu. The luminescent center in this pigment is Eu. The emission spectrum for excitation with 532 nm radiation is shown in Figure 18. A strong red emission with a maximum at 614 nm is observed. The excitation spectrum recorded with the 614 nm emission is shown in Figure 19. Similar to the TiO_2:Eu, it shows maxima at

465 nm and 535 nm, which can be attributed to the Eu. The commercial nanosuspension exhibits a narrow particle size distribution centered around 23 nm, as confirmed by dynamic-light-scattering measurements. The nanosuspensions were spin coated at 2000 rpm for 10 s onto Ag nanoantennas. AFM scans of the coated samples show smooth surfaces with roughness values of a few nanometers (see Figure 20). In contrast to the spin-coated TiO_2:Eu solutions, no large aggregates have been observed. The samples therefore seem appropriate for studying the local field enhancement around the nanoantennas.

Figure 21 shows results of samples with high (a, b) or low (c, d) film coverage. For each case, a direct comparison of scattered light in the wavelength region around the excitation wavelength (Figure 21a and Figure 21c) and red fluorescence intensity (Figure 21b and Figure 21d) is made. From this comparison, we find that the areas right above the nanoantennas (bright spots in Figure 21a and Figure 21c) appear dark in the fluorescence images (Figure 21b and Figure 21d). Also, the circular areas enclosed in between the nanoantennas (which were covered by the colloid particles during Ag evaporation) appear bright in fluorescence. Both observations seem to contradict the expectations from the simulations. In principle, the observations may be explained by inhomogeneities in the phosphor
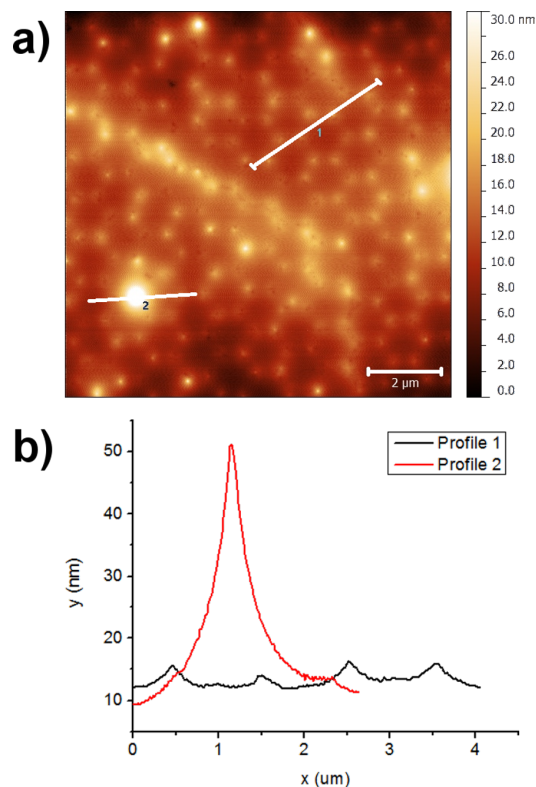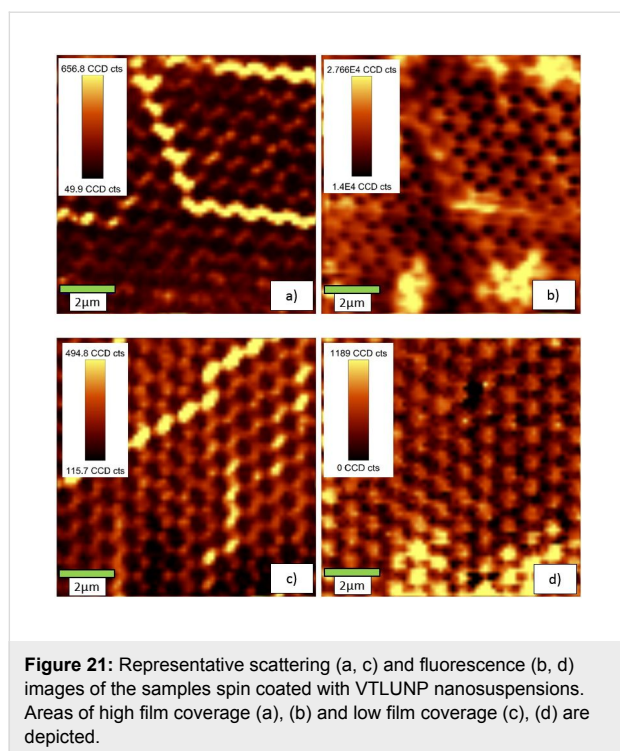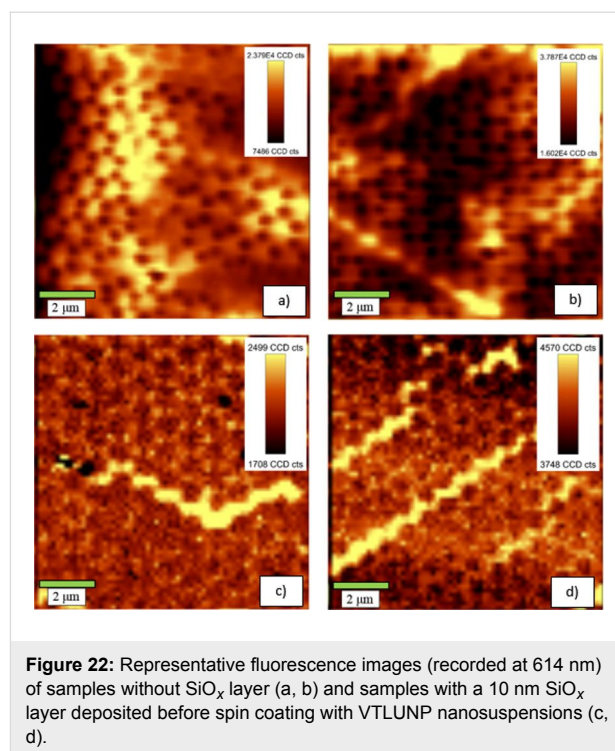

Figure 18: Emission spectrum of VTLUNP organic pigment under excitation with 532 nm radiation.
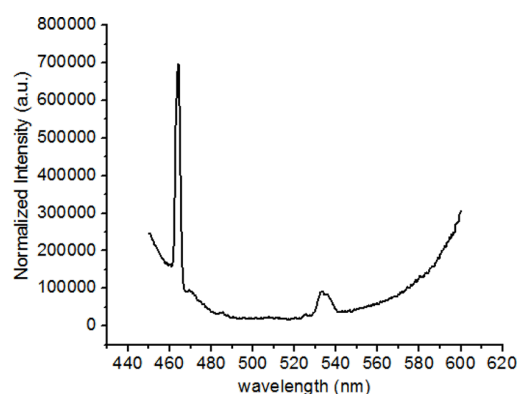
Figure 19: Excitation spectrum of VTLUNP organic pigment for emission at 614 nm.

Figure 20: (a) AFM image of Ag nanoantennas spin coated with VTLUNP (b) AFM height profiles along the lines 1 and 2 marked in (a).

Figure 21: Representative scattering (a, c) and fluorescence (b, d) images of the samples spin coated with VTLUNP nanosuspensions. Areas of high film coverage (a), (b) and low film coverage (c), (d) are depicted.

Figure 22: Representative fluorescence images (recorded at 614 nm) of samples without SiO_x layer (a, b) and samples with a 10 nm SiO_x layer deposited before spin coating with VTLUNP nanosuspensions (c, d).

layer thickness, which might be associated with local variations of the wetting behavior caused by the Ag nanoantennas. Another possible explanation is a quenching of the excitation at the metallic surface. Such a quenching of the fluorescence has been reported earlier for noble-metal nanospheres [19,20].

The quenching can be suppressed by inserting a dielectric layer between the metal and the semiconducting nanophosphors. This can either be achieved by coating of the nanoparticles, or by deposition of a dielectric layer on the metal nanoantennas. We tried the second solution by coating of the Ag nanoantennas with a 10 nm thick SiO_x layer by thermal evaporation under vacuum conditions. A similar investigation has been reported in a recent publication about surface-enhanced fluorescence of fluorescent dyes on silica-protected Au nanoantennas by Fayyaz et al. [21], where the silica film thickness was varied between 5 and 25 nm.

The resulting fluorescence images of our samples for excitation with 532 nm radiation are shown in Figure 22 in comparison with the fluorescence images of noncoated samples. The fluorescence images of the samples coated with SiO_x prior to spin coating of the VTLUNP solution (Figure 22c and Figure 22d) appear to be inverted when compared to the images without SiO_x layer (Figure 22a and Figure 22b): one can see the pattern of the nanoantennas as bright spots in Figure 22c and Figure 22d, whereas the circular regions in between appear darker. The results suggest that the quenching may be the domi-

nant effect when no dielectric spacer layer is applied. Further investigations with varying thickness of the SiO_x layer will be undertaken to clarify this phenomenon in detail. We may also expect similar quenching effects in the spin-coated TiO_2:Eu layers. However, since strong quenching is only expected for fluorescent particles in close contact with the metallic surfaces, the quenching effects may not be so obvious in the TiO_2:Eu due to a large roughness of these layers as compared to the smoother VTLUNP layers (as deduced from a direct comparison of the AFM images in Figure 16 and Figure 20).

Conclusion

Systematic studies of energy transfer in hybrid metal-oxide nanostructures have been performed. The main aim was to study local electrical-field enhancements at plasmonic Ag nanoantennas by using nanophosphors with a large shift between excitation and emission wavelength. For this purpose, we have successfully synthesized TiO_2:Eu nanophosphors, which may be used as local field probes on the nanoscale. The optical properties of the nanophosphors indicate that ion-to-ion energy transfer plays a significant role in these systems. In addition, we have demonstrated that potentially passivating coatings with stable oxide layers can be achieved by postprocessing the nanophosphors with ALD. The TiO_2:Eu nanophosphors have been tested in combination with well-defined periodic arrays of triangular Ag nano-antennas, which have been produced by nanosphere lithography. The optical properties of the Ag nano-antennas have been investigated by numerical

simulations based on solutions of Maxwell's equations. We find large resonant enhancements of the electrical field in the vicinity of the antennas, especially in the gaps of the bowtie structures. The magnitude of the field enhancement depends sensitively on the local environment of the antennas and the polarization of the incident light. In particular, we find that the presence of the nanophosphor layer itself has a significant effect on the resonances. We conclude that a well-defined arrangement of the nanophosphors is a necessary prerequisite for a quantitative determination of the energy transfer from fluorescence measurements. Based on the simulation results, we investigated procedures for the optimization of the nanophosphor layer structure. The approach used here is spin coating of nanosuspensions containing phosphor particles. Initial attempts with spin-coated TiO_2:Eu nanophosphors show that large aggregates do still form in some places, although the general particle arrangement can be improved. It is demonstrated that these aggregates lead to high local fluorescence yields, which make a quantitative interpretation of the measured fluorescence intensities difficult. Better homogeneity of the fluorescent particle layer has been obtained by spin coating the nanoantennas with a commercial Eu-based organic fluorescent nanosuspension with narrow size distribution and similar optical properties. Quenching of the Eu fluorescence at the Ag nanoantennas has been observed by confocal microscopy of the fluorescent emission. The quenching can be reduced by deposition of a 10 nm thick SiO_x spacer layer. In the systems containing this spacer layer, local enhancements of the fluorescence intensity at the nanoantenna positions can be observed.

In summary, the results show the potential for nanophosphors as local probes for energy transfer in hybrid metal-oxide nanosystems. A quantitative measurement of the energy transfer processes requires precise control of the geometry of both metal and oxide constituents of the system, and the suppression of quenching effects. In addition, numerical modeling of the electromagnetic field distribution is most important due to the dependence of the resonant plasmonic behavior on the local environment of the nanoantennas.

Acknowledgments

References

1. Fujishima, A.; Honda, K. *Nature* **1972,** *238,* 37–38. doi:10.1038/238037a0
2. Grätzel, M. *Nature* **2001,** *414,* 338–344. doi:10.1038/35104607
3. Cialla, D.; Weber, K.; Böhme, R.; Hübner, U.; Schneidewind, H.; Zeisberger, M.; Mattheis, R.; Möller, R.; Popp, J. *Beilstein J. Nanotechnol.* **2011,** *2,* 501–508. doi:10.3762/bjnano.2.54
4. Stadler, J.; Schmid, T.; Opilik, L.; Kuhn, P.; Dittrich, P. S.; Zenobi, R. *Beilstein J. Nanotechnol.* **2011,** *2,* 509–515. doi:10.3762/bjnano.2.55
5. Catchpole, K. R.; Polman, A. *Opt. Express* **2008,** *16,* 21793–21800. doi:10.1364/OE.16.021793
6. Atwater, H. A.; Polman, A. *Nat. Mater.* **2010,** *9,* 205–213. doi:10.1038/nmat2629
7. Linic, S.; Christopher, P.; Ingram, D. B. *Nat. Mater.* **2011,** *10,* 911–921. doi:10.1038/nmat3151
8. Zäch, M.; Hägglund, C.; Chakarov, D.; Kasemo, B. *Curr. Opin. Solid State Mater. Sci.* **2006,** *10,* 132–143. doi:10.1016/j.cossms.2007.04.004
9. Bora, T.; Kyaw, H. H.; Sarkar, S.; Pal, S. K.; Dutta, J. *Beilstein J. Nanotechnol.* **2011,** *2,* 681–690. doi:10.3762/bjnano.2.73
10. Baruah, S.; Mahmood, M. A.; Myint, M. T. Z.; Bora, T.; Dutta, J. *Beilstein J. Nanotechnol.* **2010,** *1,* 14–20. doi:10.3762/bjnano.1.3
11. Walhorn, V.; Paskarbeit, J.; Frey, H. G.; Harder, A.; Anselmetti, D. *Beilstein J. Nanotechnol.* **2011,** *2,* 645–652. doi:10.3762/bjnano.2.68
12. Konrad, A.; Fries, T.; Gahn, A.; Kummer, F.; Herr, U.; Tidecks, R.; Samwer, K. *J. Appl. Phys.* **1999,** *86,* 3129–3133. doi:10.1063/1.371177
13. Kaps, H.; Arefin, M. L.; Herr, U.; Paul, H. *Diffus. Defect Data, Pt. B* **2007,** *128,* 165–171.
14. Paul, H.; Kessler, D.; Herr, U. *Diffus. Defect Data, Pt. B* **2008,** *140,* 9–16.
15. Li, J. G.; Wang, X. H.; Watanabe, K.; Ishigaki, T. *J. Phys. Chem. B* **2006,** *110,* 1121–1127. doi:10.1021/jp053329l
16. Ikeda, M.; Li, J.-G.; Kobayashi, N.; Moriyoshi, Y.; Hamanaka, H.; Ishigaki, T. *Thin Solid Films* **2008,** *516,* 6640–6644. doi:10.1016/j.tsf.2007.11.037
17. Gonçalves, M. R.; Makaryan, T.; Enderle, F.; Wiedemann, S.; Plettl, A.; Marti, O.; Ziemann, P. *Beilstein J. Nanotechnol.* **2011,** *2,* 448–458. doi:10.3762/bjnano.2.49
18. Johnson, P. B.; Christy, R. W. *Phys. Rev. B* **1972,** *6,* 4370–4379. doi:10.1103/PhysRevB.6.4370
19. Mertens, H.; Koenderink, A. F.; Polman, A. *Phys. Rev. B* **2007,** *76,* 115123. doi:10.1103/PhysRevB.76.115123
20. Dulkeith, E.; Morteani, A. C.; Niedereichholz, T.; Klar, T. A.; Feldmann, J.; Levi, S. A.; van Veggel, F. C. J. M.; Reinhoudt, D. N.; Möller, M.; Gittins, D. I. *Phys. Rev. Lett.* **2002,** *89,* 203002. doi:10.1103/PhysRevLett.89.203002
21. Fayyaz, S.; Tabatabaei, M.; Hou, R.; Lagugne-Labarthet, F. *J. Phys. Chem. C* **2012,** *116,* 11665–11670. doi:10.1021/jp302191z

Guided immobilisation of single gold nanoparticles by chemical electron beam lithography

Patrick A. Schaal and Ulrich Simon[*]

Full Research Paper

Open Access

Abstract

The fabrication of periodic arrays of single metal nanoparticles is of great current interest. In this paper we present a straightforward three-step procedure based on chemical electron beam lithography, which is capable of producing such arrays with gold nanoparticles (AuNPs). Preformed 6 nm AuNPs are immobilised on thiol patterns with a pitch of 100 nm by guided self-assembly. Afterwards, these arrays are characterised by using atomic force microscopy.

Introduction

Periodic arrays of nanometre-sized metal structures hold great promise for future applications, e.g., in nanoelectronics [1-4] or in biohybrid devices [5,6]. The most common technique to generate such structures is the evaporation of a thin metal film through a resist mask structured by electron beam lithography (EBL) or other lithographic techniques [1,7]. In general, these fabrication techniques involve five or more processing steps, including formation, patterning and development of resist films, metal evaporation/sputtering and lift-off, whereby feature sizes rarely go beyond the 10 nm threshold [1]. Depending on the

chosen substrate, e.g., SiO_2, additional metal layers such as Ti are needed as adhesive layers.

In order to overcome this threshold and to facilitate the processing, alternative approaches have been developed, which utilise the self-assembly capabilities of chemically tailored metal nanoparticles. Amongst others, Enderle et al. demonstrated very recently the formation of gold nanodots by self-assembly of micelles loaded with $HAuCl_4$ and subsequent reduction by hydrogen plasma [8]. Such assembly protocols are

more facile, but are limited to the formation of self-forming periodic patterns, which are typically of hexagonal symmetry [8-10].

In order to increase the structural variability, guided immobilisation of single AuNPs by chemically structured surfaces has been introduced [11,12]. Appropriate surfaces can be obtained either by resist-based EBL and subsequent etching [11] or by soft lithographic techniques such as nanoimprint lithography [12]. As an example, Onses et al. demonstrated the fabrication of very precise patterns of single 13 nm AuNPs with pitches around 80 nm very recently [11]. However, both techniques are technically demanding and require several processing steps or need prefabricated molds and are, therefore, not easily adaptable to new designs.

Very recently, we reported the formation of electrically conducting nanopatterns formed by chemical EBL (CEBL) [13]. Therefore, we formed a chemically patterned surface by local reduction of the terminal SO_2X groups of self-assembled monolayers (SAMs) by means of an electron beam [14]. These structured SAMs guided AuNP immobilisation through covalent binding. A subsequent metallisation step enabled the formation of conducting nanopatterns in the 100 nm regime. Compared to resist-based EBL with five or more processing steps, the pattern formation was achieved in just three steps (SAM preparation, irradiation, and immobilisation), however, with significantly lower fidelity. Therefore, it would be highly desirable to develop this method further to take full advantage of the structural variability that arises from EBL and the high degree of control over size and shape of chemically tailored AuNPs to deposit ideally individual AuNPs in any type of periodic or aperiodic pattern.

In order to make new steps in this direction, in this work, we present the local reduction of sulfonic acid terminated SAMs into thiol-terminated SAMs by CEBL on electron-transparent SiO_2 membranes, which enabled us to analyse the site-selective immobilisation of AuNPs by scanning electron microscopy in transmission (SEM-T) and by atomic force microscopy (AFM). Based on these analyses, we were able to optimise the process yielding periodic patterns of single 6 nm AuNPs.

Results and Discussion
Generation of thiol groups on thin Si/SiO_2 membranes
Following the protocol we published previously [13], we studied the reduction of 2-(4-chlorosulfonylphenyl)ethyltrichlorosilane (CSPETCS) SAMs on top of electron-transparent SiO_2 layers. For this we used SiO_2 membranes, which are commonly used in SEM-T and TEM experiments

(Figure 1). Within region **A** of these substrates the vertical layer composition is 100 μm of Si covered with 40 nm of SiO_2. In contrast to this, in region **B** the 40 nm SiO_2 layer is suspended without any support. CSPETCS SAMs were fabricated by wet-chemical silanisation in dry toluene within both regions **A** and **B**. Thereby, CSPETCS SAMs with a thickness down to 1.3 ± 0.1 nm could be fabricated. Upon irradiation with electrons these monolayers can be locally reduced converting the top sulfonic acid group into a thiol group [13].
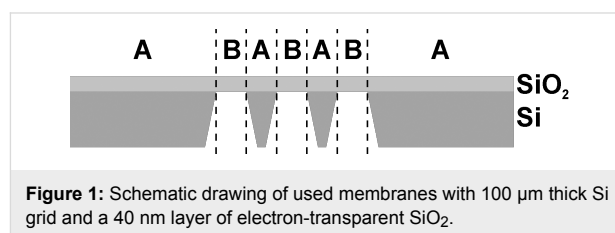

Figure 1: Schematic drawing of used membranes with 100 μm thick Si grid and a 40 nm layer of electron-transparent SiO_2.

First, we irradiated the CSPETCS layer in region **A** with electrons at acceleration voltages (EHT) of 2 kV and a base dose of 50 μC·cm^{-2} (see Supporting Information File 1 for a theoretical calculation, primary electron pathways, and estimated influence upon irradiation dose) using CAD-designs with circles of 400 nm and 200 nm, respectively (cf. Figure S1 and Figure S2 within Supporting Information File 1 for details). The exposed substrates were then incubated with a solution of 16 nm AuNP at pH 4.7. Figure 2 shows exemplary SEM pictures of the incubated patterns with intended structure diameters of 400 nm (a,b) and 200 nm (c,d). The actual average diameters were determined to 420 ± 20 nm and 230 ± 10 nm by statistical analysis. In accordance with previous experiments, this process is capable of fabricating AuNP patterns with a selective deposition in irradiated areas on silanised SiO_2 surfaces of 40 nm thickness.

In order to examine the possibility of structuring the freely suspended SiO_2 windows, we performed the same experiments within region **B** (c.f. Figure 1). After incubation with a solution of 16 nm AuNPs the generated patterns were imaged by SEM-T. Two exemplary images are shown in Figure 3. The immobilised AuNPs are well silhouetted against the electron-transparent SiO_2 background. The actual spot diameter of 400 ± 20 nm matches the intended one of 400 nm. The average particle density within the irradiated spots is $\rho_{NP}(SH) = 300 ± 30$ NP/μm^2 and significantly higher than outside the irradiated areas with $\rho_{NP}(SO_2X) < 10$ NP/μm^2.

Incubation of thiol patterns with 6 nm AuNP
Attempts to generate smaller structures, e.g., circles with diameter $d < 200$ nm, resulted in randomly and incompletely covered structures due to the decreasing structure-to-particle size ratio
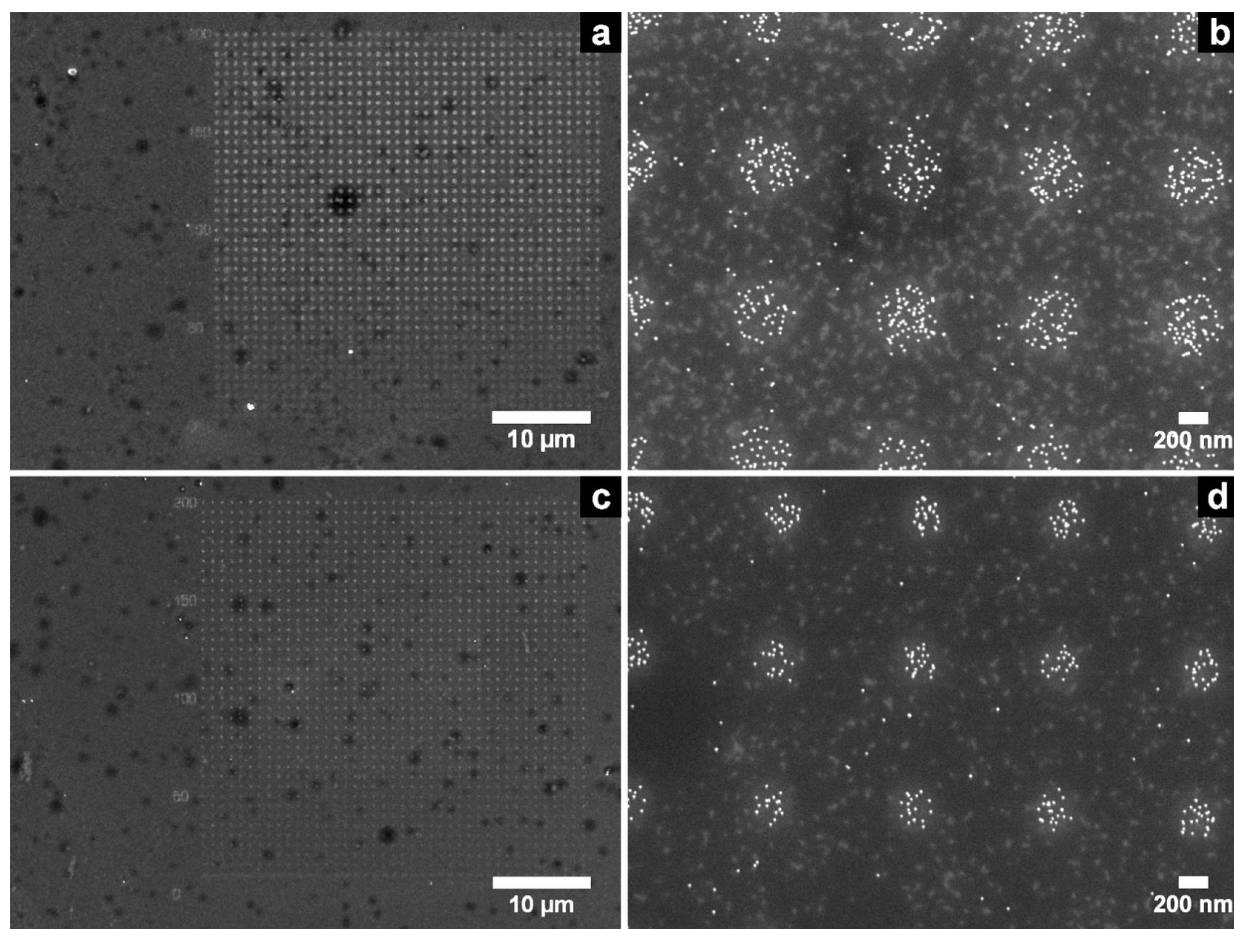
Figure 2: SEM pictures of irradiated CSPETCS layer on a Si/SiO$_2$ substrate (100 µm/40 nm) after incubation with a solution of 16 nm AuNPs. Two patterns with circular structures of different intended diameter were used: 400 nm (a,b) and 200 nm (c,d).
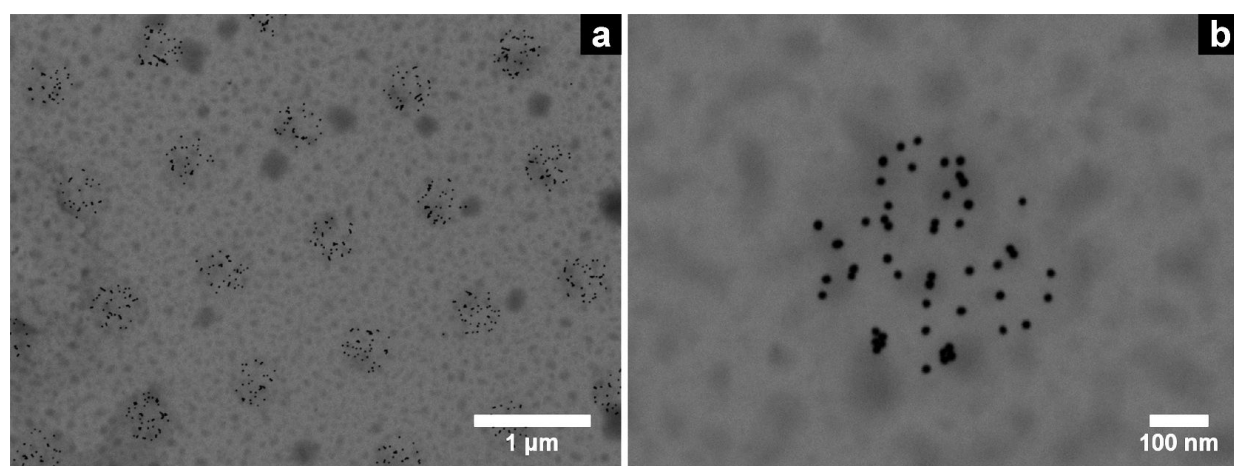

Figure 3: SEM-T micrographs of CSPETCS silanised SiO$_2$ TEM windows after irradiation and incubation with a solution of citrate-stabilised 16 nm AuNPs. The intended and the actual spot diameters are 400 nm and 400 ± 20 nm, respectively.

(d_S/d_{NP}) and the large distance between immobilised AuNPs (see Figure S4 and Figure S5 within Supporting Information File 1 for an example). In order to increase the coverage of these thiol patterns as well, we used 6 nm AuNPs with a larger d_S/d_{NP}. Figure 4 shows measurements by atomic force microscopy (AFM) of the structured surface (EHT = 2 kV and base dose of 10 $\mu C \cdot cm^{-2}$) after incubation. The density of immobilised particles within the irradiated structures is greater than 480 ± 30 NP/μm^2 and, therefore, slightly higher than the particle density of the previously shown structures.

Upon closer inspection, we found that the written and incubated structures exhibited regular super structures (Figure 5a), that resemble the used grating pattern (Figure 5b). The grating is performed on the basis of a pre-defined spacing S (also called beam step size), in this case 31 nm. The circular structure to be written is subdivided into concentric rings with decreasing diameter by a value of $2S$ (i.e., spacing of S). On the perimeters of these rings individual irradiation spots are placed, which are separated by S from each other. In order to expose this grated structure the electron beam dwells on these single spots.

To verify a direct correlation between the grating pattern and the generated super structures we measured random height profiles along the cross-sections of the circular structures (Figure 6a). Figure 6b shows an exemplary height profile within the AFM measurement in Figure 6a. From the peak-to-peak distance in this height profile the spacing between the concentric rings can be determined. The average spacing of the individual rings is $L_r = 30 \pm 8$ nm (cf. histogram of all measured spacings L_r in Figure 6c) and is, hence, originated by the initial grating spacing S. Since the actual diameter of the used Gaussian electron beam is much smaller (approx. 1 nm) than the grating distance, the electron dose applied to the SAM decreases with increasing distance from the grating spots (being lowest in the middle between two spots). The variation of the electron dose within the irradiated structure results in a variation of the thiol density. With decreasing particle size this thiol gradient becomes the driving force for the guided immobilisation into the observed super structure. Theoretical calculations show that the energy of scattered electrons of a 1 nm wide electron beam at 2 kV decreases exponentially with increasing distance from the point of incidence. With respect to a necessary threshold
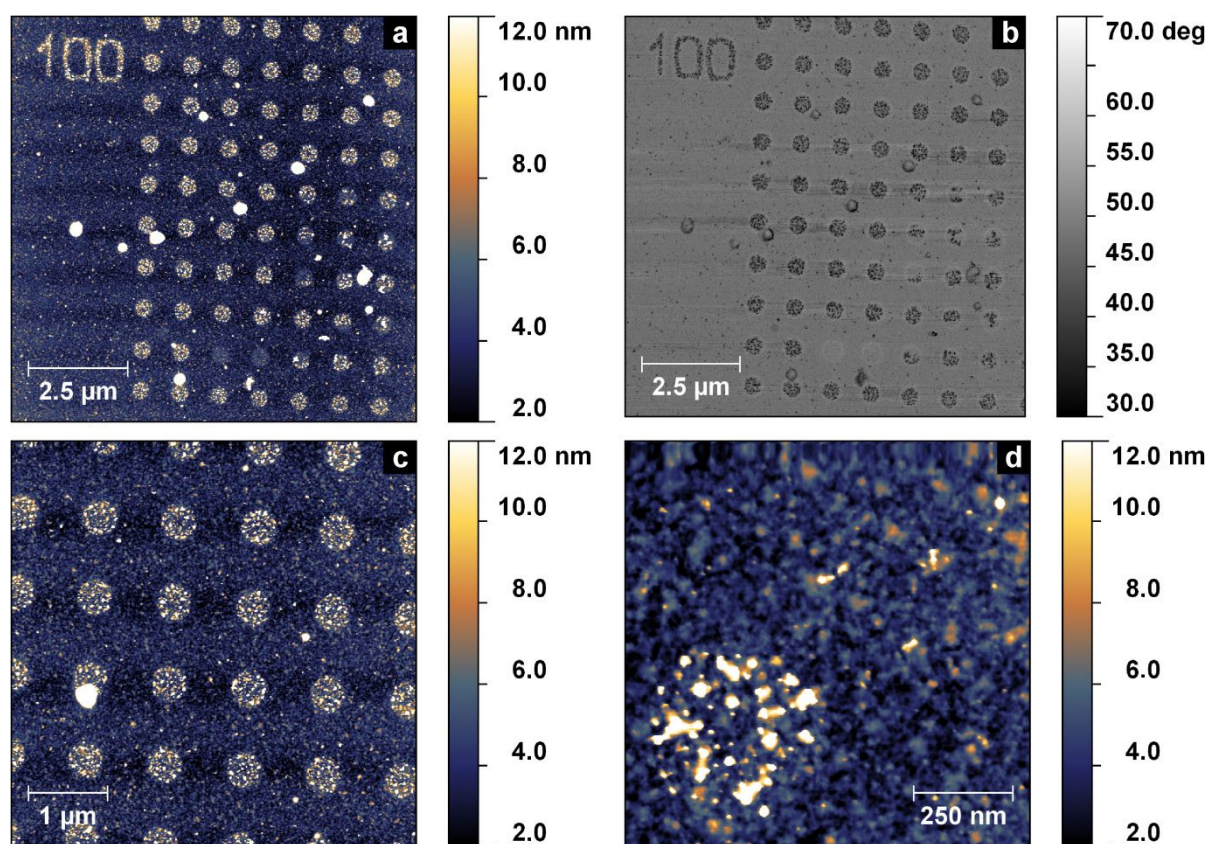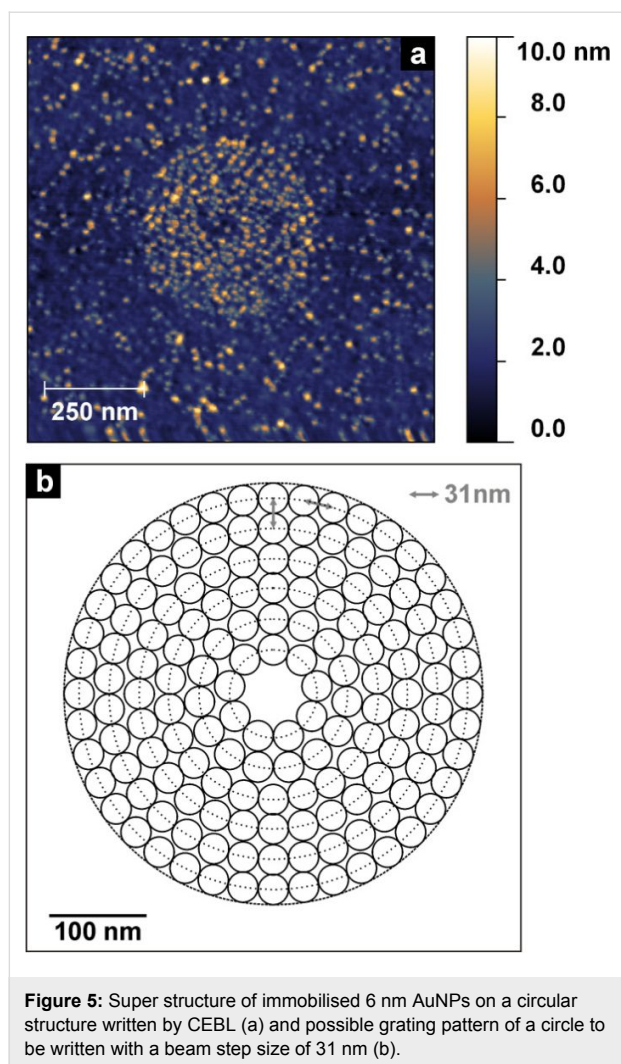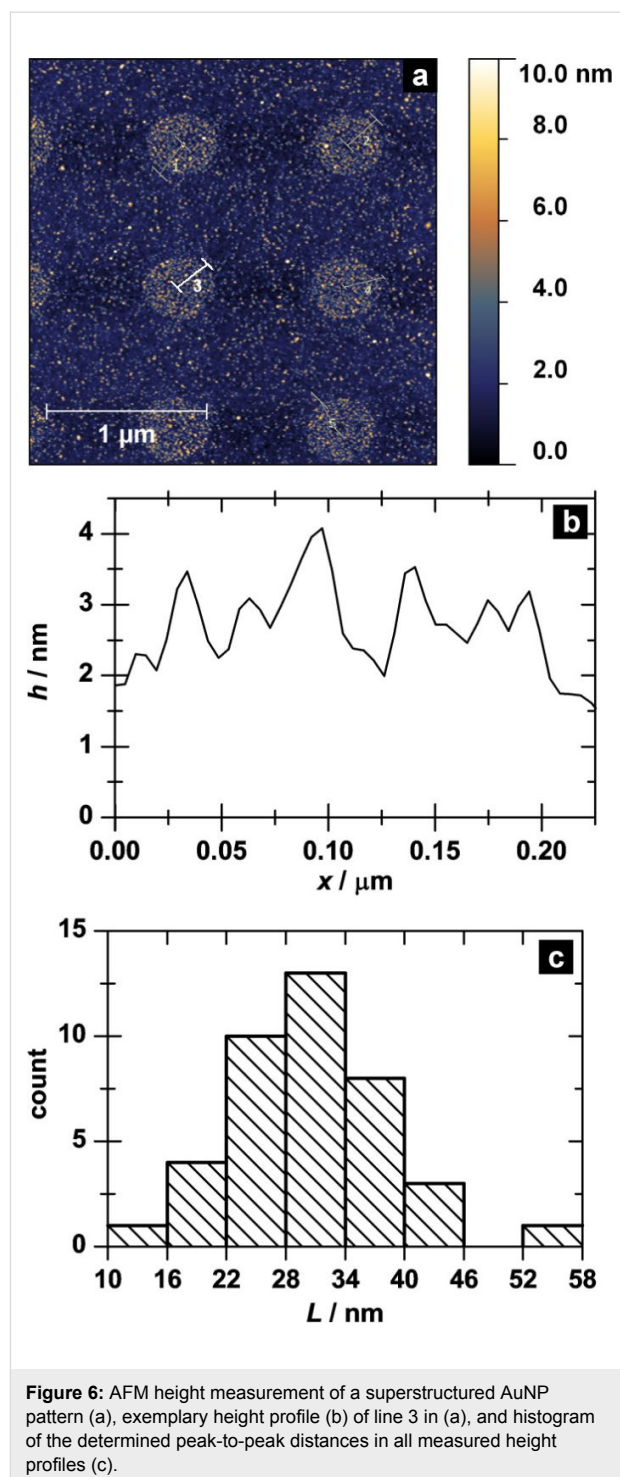

Figure 4: Height (a,c,d) and phase (b) measurements via AFM of an irradiated CSPETCS monolayer incubated with 6 nm AuNP.

Figure 5: Super structure of immobilised 6 nm AuNPs on a circular structure written by CEBL (a) and possible grating pattern of a circle to be written with a beam step size of 31 nm (b).

energy of around 10 eV for the first mechanistic step of the CEBL process (DEA, dissociative electron attachment) [15,16], the area that is effectively irradiated (i.e., where thiol groups are generated) is approximately 5–6 nm in diameter. Assuming that the immobilisation of a AuNP is most stable with a maximum contact area between AuNP and SAM, particles exhibit more linking possibilities with increasing size. This results in a significantly lower freedom of displacement for particles that match the spot size (i.e., 6 nm AuNPs in the present study).

Hence, it became possible to assemble single nanoparticles through guided immobilisation on CEBL-structured CSPETCS SAMs. Due to forward scattering of the electron beam within the substrate, primary and secondary electrons are able to exit the substrate outside of the actual area of beam incidence, resulting in SAM exposure outside the irradiated area. This phenomenon results in a higher effective dose of an irradiation point due to all other irradiation points in the near vicinity. A general problem in producing chemical patterns that are fine

Figure 6: AFM height measurement of a superstructured AuNP pattern (a), exemplary height profile (b) of line 3 in (a), and histogram of the determined peak-to-peak distances in all measured height profiles (c).

enough for guided single-particle immobilisation by CEBL is that with decreasing feature size and density, higher electron doses are needed in order to achieve a proper SAM reduction. This effect is also known from conventional lithography techniques and is called the "proximity effect" [17,18]. Unfortunately, higher doses and prolonged exposure times result in blurry and diffuse pattern generation.

In order to overcome the need for prolonged exposure we designed a periodic high-density pattern of single irradiation points (cf. Figure S6 in Supporting Information File 1). A CSPETCS SAM was then structured with this pattern using standard CEBL at EHT = 2 kV and a base dose of 10 μC·cm^{-2}. After incubation with citrate-stabilised 6 nm AuNP at pH 4.7, we analysed the substrate by AFM. Figure 7a and b show height measurements of the incubated surface.
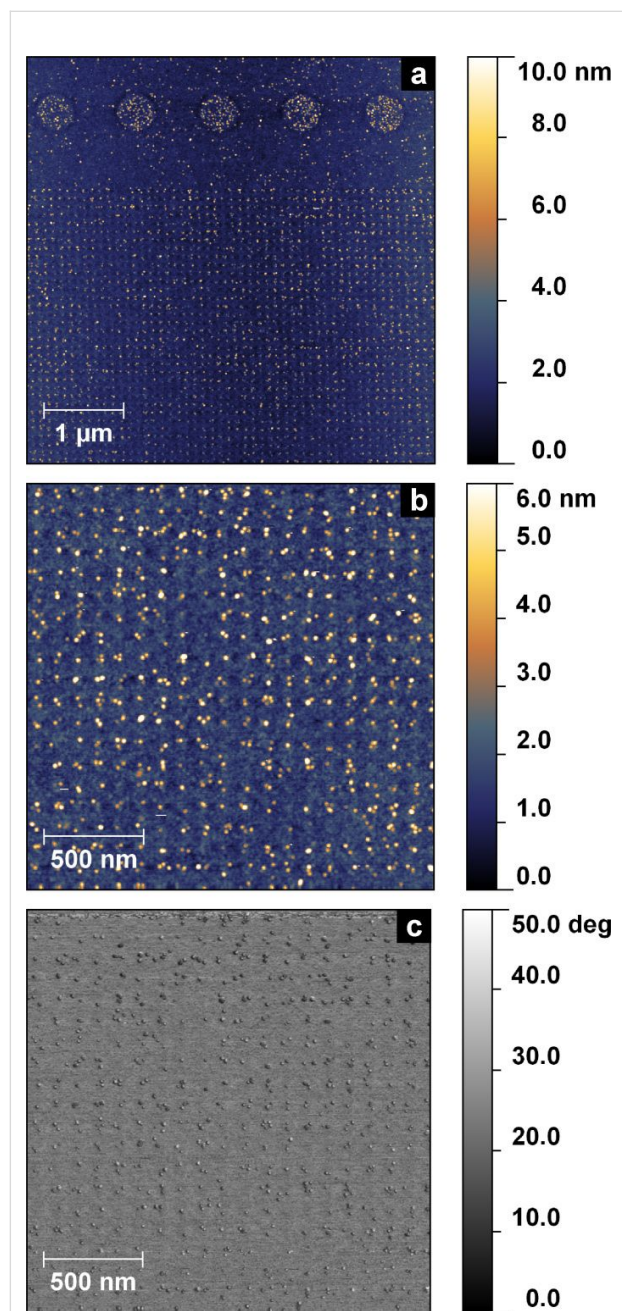
To analyse the precise arrangement of the immobilised AuNP we performed spatial autocorrelation (AC) in the x- and y-direction, the result of which are shown in Figure 8a and b. Both graphs show a high degree of order in both directions with spatial periodicities of $\Delta\tau_x = 103 \pm 3$ nm and $\Delta\tau_y = 103 \pm 2$ nm. This high periodicity proves the guided immobilisation of AuNP by the fabricated thiol array on the surface. In addition we performed a statistical analysis of the number of AuNPs per irradiation spot. The resulting histogram is shown in Figure 8c.
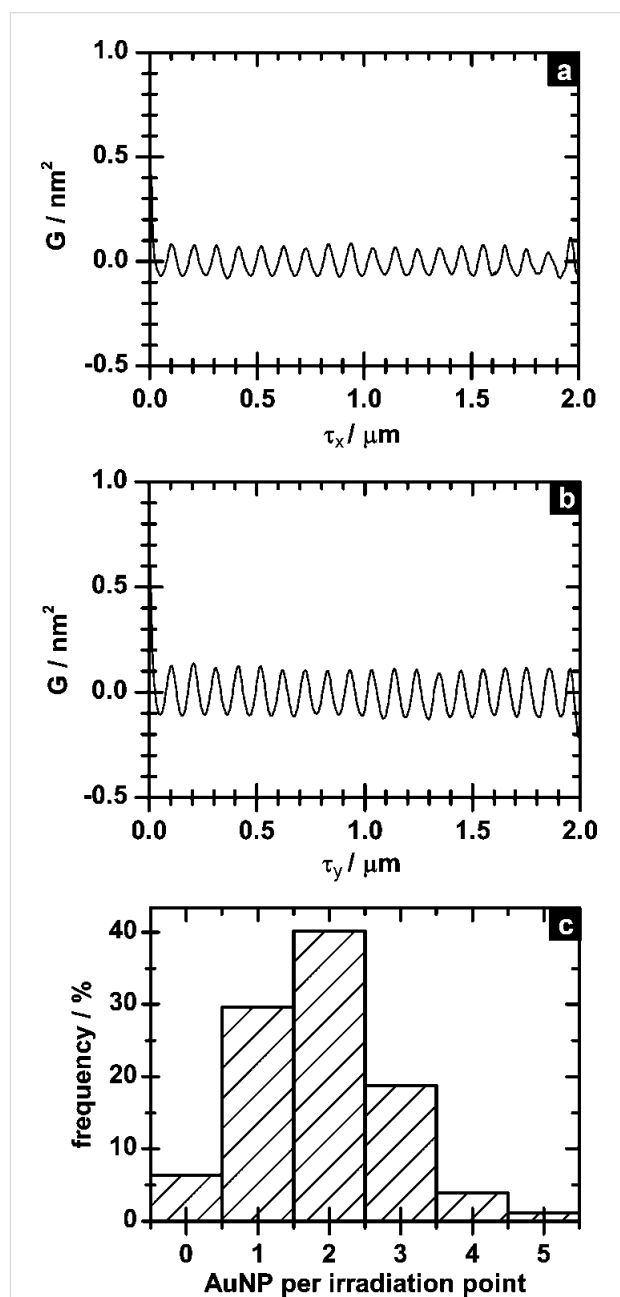

Figure 7: AFM measurements of height (a, b) and phase (c) of a CSPETCS SAM patterned by pointwise irradiation with electrons after incubation with citrate-stabilised 6 nm AuNP.

Figure 8: Horizontal (a) and vertical (b) spatial autocorrelation of AFM height measurement in Figure 7b and histogram of the number of AuNPs per irradiation spot (c).

Approximately 70% of all irradiation spots are covered with one or two AuNPs, indicating that the irradiation spots are indeed small enough to provided single-particle immobilisation. Hence, accuracy and immobilisation fidelity are comparable to other approaches presented in the literature with 13 nm AuNPs [11,12]. Since we immobilised significantly smaller AuNPs (6 nm), one can assume that the individual spots generated in our approach are approximately half the size. In addition, our approach benefits from a lower number of processing steps (i.e., three: SAM formation and irradiation followed by AuNP immobilisation).

Conclusion

In this work we present the fabrication of regular arrays of single AuNPs. These arrays were formed by guided immobilisation of AuNPs through chemically patterned SAMs in three processing steps. Through point-by-point electron irradiation we generated thiol patterns with a periodic pitch of 100 nm in the horizontal and vertical directions. AFM measurements proved that this periodicity was retained after immobilisation of 6 nm AuNPs. Due to the small size of an individual irradiation point approximately 70% of the thiol spots were covered with only one or two AuNPs. Furthermore, we could decorate free-standing 40 nm SiO_2 layers with AuNPs using the same approach and visualise the obtained AuNP patterns with SEM-T.

In the future, we are interested in transferring the generation of single AuNP arrays to other technically relevant substrates than Si/SiO_2. Therefore, we conducted initial experiments by fabrication of AuNP patterns on indium tin oxide (ITO) covered foils of polyethylene terephthalate (PET) (see Supporting Information File 1 for the preliminary results), which are quite promising.

Experimental
Materials

In this work two different kinds of oxide surfaces were used. Experiments on SiO_2 surfaces were conducted by using 40 nm thick SiO_2 membranes on 100 µm Si grids (suitable for TEM analyses) from Plano GmbH. In addition, flexible ITO-coated PET substrates from Aldrich were used. Toluene from Sigma Aldrich was dried over Na/benzophenone ketyl radical and distilled afterwards. 2-(4-Chlorosulfonylphenyl)ethyltrichlorosilane (CSPETCS) was purchased as a 50 wt % solution in toluene from ABCR GmbH. Ethanol (p.a.) was purchased from Grüssing GmbH. Ultrapure water was prepared by using a Purelab Ultra from Elga. Hydrogen tetrachloroaurate(III) trihydrate, sodium borohydride, and trisodium citrate dihydrate were purchased from Sigma Aldrich or Merck. Unless stated otherwise, all substances were used without any further purification.

Sample cleaning and silanisation

Prior to cleaning ITO-coated PET foils were cut into proper pieces. Both types of substrates (SiO_2 and ITO) were cleaned in oxygen plasma at $p(O_2) = 0.4$ mbar, $f = 40$ kHz, and $P = 100$ W, first for 2 min and then for 4 min. In the case of Si/SiO_2 substrates the initial SiO_2 thickness was measured by ellipsometry between both plasma cleaning steps. All samples were transferred directly into silanisation solutions after venting and silanised in dry toluene by the Schlenk technique. For this, a stem solution of 10 mM CSPETCS in dry toluene was prepared first. Cleaned samples were put into dried Schlenk tubes filled with 3 mL of dry toluene, and 1 mL of stem solution was added. The tube was then heated to 40 °C for 30 min. Afterwards all samples were thoroughly cleaned with ethanol, dried in a nitrogen stream, and annealed at 130 °C for 15 min.

E-beam lithography

Lithographic patterns were generated using a scanning electron microscope (Zeiss LEO Supra 35-VP) equipped with an Elphy Plus pattern generator (RAITH, software Elphy Plus version 4). Patterns were exposed at an accelerating voltage of 2 kV and basic electron doses of 10 µC·cm^{-2} and 50 µC·cm^{-2}, respectively.

Synthesis and deposition of AuNP

AuNPs with a diameter of 16 nm were synthesised according to known procedures from Turkevich and Frens by using 0.056 mM of tetrachloroaurate(III) trihydrate and 0.178 mM of trisodium citrate dehydrate [19-21]. Afterwards, the pH value was adjusted to 4.7 by centrifugation and redispersion in 10 mM citrate buffer.

In addition to citrate-stabilised 16 nm AuNPs, we synthesised citrate-stabilised AuNPs with a diameter of 6 nm. These particles were prepared by using a modified procedure reported by Patil et al. [22-24]. First, 50 mL of a stirred 0.5 mM solution of hydrogen tetrachloroaurate(III) was reduced by dropwise addition of 4.5 mL of a 48.5 mM solution of sodium borohydride. The red solution was stirred for 5 min and 2.5 mL of a 50 mM solution of trisodium citrate dihydrate was added as a capping agent. Finally, the solution was stirred for an additional 5 min. In order to adjust the pH value to 4.7, 50 mM citrate buffer was added until the buffer concentration in solution was equal to 10 mM.

Irradiated samples were incubated with this AuNP solution for 45 min up to 60 min in a closed chamber in order to prevent drop evaporation. Finally, the substrates were rinsed with a copious amount of ultrapure water and dried in a nitrogen stream.

Ellipsometry

To determine the SAM thicknesses ellipsometric measurements were performed by using a NFT I-Elli 2000 imaging ellipsometer equipped with a HeNe laser ($\lambda = 632.8$ nm). In order to calculate the film thicknesses we use values of $n = 3.8650$ and $k = 0.0200$ for Si and $n = 1.4650$ and $k = 0.0000$ for silicon dioxide and the organic layer [25,26].

AFM measurements

AFM measurements were conducted with a Digital Instruments NanoScope IIIa by using super sharp tips SSS-NCH-50 from Nanosensors with small tip diameters of approximately 2 nm and force constants between 10 N·m^{-1} and 130 N·m^{-1}. Image processing was performed by using the open-source software gwyddion 2.28 (http://gwyddion.net) [27]. In general, measurements were post-processed with the commands "Level data by mean plane subtraction", "Correct lines by matching height median" and "Correct horizontal scars (strokes)". In addition, measurements with an edge length greater than 5 µm or distinct curvature were also corrected with "Remove polynomial background (degree: 2)".

Calculation of primary electron paths

Paths of primary electrons in solid substrates were calculated with CASINO v2.48 (monte CArlo SImulation of electroN trajectory in sOlids) [28]. Therefore the following density values were used: $\rho(\text{Si}) = 2.3290$ g·cm^{-3} [29], $\rho(\text{SiO}_2) = 2.196$ g·cm^{-3} [29], $\rho(\text{CSPETCS}) = 1.35$ g·cm^{-3} (estimation using density values of commercially available solutions).

Supporting Information

Figures S1, S2 and S6 present CAD-drawings of the patterns used within the CEBL process. Figure S3 discusses theoretical calculations of primary electron pathways within the used substrates. SEM pictures of 100 nm structures incubated with 16 nm AuNPs are shown in Figures S4 and S5. Figure S7 presents preliminary results of AuNP pattern formation on ITO-covered PET foils by this approach.

Supporting Information File 1

Additional CAD-drawings, theoretical calculations and SEM pictures
[http://www.beilstein-journals.org/bjnano/content/supplementary/2190-4286-4-39-S1.pdf]

Acknowledgements

References

1. Clément, N.; Patriarche, G.; Smaali, K.; Vaurette, F.; Nishiguchi, K.; Troadec, D.; Fujiwara, A.; Vuillaume, D. *Small* **2011**, *7,* 2607–2613. doi:10.1002/smll.201100915
2. Service, R. F. *Science* **2006**, *314,* 1868–1870. doi:10.1126/science.314.5807.1868
3. Yang, X.; Xiao, S.; Wu, W.; Xu, Y.; Mountfield, K.; Rottmayer, R.; Lee, K.; Kuo, D.; Weller, D. *J. Vac. Sci. Technol., B* **2007**, *B25,* 2202–2209. doi:10.1116/1.2798711
4. Balcells, L.; Abad, L.; Rojas, H.; Perez del Pino, A.; Estrade, S.; Arbiol, J.; Peiro, F.; Martínez, B. *Small* **2008**, *4,* 365–371. doi:10.1002/smll.200700537
5. Gilles, S.; Winter, S.; Michael, K. E.; Meffert, S. H.; Li, P.; Greben, K.; Simon, U.; Offenhäusser, A.; Mayer, D. *Small* **2012**, *8,* 3357–3367. doi:10.1002/smll.201200465
6. Liu, P.; Sun, J.; Huang, J.; Peng, R.; Tang, J.; Ding, J. *Nanoscale* **2010**, *2,* 122–127. doi:10.1039/b9nr00124g
7. Tobing, L. Y. M.; Tjahjana, L.; Zhang, D. H. *Nanotechnology* **2013**, *24,* 075303. doi:10.1088/0957-4484/24/7/075303
8. Enderle, F.; Dubbers, O.; Plettl, A.; Ziemann, P. *Beilstein J. Nanotechnol.* **2012**, *3,* 773–777. doi:10.3762/bjnano.3.86
9. Vogel, N.; Ziener, U.; Manzke, A.; Plettl, A.; Ziemann, P.; Biskupek, J.; Weiss, C. K.; Landfester, K. *Beilstein J. Nanotechnol.* **2011**, *2,* 459–472. doi:10.3762/bjnano.2.50
10. Kästle, G.; Boyen, H.-G.; Weigl, F.; Lengl, G.; Herzog, T.; Ziemann, P.; Riethmüller, S.; Mayer, O.; Hartmann, C.; Spatz, J. P.; Möller, M.; Ozawa, M.; Banhart, F.; Garnier, M. G.; Oelhafen, P. *Adv. Funct. Mater.* **2003**, *13,* 853–861. doi:10.1002/adfm.200304332
11. Onses, M. S.; Liu, C.-C.; Thode, C. J.; Nealey, P. F. *Langmuir* **2012**, *28,* 7299–7307. doi:10.1021/la300552w
12. Gilles, S.; Kaulen, C.; Pabst, M.; Simon, U.; Offenhäusser, A.; Mayer, D. *Nanotechnology* **2011**, *22,* 295301. doi:10.1088/0957-4484/22/29/295301
13. Schaal, P. A.; Besmehn, A.; Maynicke, E.; Noyong, M.; Beschoten, B.; Simon, U. *Langmuir* **2012**, *28,* 2448–2454. doi:10.1021/la204393h
14. Lud, S. Q.; Neppl, S.; Richter, G.; Bruno, P.; Gruen, D. M.; Jordan, R.; Feulner, P.; Stutzmann, M.; Garrido, J. A. *Langmuir* **2010**, *26,* 15895–15900. doi:10.1021/la102225r
15. Turchanin, A.; Käfer, D.; El-Desawy, M.; Wöll, C.; Witte, G.; Gölzhäuser, A. *Langmuir* **2009**, *25,* 7342–7352. doi:10.1021/la803538z
16. Arumainayagam, C. R.; Lee, H.-L.; Nelson, R. B.; Haines, D. R.; Gunawardane, R. P. *Surf. Sci. Rep.* **2010**, *65,* 1–44. doi:10.1016/j.surfrep.2009.09.001
17. Menz, W.; Mohr, J.; Paul, O. *Mikrosystemtechnik für Ingenieure;* Wiley-VCH, 2005.
18. Chang, T. H. P. *J. Vac. Sci. Technol.* **1975**, *12,* 1271–1275. doi:10.1116/1.568515
19. Frens, G. *Nature* **1973**, *241,* 20–22.
20. Turkevich, J.; Stevenson, P. C.; Hillier, J. *J. Phys. Chem.* **1953**, *57,* 670–673. doi:10.1021/j150508a015
21. Turkevich, J.; Stevenson, P. C.; Hillier, J. *Discuss. Faraday Soc.* **1951**, *11,* 55–75. doi:10.1039/df9511100055
22. Patil, V.; Malvankar, R. B.; Sastry, M. *Langmuir* **1999**, *15,* 8197–8206. doi:10.1021/la990170t

23. Aryal, S.; Bahadur, K. C. R.; Bhattarai, N.; Kim, C. K.; Kim, H. Y. *J. Colloid Interface Sci.* **2006,** *299,* 191–197. doi:10.1016/j.jcis.2006.01.045

24. Aryal, S.; Remant, B. K. C.; Dharmaraj, N.; Bhattarai, N.; Kim, C. H.; Kim, H. Y. *Spectrochim. Acta, Part A* **2006,** *63,* 160–163. doi:10.1016/j.saa.2005.04.048

25. Kim, J.; Seidler, P.; Fill, C.; Wan, L. S. *Surf. Sci.* **2008,** *602,* 3323–3330. doi:10.1016/j.susc.2008.09.001

26. Pasternack, R. M.; Amy, S. R.; Chabal, Y. J. *Langmuir* **2008,** *24,* 12963–12971. doi:10.1021/la8024827

27. Nečas, D.; Klapetek, P. *Cent. Eur. J. Phys.* **2012,** *10,* 181–188. doi:10.2478/s11534-011-0096-2

28. Drouin, D.; Couture, A. R.; Joly, D.; Tastet, X.; Aimez, V.; Gauvin, R. *Scanning* **2007,** *29,* 92–101. doi:10.1002/sca.20000

29. Lide, D. R., Ed. *CRC Handbook of Chemistry and Physics;* CRC Press: Boca Raton Ann Arbor Boston, 2005.

The role of electron-stimulated desorption in focused electron beam induced deposition

Willem F. van Dorp[*1], Thomas W. Hansen[2], Jakob B. Wagner[2] and Jeff T. M. De Hosson[1]

Full Research Paper

Abstract

We present the results of our study about the deposition rate of focused electron beam induced processing (FEBIP) as a function of the substrate temperature with the substrate being an electron-transparent amorphous carbon membrane. When $W(CO)_6$ is used as a precursor it is observed that the growth rate is lower at higher substrate temperatures. From Arrhenius plots we calculated the activation energy for desorption, E_{des}, of $W(CO)_6$. We found an average value for E_{des} of 20.3 kJ or 0.21 eV, which is 2.5–3.0 times lower than literature values. This difference between estimates for E_{des} from FEBIP experiments compared to literature values is consistent with earlier findings by other authors. The discrepancy is attributed to electron-stimulated desorption, which is known to occur during electron irradiation. The data suggest that, of the $W(CO)_6$ molecules that are affected by the electron irradiation, the majority desorbs from the surface rather than dissociates to contribute to the deposit. It is important to take this into account during FEBIP experiments, for instance when determining fundamental process parameters such as the activation energy for desorption.

Introduction

When the electron beam in an electron microscope is focused on a sample in the presence of a precursor gas, it can be used to locally modify the sample. This process has gained increasing interest over the past ten years and is named focused electron beam induced processing (FEBIP) [1-3]. The molecules from the precursor gas (transiently) adsorb on the sample surface and dissociate into fragments when they are exposed to the electron

beam. If these fragments react with the target material to form a gaseous product, the target is etched locally (focused electron beam induced etching). If on the other hand the fragments form a residue, a deposit grows on the sample surface (focused electron beam induced deposition). In either case, the sample can be modified directly with the electron beam, in principle without the use of any extra processing before or after the electron

exposure. FEBIP is applied in various fields. Because electrons can be focused into narrow beams, small patterns can be defined with FEBIP. Sub-10 nm features can be written with the e-beam [4-6] and a deposition can even be carried out molecule by molecule in a transmission electron microscope [7]. FEBIP is used to repair masks for ultraviolet and extreme ultraviolet-light lithography [8] and to create, for instance, photonic devices [9], nanowires [10], tips for probe microscopy [11], and magnetic nanostructures [12,13]. FEBIP is a complex process, in which many parameters are involved. Examples are the residence times of the precursor molecules on the surface, the cross section or the reaction rate of dissociation, the local gas flux at the sample, etc. If we want to understand and model FEBIP, we need to understand how these parameters contribute to the final product.

In this paper we determined the activation energy for desorption, E_{des}, from a FEBIP experiment. The desorption energy plays a significant role in FEBIP, since (amongst others) it determines the residence time of the precursor molecules on the surface, which in turn affects the growth rate. The activation energy for desorption can be determined from FEBIP experiments by measuring the deposition rate as a function of substrate temperature and constructing an Arrhenius plot. Christy measured E_{des} in a FEBIP experiment for a siloxane (tetramethyl tetraphenyl trisiloxane, DC-704 pump oil) and found that the value found from the FEBIP experiment underestimates the desorption energy by a factor of two to three compared to reference values [14,15]. Li et al. have performed the same measurement for WF_6 [16] and found a desorption energy that was three to five times lower than expected. Li et al. explained this difference with electron-stimulated desorption. Electron-stimulated desorption is known to occur during electron irradiation, being the result of secondary electron emission. According to Madey and Yates, "electron bombardment can promote the desorption of ionic and neutral atomic and molecular species from the surface, can alter the bonding of surface species and can cause polymerization" [17]. While the latter two processes are driving forces for FEBIP, the amount of desorption from the surface may be significant during electron irradiation.

We determined the growth rate for $W(CO)_6$ as a function of substrate temperature and compare the extracted energies E_{des} with values found in the literature.

Results and Discussion

Arrays of dots were written in an environmental transmission electron microscope on an electron-transparent holey carbon membrane mounted on a Au grid. The substrate temperature was varied between 306 K to 371 K (from 33 °C to 98 °C, respectively) and the irradiation times per dot were varied from 0.1 to 12 s. The precursor was $W(CO)_6$ and the precursor pressure during writing was 1.7 Pa. Figure 1a shows an example of a dot array, written with an irradiation time of 6 s per dot at a substrate temperature of 341 K.

The annular dark field (ADF) signal was used for imaging. In ADF images the dot intensity is proportional to the deposited mass, assuming a constant composition of the deposited material. Therefore, the mass of each dot can be determined by integrating the ADF intensity on each position in the array. The details of this method are described in [18]. We have varied the beam current to determine whether the growth is limited by the electron flux or the precursor flux. The beam current was varied from spot 10 (low beam current) to spot 7 (high beam current). The ratio between the beam currents was measured by integrating the intensity of Ronchigrams [19] recorded on a charge coupled device (CCD) camera. The integrated intensity of the Ronchigram is proportional to the incident beam current. The
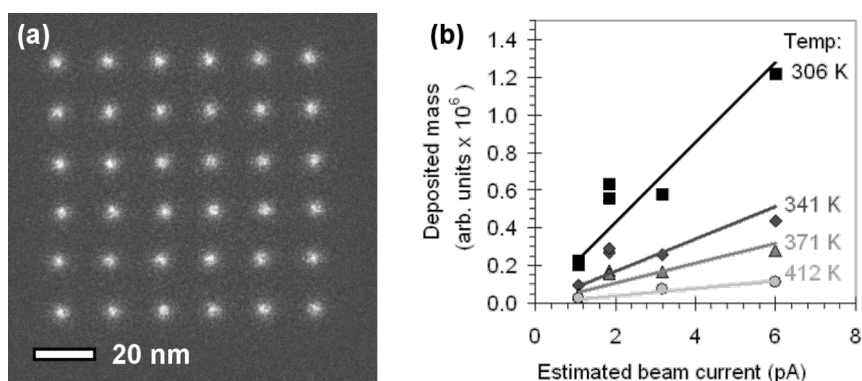

Figure 1: (a) An array of dots written at a substrate temperature of 306 K (33 °C) and a dwell time of 3 s per dot. (b) The deposited mass as a function of beam current and substrate temperature. The dwell time was 3 s per dot for all arrays.

beam currents were estimated by correlating the counts of the CCD camera in STEM-mode (in arbitrary units) to the reading of the fluorescent screen in TEM-mode (in A/cm^2). The estimated beam currents are given in Table 1 and range between 1 and 6 pA, which is consistent with values reported in literature [20,21]. Figure 1b shows the average deposited mass per dot as a function of beam current and substrate temperature. In this case the dwell time was 3 s per dot for all arrays. From the fact that the deposited mass increases with the beam current, we conclude that the growth is electron-limited at all substrate temperatures.

Table 1: The counts on the CCD camera and the estimated beam current as a function of spot size.

spot	CCD camera counts (arb. units)	estimated beam current (pA)
10	2.1	1.1
9	3.5	1.9
8	5.9	3.2
7	11.0	6.0

The effect of the dwell time is studied by writing arrays of dots with spot 9 at three temperatures, 306 K, 341 K and 371 K. The average deposited mass per dot is plotted as a function of the dwell time in Figure 2a (see below), from which E_{des} can be determined. Following the model proposed by Müller et al. [22], the precursor coverage, $N \cdot$(cm^{-2}), depends on the adsorption from the gas phase, the diffusion of precursor molecules over the surface, the number of molecules consumed in the reaction with the electrons and desorption to the gas phase:

where g is the sticking factor, F is the gas flux, N_0 is the density of adsorption sites in a monolayer, D is the diffusion coefficient, $\sigma_{(E)}$ is the cross section for dissociation, J is the electron flux, and τ is the residence time of the molecules on the surface. The first term describes adsorption of precursor molecules from the gas phase on available sites on the substrate. The second term describes the number of molecules arriving at the writing position due to surface diffusion, the contribution of which depends on the concentration gradient. The last two terms describe dissociation by the electron beam and desorption from the substrate to the gas phase. The growth rate, R (cm·s^{-1}), can be defined as:

$$R = V_{molecule} \sigma_{(E)} NJ \qquad (2)$$

with $V_{molecule}$ (cm^3) being the volume of a deposited molecule.

Equation 1 has two temperature-dependent terms: diffusion and desorption. If, in a first approach, we assume that the supply of precursor molecules to the writing position through diffusion does not play a significant role, the effect of the substrate temperature follows simply from Equation 1. The residence time τ of the precursor molecule on the sample depends on temperature:

$$\tau = 1/\upsilon \exp\left(E_{des}/k_B T\right) \qquad (3)$$

When the substrate temperature increases, the residence time of the molecules on the surface will become shorter and the desorption term in Equation 1 becomes larger. The precursor

$$dN/dt = gF\left(1 - N/N_0\right) + D\left(\delta^2 n/\delta r^2 - \delta n/r\delta r\right) - \sigma_{(E)} NJ - N/\tau \qquad (1)$$
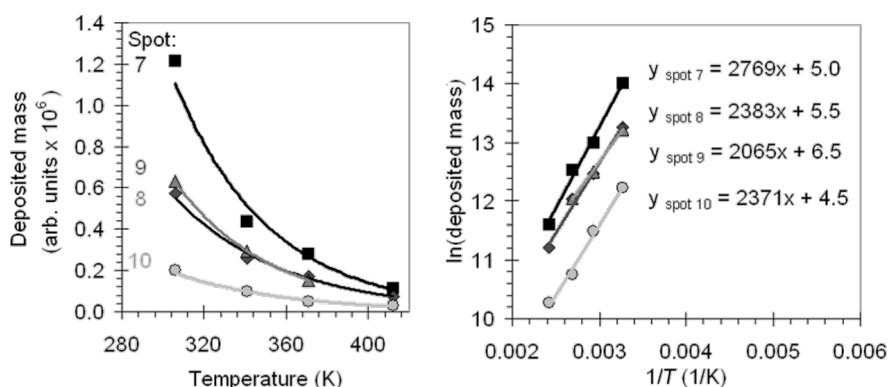

Figure 2: (a) The average deposited mass per dot as a function of substrate temperature and beam current. (b) The Arrhenius plot for the four beam currents, constructed from the data in (a).

coverage, N, decreases, which leads to a lower growth rate R. In Figure 2a the same data from Figure 1b is plotted again, this time as a function of substrate temperature. The behavior described by Equation 3 is observed in Figure 1b and Figure 2a; for all beam currents the amount of deposited mass becomes smaller at higher temperatures. Based on the data in Figure 2a we made an Arrhenius plot (Figure 2b), with the natural logarithm of the average deposited mass per array as a function of $1/T$. The slope of the fitted linear function is proportional to E_{des}/k_B. The values for E_{des} we calculated from the data in Figure 2b vary between 17.2 kJ/mol and 23.0 kJ/mol or 0.18 eV and 0.24 eV.

Since the dots are small (a full width at half maximum between 3 and 5 nm), surface diffusion is potentially an important precursor supply mechanism. Both desorption and diffusion are thermally activated according to the same exponential law. For an adsorbed precursor molecule the energy threshold for desorption E_{des} is much larger than the threshold E_{diff} to move from one adsorption site to an adjacent one [2]. So while molecules diffuse faster across the surface at higher temperatures, effectively the diffusion path length becomes shorter because desorption will occur sooner. This reduces the total number of precursor molecules that are transported by surface diffusion to the writing location.

We therefore verified whether a contribution of surface diffusion is observed in the measurements. The data presented in Figure 1b (and in Figure 2a) is the result of spot exposures with a fixed dwell time of 3 s. The number of precursor molecules that arrive at the writing location through surface diffusion is time-dependent. If the contribution of the surface diffusion to the precursor transport is significant, this becomes apparent when the dwell time is varied. We deposited arrays with dwell times ranging from 0.1 s to 12.0 s as a function of the substrate

temperature, all with spot 9 (i.e., a constant current density). We determine the growth rate R by taking the slope of the fitted linear functions in Figure 3a. In Figure 3b an Arrhenius plot is shown, where $\ln(R)$ is plotted as a function of $1/T$. We found a linear dependency, from which we calculated that $E_{des} = 21.7$ kJ/mol or 0.22 eV.

The values for E_{des} obtained from the deposition experiments are collected in Figure 4. It is observed that the value for E_{des} obtained with varying dwell times (from 0.1 s to 12.0 s) falls within the scatter of the data obtained with a constant dwell time of 3 s. This suggests that surface diffusion does not play a significant role in these experiments. This finding is consistent with the value of the gas pressure. We can calculate the number of precursor molecules striking an area on the surface from the gas phase with [23]:

$$F = 3.513 \times 10^{22} P (MT)^{-0.5} \qquad (4)$$

with F being the flux of molecules arriving at the surface, P the pressure in Torr, and M the molecular mass. A pressure of 1.7 Pa gives a flux of 1.4×10^{18} molecules·cm^{-2}·s^{-1}, or 1.4×10^4 molecules·nm^{-2}·s^{-1}. Assuming a dot diameter of 4 nm and taking into account that both the upper and lower surface of the holey carbon membrane are exposed to the precursor gas, the flux on the dot area is 3.5×10^5 molecules·s^{-1}. In comparison, an estimated 300–1500 molecules W(CO)$_6$ are necessary to form a 4 nm dot [18]. The dwell time per dot is 3 s, which makes the flux of precursor molecules arriving from the gas phase about three orders of magnitude larger than the consumption by the e-beam. Even when the sticking coefficient is smaller than 1, the transport of precursor molecules through the gas phase is sufficient to grow the dots, making the contribution from surface diffusion non-dominant in this experiment.
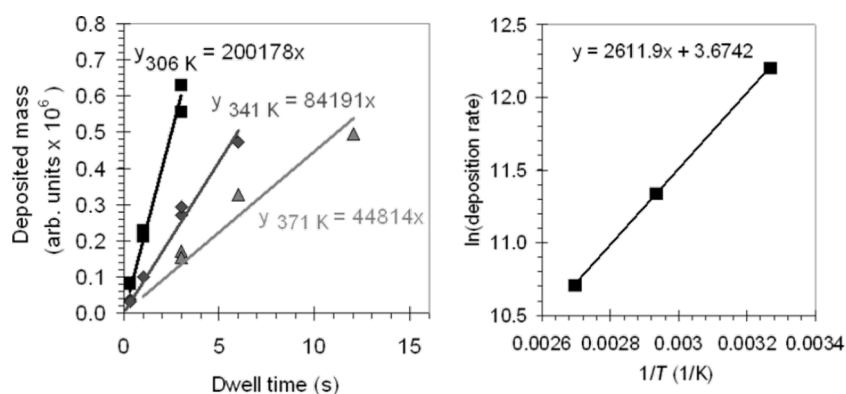

Figure 3: (a) The average deposited mass per dot as a function of dwell time and substrate temperature. The dots are written with spot 9. (b) The Arrhenius plot (the natural logarithm of the deposition rate as a function of the inverse of the temperature) constructed from the data in (a).
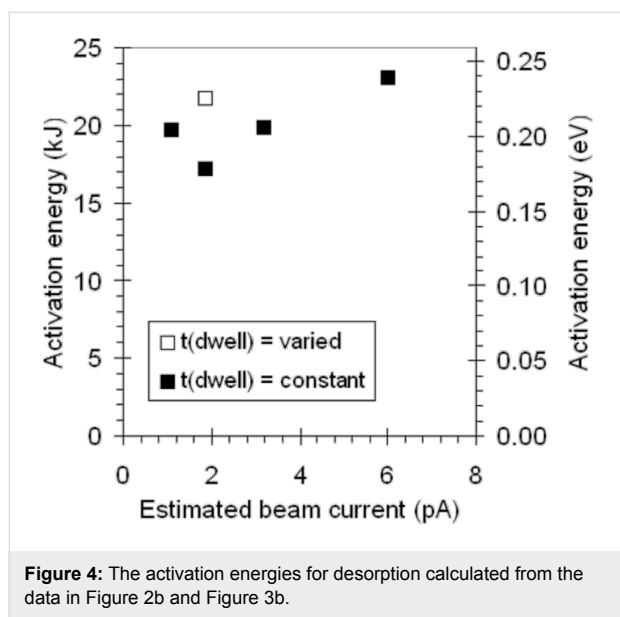
Figure 4: The activation energies for desorption calculated from the data in Figure 2b and Figure 3b.

Figure 4 shows that the activation energy for desorption E_{des}, calculated for $W(CO)_6$, varies significantly, from 17.2 kJ/mol to 23.0 kJ/mol. Assuming a random variation, the average value for E_{des} is 20.3 kJ/mol (or 0.21 eV).

A reference value for $W(CO)_6$ determined by temperature-programmed desorption (TPD) measurements is 53.8 kJ/mol or 0.56 eV (for desorption from multilayers of $W(CO)_6$) [24]. It is observed that the values found in the FEBIP experiments are lower by a factor of 2.5–3.0. A possible explanation for this difference is the fact that the desorption energy is substrate-dependent. The FEBIP and TPD values have been determined using different substrates (amorphous carbon and Ni(100) [24], respectively). However, this does not explain the large discrepancy between the values. Measurements of E_{des} for $MeCpPt(IV)Me_3$ (a well-known precursor for FEBIP) differ only by about 10% for the substrates Au(110) and a mixture of amorphous carbon and platinum [25]. This indicates that the factor of 2.5–3.0, which we observed here, cannot be explained solely by a substrate effect.

This conclusion is consistent with the report from Christy for a siloxane [14] and from Li et al. for WF_6 [16]. The values for the activation energy Li et al. obtained from FEBIP experiments range from 71 meV to 210 meV, depending on the beam current (51 pA to 3400 pA) and acceleration voltage (5 to 30 kV). Similar to our findings, these values for E_{des} are a factor of 1.5 to 5.0 lower than the values found by TPD [26-28]. A difference to our results is that the calculated E_{des} does not decrease strongly with increasing beam current as Li et al. observe. However, this can be explained with a smaller range of beam currents that we use in our experiments. Li et al. varied the

beam currents between 51pA and 3400 pA, in our experiments the estimated beam currents are between 1 and 6 pA.

The results demonstrate that indeed electron-stimulated desorption plays a significant role in FEBIP. The FEBIP value for E_{des} is three times lower than the TPD value, which we assume is more realistic. In order to find a realistic value for E_{des} from the FEBIP experiment, the difference between the growth rate at the lowest temperature (306 K) and the highest temperature (371 K) would need to be 25 times larger than it is in the actual experiment. In other words, of the $W(CO)_6$ molecules that are affected by the electron irradiation, the majority desorbs from the surface rather than dissociates to contribute to the deposit.

This effect is not limited to WF_6 or $W(CO)_6$, but extends to electron-induced chemistry in general. According to Madey and Yates, "generally many more neutrals than ions are observed in electron-stimulated desorption" [17]. Menzel concludes that "neutrals and ions are observed to desorb under electron impact, with the neutrals contributing more than 95% of the total yield in most cases" [29]. Although the percentage of neutrals may vary with the incident electron energy [29], from our experiments it is clear that it is still significant at energies used in FEBIP. This can be important to take into account when calculating parameters such as residence times, cross sections, etc. from the amount of deposited or etched material in FEBIP experiments.

Conclusion

The deposition rate of focused electron beam induced processing (FEBIP) has been studied as a function of the substrate temperature. Using the precursor $W(CO)_6$ it was observed that the growth rate is lower at higher substrate temperatures. The measurements enables us to construct Arrhenius plots based on the measurement data, from which we calculated the activation energy for desorption, E_{des}. We found an average value for E_{des} of 20.3 kJ or 0.21 eV. This is about 2.5–3.0 times lower than literature values. This difference between values measured with FEBIP and those reported in literature is consistent with findings by Christy [14] and Li et al. [16].

We contribute this discrepancy to electron-stimulated desorption, which is known to occur during electron irradiation. Electron-stimulated desorption is observed for many adsorbates and is induced by secondary electron emission. Our experimental result suggests that, of the $W(CO)_6$ molecules that are affected by the electron irradiation, the majority desorbs from the surface rather than dissociates to contribute to the deposit. This is important to take into account during FEBIP experiments, for instance when determining fundamental process parameters such as the activation energy for desorption.

Experimental

Experiments were performed on a FEI Titan 80-300 environmental scanning transmission electron microscope (STEM). A differential pumping system enabled a pressure of up to 10^3 Pa at the sample, while keeping the rest of the column at high vacuum. The microscope was operated at 300 kV [30]. The STEM images were recorded with the annular dark field (ADF) detector at a camera length of 245 mm (inner detector angle 30 mrad). Before the deposition experiments the microscope and the sample holder were plasma cleaned. The precursor was $W(CO)_6$ (CAS 14040-11-0), a low-vapor pressure solid ($\approx$0.034 mbar at 25 °C [31]). The precursor pressure during writing was 1.7 Pa. Holey carbon membranes mounted on a Au grid were used as substrates for the FEBIP. Prior to the deposition experiments the sample was heated to 573 K (300 °C) for 45 min in the microscope at high vacuum conditions (10^{-4} Pa) in order to minimize contamination during writing.

Acknowledgements

References

1. Huth, M.; Porrati, F.; Schwalb, C.; Winhold, M.; Sachser, R.; Dukic, M.; Adams, J.; Fantner, G. *Beilstein J. Nanotechnol.* **2012,** *3,* 597–619. doi:10.3762/bjnano.3.70
2. Utke, I.; Hoffman, P.; Melngailis, J. *J. Vac. Sci. Technol., B* **2008,** *26,* 1197–1276. doi:10.1116/1.2955728
3. van Dorp, W. F.; Hagen, C. W. *J. Appl. Phys.* **2008,** *104,* 081301. doi:10.1063/1.2977587
4. van Kouwen, L.; Botman, A.; Hagen, C. W. *Nano Lett.* **2009,** *9,* 2149–2152. doi:10.1021/nl900717r
5. Mackus, A. J. M.; Dielissen, S. A. F.; Mulders, J. J. L.; Kessels, W. M. M. *Nanoscale* **2012,** *4,* 4477–4480. doi:10.1039/c2nr30664f
6. Jiang, H.; Borca, C. N.; Xu, B.; Robertson, B. W. *Int. J. Mod. Phys. B* **2001,** *15,* 3207–3213. doi:10.1142/S021797920100749X
7. van Dorp, W. F.; Zhang, X.; Feringa, B. L.; Hansen, T. W.; Wagner, J. B.; De Hosson, J. T. M. *ACS Nano* **2012,** *6,* 10076–10081. doi:10.1021/nn303793w
8. Lassiter, M. G.; Liang, T.; Rack, P. D. *J. Vac. Sci. Technol., B* **2008,** *26,* 963–967. doi:10.1116/1.2917076
9. Seo, M.-K.; Kang, H.-J.; Kim, M.-K.; Ahn, B.-H.; Kim, J.-Y.; Jeong, K.-Y.; Park, H.-G.; Lee, Y.-H. *Opt. Express* **2009,** *17,* 6790–6798. doi:10.1364/OE.17.006790
10. Porrati, F.; Begun, E.; Winhold, M.; Schwalb, C. H.; Sachser, R.; Frangakis, A. S.; Huth, M. *Nanotechnology* **2012,** *23,* 185702. doi:10.1088/0957-4484/23/18/185702
11. Comstock, D. J.; Elam, J. W.; Pellin, M. J.; Hersam, M. C. *Rev. Sci. Instrum.* **2012,** *83,* 113704. doi:10.1063/1.4767248
12. Serrano-Ramón, L.; Córdoba, R.; Rodríguez, L. A.; Magén, C.; Snoeck, E.; Gatel, C.; Serrano, I.; Ibarra, M. R.; De Teresa, J. M. *ACS Nano* **2011,** *5,* 7781–7787. doi:10.1021/nn201517r
13. Gavagnin, M.; Wanzenboeck, H. D.; Belić, D.; Bertagnolli, E. *ACS Nano* **2013,** *7,* 777–784. doi:10.1021/nn305079a
14. Christy, R. W. *J. Appl. Phys.* **1960,** *31,* 1680–1683. doi:10.1063/1.1735915
15. Stewart, T. B.; Arnold, G. S.; Hall, D. F.; Marten, H. D. *J. Phys. Chem.* **1989,** *93,* 2393–2400. doi:10.1021/j100343a037
16. Li, W.; Joy, D. C. *J. Vac. Sci. Technol., A* **2006,** *24,* 431–436. doi:10.1116/1.2187995
17. Madey, T. E.; Yates, J. T., Jr. *J. Vac. Sci. Technol.* **1971,** *8,* 525–555. doi:10.1116/1.1315200
18. van Dorp, W. F.; van Someren, B.; Hagen, C. W.; Kruit, P.; Crozier, P. A. *J. Vac. Sci. Technol., B* **2006,** *24,* 618–622. doi:10.1116/1.2170099
19. Browning, N. D.; Arslan, I.; Moeck, P.; Topuria, T. *Phys. Status Solidi B* **2001,** *227,* 229–245. doi:10.1002/1521-3951(200109)227:1<229::AID-PSSB229>3.0.CO;2-F
20. Ketharanathan, S.; Sharma, R.; Crozier, P. A.; Drucker, J. *J. Vac. Sci. Technol., B* **2006,** *24,* 678–681. doi:10.1116/1.2178372
21. Egerton, R. F.; Crozier, P. A.; Rice, P. *Ultramicroscopy* **1987,** *23,* 305–312. doi:10.1016/0304-3991(87)90240-3
22. Müller, K. *Optik* **1971,** *33,* 296–311.
23. Ohring, M. *The Materials Science of Thin Films;* Academic Press: San Diego, CA, USA, 1992.
24. Zaera, F. *J. Phys. Chem.* **1992,** *96,* 4609–4615. doi:10.1021/j100190a086
25. van Dorp, W. F.; Wnuk, J. D.; Gorham, J. M.; Fairbrother, D. H.; Madey, T. E.; Hagen, C. W. *J. Appl. Phys.* **2009,** *106,* 074903. doi:10.1063/1.3225091
26. Jackman, R. B.; Foord, J. S. *Appl. Phys. Lett.* **1986,** *49,* 196–198. doi:10.1063/1.97168
27. Chen, W.; Roberts, J. T. *Surf. Sci.* **1995,** *324,* 169–184. doi:10.1016/0039-6028(94)00726-8
28. Jackman, R. B.; Foord, J. S. *Surf. Sci.* **1988,** *201,* 47–58. doi:10.1016/0039-6028(88)90596-1
29. Menzel, D. *J. Vac. Sci. Technol.* **1982,** *20,* 538–543. doi:10.1116/1.571428
30. Hansen, T. W.; Wagner, J. B.; Dunin-Borkowski, R. E. *Mater. Sci. Technol.* **2010,** *26,* 1338–1344. doi:10.1179/026708310X12756557336355
31. Lai, K. K.; Lamb, H. H. *Thin Solid Films* **2000,** *370,* 114–121. doi:10.1016/S0040-6090(00)00943-3